

“Crystal structures and vibrational properties of chalcogenides: the role of temperature and pressure”

Von der Fakultät für Georessourcen und Materialtechnik
der Rheinisch-Westfälischen Technischen Hochschule Aachen

zur Erlangung des akademischen Grades eines

Doktors der Naturwissenschaften

genehmigte Dissertation

vorgelegt von M.Sc.

Markus Guido Herrmann

aus Bad Schwalbach

Berichter: PD Dr. rer. nat. habil. Karen Friese
Univ.-Prof. Dr. rer. nat. Georg Roth

Tag der mündlichen Prüfung: 24. Juni 2019

Diese Dissertation ist auf den Internetseiten der Universitätsbibliothek
online verfügbar

Declaration of Authorship

Hiermit versichere ich, Markus Guido Herrmann, an Eides statt, dass ich die vorliegende Arbeit "Crystal structures and vibrational properties of chalcogenides: the role of temperature and pressure" selbstständig und ohne fremde Hilfe angefertigt habe und mich keiner anderer als der im beigefügten Verzeichnis angegebenen Hilfsmittel bedient habe. Alle Stellen, die wörtlich oder sinngemäß aus Veröffentlichungen oder anderen Quellen entnommen wurden, sind als solche kenntlich gemacht. Des Weiteren versichere ich, dass ich die Arbeit zu keinem früheren Zeitpunkt in einem anderen Prüfungsverfahren eingereicht habe.

I, Markus Guido Herrmann, declare that this thesis entitled as "Crystal structures and vibrational properties of chalcogenides: the role of temperature and pressure" and the work presented in it are my own. I confirm that all information which has been derived from other sources are indicated in the text. I have not submitted this thesis to any other doctorate examinations at any previous time.

Signed:

Date:

Contents

Declaration of Authorship	i
Abstract/Zusammenfassung	1
1 Introduction	5
2 Theory	8
2.1 Crystal structure determination	8
2.1.1 Single crystal vs. powder diffraction	8
2.1.2 The phase problem	8
2.1.3 Structure solution: Direct Methods	9
2.1.4 Structure refinement	10
2.1.4.1 Least square method	10
2.1.4.2 Le Bail method	10
2.1.5 Agreement factors	12
2.2 Inelastic Neutron Scattering	13
2.2.1 Elastic and inelastic scattering	13
2.2.2 Scattering cross section and scattering function	14
2.2.3 The one-phonon scattering function and the incoherent ap- proximation	15
2.2.4 The ARCS beamline	16
2.2.5 Data transformation	17
2.3 Nuclear Resonant Scattering	17
2.3.1 Mössbauer spectroscopy	17
2.3.2 The Nuclear Resonant Scattering Station at the beamline P01, PETRA-III (DESY)	19
2.3.3 Nuclear Inelastic Scattering	21
2.3.3.1 Nuclear Inelastic Scattering and Nuclear Inelastic Ab- sorption	21
2.3.3.2 The nuclear absorption spectrum	22
2.3.3.3 Determination of (partial) phonon density of states	23
2.4 The Phonon Density of States: Important relations	25
2.5 Equations of State	26
2.6 Heat capacity measurements	26
2.6.1 Theory of heat capacity	26
2.6.2 The lattice contribution to the total heat capacity	27

2.6.3	Validity of the Debye model - the non-Debye model	28
2.6.4	Thermodynamics of solid solutions	29
2.6.5	Experimental determination of heat capacity: Thermal relaxation calorimetry	29
3	Experimental part	32
3.1	Synthesis	32
3.1.1	Synthesis of $\text{Sb}_2\text{Te}_{3-x}\text{Se}_x$ mixed crystals	32
3.1.1.1	Introduction	32
3.1.1.2	Synthesis of polycrystalline samples of Sb_2Te_3 and Sb_2Se_3	33
3.1.1.3	Synthesis of polycrystalline $\text{Sb}_2\text{Te}_{3-x}\text{Se}_x$ mixed crystals	33
3.2	Sample characterization	34
3.2.1	Powder diffraction	34
3.3	Low-temperature heat capacity measurements	34
3.4	High-pressure diffraction	35
3.4.1	Diamond anvil cell	35
3.4.2	Ruby fluorescence method	36
3.4.3	The Extreme Conditions Beamline P02.2 at PETRA III, DESY	36
3.4.4	High-pressure powder diffraction	37
3.5	Inelastic neutron scattering: Experimental details	38
3.6	Nuclear inelastic scattering	38
3.6.1	Experimental details	38
3.6.2	Energy resolution	39
4	Data processing	42
4.1	Determination of lattice parameter from powder data	42
4.2	Processing of high-pressure single crystal diffraction data	42
4.3	Extraction of (partial) phonon density of states from inelastic neutron and nuclear inelastic scattering data	43
4.3.1	Binning of INS and NIS raw data	43
4.3.2	Processing of inelastic neutron scattering (INS) data	43
4.3.2.1	Extraction of total phonon density of states from INS data	43
4.3.2.2	Normalization of total phonon density of states	46
4.3.2.3	Calculation of heat capacity from INS data	46
4.3.3	Processing of nuclear inelastic scattering (NIS) data	47
4.3.3.1	Extraction of the partial phonon density of states from NIS data	47
4.3.3.2	Normalization of partial phonon density of states	47
4.3.3.3	Application of the homology relation	47
4.3.4	Calculation of Debye temperatures from INS and NIS data	48

4.3.5	Extraction of Se partial phonon density of states	48
5	Results	50
5.1	High-pressure and low-temperature behavior of $\text{GeSe}_x\text{Te}_{1-x}$ compounds	50
5.1.1	Introduction	50
5.1.1.1	The $\text{GeSe}_x\text{Te}_{1-x}$ solid solution: state of the art	50
5.1.1.2	Aims of this study	56
5.1.2	Sample characterization	57
5.1.3	Low-temperature behavior	59
5.1.3.1	GeTe , $\text{GeSe}_{0.2}\text{Te}_{0.8}$, $\text{GeSe}_{0.5}\text{Te}_{0.5}$ and $\text{GeSe}_{0.75}\text{Te}_{0.25}$	59
5.1.3.2	GeSe	62
5.1.4	High-pressure behavior	63
5.1.5	Comparison of the effect of high-pressure and low-temperature	67
5.1.6	The GeTe -III polymorph	68
5.1.7	High-pressure phase diagram	75
5.2	Lattice dynamics of the $\text{Sb}_2\text{Te}_{3-x}\text{Se}_x$ solid solution	77
5.2.1	Introduction	77
5.2.1.1	The $\text{Sb}_2\text{Te}_{3-x}\text{Se}_x$ solid solution: state of the art	77
5.2.1.2	Lattice dynamics of $\text{Sb}_2\text{Te}_{3-x}\text{Se}_x$ compounds	80
5.2.1.3	Aims of this study	82
5.2.2	Sample characterization	84
5.2.3	High-pressure behavior of Sb_2Te_3	86
5.2.4	Low-temperature heat capacity	87
5.2.5	Lattice dynamics of $\text{Sb}_2\text{Te}_{3-x}\text{Se}_x$ ($x=0, 0.6, 1.2, 1.8$)	95
5.2.5.1	Inelastic neutron scattering	95
5.2.5.2	^{121}Sb and ^{125}Te nuclear inelastic scattering	99
5.2.5.2.1	Parameters describing the lattice dynamics	99
5.2.5.2.2	Comparison of the ^{121}Sb and ^{125}Te NIS data	99
5.2.5.2.3	Lattice dynamics of $\text{Sb}_2\text{Se}_{0.6}\text{Te}_{2.4}$	102
5.2.5.2.4	Lattice dynamics of $\text{Sb}_2\text{Se}_{1.2}\text{Te}_{1.8}$	104
5.2.5.2.5	Lattice dynamics of $\text{Sb}_2\text{Se}_{1.8}\text{Te}_{1.2}$	105
5.2.5.3	Se partial phonon density of states	108
5.2.6	Lattice dynamics of Sb_2Se_3	108
6	Conclusions	113
7	Outlook	117
	Acknowledgements	119
A	Unit cell transformations	121

B Nuclear inelastic scattering	123
B.1 ^{121}Sb and ^{125}Te Mössbauer spectroscopy	123
B.2 Resolution functions	124
C $\text{GeSe}_x\text{Te}_{1-x}$ solid solution	127
C.1 Indexed powder patterns	127
C.1.1 $\text{GeSe}_x\text{Te}_{1-x}$ ($x=0, 0.2, 0.5, 0.75, 1$) mixed crystals	127
C.1.2 GeSe	128
C.1.3 $\text{GeSe}_{0.75}\text{Te}_{0.25}$	128
C.2 High-pressure powder patterns	129
C.2.1 GeTe	129
C.2.2 $\text{GeSe}_{0.2}\text{Te}_{0.8}$	131
C.2.3 $\text{GeSe}_{0.5}\text{Te}_{0.5}$	132
C.2.4 $\text{GeSe}_{0.75}\text{Te}_{0.25}$	133
C.3 Indexing of the GeTe-III phase of $\text{GeSe}_{0.5}\text{Te}_{0.5}$	134
C.4 Ge and Te/Se coordination in GeTe-III and β -GeSe	135
D $\text{Sb}_2\text{Te}_{3-x}\text{Se}_x$ solid solution	136
D.1 Debye temperatures	136
D.2 Low-temperature heat capacity	136
D.3 Indexed powder patterns	138
D.4 Temperature dependence of the lattice parameter	139
D.5 Total phonon density of states	140
D.6 Total scattering functions	141
D.7 Temperature-dependent mode shifts	142
Bibliography	144

List of Figures

1.1	Bonding map of phase-change materials	5
2.1	Scattering triangle for elastic and inelastic scattering	13
2.2	The ARCS beamline at the ORNL	17
2.3	Principle of the resonance absorption	18
2.4	Experimental setup for nuclear inelastic scattering measurements	20
2.5	Nuclear absorption spectrum of α -iron	22
2.6	Data treatment of the ^{121}Sb NIS data of $\text{Sb}_2\text{Se}_{1.8}\text{Te}_{1.2}$	23
2.7	Scheme of a PPMS puck for heat capacity measurements	30
3.1	Boiling points of Se and Te in dependence of the pressure	33
3.2	The diamond anvil cell	35
3.3	Sketch of the Extreme Conditions Beamline P02.2 at PETRA III	37
3.4	NIS sample container	39
3.5	Instrumental resolution functions of the sapphire backscattering monochromator	40
4.1	Data treatment of the INS data of $\text{Sb}_2\text{Se}_{0.6}\text{Te}_{2.4}$, Part 1	44
4.2	Data treatment of the INS data of $\text{Sb}_2\text{Se}_{0.6}\text{Te}_{2.4}$, Part 2	45
5.1	Phase diagram of the $\text{GeSe}_x\text{Te}_{1-x}$ solid solution	50
5.2	Projections of the crystal structures of GeTe-I, $\text{GeSe}_{0.75}\text{Te}_{0.25}$ and GeSe-I	52
5.3	Six-membered Ge-Se/Te rings in the structures of GeTe-I, $\text{GeSe}_{0.75}\text{Te}_{0.25}$ and GeSe-I	53
5.4	High-pressure behavior of GeTe and GeSe	54
5.5	Lattice parameter of the $\text{GeSe}_x\text{Te}_{1-x}$ ($x=0, 0.2, 0.5$) samples	58
5.6	Relative Lattice parameter of the $\text{GeSe}_x\text{Te}_{1-x}$ ($x=0, 0.2, 0.5, 0.75$) samples	60
5.7	Temperature dependence of the c/a ratio of the $\text{GeSe}_x\text{Te}_{1-x}$ ($x=0, 0.2, 0.5, 0.75$) samples	61
5.8	Temperature dependence of the unit cell volumes of the $\text{GeSe}_x\text{Te}_{1-x}$ ($x=0, 0.2, 0.5, 0.75$) samples	61
5.9	Temperature dependence of the lattice parameter of GeSe-I	62
5.10	Pressure dependence of the formula volumes of the $\text{GeSe}_x\text{Te}_{1-x}$ ($x=0, 0.2, 0.5, 0.75$) mixed crystals	63
5.11	Pressure dependence of the primitive lattice parameter of the GeTe-I and GeTe-II phase	65

5.12	Temperature and pressure dependence of the c/a ratios of the GeTe-I and GeTe-II phases	68
5.13	Projections of the ab , ac and bc plane of the GeTe-III structure	70
5.14	Six-membered Ge-Te/Se rings in the GeTe-III and β -GeSe structure	71
5.15	Comparison between the structures of GeTe-III and β -GeSe	72
5.16	Pressure dependence of the lattice parameter of the GeTe-III polymorph	74
5.17	Pressure-composition phase diagram of the $\text{GeSe}_x\text{Te}_{1-x}$ solid solution	75
5.18	Crystal structures of Sb_2Te_3 and Sb_2Se_3	77
5.19	Crystal structures of α - Sb_2Te_3 and β - Sb_2Te_3	78
5.20	Temperature-composition phase diagram of the $\text{Sb}_2\text{Te}_{3-x}\text{Se}_x$ solid solution	79
5.21	^{121}Sb and ^{125}Te partial and the total phonon density of states of Sb_2Te_3	81
5.22	Powder patterns of the $\text{Sb}_2\text{Te}_{3-x}\text{Se}_x$ ($x = 0, 0.6, 1.2, 1.8, 3$) samples	84
5.23	Lattice parameter and unit cell volumes of the $\text{Sb}_2\text{Te}_{3-x}\text{Se}_x$ samples	85
5.24	High-pressure stability fields of α - and β - Sb_2Te_3	87
5.25	Low-temperature heat capacity of Sb_2Te_3 and Sb_2Se_3	88
5.26	Debye temperatures of the $\text{Sb}_2\text{Te}_{3-x}\text{Se}_x$ ($x=0, 0.6, 1.2, 1.8, 3$) mixed crystals	91
5.27	Enthalpy and Entropy of $\text{Sb}_2\text{Te}_{3-x}\text{Se}_x$ ($x=0, 0.6, 1.2, 1.8, 3$) mixed crystals	93
5.28	Excess heat capacity and excess enthalpy of $\text{Sb}_2\text{Se}_{0.6}\text{Te}_{2.4}$ and $\text{Sb}_2\text{Se}_{1.2}\text{Te}_{1.8}$	94
5.29	Total phonon density of states of the $\text{Sb}_2\text{Te}_{3-x}\text{Se}_x$ ($x=0, 0.6, 1.2, 1.8$) mixed crystals	96
5.30	Total phonon density of states of $\text{Sb}_2\text{Se}_{0.6}\text{Te}_{2.4}$ at 35, 150 and 300 K	97
5.31	Total scattering functions of the $\text{Sb}_2\text{Te}_{3-x}\text{Se}_x$ ($x=0, 0.6, 1.2, 1.8, 3$) mixed crystals and the Al can	97
5.32	Temperature-induced mode shifts in $\text{Sb}_2\text{Se}_{1.2}\text{Te}_{1.8}$	98
5.33	^{121}Sb and ^{125}Te partial PDOS of the $\text{Sb}_2\text{Te}_{3-x}\text{Se}_x$ mixed crystals	100
5.34	Homology relation applied to the ^{121}Sb and ^{125}Te partial PDOS of the $\text{Sb}_2\text{Te}_{3-x}\text{Se}_x$ mixed crystals	101
5.35	Lattice dynamics of $\text{Sb}_2\text{Se}_{0.6}\text{Te}_{2.4}$	103
5.36	Lattice dynamics of $\text{Sb}_2\text{Se}_{1.2}\text{Te}_{1.8}$	105
5.37	Lattice dynamics of $\text{Sb}_2\text{Se}_{1.8}\text{Te}_{1.2}$	106
5.38	Se partial phonon density of states of $\text{Sb}_2\text{Se}_{0.6}\text{Te}_{2.4}$ and $\text{Sb}_2\text{Se}_{1.8}\text{Te}_{1.2}$	107
5.39	Experimental and theoretical phonon density of states of Sb_2Se_3	109
5.40	Comparison between the experimental and theoretical total and partial phonon density of states of Sb_2Se_3	110
5.41	Temperature-induced mode shifts in the total phonon density of states of Sb_2Se_3	112
B.1	Decay schemes of ^{121m}Sn , ^{125}Sb and ^{125}I sources	123
B.2	Resolution function of the ^{121}Sb NIS data of Sb_2Te_3	124
B.3	Resolution function of the ^{121}Sb NIS data of $\text{Sb}_2\text{Se}_{0.6}\text{Te}_{2.4}$	125

B.4	Resolution function of the ^{125}Te NIS data of $\text{Sb}_2\text{Se}_{0.6}\text{Te}_{2.4}$	125
B.5	Resolution function of the ^{121}Sb NIS data of $\text{Sb}_2\text{Se}_{1.2}\text{Te}_{1.8}$	126
B.6	Resolution function of the ^{121}Sb NIS data of Sb_2Se_3	126
C.1	Powder patterns of the $\text{GeSe}_x\text{Te}_{1-x}$ ($x=0, 0.2, 0.5, 0.75, 1$) samples . . .	127
C.2	Indexed powder patterns of GeSe	128
C.3	Indexed powder patterns of $\text{GeSe}_{0.75}\text{Te}_{0.25}$	128
C.4	High-pressure powder patterns of GeTe	129
C.5	Powder patterns of GeTe	130
C.6	High-pressure powder patterns of $\text{GeSe}_{0.2}\text{Te}_{0.8}$	131
C.7	High-pressure powder patterns of $\text{GeSe}_{0.5}\text{Te}_{0.5}$	132
C.8	High-pressure powder patterns of $\text{GeSe}_{0.75}\text{Te}_{0.25}$	133
C.9	Indexing of the GeTe -III phase of $\text{GeSe}_{0.5}\text{Te}_{0.5}$	134
D.1	Low-temperature heat capacity of $\text{Sb}_2\text{Se}_{0.6}\text{Te}_{2.4}$	136
D.2	Low-temperature heat capacity of $\text{Sb}_2\text{Se}_{1.2}\text{Te}_{1.8}$	137
D.3	Low-temperature heat capacity of $\text{Sb}_2\text{Se}_{1.8}\text{Te}_{1.2}$	137
D.4	Indexed powder patterns of Sb_2Se_3	138
D.5	Temperature-dependent lattice parameter of the $\text{Sb}_2\text{Te}_{3-x}\text{Se}_x$ samples .	139
D.6	Total phonon density of states of the $\text{Sb}_2\text{Te}_{3-x}\text{Se}_x$ ($x=0, 0.6, 1.2, 1.8$) mixed crystals at 150 K	140
D.7	Total phonon density of states of the $\text{Sb}_2\text{Te}_{3-x}\text{Se}_x$ ($x=0, 0.6, 1.2, 1.8$) mixed crystals at 300 K	140
D.8	Total phonon density of states of $\text{Sb}_2\text{Se}_{1.2}\text{Te}_{1.8}$ at several temperatures .	141
D.9	Total scattering functions of the $\text{Sb}_2\text{Te}_{3-x}\text{Se}_x$ ($x=0, 0.6, 1.2, 1.8, 3$) mixed crystals measured at 150 K	141
D.10	Total scattering functions of the $\text{Sb}_2\text{Te}_{3-x}\text{Se}_x$ ($x=0, 0.6, 1.2, 1.8, 3$) mixed crystals measured at 300 K	142
D.11	Temperature-dependent mode shifts of Sb_2Te_3	142
D.12	Temperature-dependent mode shifts of $\text{Sb}_2\text{Se}_{0.6}\text{Te}_{2.4}$	143
D.13	Temperature-dependent mode shifts of $\text{Sb}_2\text{Se}_{1.8}\text{Te}_{1.2}$	143

List of Tables

3.1	Melting and boiling points of Sb, Se and Te	32
3.2	Yields of the synthesized $\text{Sb}_2\text{Te}_{3-x}\text{Se}_x$ ($x=0.6, 1.2, 1.8$) mixed crystals	34
3.3	Masses of the $\text{Sb}_2\text{Te}_{3-x}\text{Se}_x$ samples used for the heat capacity measurements	35
3.4	Instrumental resolution functions of the sapphire backscattering monochromator	39
4.1	Cut-off energies of the $\text{Sb}_2\text{Te}_{3-x}\text{Se}_x$ ($x=0, 0.6, 1.2, 1.8, 3$) mixed crystals	46
4.2	Scaling factors for the ^{121}Sb and ^{125}Te partial phonon density of states of the $\text{Sb}_2\text{Te}_{3-x}\text{Se}_x$ ($x=0, 0.6, 1.2, 1.8$) samples	48
5.1	c/a ratios of the $\text{GeSe}_x\text{Te}_{1-x}$ mixed crystals	57
5.2	The $a/c, b/c$ and a/b ratio of the GeSe sample	57
5.3	Bulk moduli, formula volumes and transition pressures of the $\text{GeSe}_x\text{Te}_{1-x}$ ($x=0, 0.2, 0.5, 0.75$) samples	66
5.4	Details of the structure refinement on the new GeTe-III structure	69
5.5	Atomic positions and thermal displacement parameter of GeTe-III	69
5.6	Indexed GeTe-III powder patterns	73
5.7	Lattice parameter ratios of the $\text{Sb}_2\text{Te}_{3-x}\text{Se}_x$ ($x=0, 0.6, 1.2, 1.8, 3$) mixed crystals	86
5.8	Fit parameters obtained from the fits on the heat capacity data of the $\text{Sb}_2\text{Te}_{3-x}\text{Se}_x$ ($x=0, 0.6, 1.2, 1.8, 3$) mixed crystals	89
5.9	Element/isotope-specific Lamb-Mössbauer factors, mean force constants and Debye temperatures of the $\text{Sb}_2\text{Te}_{3-x}\text{Se}_x$ ($x=0, 0.6, 1.2, 1.8$) mixed crystals	99
5.10	Element/isotope-specific Lamb-Mössbauer factors, mean force constants and Debye temperatures of Sb_2Se_3	108
5.11	Lattice parameter of Sb_2Se_3	111
C.1	Ge coordination in GeTe-III and β -GeSe	135
C.2	Te/Se coordination in GeTe-III and β -GeSe	135
D.1	Debye temperatures of the $\text{Sb}_2\text{Te}_{3-x}\text{Se}_x$ ($x=0, 0.6, 1.2, 1.8, 3$) mixed crystals	136

List of Abbreviations

ARCS	wide Angular-Range Chopper Spectrometer
APD	Avalanche Photo-Diode
CRL	Compound Refractive Lens
DAC	Diamond Anvil Cell
DESY	Deutsches Elektronensynchrotron
DCM	Double Crystal Monochromator
FCC	Face-Centered Cubic
FWHM	Full Width at Half Maximum
INS	Inelastic Neutron Scattering
NFS	Nuclear Forward Scattering
NIA	Nuclear Inelastic Absorption
NIS	Nuclear Inelastic Scattering
NRS	Nuclear Resonant Scattering
ORNL	Oak Ridge National Laboratory
PDOS	Phonon density of states
PETRA-III	Positron-Electron Tandem Ring Accelerator
PPMS	Physical Property Measurements System
SNS	Spallation Neutron Source
TOF	Time of Flight
(LT)XRD	(Low-temperature) X-ray Diffraction

Physical Constants

Speed of Light	$c_0=2.99792458 \cdot 10^8 \text{ m} \cdot \text{s}^{-1}$
Reduced Planck constant	$\hbar=6.582119514 \cdot 10^{-16} \text{ eV} \cdot \text{s}$
Avogadro constant	$N_A=6.022140857 \cdot 10^{23} \text{ mol}^{-1}$
Boltzmann constant	$k_B=8.6173303 \cdot 10^{-5} \text{ eV} \cdot \text{K}^{-1}$
Universal gas constant	$R=N_A \cdot k_B=8.314598 \text{ J} \cdot \text{mol}^{-1} \cdot \text{K}^{-1}$

Abstract

Phase-change materials (e. g. GeTe, GeSe, Sb₂Te₃ and Sb₂Se₃) are characterized by an ultra-fast switching between an amorphous and a crystalline phase and thus, these materials are considered to be hopeful candidates for applications in future computer-based memories which allow a more reliable, more efficient and more capable data storage. In the crystalline phase a strong properties contrast between the tellurides and selenides is observed and it was concluded that this is due to different bonding schemes. While the tellurides are believed to exhibit a metavalent bonding scheme, the selenides are covalently bonded. However, up to now, the metavalent bonding scheme is still under discussion and it is not completely understood.

This study is focused on the GeSe_xTe_{1-x} and Sb₂Te_{3-x}Se_x solid solutions which are both relevant systems of phase-change materials. According to the conception of the metavalent bonding scheme it is expected that composition-induced changes and the application of low-temperature and/or high-pressure lead to either a weakening or a collapse of this bonding, however, an experimental conformation is missing.

The influence of composition-induced changes, low-temperature and high-pressure on the structural parameter of compounds from the GeSe_xTe_{1-x} ($x=0, 0.2, 0.5, 0.75, 1$) solid solution was investigated by a combination of powder and single crystal diffraction. At ambient conditions, three phases, a rhombohedral ($0 \leq x(\text{Se}) \leq 0.52$), a hexagonal ($0.58 \leq x(\text{Se}) \leq 0.86$) and an orthorhombic ($0.91 \leq x(\text{Se}) \leq 1$) one, exist in this system. All phases are stable down to at least 25 K and no evidences for structural phase transition have been observed. The thermal behavior of the rhombohedral compounds differs significantly from the one of hexagonal GeSe_{0.75}Te_{0.25} which is explained by the additional Ge··Ge and Se/Te··Se/Te interactions which are only present in the crystal structure of the hexagonal phase. Compounds from the stability field of the rhombohedral phase ($x=0, 0.2, 0.5$) follow the pressure transition pathway:



A first-order nature for all observed phase transitions is suggested. It was found that all phase transitions are reversible. For the GeTe-III polymorph, a new crystal structure was determined and it was demonstrated that earlier structural models are erroneously. GeTe-III is isostructural to β -GeSe, a high-pressure and high-temperature polymorph of GeSe, and crystallizes in the orthorhombic space group *Pnma* with lattice parameter of $a=7.3690(18)$ Å, $b=3.9249(10)$ Å and $c=5.698(9)$ Å. In the structure, Ge··Ge and long-ranged Te··Te interactions are present. Hexagonal GeSe_{0.75}Te_{0.25} is

stable up to at least 23 GPa. While the GeTe-I and GeTe-II phases are believed to be metavalently bonded, the GeTe-III phase and $\text{GeSe}_{0.75}\text{Se}_{0.25}$ are predominately covalently bonded. Thus, the metavalent bonding scheme in the system $\text{GeSe}_x\text{Te}_{1-x}$ is limited by the formation of $\text{Ge}\cdot\cdot\text{Ge}$ and $\text{groupVI}\cdot\cdot\text{groupVI}$ interactions and it can be broken by both, the application of high pressure and composition-induced changes.

The influence of low-temperature and composition-induced changes on the lattice dynamics of the $\text{Sb}_2\text{Te}_{3-x}\text{Se}_x$ solid solution was studied by a combination of low-temperature heat capacity measurements and X-ray and neutron spectroscopic techniques. For compounds from the stability field of the tetradymite structure type ($0 \leq x(\text{Se}) \leq 1.8$) a significant composition-induced increase of the Debye temperature was found indicating a lattice hardening and a stiffening of the chemical bonds with increasing Se content. The total and Sb and Te partial phonon density of states were determined and a detailed analysis of the vibrational properties was performed. It was found that the bonding character of part of the Sb-Se/Te bonds change significantly with increasing Se content. The application of low-temperature and composition-induced changes lead to a weakening of the metavalent bonding character in the system $\text{Sb}_2\text{Te}_{3-x}\text{Se}_x$, however, in a way which differs from what was suggested in previous studies. The experimental data obtain on Sb_2Se_3 are in excellent agreement with the results of a theoretical study reported in the literature.

Zusammenfassung

Phasenwechselmaterialien (z. B. GeTe, GeSe, Sb₂Te₃ und Sb₂Se₃) sind durch einen ultra-schnellen Phasenübergang zwischen einer amorphen und kristallinen Phase gekennzeichnet, durch welchen sie für Anwendungen in der Entwicklung von effizienteren, verlässlicheren und belastbareren Datenspeichern in Frage kommen. In früheren Untersuchungen wurde ein starker Eigenschaftskontrast zwischen den kristallinen Telluriden und Seleniden nachgewiesen, welcher auf verschiedene Bindungsarten in beiden Substanzklassen zurückgeführt wurde. Während die Telluride einen metavalenten Bindungstyp aufweisen, sind die Selenide überwiegend kovalent gebunden. Die metavalente Bindung ist noch nicht vollständig verstanden und Gegenstand der aktuellen Forschung.

In dieser Arbeit wurden die Mischkristallreihen GeSe_xTe_{1-x} und Sb₂Te_{3-x}Se_x, die zu den wichtigsten Systemen im Bereich der Phasenwechselmaterialien zählen, untersucht. Gemäß dem Modell des metavalenten Bindungstyps, führen Variationen des Se-Gehalts ebenso wie die Anwendung hoher Drücke und/oder tiefer Temperaturen zu einer Abschwächung bzw. einem Bruch der Bindung. Ein experimenteller Nachweis dieser Hypothese wurde bisher noch nicht erbracht.

Der Einfluss einer Variation des Se-Gehalts sowie von tiefen Temperaturen und hohen Drücken auf die strukturellen Eigenschaften von Mischkristallen aus dem System GeSe_xTe_{1-x} wurde mit Hilfe einer Kombination von Einkristall- und pulverdiffraktometrischen Methoden untersucht. Bei Raumbedingungen wurden drei Phasen, eine rhomboedrische ($0 \leq x(\text{Se}) \leq 0.52$), eine hexagonale ($0.58 \leq x(\text{Se}) \leq 0.86$) und eine orthorhombische ($0.91 \leq x(\text{Se}) \leq 1$), in Abhängigkeit des Se-Gehalts im System GeSe_xTe_{1-x} nachgewiesen. Alle Phasen sind bis mindestens 25 K stabil und es wurden keine Anzeichen für strukturelle Phasenumwandlungen beobachtet. Das thermische Verhalten der rhomboedrischen Mischkristalle unterscheidet sich signifikant vom der hexagonalen Phase. Dies wurde auf die zusätzlichen Ge··Ge- und Se/Te··Se/Te-Wechselwirkungen, welche ausschließlich in der Kristallstruktur der hexagonalen Phase nachgewiesen wurden, zurückgeführt. Für die Mischkristalle aus dem Stabilitätsfeld der rhomboedrischen Phase ($x=0, 0.2, 0.5$) wurden nachfolgende druckinduzierte Phasenumwandlungen beobachtet:



Die Ergebnisse dieser Arbeit lassen auf Phasenumwandlungen 1. Ordnung schließen. Dabei sind alle Phasenumwandlungen reversibel. Für die Phase GeTe-III wurde eine neue Kristallstruktur bestimmt und es wurde gezeigt, dass vorausgegangene Strukturmodelle fehlerhaft sind. GeTe-III ist isostrukturell zu β -GeSe, einem Hochdruck-

und Hochtemperaturpolymorph von GeSe, und kristallisiert in der orthorhombischen Raumgruppe $Pnma$ mit Gitterparametern von $a=7.3690(18)$ Å, $b=3.9249(10)$ Å und $c=5.698(9)$ Å. In der Kristallstruktur wurden Ge·Ge- und langreichweitige Te·Te-Wechselwirkungen nachgewiesen. $\text{GeSe}_{0.75}\text{Se}_{0.25}$ ist bis mindestens 23 GPa stabil. Während die Phasen GeTe-I und GeTe-II als metavalent gebunden angesehen werden, weisen $\text{GeSe}_{0.75}\text{Se}_{0.25}$ und GeTe-III einen überwiegend kovalenten Bindungstyp auf. Somit konnte gezeigt werden, dass die metavalente Bindung im System $\text{GeSe}_x\text{Te}_{1-x}$ durch die Bildung von Ge·Ge- und langreichweitigen GruppeVI·GruppeVI-Wechselwirkungen begrenzt ist. Ein Bruch der metavalenten Bindung kann sowohl durch die Anwendung hoher Drücke als auch Variationen des Se-Gehalts herbeigeführt werden.

Der Einfluss von tiefen Temperaturen und Variationen des Se-Gehalts auf die Gitterdynamik von Mischkristallen aus dem System $\text{Sb}_2\text{Te}_{3-x}\text{Se}_x$ wurde mit Hilfe von Tieftemperaturwärmekapazitätsmessungen und Röntgen- und Neutronenspektroskopischen Methoden untersucht. Für Mischkristalle aus dem Stabilitätsfeld des Tetradymit-Strukturtyps ($0 \leq x(\text{Se}) \leq 1.8$) wurde ein signifikanter Anstieg der Debye-Temperatur mit zunehmendem Se-Gehalt nachgewiesen, welcher auf eine Versteifung des Kristallgitters und der chemischen Bindungen zurückzuführen ist. Die gesamte sowie die Sb- und Te-Phononzustandsdichten wurden bestimmt und eine detaillierte Analyse der Gitterdynamik durchgeführt. Es zeigte, dass sich mit zunehmendem Se-Gehalt der Bindungscharakter einiger Sb-Se/Te-Bindungen signifikant ändert. Die Anwendung tiefer Temperaturen und Variationen des Se-Gehalts führen zu einer Abschwächung des metavalenten Bindungscharakters im System $\text{Sb}_2\text{Te}_{3-x}\text{Se}_x$, allerdings in einer Art und Weise, welche im Widerspruch zu dem in vorausgegangenen Arbeiten diskutierten Modell steht. Die für Sb_2Se_3 bestimmten experimentellen Daten stimmen sehr gut mit den Ergebnissen von vorausgegangenen theoretischen Rechnungen überein.

Chapter 1

Introduction

Phase-change materials (e. g. GeTe, GeSe, Sb₂Te₃, Sb₂Se₃) are characterized by an ultra-fast switching between an amorphous and a crystalline phase [1, 2, 3, 4]. The

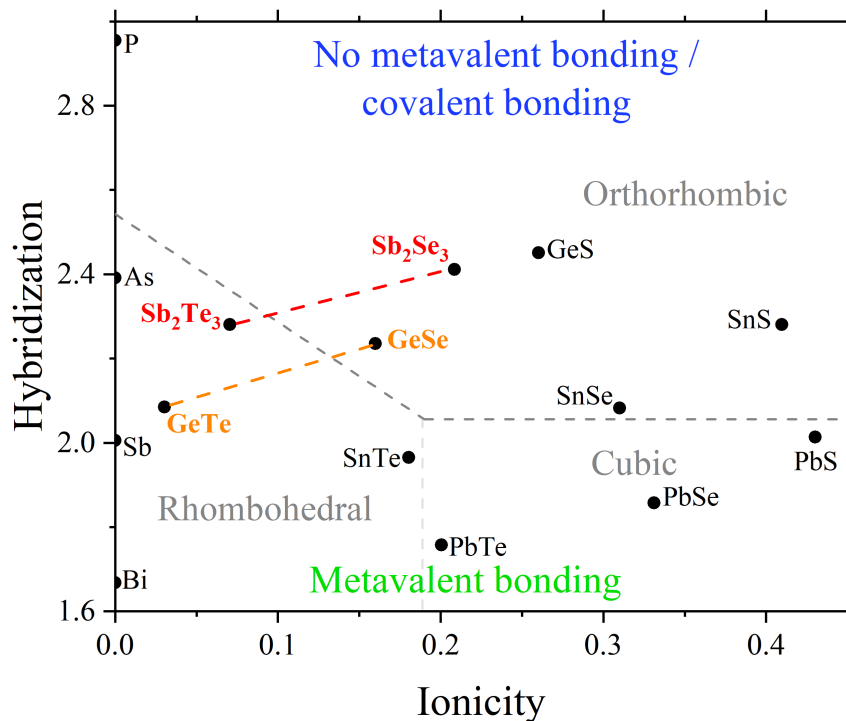


FIGURE 1.1: The bonding map of phase-change materials [5]. The two systems investigated in this thesis are indicated.

transition is accompanied by a pronounced change of the optical and electrical properties [2, 3, 4]. Due to the switching kinetics and property contrasts paired with transition temperatures of about 393-693 K, phase-change materials (PCM) were considered to be potential candidates for non-volatile optical data storage and e.g. PCM-based DVD's have been developed previously [2, 4]. Nowadays, the request for still faster, more efficient and more reliable data storage is unbroken. Thus, the understanding of the switching kinetics and mechanisms as well as the structural stability and the lattice dynamics of phase-change materials is of key importance in order to find promising materials that satisfy the request for more capable data storage.

Also in the crystalline phases a pronounced property contrast between the tellurides

and selenides has been observed previously and it was demonstrated that the thermoelectric [6, 7] and optical [8, 7] properties of crystalline GeTe and Sb₂Te₃, respectively, change significantly when Te is exchanged by Se. In the literature (e.g. [9, 10]), it was suggested that this is mainly due to different bonding scheme in the respective crystal structures of the selenides and tellurides. While the selenides are predominantly covalently bonded, for the tellurides a so-called "metavalent" bonding scheme was suggested.

Previously, Littlewood [5] has studied the bonding properties of phase-change materials by theoretical calculations and he developed a materials map in which the different bonding schemes can be clearly distinguished. For this, he introduced two bonding indicators which are the hybridization and the ionicity. While the former indicator is correlated with localization of electrons between the bonded atoms, the later one provides information on the polarity of the bonding. In general, three different structure types have been observed for binary phase-change materials which are a rhombohedral, a cubic and an orthorhombic one (figure 1.1) [5]. Phase-change materials with a comparatively low symmetric orthorhombic structure (e.g. GeSe, Sb₂Se₃) are located in the field of covalently bonded compounds, whereas chalcogenides with higher symmetric rhombohedral (e.g. GeTe, Sb₂Te₃) and cubic structures, respectively, exhibit a metavalent bonding scheme.

In all compounds shown in figure 1.1 an octahedral coordination around the group IV, V and VI elements is favorable [5]. However, for phase-change materials like GeTe and GeSe there are in average only three p electrons available per atom and the $8-N$ rule predicts therefore only three covalent Ge-Te/Se bonds per atom. In a covalently bonded phase-change material, the tendency to localize bonding electrons between the atoms is large and thus, the octahedral coordination is obtained by three shorter covalent bonds and three significantly longer interactions. Thus, the covalent bonding scheme is in agreement with the $8-N$ rule [11].

In contrast to this, for metavalent bonded phase-change materials, the tendency to localize the bonding electrons is smaller than for covalently bonded compounds, but still larger than for metallically bonded ones. The metavalent bonding is characterized by a complete delocalization of the bonding electrons similar to the metallic bonding scheme [5]. However, in contrast to metallic bonding in which s or d electrons are delocalized, in metavalently bonded materials the bonding is preferentially promoted by p electrons (which usually tend to form covalent bonds). Obviously, in order to gain an octahedral coordination, in metavalently bonded materials the bonding is formed by less than two electrons per bond and thus, the $8-N$ rule is broken [11]. It should be mentioned at this point that the contribution of s electrons to the bonding scheme by hybridization is much larger in covalently bonded compounds than in materials with a metavalent bonding scheme [5, 11].

In figure 1.1, for all depicted phase-change materials with a cubic structure the metavalent bonding leads to six equally long bonds, whereas for all shown compounds with a rhombohedral structure there is an additional contribution of a Peierl's

distortion to the bonding scheme which weakens the strength of the metavalent bonding character.

This thesis is focused on two relevant systems of phase-change materials: $\text{GeSe}_x\text{Te}_{1-x}$ and $\text{Sb}_2\text{Te}_{3-x}\text{Se}_x$. According to figure 1.1, an exchange of Te by Se brings the material's composition closer to the boundary of the covalently bonded compounds and thus, a weakening of the metavalent bonding in GeTe and Sb_2Te_3 is expected with increasing Se content. The exchange of Te by Se is accompanied by a reduction of the unit cell volume which can be also reached by the application of hydrostatic pressure and/or cooling of the compounds. Thus, it is expected that such variations in pressure and/or temperature lead to a weakening or a collapse of the metavalent bonding in the selected systems, however, up to now, an experimental confirmation of this hypothesis is missing.

Here, the influence of high-pressure, low-temperature and compositional changes on the structural parameter is studied on compounds from the $\text{GeSe}_x\text{Te}_{1-x}$ solid solution. The results of a detailed structural analysis are provided and it is demonstrated in which way the structural parameter (e.g. lattice parameter, distances, coordination, ...) are influenced by variations of the Se content, pressure and temperature. A stability field for the existence of the metavalent bonding in this system is provided.

In previous studies, the lattice dynamics of several binary phase-change materials e.g. GeTe , GeSe , Sb_2Te_3 and Sb_2Se_3 was studied experimentally by inelastic neutron scattering [12, 13] and nuclear inelastic scattering measurements [14, 15] and theoretically by first-principles calculations [16, 17, 18, 19, 20]. It was concluded that the simultaneous hardening of acoustical and softening of optical phonons during the transition from the amorphous to the crystalline phase can be considered as a benchmark for the metavalent bonding [17, 14, 21]. The resulting strong coupling between acoustical and optical phonons causes the pronounced contrast of the transport and optical properties [21, 17].

However, up to now, it is not completely understood how composition-induced changes and low-temperature influence the lattice dynamics and the bonding in the crystalline phase of these compounds. Therefore, the lattice dynamics of several compounds from the $\text{Sb}_2\text{Te}_{3-x}\text{Se}_x$ solid solution is investigated in this thesis by a combination of low-temperature heat capacity, inelastic neutron scattering and nuclear inelastic scattering measurements. The results of these studies provide further insights on the metavalent bonding in this system.

The general aim of this study is to understand the nature and the limits of the metavalent bonding in the systems $\text{Ge}_x\text{Te}_{1-x}$ and $\text{Sb}_2\text{Te}_{3-x}\text{Se}_x$ in more details. From our results we aim to get a deeper understanding of this bonding scheme. This might be of relevance for a more efficient material tuning for future applications in novel data storage.

Chapter 2

Theory

2.1 Crystal structure determination

2.1.1 Single crystal vs. powder diffraction

Single crystals are characterized by a periodic, 3-dimensional arrangement of unit cells which form the lattice of the compounds. As a result of the periodicity, Bragg scattering on the Miller planes of the crystal is only possible for well defined 2Θ angles. Thus, in the diffraction pattern of a single crystal, the reflections originating from families of parallel Miller planes occur as spots. By varying the orientation between the detector and the single crystal numerous of these reflections are measured. As a result one gains a 3-dimensional representation of reciprocal space. Reflections from different Miller planes but with equal d -spacing (e.g. for a cubic crystal the peaks (300) and (221)) are distinguishable in a single crystal diffraction experiment [22].

Polycrystalline samples -in an ideal case- are composed of statistically distributed grains in all possible orientations. Thus, for a given 2Θ angle, reflections from different Miller planes can fulfill Bragg's equation simultaneously and reflections from different Miller planes but with equal d -spacing (e.g. for a cubic crystal the peaks (300) and (221)) overlap and contribute to the same diffraction ring [23, 24].

2.1.2 The phase problem

The structure factor, F_{hkl} , is a very important quantity in crystallography as its Fourier transform is connected with the electron density (equations (2.1a) and (2.1b)) [22].

$$F_{hkl} = \sum_{i=1}^n f_j \cdot \exp(2 \cdot \pi \cdot i \cdot (h \cdot x_j + k \cdot y_j + l \cdot z_j)) \quad (2.1a)$$

$$\rho_{x,y,z} = \frac{1}{V} \cdot \sum_{hkl} F_{hkl} \exp(2 \cdot \pi \cdot i \cdot (h \cdot x_j + k \cdot y_j + l \cdot z_j)) \quad (2.1b)$$

Here, f_j corresponds to the atomic form factor of the atom j , hkl define Miller indices of the reflections, x_j, y_j, z_j are atomic coordinates of the atom j and V is the volume of the unit cell [22].

In a diffraction experiment one measures the intensities, I_{hkl} , of the reflections hkl which are proportional to the square of the absolute value of the structure factor,

$|F_{hkl}|^2$, by $I_{hkl} \propto |F_{hkl}|^2$ [22]. The consequence of this proportionality is that the obtained intensities are connected only with the amplitudes f_j^2 of the structure factor. Thus, information on the phases, $\exp(2 \cdot \pi \cdot i \cdot (h \cdot x_j + k \cdot y_j + l \cdot z_j))$, are not directly accessible from the measured intensities [22].

This dilemma is denoted as the "phase problem of crystallography" [22]. As the phases are connected with the atomic positions x_j, y_j, z_j of the atom j it is not possible to determine crystal structures without knowing the phases [22].

2.1.3 Structure solution: Direct Methods

Many algorithms have been developed in order to solve the "phase problem" and to deduce the phase information from diffraction data [22, 25]. These algorithms provide a first model of the electron density distribution with initial values for the lattice parameter, the atomic position and the thermal displacement parameter and thus, they yield a first approximate structural model [22, 25].

In this study, the direct methods which were established by J. Karle and H. A. Hauptman have been used for structure solution. The algorithm assumes that the electron density of a crystal is a) never negative and b) localized at the atomic position which corresponds to a picture of point-like atoms [22, 25]. As one can see from equation (2.1a), the structure factor depends on the atomic form factors of the involved atoms. The atomic form factors show a strong Θ dependence in case of X-ray radiation [22]. Thus, in order to realize point-like atoms so-called E values, E_{hkl} (equation (2.2)), have to be considered [22, 25].

$$E_{hkl}^2 = k \cdot \frac{F_{hkl}^2}{\langle F_{hkl}^2 \rangle} = k \cdot \frac{F_{hkl}^2}{\epsilon \cdot \sum f_j^2} \quad (2.2)$$

E values are angle-independent structure factors that are normalized to an estimated value, $\langle F_{hkl}^2 \rangle$, which corresponds to the amplitude of the structure factor multiplied by a weighting factor ϵ . In equation (2.2), k is a scale factor which scales the estimated values to F_{000}^2 and thus, to the total number of electrons [22, 25].

The fundamental relation essential for the application of direct methods is the so-called Sayre equation (2.3a) [22, 25] from which the relation for the phases follows (equation (2.3b)).

$$F_{hkl} = k \cdot \sum_{h'k'l'} F_{h'k'l'} \cdot F_{h-h' k-k' l-l'} \quad (2.3a)$$

$$\phi_{hkl} \approx \phi_{h'k'l'} + \phi_{h-h' k-k' l-l'} \quad (2.3b)$$

Sayre recognized that for a certain group of strong reflections the F values and their corresponding phases, ϕ , are connected to each other [22, 25]. Sayre's equation implies that the structure factor / the phase of a reflection hkl can be estimated by the sum of the products of two (or three) structure factors / phases of other reflections

whose indices ($h'k'l'$ and $h - h' \quad k - k' \quad l - l'$) sum to the values of hkl . These are the so-called triplet relationships. In case of centrosymmetric crystals, the phases of the structure factor are either 0 or π . Hence, in case of a centrosymmetric structure the phase-problem is reduced to a problem of unknown algebraic signs [22, 25].

Obviously, there are many of such triplet relationships and this results in an equation system of connected F values and phases which in favorable cases can be solved numerically by a brute-force algorithm [22, 25]. Also other relationships e.g. quartet relations play an important role in direct methods. For further details, the reader is referred to references [22, 25].

2.1.4 Structure refinement

2.1.4.1 Least square method

The least squares method is a mathematical procedure to determine the best fit model of experimental data under a continuous optimization of the fit parameters [22]. In crystallography, least squares methods are applied in a structure refinement in order to minimize the difference, Δ , between a structural model connected with $y_{i,\text{calc}}$, obtained either from a structure solution or from reference data, and the experimentally determined intensities, $y_{i,\text{obs}}$ (equation (2.4)) [22].

$$\Delta = w_i \cdot \sum_i (\delta)^2 = w_i \cdot \sum_i (y_{i,\text{obs}} - y_{i,\text{calc}})^2 \quad (2.4)$$

In equation (2.4), the weighting factor $w_i = \sigma_i^{-2}$ depends on the standard deviation σ_i in each 2Θ position i of the measured diffraction data [23, 24, 22]. For the application of the least squares algorithm it is mandatory that the data-to-parameter ratio is strongly overdetermined which means that the number of data points is much larger than the number of fit parameter (usually, at least 10:1). As seen from equation (2.1a), there is an exponential dependence of the structure factor on the parameters and thus, for a successful application of the least squares algorithm a linearization of F_{hkl} is mandatory [22]. This is done by developing the structure factor F_{hkl} in a Taylor row which is aborted after the 2nd member. Further information on the mathematical treatment can be found in the relevant textbooks. The least squares method is based on an iterative algorithm and each cycle yields the starting values for the next one. The algorithm is finished if Δ is either zero or converges against a constant value [22].

2.1.4.2 Le Bail method

Powder patterns measured in a diffraction experiment contain information about numerous structural (e. g. lattice parameters, atomic position, ...) and instrumental (e. g. zero point shift, peak profile, ...) parameters. However, as a result of the peak overlap the accessible information content from the peak intensities is significantly

reduced. In order to deduce at least a part of the information from the powder pattern one has to fit the experimental data using a suitable mathematical algorithm. These algorithms are the Pawley, Le Bail and Rietveld refinement [23, 24].

In this study, only the Le Bail method was used in order to refine the lattice parameters of the investigated samples. Therefore, a brief description of this refinement strategy is given.

The Le Bail refinement is a least squares algorithm, which aims to minimize the error sum of squares Δ between the intensities at $2\Theta_i$ position i of a measured ($y_{i,obs}$) and a calculated ($y_{i,calc}$) diffractogram (see also equation (2.4)) [23, 24]. For the application of the Le Bail refinement pre-determined lattice parameter, either obtained from a structure solution or from an indexing of the measured powder pattern, have to be known [23, 24]. Ideally, the space group is also known, yet part of the information of the space group symmetry can be deduced by analyzing the systematical extinctions. The lattice parameter combined with the space group symmetry yield the initial peak positions $2\Theta_k$ of all possible Bragg peaks. In equation (2.5), a simplified expression for the calculation of the intensities $y_{i,calc}$ of a single crystalline phase is shown [23, 24].

$$y_{i,calc} = \sum_k I_k \cdot G(2\Theta_i - 2\Theta_k) + b_{ig} \quad (2.5)$$

I_k is the intensity at the peak position $2\Theta_k$ and b_{ig} is a function to describe the background. The profile function $G(2\Theta_i - 2\Theta_k)$ defines the peak shape. Usually, a pseudo Voigt function (equation (2.6) is chosen [23, 24].

$$G(2\Theta_i - 2\Theta_k) = \underbrace{\mu \cdot \left(\frac{\sqrt{4}}{\pi \cdot H_{k,Lorentzian}} \right) \cdot \left(\frac{1}{1 + 4 \cdot X_{ik}^2} \right)}_{\text{Lorentzian part}} + \underbrace{(1 - \mu) \cdot \left(\frac{\sqrt{4 \cdot \ln 2}}{\sqrt{\pi} \cdot H_{k,Gaussian}} \right) \cdot \exp(-4 \cdot \ln 2 \cdot X_{ik}^2)}_{\text{Gaussian part}} \quad (2.6)$$

The pseudo Voigt function contains a Lorentzian and Gaussian part which are both normalized to their half maximum widths $H_{k,j}$ and the ratio of each part is defined by the mixing parameter μ [23, 24]. The parameter X_{ik} in equation (2.6) is given by $X_{ik} = \frac{2\Theta_i - 2\Theta_k}{H_{k,j}}$ [23, 24]. The full width at half maximum parameter $H_{k,Lorentzian}$ depends on the fit parameter LX and LY (equation (2.7))[23, 24].

$$H_{k,Lorentzian} = LX \cdot \tan \Theta + \frac{LY}{\cos \Theta} \quad (2.7)$$

LX is proportional to the reciprocal crystallite size (see also Scherrer equation [23, 24]) and hence, it is correlated with the coherently scattering area. LY is an indicator for a possible microstrain on the sample. The half maximum width of the Gaussian part is given by the so-called Caglioti function, which contains the angle-independent fit parameter GW and the angle-dependent parameter GU and GV

(equation (2.8)) [23, 24].

$$H_{k,\text{Gaussian}} = \sqrt{GW + GV \cdot \tan \Theta + GU \cdot \tan^2 \Theta} \quad (2.8)$$

The zero point shift is a further important instrumental parameter, which corrects the shift of the zero point due to a not ideally placed sample in the beam. The zero point shift is a constant value, which has to be added to all calculated peak positions [23, 24].

In contrast to a Rietveld refinement, the Le Bail method neglects the crystal structure and hence, the structure factor [23, 22, 24]. Therefore, at the beginning of a Le Bail refinement the peaks are fitted with arbitrary starting values for I_k , $G(2\Theta_i - 2\Theta_k)$ and b_{ig} . In the following refinement steps, the refinement parameter of the profile and background function as well as the lattice parameter are optimized under a re-distribution of the calculated intensities until the Δ value from equation (2.4) is minimized [23, 24].

2.1.5 Agreement factors

In order to evaluate the progress and accuracy of a single crystal structure refinement, several agreement factors have to be considered. The internal agreement factor, R_{int} , is the basis for the determination of the Laue-group (equation (2.9)) [22].

$$R_{\text{int}} = \frac{\sum |F_{\text{obs}}^2 - \langle F_{\text{obs}}^2 \rangle|}{\sum F_{\text{obs}}^2} \quad (2.9)$$

In equation (2.9), F_{obs}^2 represents the intensities of all independent reflections measured in the experiment, whereas $\langle F_{\text{obs}}^2 \rangle$ describes the average of the symmetry-equivalent reflections merged under the selected crystal symmetry. It is obvious, that the higher the crystal symmetry, the more reflections are merged. If the differences between F_{obs}^2 and $\langle F_{\text{obs}}^2 \rangle$ are large, this could indicate that the crystal symmetry is too high and should be reduced [26].

The progress of the crystal structure refinement can be evaluated by considering different agreement factors, R , and their weighted variants, R_w (equation (2.10)).

$$R = \frac{\sum |Y_{\text{obs}} - Y_{\text{calc}}|}{\sum Y_{\text{obs}}} \quad \text{and} \quad R_w = \left(\frac{\sum w \cdot |Y_{\text{obs}} - Y_{\text{calc}}|^2}{\sum w \cdot Y_{\text{obs}}^2} \right)^{\frac{1}{2}} \quad (2.10)$$

In equation (2.10), Y can either be a function of the intensities I , F_{hkl}^2 or F_{hkl} and w is a weighting factor [27].

In order to evaluate the quality of a Le Bail refinement, the statistical parameter R_p and R_{wp} are usually considered. The value R_p and the weighted value R_{wp} are given

by equation (2.11) [23, 24].

$$R_p = \frac{\sum_i |y_{i,obs} - y_{i,calc}|}{\sum_i y_{i,obs}} \quad \text{and} \quad R_{wp} = \sqrt{\frac{\sum_i w_i \cdot |y_{i,obs} - y_{i,calc}|^2}{\sum_i y_{i,obs}}} \quad (2.11)$$

In equation (2.11), $y_{i,obs/calc}$ are the intensities of measured ("obs") and calculated ("calc") profile points and w_i is a weighting factor.

In general, all R values are given in percentages and in an ideal case they become zero as in that case the error sum of squares becomes zero [23, 24, 22].

Finally, the χ^2 value is a statistical parameter which is used in the evaluation of single crystal and powder refinements. This parameter is normalized to the statistical degrees of freedom, defined by the difference between the number of observed data points, N_{obs} , and the number of parameters, $N_{parameter}$, involved in the refinement step (equation (2.12)).

$$\chi^2 = \frac{\sum_i w_i \cdot |\delta|^2}{N_{obs} - N_{parameter}} \quad (2.12)$$

Here, δ is the difference between the measured and calculated intensities either from a single crystal or powder experiment (see also equation (2.4)). In an ideal case χ^2 becomes 1 [23, 24, 22].

2.2 Inelastic Neutron Scattering

2.2.1 Elastic and inelastic scattering

If a neutron beam interacts with a sample different scattering processes which are - in general - the elastic and inelastic scattering, occur in parallel (figure 2.1). In the following figure the wave vector of the incident beam is denoted as k_0 , while the one of the scattered beam corresponds to k_s .

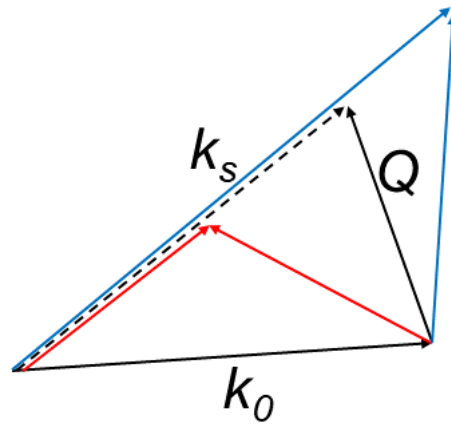


FIGURE 2.1: The scattering triangles for elastic (black) and inelastic scattering with phonon creation (red) and phonon annihilation (blue), respectively.

In case of an elastic scattering process, the energy, E_0 , of the incident beam is equal to

the one of the scattered beam, E_s , and only the direction of k_s is changed with respect to the one of k_0 [28, 29]. The difference vector, Q , between k_s and k_0 corresponds to a reciprocal lattice vector, G , so that for an elastic scattering process $k_s - k_0 = Q = G$ (figure 2.1).

In the sample, phonons with discrete energy levels, $\hbar \cdot \omega$ (\hbar : reduced Planck constant; ω : Phonon frequency), are present. In an inelastic scattering process, the incident beam interacts under an energy ($\hbar \cdot \omega$) and momentum ($\hbar \cdot q$) transfer with the phonons of the sample [28, 29]. This interaction results either in a creation or an annihilation of a phonon in the sample [28, 29]. Equations (2.13a) and (2.13b) summarize the underlying law of energy and momentum conversion, respectively [28, 29].

$$E_s - E_0 = \pm \hbar \omega \quad (2.13a)$$

$$\hbar k_s - \hbar k_0 = \hbar Q = \hbar G \pm \hbar q \quad (2.13b)$$

The phonon creation and annihilation, respectively, is taken into account by the \pm sign. While (+) corresponds to an annihilation process, (−) describes the phonon creation [28, 29]. Here, $\hbar q$ corresponds to the so-called crystal momentum, which describes the momentum transferred to the sample [28, 29]. Figure 2.1 compares the scattering triangles for the phonon creation and annihilation process with the one of the elastic scattering. The contribution of the phonon wave vector q is reflected by the length of the k_s vector.

2.2.2 Scattering cross section and scattering function

In a neutron scattering experiment one measures the fraction of the flux Φ of the incident neutron beam scattered by the sample [30]. This fraction is denoted as scattering cross section σ . In case one measures the total signal scattered by the sample, one measures the total scattering cross section [30]. If only the part of the neutron beam scattered in a solid angular element $d\Omega$ is measured, one determines the differential cross section $\frac{d\sigma}{d\Omega}$ [30]. The differential cross section corresponds to an elastic scattering experiment as the energy of the scattered neutrons remains unchanged [30]. In case one measures the neutron beam scattered by a sample in $d\Omega$ and in an energy interval dE , one determines the double differential scattering cross section $\frac{d^2\sigma}{d\Omega dE}$ [30]. The double differential cross section describes an inelastic scattering experiment as it takes into account that the energy of the scattered neutrons is changed due to the scattering process in the sample [30].

The double differential cross section is connected to the scattering function, $S(Q, E)$ (equation (2.14)), where k_0 and k_s represent the wave vector of the incident and scattered beam, respectively [31].

$$\frac{d^2\sigma}{dEd\Omega} = \frac{k_s}{k_0} \cdot S(Q, E) \quad (2.14)$$

The scattering function describes all kinds of interactions between the incident neutron beam and the sample. It was demonstrated [32, 33] that in terms of the conventional harmonic phonon expansion the scattering function, $S(Q, E)$, can be expressed by a sum of an elastic ($S_0(Q, E)$), an one-phonon ($S_1(Q, E)$) and a multi-phonon ($S_m(Q, E)$) contribution (equation (2.15)).

$$S(Q, E) = S_0(Q, E) + S_1(Q, E) + S_m(Q, E) \quad (2.15)$$

Each of these scattering functions has a coherent and an incoherent contribution [30, 32, 33]. In case of coherent scattering, there are fixed phase relations between the scattered waves and thus, constructive interference occurs. Moreover, a coherent scattering process depends on the direction of the scattering vector. In contrast to this, in an incoherent scattering process the phase relations between the scattered waves are random and thus, a constructive interference is not possible. Moreover, the incoherent scattering is uniform and isotropic in all directions [30].

Bragg peaks are the result of a coherent elastic scattering process as the periodicity of the sample's crystal structure allows a constructive interference between the scattered waves [30, 32, 33]. Incoherent elastic scattering reflects single-particle motion and thus, contributes only to the background in a diffraction experiment [30].

2.2.3 The one-phonon scattering function and the incoherent approximation

For an inelastic neutron scattering from a polycrystalline sample the one-phonon scattering function, $S_1(Q, E)$, on the neutron-energy loss side (Phonon creation) is described by the expression shown in equation (2.16) [33, 34, 32].

$$S_1(Q, E) = \frac{1}{N} \cdot \sum_{ij} \frac{b_i \cdot b_j}{\langle b^2 \rangle} \cdot \exp(-(W_i + W_j) \cdot \exp(iQ \cdot (R_i - R_j))) \cdot \sum_m \frac{\hbar \cdot (Q \cdot \xi_i) \cdot (Q \cdot \xi_j)}{\omega_m \cdot (M_i \cdot M_j)^{\frac{1}{2}}} \cdot \langle n_m + 1 \rangle \delta(E - \hbar\omega_m) \quad (2.16)$$

In equation (2.16), N , i and j , and ω_m , correspond to the number of oscillators, the atomic species i and j , and the frequency of the m th normal mode. The parameters $b_{i/j}$, $W_{i/j}$, $R_{i/j}$ and $\xi_{i/j}$ are the neutron scattering length b , the Debye Waller factor W , the atomic equilibrium position R , and the displacement vector ξ , of i and j . $n_m = [\exp(\hbar\omega_m/k_B T) - 1]^{-1}$ is a population factor and the factor $(Q \cdot \xi_i) \cdot (Q \cdot \xi_j)$ describes the correlation between the atomic species i and j [33, 34, 32]. In general, equation (2.16) contains a coherent ($i \neq j$) and an incoherent ($i = j$) contribution, where the former one is usually the dominating one as the coherent scattering length of most isotopes is larger compared to the corresponding incoherent one.

Usually, the coherent inelastic neutron scattering from a polycrystalline sample is treated under the incoherent approximation [33, 34, 32]. In a polycrystalline sample the grains are randomly distributed and thus, the scattering function $S_1(Q, E)$ can be

averaged over an extended Q range [33, 34, 32]. The consequence of this is, that the correlations between the atoms i and j get lost, and hence, the factor $(Q \cdot \xi_i) \cdot (Q \cdot \xi_j)$ can be replaced by its average $\frac{1}{3} \cdot Q^2 \cdot \xi_i^2 \delta_{ij}$ [33, 34, 32]. As a result of the incoherent approximation the double differential cross sections of the coherent and incoherent scattering, $(\frac{d^2\sigma}{dE d\Omega})_{\text{coh}} \approx (\frac{d^2\sigma}{dE d\Omega})_{\text{incoh}}$, are approximately identical [30].

In the scope of the incoherent approximation, the scattering function $S_1(Q, E)$ can be simplified to the expression shown in equation (2.17) [32, 34].

$$S_1(Q, E) = \sum_i \frac{b_i^2}{\langle b^2 \rangle} \cdot \exp(-2W_i) \cdot \frac{Q^2}{2M_i} \cdot \frac{g_i(\omega)}{E} \cdot \langle n_m + 1 \rangle \quad (2.17)$$

Obviously, the scattering function $S_1(Q, E)$ is connected with the sum of the partial phonon density of states, $g_i(\omega)$, of the atoms i in the sample. The partial phonon density of states are connected with the total one, $G(\omega)$, by equation (2.18).

$$G(\omega) = \sum_i \frac{4\pi \cdot b_i^2}{m_i} \cdot g_i(\omega) \quad (2.18)$$

Here, $\frac{4\pi \cdot b_i^2}{m_i}$ is an element-specific weighting factor [33]. As one measures the total double differential cross section in an inelastic neutron scattering experiment, this technique gives access to the total phonon density of states, $G(\omega)$, of a compound.

2.2.4 The ARCS beamline

All inelastic neutron scattering experiments described in this study have been performed at the beamline ARCS at the Spallation Neutron Source (SNS) facility at the Oak Ridge National Laboratory (ORNL), Tennessee, USA. The beamline is well described in previous publications [35, 36] and thus, only a short description of the main parts is given here.

ARCS is a wide-angular time-of-flight chopper spectrometer. A scheme of the beamline is shown in figure 2.2. At the T_0 chopper, a polychromatic, short neutron pulse containing the desired energy range is selected by adjusting a suitable rotation speed. Moreover, undesirable radiations (e. g. γ -rays) and too fast or too slow neutrons, respectively, are blocked [35, 36]. The selected neutron pulse is guided to the Fermi chopper where it is monochromatized. The initial intensity, I_0 , of the monochromatized beam is detected by a beam monitor. The monochromatized beam is guided to the sample stage of the spectrometer which is equipped with a He cryostat. The flight-time between the Fermi chopper and the sample is well known. The monochromatized neutron beam interacts with the sample and several scattering processes occur. The scattered neutrons are detected and normalized to I_0 later by the beamline software [35, 36]. While elastically scattered neutrons arrive at the detector array at the time t_0 , inelastically scattered ones arrive either earlier (phonon annihilation, Anti-Stokes process) or later (phonon creation, Stokes process) [37].

The detector array of the beamline consists of 920 sensitive ^3He tubes and covers a

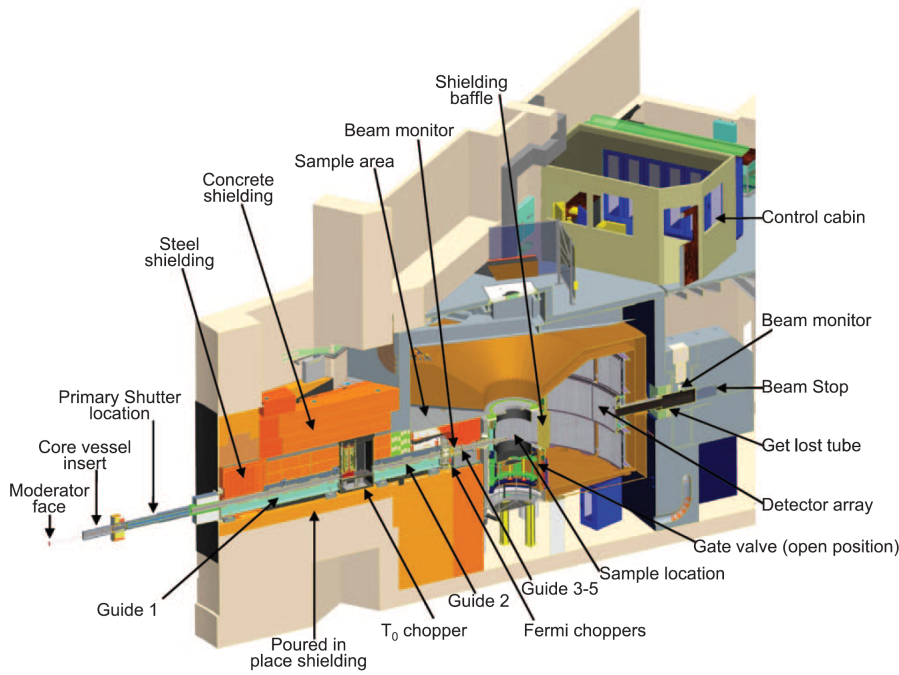


FIGURE 2.2: A scheme of the ARCS beamline at the ORNL [35].

vertical/horizontal angular range of -27 to 26° / -28 to 135° . The detector array measures the time-of-flight spectrum of the sample in $I(2\Theta, t)$ or $I(2\Theta, K)$ (I , 2Θ , t , K : intensity, scattering angle, flight-time, detector number) [35, 36].

2.2.5 Data transformation

Usually, the physics of the studied system is expressed in terms of $S(Q, E)$ or $S(Q, \omega)$ and thus, a data transformation of the time-of-flight data is mandatory. It was demonstrated that the time-of-flight raw data are connected with the scattering function $S(Q, \omega)$ via equation (2.19) [37].

$$I(2\Theta, K) \propto S(Q, \omega) \cdot \frac{1}{t^4} \quad (2.19)$$

Obviously, the factor t^{-4} causes a non-linear dependence between the time-of-flight data and $S(Q, \omega)$. Thus, the intensity of early arriving neutrons is increased, however, at the cost of a reduction of the energy resolution [37].

2.3 Nuclear Resonant Scattering

2.3.1 Mössbauer spectroscopy

The Mössbauer spectroscopy is a technique developed to probe nuclear transitions between a ground state and an excited state with a high energy resolution. Hence,

Mössbauer spectroscopy yields information about the local structure and the chemical and magnetic environment of the nuclei [38, 39, 40].

In figure 2.3 the principle of the resonance absorption is shown in a simplified way. A

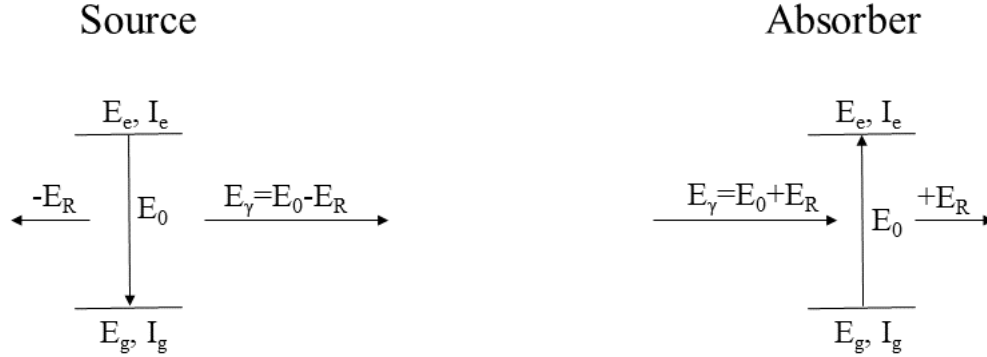


FIGURE 2.3: The principle of the resonance absorption.

nucleus of the radioactive parent isotope, denoted as source, decays under emission of a γ -quantum with energy E_0 from an excited state characterized by the energy E_e and spin I_e to its ground state with energy E_g and spin I_g . The emitted γ -quantum is absorbed by a second nucleus of the same type, denoted as absorber, as the energy of the photon matches the transition energy of this nucleus.

For a free atom or a molecule in a gas phase or in a liquid, the emission and absorption of a γ -quantum is accompanied by a recoil effect. The corresponding recoil energy, E_R , of an atom with mass m is given by

$$E_R = \frac{E_\gamma^2}{2 \cdot m \cdot c^2}. \quad (2.20)$$

Due to the recoil effect, the energy of the emitted photon, E_0 , is reduced by E_R , to $E_\gamma = E_0 - E_R$, while an additional contribution of E_R to E_0 is necessary for the absorption of the γ -quantum (see figure 2.3). As a consequence of the recoil effect a resonance absorption is impossible, yet it can be achieved by adding additional Doppler energy by moving the source periodically.

In a solid, the atoms are tightly bonded in the lattice as the bonding energy is much larger than E_R . Due to the large mass M of the solid, the transfer of recoil-energy, $E_R = \frac{E_\gamma^2}{2 \cdot M \cdot c^2}$, is negligible small [38, 39, 40]. Therefore, a recoil-free absorption or emission of γ -quanta takes places which is the basis of the so-called Mössbauer effect.

In Mössbauer spectroscopy the Lamb-Mössbauer factor, $f_{LM}(T)$, is correlated with the probability of a recoil-free resonant γ -absorption and yields important information about the bonding rigidity (equation (2.21) and (2.22)) [41, 42],

$$f_{LM}(T) = \exp(-k^2 \cdot \langle x^2 \rangle) = \exp\left(-\frac{\langle x^2 \rangle \cdot E_\gamma^2}{\hbar^2 \cdot c^2}\right) \quad (2.21)$$

$$f_{\text{LM}}(T) = \exp \left(-\frac{6 \cdot E_{\text{R}}}{k_{\text{B}} \cdot \Theta_{\text{D}}} \cdot \left(\frac{1}{4} + \left(\frac{T}{\Theta_{\text{D}}} \right)^2 \cdot \int_0^{\Theta_{\text{D}}/T} \frac{x}{\exp(x) - 1} dx \right) \right). \quad (2.22)$$

Here, $\langle x^2 \rangle$ is the mean square atomic displacement, $k = \frac{2\pi}{\lambda}$ is the magnitude of the wave vector \vec{k} , E_{γ} is the energy of the emitted γ quantum, \hbar is the reduced Planck constant, c is the light speed, E_{R} is the recoil energy, k_{B} is the Boltzmann constant, and Θ_{D} is the Debye temperature. The Lamb-Mössbauer factor becomes large, if

- the recoil energy E_{R} is small.
- the Debye temperature and hence, the rigidity of the bonding of the solid is large.
- the atomic displacement is small. Therefore, low temperature is required in order to gain a sufficiently large Mössbauer effect.

The residual factor $(1 - f_{\text{LM}}(T))$ is determined by recoil-processes due to the creation and annihilation of phonons by nuclear inelastic scattering. Hence, this factor gives access to the lattice dynamics of the solid. Therefore, the idea to extend Mössbauer spectroscopy to measure the nuclear absorption spectrum is straightforward. However, in order to determine the phonon spectra by conventional Mössbauer spectroscopy the following main problems arise [41, 42]:

- Scans of the entire energy range of a phonon spectrum with the technique of Doppler shift requires Doppler velocities in the frequency range of ultrasound.
- The cross section of the nuclear inelastic scattering is weak over the entire energy range of the phonon spectrum. Hence, a very intense radiation source is required.
- A high background contribution caused by transmitted or electronically scattered radiation has to be avoided.

Nuclear Resonant Scattering (NRS) is a method which solves the above-mentioned problems of the conventional Mössbauer spectroscopy and allows a) the measurement of the nuclear absorption spectrum of a Mössbauer-active isotope by nuclear inelastic scattering (NIS) and b) the determination of hyperfine parameters by nuclear forward scattering (NFS) [41, 42].

2.3.2 The Nuclear Resonant Scattering Station at the beamline P01, PETRA-III (DESY)

The experimental setup of the Nuclear Resonant Scattering Station at the beamline P01 at the synchrotron PETRA III (DESY, Hamburg) is shown schematically in figure 2.4. After passing the undulator, the energy of the incoming synchrotron beam is tuned to the resonance energy of a Mössbauer-active nucleus (for further details see appendix B.1) using a double-crystal monochromator (DCM). The energy resolution

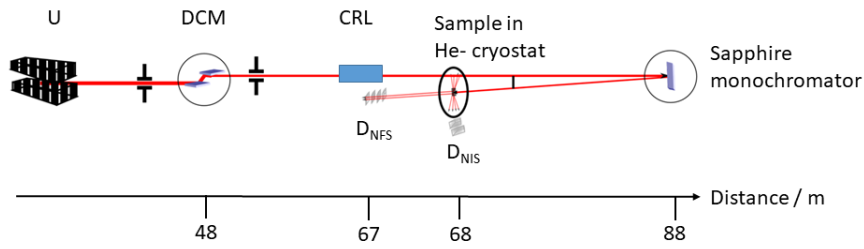


FIGURE 2.4: A scheme of the experimental setup for nuclear inelastic scattering measurements at the beamline P01 (DESY) adapted from reference [43]. U: undulator, DCM: double crystal monochromator, $D_{\text{NIS}}/D_{\text{NFS}}$: NIS/NFS APD.

of the DCM is around a few eV. The monochromized beam is focused by an assembly of Be lenses, so-called compound refractive lenses (CRL), from about $3\text{ mm} \times 3\text{ mm}$ to about $300\text{ }\mu\text{m} \times 200\text{ }\mu\text{m}$ in the horizontal and vertical direction, respectively. A high energy resolution of about a few meV or less is gained by using a sapphire backscattering monochromator characterized by an excellent crystal quality [44, 45]. The monochromator allows to probe Mössbauer isotopes with transition energies between 20-60 keV [44]. For several Mössbauer isotopes, sapphire reflections (e. g. for ^{121}Sb : (8 16 40); ^{125}Te : (9 1 68)), which yield a highly intense backscattered beam, are known and used [44].

In order to tune the energy transferred to the sample, the monochromator crystal is placed in a cryostat [44]. By changing the temperature, the d -spacing of the considered Miller plane and hence, the energy of the beam is changed. For several Mössbauer isotopes, e. g. ^{121}Sb and ^{125}Te , the correlation between the temperature, d -spacing and energy change was studied previously and is well established [44]. Therefore, by choosing a suitable temperature profile, the phonon spectrum of the sample can be measured. After passing the sapphire backscattering monochromator, the beam interacts with the sample, which is also placed in a cryostat. In general, for compounds containing ^{121}Sb and/or ^{125}Te , the Lamb-Mössbauer factor is very small at room temperature and a pronounced contribution of multi-phonon scattering to the NIS signal is observed. Therefore, measurements of ^{121}Sb and/or ^{125}Te containing compounds are performed at low temperatures, typically far below 100 K.

In order to determine the nuclear absorption spectrum of a Mössbauer-active isotope, one has to distinguish between quanta produced by NIS and other sources resulting from fluorescence or electronic scattering [41, 42]. This is realized by using the pulsed nature of synchrotron radiation [41, 42]. While the quanta of NIS are delayed in time by ns to μs due to the finite lifetime of the excited state, the radiation of the other processes are only present at the moment when the synchrotron pulse hits the sample. Therefore, the quanta from NIS are counted between the synchrotron pulses. To realize this, fast responding and high sensitive detectors are mandatory and avalanche-photodiodes (APD) match these requirements [41, 42]. In order to measure the phonon spectrum of the sample two APD detectors are used. The NIS

detector, (D_{NIS}), is placed close to the sample, whereas the NFS detector is placed at a larger distance of few meters to the sample. While the NIS APD detects the total absorption spectrum of the sample, the NFS detector counts only the elastic scattered part and hence, it only measures the elastic line. From the FWHM of the elastic line one can deduce information about the instrumental resolution of the sapphire monochromator [41, 42, 44].

In this study only NIS was used and therefore, the following discussion concentrates on this technique.

2.3.3 Nuclear Inelastic Scattering

2.3.3.1 Nuclear Inelastic Scattering and Nuclear Inelastic Absorption

Up to now, the method discussed here was described as "nuclear inelastic scattering", because in the literature this is the most often used term for this technique and moreover, it emphasizes the similarity to inelastic neutron scattering. However, this term is not completely precise and might lead to a misunderstanding, especially if the term is considered as a definition of the involved physical processes [41, 42].

An excited nuclear state decays to its ground state either by an emission of a photon or by an internal conversion [41, 42]. By decaying via the first channel, the energy of the emitted photon either matches the transition energy or is shifted relative to E_γ by an inelastic scattering processes. The probability of this radioactive decay channel is given by $1/(1+\alpha)$, where α is the conversion coefficient. This decay channel is called nuclear inelastic scattering [41, 42]. By decaying via an internal conversion the transition energy is transferred to an inner electron, e. g. in the K-shell, which subsequently leaves the atom [41, 42]. The resulting hole in the inner shell is filled by an electron from an energetically higher lying shell under an emission of a X-ray quantum and/or Auger electrons. The probability of the internal conversion is $\alpha/(1+\alpha)$. In the following, the internal conversion decay channel will be denoted as nuclear inelastic absorption (NIA).

In this study, the quanta resulting from the internal conversion were detected by the NIS and NFS APDs, as the detection of the X-ray radiation features some important practical advantages compared to the analysis of the γ -quanta resulting from the nuclear inelastic scattering process. If the γ -quanta are measured, the momentum transfer has to be considered and therefore, the orientation of the detector relative to the incoming beam has to be well defined [41, 42]. In contrast to this, the signal of NIA is independent from the momentum transfer in the sample and thus, the orientation of the detector relative to the incoming beam is not crucial [41, 42]. Moreover, the conversion coefficient of many Mössbauer isotopes is $\alpha \gg 1$ and hence, the probability of the nuclear inelastic scattering is only around a few percentages. A further reduction of the probability of this process occurs due to trapping of the γ -ray radiation in the sample. Finally, the efficiency of the APD detectors is higher for X-rays.

All of these considerations make NIA to an ideal tool for the determination of the nuclear absorption spectra of Mössbauer-active isotopes [41, 42].

2.3.3.2 The nuclear absorption spectrum

Figure 2.5 shows the nuclear absorption spectrum of α -iron [42] as an example. As

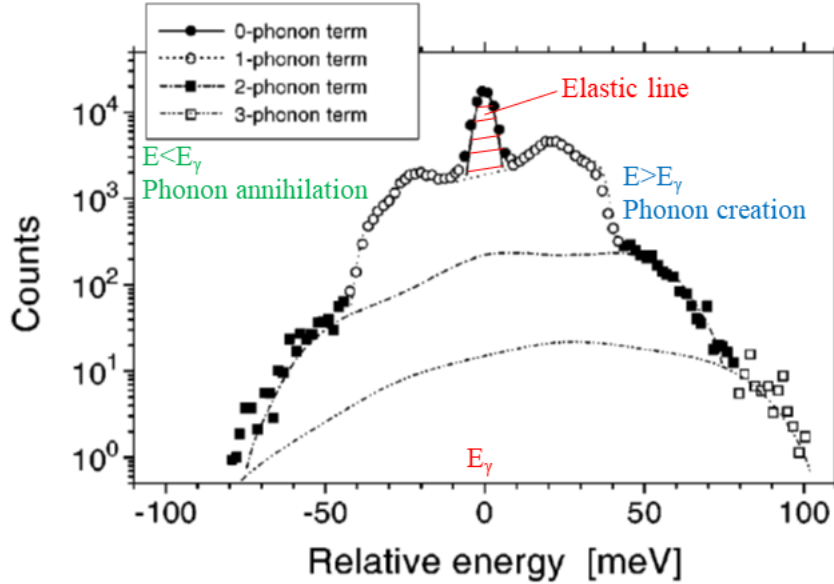


FIGURE 2.5: The nuclear absorption spectrum of α -iron (adapted from reference [42]).

mentioned above, the energy of the incoming synchrotron beam is tuned around the transition energy of the Mössbauer isotope by varying the temperature of the sapphire monochromator [44]. If the energy of the beam matches the nuclear transition energy, the photon is absorbed by the Mössbauer isotope in a zero-phonon process [41, 42, 46]. This is an elastic process resulting in a high central peak in the absorption spectrum around E_γ , the so-called elastic line. In figure 2.5, the contribution of the elastic scattering to the total nuclear absorption spectrum of α -iron is depicted and denoted as "0-phonon-term".

Features at higher or lower energies with respect to the elastic line are originated by inelastic absorption processes which are accompanied either by the creation ($E > E_\gamma$) or annihilation ($E < E_\gamma$) of n phonons [41, 42, 46]. In figure 2.5, the contributions of several inelastic scattering events to the total nuclear absorption spectrum of α -iron are shown and denoted as " n -phonon-term", where $n=1, 2, 3$ describes the number of phonons which are either created or annihilated in the scattering process. In the 1-phonon process the absorption of a X-ray quantum results in the creation/annihilation of a single phonon. Scattering events with $n > 1$ are multi-phonon processes in which the absorption of a X-ray quantum causes the creation/annihilation of more than one phonons. The probability of the phonon-assisted absorption at a given energy is correlated with the number of available

phonon states. Hence, the nuclear absorption spectrum gives access to the (partial) phonon density of states of the Mössbauer isotope [41, 42, 46].

2.3.3.3 Determination of (partial) phonon density of states

Figure 2.6a) shows the total nuclear absorption spectrum of $\text{Sb}_2\text{Se}_{1.8}\text{Te}_{1.2}$ as an example. The spectrum is correlated with the total scattering function, $S(E)$ (equation

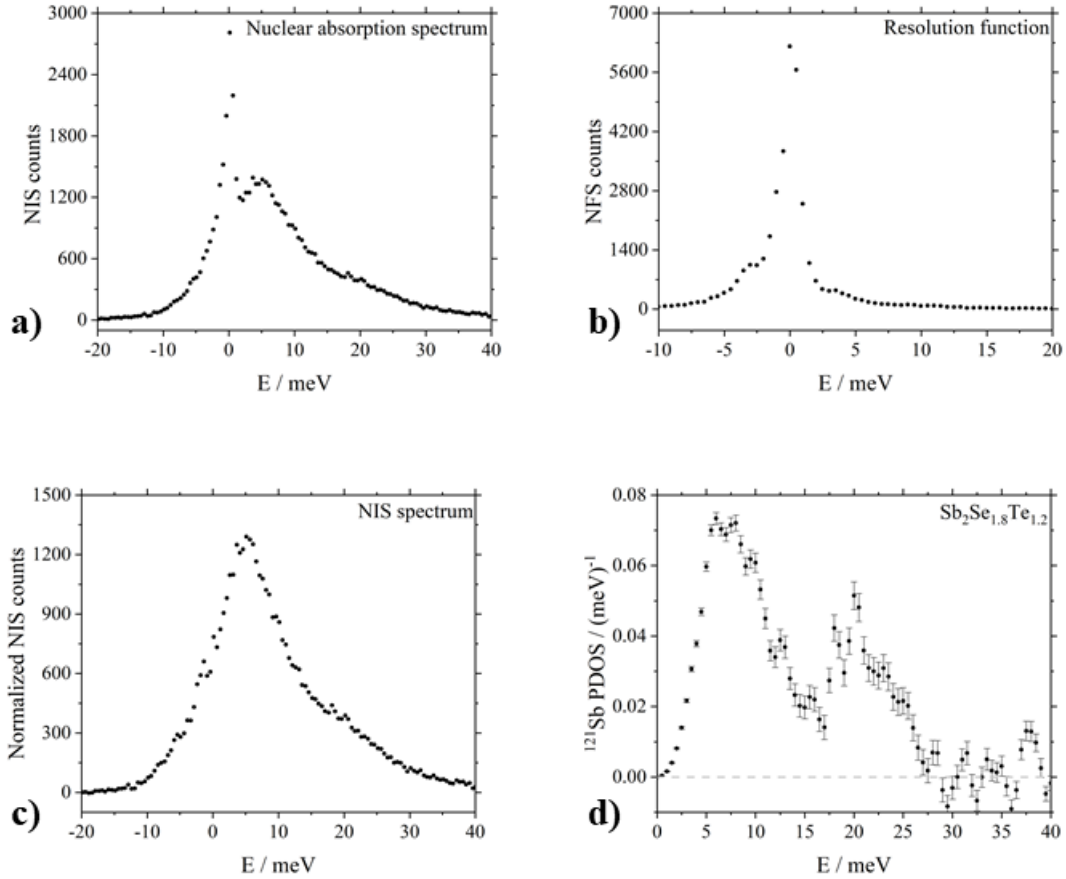


FIGURE 2.6: Data treatment of the ^{121}Sb NIS data collected on the $\text{Sb}_2\text{Se}_{1.8}\text{Te}_{1.2}$ sample. a) Total nuclear absorption spectrum, b) resolution function, c) normalized NIS spectrum, d) ^{121}Sb partial phonon density of states.

(2.23)), which can be expressed in terms of the harmonic approximation by [41, 42, 47, 48, 46]

$$S(E) = f_{\text{LM}} \cdot \left(\delta(E) + \sum_{n=1}^n S_n(E) \right). \quad (2.23)$$

In equation (2.23), the elastic contribution (figure 2.6b)), $\delta(E)$, is described by a Dirac delta function, whereas the residual inelastic scattering function is mathematically decomposed in a sum of single scattering functions, $S_n(E)$, which describe n -phonon scattering processes. The single-phonon term, $S_1(E)$, is connected with the (partial)

phonon density of states, $g(E)$, (equation (2.24)) by

$$S_1(E) = \frac{E_R \cdot g(E)}{E \cdot (1 - \exp(-E/k_B \cdot T))}. \quad (2.24)$$

In order to determine the (partial) phonon density of states, a separation of the single-phonon contribution (equation (2.24)) from all other ones in equation (2.23) is necessary which is done by the following steps:

Step 1: Subtraction of the elastic line and normalization

The pure inelastic contribution is obtained by a subtraction of the instrumental resolution function measured with the NFS APD from the normalized total nuclear absorption spectrum [41, 42]. A normalization of the difference spectrum is gained by using the first Lipkin sum rule (equation (2.25)) according to which the first momentum of the NIS spectrum, F^1 , is equal to the recoil energy (equation (2.20))

$$F^1 = \int_{-\infty}^{+\infty} E \cdot S(E) dE = E_R. \quad (2.25)$$

Thus, in the process of the data treatment, the spectrum is required to fulfill this condition.

From the normalized difference spectrum, in the following denoted as "NIS spectrum" (figure 2.6c)), the Lamb-Mössbauer factor can then be calculated according to equation (2.26) [49]

$$f_{LM} = 1 - \int_{-\infty}^{-0} S(E) dE + \int_0^{\infty} S(E) dE. \quad (2.26)$$

As seen in equation (2.24), the (partial) phonon density of states depends on the sample temperature T . However, in a nuclear inelastic scattering experiment the sample temperature is not necessarily equal to the one adjusted at the cryostat. This is due to the fact that the highly intense synchrotron beam interacts directly with the sample which causes a heating-up of the sample. In order to estimate the correct sample temperature, the Bose-Einstein-statistics, n_B , can be used [49]. This statistics describes the probability for the occupancy of phonon states. The probability of nuclear absorption by phonon creation is proportional to $(n_B + 1) = 1/(1 - \exp(-\beta E))$, whereas the one of the phonon annihilation is proportional to $n_B = 1/(\exp(\beta|E|))$; $\beta = k_B \cdot T$ [49]. From the probabilities of both phonon-assisted nuclear absorption processes one can derive the sample temperature. At this temperature, the intensity ratio for the phonon creation and annihilation are equal at a given energy $|E|$ [49].

Step 2: Subtraction of multi-phonon contribution

In the last step of the data treatment, the single-phonon term is separated from the multi-phonon contributions described by the scattering functions $S_n(E) > 1$ in equation (2.23). This is done by using the so-called Fourier-log method [50, 51]. Finally,

the (partial) phonon density of states (figure 2.6d)) is calculated from $S_1(E)$ according to equation (2.27)

$$g(E) = \frac{S_1(E) \cdot E \cdot (1 - \exp(-E/k_B \cdot T))}{E_R}. \quad (2.27)$$

2.4 The Phonon Density of States: Important relations

The total phonon density of states, $G(E)$, obtained from an inelastic neutron scattering experiment is connected with the total heat capacity of the studied material (equation (2.28)) by

$$c_V(T) = 3 \cdot n \cdot R \cdot \int_0^\infty G(E) \cdot \frac{x^2 \cdot \exp(x)}{(\exp(x) - 1)^2} dE. \quad (2.28)$$

Here, $x = E/k_B \cdot T$, E is the energy, T is the temperature, R is the universal gas constant, and n corresponds to the number of oscillators. Element-specific Debye temperatures, $\Theta_{D,i}$ (equation (2.29)), and element-specific mean-force constants, F_i (equation (2.30)), are accessible from the (partial) phonon density of states, $g(E)$,

$$\Theta_{D,i} = \left(\frac{3}{(k_B^2 \cdot \int_0^\infty g(E) dE / E^2)} \right)^{\frac{1}{2}} \quad (2.29)$$

$$F_i = M_i \cdot \int_0^\infty g(E) E^2 dE / \hbar^2. \quad (2.30)$$

Both quantities yield information about the rigidity of the bonding of each Mössbauer isotope [14, 52]. In all equations, \hbar is the reduced Planck constant, k_B is the Boltzmann constant, and M_i is the mass of the Mössbauer isotope [14, 52].

For isostructural mixed crystals with different compositions the mode positions in the element-specific PDOS of composition A are shifted relatively to the corresponding ones of composition B [14, 52]. This relative shift is due to changes of the unit cell volume caused by variations of the lattice parameter and - if relevant - the different mass fractions of the considered Mössbauer isotope in both mixed crystals. However, there can be an additional contribution to the observed shift caused by changes in the bonding scheme [14, 52]. In order to evaluate whether the bonding scheme is changed or not as a consequence of the compositional variation one can use the homology relation:

$$\frac{E_B}{E_A}(LP) = \left(\frac{M_A}{M_B} \cdot \frac{LP_A^2}{LP_B^2} \right)^{\frac{1}{2}} \quad \frac{E_B}{E_A}(V) = \left(\frac{M_A}{M_B} \cdot \frac{V_A^{\frac{2}{3}}}{V_B^{\frac{2}{3}}} \right)^{\frac{1}{2}}. \quad (2.31)$$

In equation (2.31), E_A and E_B is the mode energy of the same mode in the element-specific PDOS obtained from the mixed crystals A and B and M_A/M_B is the mass fraction of the considered Mössbauer isotope. $V_A^{\frac{2}{3}}/V_B^{\frac{2}{3}}$ is the ratio of the unit cell

volumes from which one gains a volume-averaged scaling factor, $\frac{E_B}{E_A}(V)$. In case of polycrystalline samples, this scaling factor reflects how the observed mode shifts are influenced by the composition-induced changes of the unit cell volume (and the mass fraction of the considered Mössbauer isotope). The lattice parameter ratios, $\frac{LP_A^2}{LP_B^2}$, give access to direction-dependent scaling factors, $\frac{E_B}{E_A}(LP)$. By using the scaling factors calculated from the homology relation, the energy values of the element-specific PDOS of mixed crystal *B* can be scaled to allow a direct comparison to mixed crystal *A* [14, 52].

2.5 Equations of State

In thermodynamics, a system is defined by a set of variables which are connected to each other by so-called equations of state. In an ambient temperature high-pressure diffraction experiment, these variables are the pressure and the unit cell volume or lattice parameter of the compound, respectively. In order to describe the pressure-induced change, $p(V)$, of the unit cell volume, V , with respect to the unit cell volume at zero pressure, V_0 , a third order Birch-Murnaghan isothermal equation of state (equation (2.32)) was used in this study [53]

$$p(V) = \frac{3}{2} \cdot B_0 \cdot \left[\left(\frac{V}{V_0} \right)^{-\frac{7}{3}} - \left(\frac{V}{V_0} \right)^{-\frac{5}{3}} \right] \cdot \left[1 + \frac{3}{4} \cdot (B'_0 - 4) \cdot \left[\left(\frac{V}{V_0} \right)^{-\frac{2}{3}} - 1 \right] \right]. \quad (2.32)$$

Here, B_0 corresponds to the bulk modulus and B'_0 is its first derivative [53]. The bulk modulus can be considered as a material-specific resistance against compression. For all high-pressure polymorphs, a Murnaghan equation of states (equation (2.33)) was used to describe the pressure-induced changes of the unit cell volume [54]

$$p(V) = p_{\text{tr}} + \frac{B_{\text{tr}}}{B'_{\text{tr}}} \cdot \left[\left[\left(\frac{V_{\text{tr}}}{V} \right)^{B'_{\text{tr}}} \right] - 1 \right] \quad (2.33)$$

where, p_{tr} , B_{tr} , B'_{tr} and V_{tr} correspond to the transition pressure, the bulk modulus and its derivative at p_{tr} , and the transition volume [54].

2.6 Heat capacity measurements

2.6.1 Theory of heat capacity

In general, the heat capacity, C , is defined as the ratio, $C = \frac{dQ}{dT}$, between a heat amount, dQ , which has to be applied to a body in order to change its temperature, T , by dT [55]. In thermodynamics two different heat capacities, c_p and c_V , are known. The former one is defined for a constant pressure, p , and the later one for constant

volume, V . For a solid, the difference in c_p and c_V is given by

$$c_p - c_V = \frac{T \cdot V \cdot \alpha_V^2}{\kappa_T}, \quad (2.34)$$

where α_V is the volume thermal expansion coefficient and κ_T is the isothermal compressibility (equation (2.34)) [55]. Especially at low temperature the difference $c_p - c_V$ is small and it is often assumed that $c_p \approx c_V$ [55].

The heat capacity c_p is connected with the thermodynamic quantities enthalpy, $H(T)$ (equation (2.35a)), and entropy, $S(T)$ (equation (2.35b)), so that, if c_p is known, $S(T)$ and $H(T)$ can be estimated [55].

$$dH(T) = c_p dT \quad (2.35a)$$

$$dS(T) = \frac{c_p}{T} dT \quad (2.35b)$$

The experimentally determined heat capacity of a solid contains numerous contributions, from which the most prominent ones are caused by the excitations of phonons, electrons and magnons. Moreover, additional contributions, e. g. from impurities, do also influence the measured heat capacity data [28, 29]. Many models have been developed in order to gain an understanding and a mathematical description of the temperature dependence of the heat capacity of the different contributions [28, 29]. For the compounds investigated in this study, the most important contribution originates from phonons. Therefore, the following theoretical descriptions will be focused on this vibrational contribution only.

2.6.2 The lattice contribution to the total heat capacity

Petit and Dulong assumed based on the principles of the classical mechanics that the atoms of a solid can be considered as harmonic oscillators which vibrate independently from each other around their equilibrium positions. They predicted that the heat capacity of a solid is a temperature-independent constant given by $c_V = 3 \cdot n \cdot R$, where R is the universal gas constant and n corresponds to the number of oscillators [28, 29]. While the Petit-Dulong law describes the high temperature behavior of the heat capacity of many solids far above the Debye temperature in a satisfactory way, a description of the low temperature behavior fails.

In contrast to classical mechanics, quantum mechanics assumes that the energy levels, E , of a harmonic oscillator are quantized with $E = (r + \frac{1}{2}) \cdot h \cdot \omega$, where r is the quantum number, ω is the frequency, and \hbar is the reduced Planck constant. In the Debye model the population of these energy level is described by the Bose-Einstein statistics [28, 29]. Moreover, the Debye model approximates all phonon branches by three branches –one longitudinal (v_L) and two transversal (v_T)– which are connected with the average ultrasound velocity, v_S ($\frac{3}{v_S^3} = \frac{1}{v_T^3} + \frac{2}{v_L^3}$). Debye considered a continuous phonon density of states ($G(\omega) \propto \omega^2$), which is limited by the cut-off

frequency ω_D . At ω_D the area below the real PDOS is equal to the one below the Debye PDOS [28, 29].

For the temperature-dependence of the isochoric heat capacity $c_V(T)$, Debye found the general expression shown in equation (2.36), in which $\Theta_D = \hbar\omega_D/k_B$ is the Debye temperature and k_B is the Boltzmann constant [28, 29]

$$c_V(T) = 9 \cdot n \cdot R \cdot \left(\frac{T}{\Theta_D} \right)^3 \int_0^{\Theta_D/T} \frac{x^4 \cdot e^x}{(e^x - 1)^2} dx. \quad (2.36)$$

From equation (2.36) the high and low temperature maximum of the vibrational heat capacity have been derived (equation (2.37)):

$$c_V(T) = \begin{cases} T \rightarrow \infty : 3 \cdot n \cdot R \\ T \rightarrow 0 : \frac{12\pi^4}{5} \cdot n \cdot R \cdot \left(\frac{T}{\Theta_D} \right)^3 \end{cases} \quad (2.37)$$

For high temperatures, $T \rightarrow \infty$, equation (2.36) converges against the Petit-Dulong law. For low temperatures, $T \rightarrow 0$, the Debye model yields the expression shown in equation (2.37). By plotting c_V vs. T^3 , these expression allows the straightforward estimation of the Debye temperature [28, 29].

2.6.3 Validity of the Debye model - the non-Debye model

According to equation (2.37) the Debye model predicts that a plot of c_V/T^3 converges for $T \rightarrow 0$ K against a constant value of $12\pi^4 \cdot n \cdot R/5 \cdot \Theta_D^3$. Moreover, for higher temperatures the Debye model suggests a continuous decrease of c_V/T^3 until its value converges to zero. However, the results of many experimental studies have shown unambiguously that the Debye model is only valid for very low temperatures of $0 \leq T < \Theta_D/50$. In this temperature range, the experimental data show the proposed T^3 dependence [56, 57, 58, 59]. In the adjacent cryogenic temperature range, $\Theta_D/50 \leq T < \Theta_D/15$, the experimental c_p/T^3 values show a local maximum instead of a continuous decrease and hence, there is a temperature dependence that is not thoroughly described by the Debye model [56, 57, 58, 59].

In order to gain an accurate description of the measured heat capacity over the entire temperature range, Pässler [57] developed the so-called non-Debye model. In the low temperature regime, $0 \leq T < \Theta_D/15$, the heat capacity follows $c_V = c_3 \cdot T^3 + c_5 \cdot T^5 + c_7 \cdot T^7 + \dots$, where c_3, c_5 and c_7 are exclusively positive parameters, and where c_3 is correlated with the Debye temperature according to equation (2.38) [57],

$$\Theta_D = \left(\frac{12 \cdot \pi^4 \cdot n \cdot R}{5 \cdot c_3} \right)^{\frac{1}{3}}. \quad (2.38)$$

Terms of higher order, e. g. T^9, T^{11}, \dots can be neglected [57]. In order to gain an accurate mathematical description of the temperature dependence of c_p/T^3 , Pässler [57] introduced a Taylor series of dimensionless expansion coefficients, b_{2n} , whose

amplitude depends on the value of the scaling temperature T_0 (equation (2.39)),

$$c_{Vh}(T) = \frac{c_3 \cdot T^3 + c_5 \cdot T^5 + c_7 \cdot T^7}{\left(1 + \sum_{n=3}^7 b_{2n} \cdot \left(\frac{T}{T_0}\right)^{2n}\right)^{0.5}}. \quad (2.39)$$

It has to be pointed out that no corrections for anharmonicity are involved in equation (2.39) and hence, $c_{Vh}(T)$ corresponds to the heat capacity of an assembly of harmonic lattice oscillators [57]. Therefore, Pässler [57] introduced additional parameters (A_1, A_2, A_3) for an anharmonicity correction resulting in the expression given in equation (2.40) [57],

$$c_{p,fit}(T) = c_{Vh}(T) \cdot \left(1 + \frac{c_{Vh}(T)}{3 \cdot n \cdot R} \cdot \sum_{n=1}^3 A_n \cdot T^n\right). \quad (2.40)$$

The anharmonicity coefficients include a correction for the thermal expansion and anharmonic contributions to the total heat capacity. Usually the first-order anharmonicity coefficient, A_1 , is sufficient for an accurate description of the temperature dependence of the heat capacity [57].

2.6.4 Thermodynamics of solid solutions

Kopp and Neumann suggested based on Vegard's rule that the heat capacity, C_{AB} , of a solid solution A_xB_{1-x} can be calculated from the heat capacity of the endmembers C_i using the relationship:

$$C_{AB} = \sum_{i=1}^N C_i \cdot x_i \quad (2.41)$$

where x_i denotes the fraction of each endmember i in the solid solution (equation (2.41)).

However, in many cases the Kopp-Neumann rule does not match the measured heat capacity and a non-ideal miscibility is observed. As a result, an excess heat capacity is found which can be calculated by taking the difference between the measured data and the prediction from the Kopp-Neumann rule. Considering equations (2.35a) and (2.35b) it follows that in case of non-ideal heat capacity the enthalpy and entropy also show an excess behavior.

2.6.5 Experimental determination of heat capacity: Thermal relaxation calorimetry

Thermal relaxation calorimetry is a technique to determine the heat capacity of a sample by analysing the thermal response of a sample/platform assembly to a change of the thermal conditions caused by a heating or a cooling pulse. Figure (2.7) depicts schematically the heat flow in a typical thermal relaxation calorimeter e. g. a PPMS DynaCool [60, 61, 62]. In figure (2.7) the sample is attached to the surface of a platform by a thin layer of grease. The thermal coupling between the

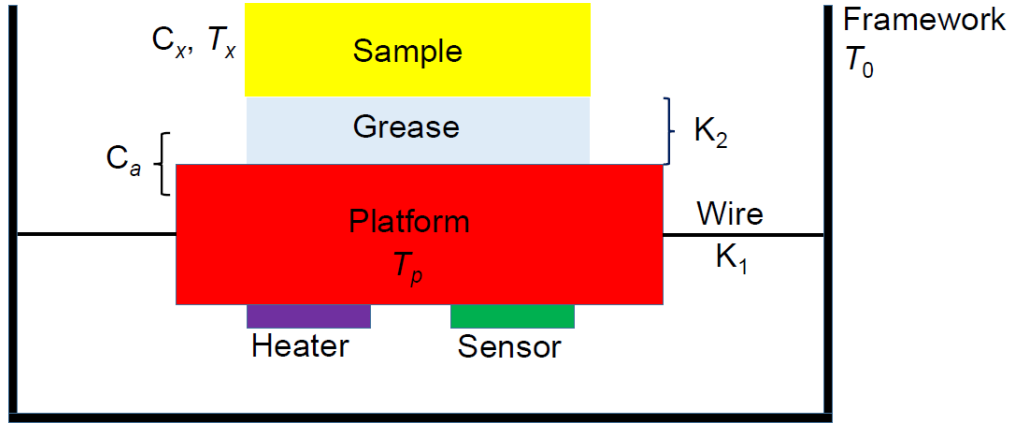


FIGURE 2.7: Scheme of a PPMS puck for heat capacity measurements.

sample and the platform is defined by the thermal conductance K_2 of the grease. The platform is linked over conducting wires with known electrical conductance to the framework of the puck. The thermal coupling between the platform and the framework is given by the thermal conductance K_1 . The framework of the puck is held at a constant bath temperature T_0 . The platform is equipped with a temperature sensor and a heater [60, 61, 62].

The thermal behavior of the assembly is described by the coupled differential equations (2.42a) and (2.42b):

$$P = C_a \frac{dT_p}{dt} + K_2 (T_p - T_x) + K_1 (T_p - T_0) \quad (\text{a}) \quad (2.42\text{a})$$

$$0 = C_x \frac{dT_x}{dt} + K_2 (T_x - T_p) \quad (\text{b}) \quad (2.42\text{b})$$

Here, C_a is the total heat capacity of the platform and the grease and C_x is the heat capacity of the sample, T_x and T_p are the temperature of the sample and the platform, respectively [60, 61, 62]. The former equation describes the heating process when a heat pulse, $P \neq 0$, is applied by the heater and the later one characterizes the cooling of the sample when the heater is off, $P = 0$.

In case of a very strong coupling between the sample and the platform, $T_x \approx T_p$ and it can be assumed that $K_2 \gg K_1$ and hence, equations (2.42a) and (2.42b) can be combined to the expression shown in equation (2.43) [60, 61, 62],

$$(C_a + C_x) \frac{dT_p}{dt} = P + K_1 (T_p - T_0). \quad (2.43)$$

After the heat pulse is switched off ($P = 0$), the assembly will cool down to the bath temperature T_0 . The temperature relaxation $T_p(t)$ of such an assembly, which corresponds to the solution of the differential equation (2.43), is given by equation

(2.44) with the time-constant $\tau = (C_x + C_a) / K_1$ and $\Delta T = T_p - T_0$ [60, 61, 62],

$$T_p(t) = T_0 + \Delta T \exp(-t/\tau). \quad (2.44)$$

Equation (2.44) corresponds to the so-called one- τ model. The heat capacity is determined by fitting the detected thermal relaxation of the sample. It has to be noted that K_1 is detected during the application of the heat pulse and hence, it is known. The two unknown heat capacities C_x and C_a , are connected with τ . Hence, the determination of the sample's heat capacity C_x is done in two steps. At first, in the addenda measurement the total heat capacity C_a of the platform/grease assembly is measured. In the second step the total heat capacity $C_{\text{total}} = C_a + C_x$ is determined. The sample's heat capacity is then calculated from the difference $C_x = C_{\text{total}} - C_a$ [60, 61, 62].

In practice, for many samples the thermal coupling between the sample and the platform can be considered to be not very strong and thus, $K_2 \gg K_1$ cannot be determined reliably. Therefore, the one- τ model is not suitable to determine the heat capacity of such a sample and the so-called two- τ model is used for the determination of the heat capacity. The two- τ model is a much more complex fitting model which contains two time-constants, τ_1 and τ_2 . However, the general idea to fit the thermal relaxation of the sample in order to determine the heat capacity remains the same. A detailed description of the two- τ can be found in [60, 61] and references inside. In practice, the PPMS software applies both models to the experimental data and uses the one that is better suited for the determination of the sample's heat capacity.

Chapter 3

Experimental part

3.1 Synthesis

For this study, several compounds from the $\text{Sb}_2\text{Te}_{3-x}\text{Se}_x$ solid solutions were synthesized. Samples of several mixed crystals from the $\text{GeSe}_x\text{Te}_{1-x}$ ($x=0, 0.2, 0.5, 0.75, 1$) solid solution, which were studied in the course of this project, were synthesized by Michael Küpers (Institute for Anorganic Chemistry, RWTH Aachen). Details are given in references [63, 64].

3.1.1 Synthesis of $\text{Sb}_2\text{Te}_{3-x}\text{Se}_x$ mixed crystals

3.1.1.1 Introduction

In previous publications, the synthesis of $\text{Sb}_2\text{Te}_{3-x}\text{Se}_x$ single crystals and polycrystalline samples was reported. These studies showed that Chemical Vapor Transport (CVT) [65], the Bridgman-Stockbarger method [66], high-energy ball milling [67] and solid-state synthesis in quartz glass ampoules [68] are suitable routes for the synthesis.

In this study, both the Bridgman-Stockbarger method and synthesis in quartz glass ampoules were used to synthesize polycrystalline $\text{Sb}_2\text{Te}_{3-x}\text{Se}_x$ ($x=0, 0.6, 1.2, 1.8, 3$) mixed crystals.

In table 3.1, the ambient pressure melting and boiling points of antimony [69, 70], selenium [69, 71] and tellurium [69, 72] are summarized. The melting points of the endmembers, Sb_2Te_3 and Sb_2Se_3 , are both around 893 K [73]. Therefore, the main

TABLE 3.1: Ambient pressure melting and boiling points of antimony [69, 70], selenium [69, 71] and tellurium [69, 72].

Element	Melting point / K	Boiling point / K
Antimony, Sb	903 [70]	1908 [69]
Selenium, Se	494.2(1) [71]	958.2 [69]
Tellurium, Te	722.8(1) [72]	1263 [69]

problem of the synthesis of $\text{Sb}_2\text{Te}_{3-x}\text{Se}_x$ mixed crystals is the low ambient pressure boiling point of Selenium which causes a strong Se vaporization rate at typical reaction temperatures of around 923 K. In figure 3.1, the boiling points of Selenium [74] and Tellurium [75] as a function of the pressure are shown. Both boiling points

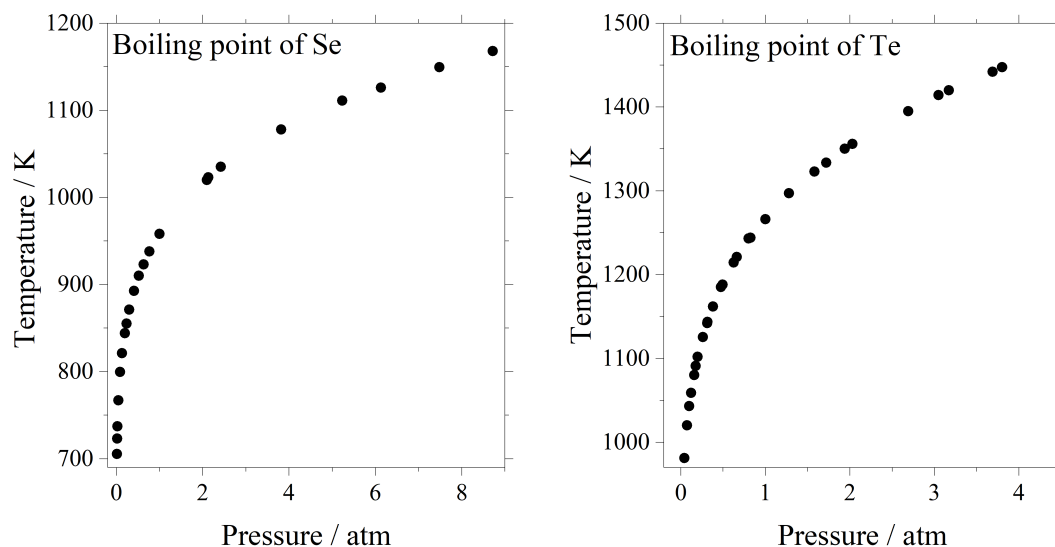


FIGURE 3.1: Boiling points of Se [74] and Te [75] in dependence of the pressure.

show a strong pressure dependence. In order to reduce the vaporization rate of Selenium, the ampoules were loaded under a Ar pressure of 0.8 bar. Using the ideal gas equation ($p \cdot V = R \cdot n \cdot T$) a pressure of around 2.5 atm at 923 K was estimated.

3.1.1.2 Synthesis of polycrystalline samples of Sb_2Te_3 and Sb_2Se_3

Polycrystalline ingots of the endmembers Sb_2Te_3 and Sb_2Se_3 were synthesized using the Bridgman-Stockbarger method. For the synthesis, commercially available powders of Sb_2Te_3 (Alfa Aesar, 5 N) and Sb_2Se_3 (Alfa Aesar, 5 N) were used as starting materials. About 5 g of one of the starting materials were filled in a quartz glass ampoule (external diameter 28 mm, height about 150 mm). The ampoule was evacuated, filled with Ar (0.8 bar) and mounted in the Bridgman-Stockbarger apparatus. A graphite heater was mounted around the ampoule, then the apparatus was closed and evacuated. At a vacuum of about 10^{-5} mbar, the furnace was heated up to 923 K and kept at this temperature for 4 h. Then, the position of the ampoule was lowered with a rate of $1.5 \text{ mm} \cdot \text{h}^{-1}$ and the synthesis was performed for a time of 100 h. The obtained samples were light gray ingots with metallic luster. About 5 g (yield of about 100 %) of each sample were synthesized.

3.1.1.3 Synthesis of polycrystalline $\text{Sb}_2\text{Te}_{3-x}\text{Se}_x$ mixed crystals

Polycrystalline samples of $\text{Sb}_2\text{Te}_{3-x}\text{Se}_x$ mixed crystals ($x=0.6, 1.2, 1.8$) were synthesized from stoichiometrically weighted amounts of elemental Sb, Te and Se. The starting materials were filled in quartz glass crucibles (external diameter 20 mm, length about 40 mm) and the crucibles were placed in ampoules of the same material (external diameter 24 mm, length about 110 mm). On top of each crucible a quartz glass plug was placed. The ampoules were evacuated, pressurized to 0.8 bar Ar,

TABLE 3.2: Yields of the synthesized $\text{Sb}_2\text{Te}_{3-x}\text{Se}_x$ ($x=0.6, 1.2, 1.8$) mixed crystals.

Sample	$\text{Sb}_2\text{Se}_{0.6}\text{Te}_{2.4}$	$\text{Sb}_2\text{Se}_{1.2}\text{Te}_{1.8}$	$\text{Sb}_2\text{Se}_{1.8}\text{Te}_{1.2}$
Yield %	99	97	99

transferred into a high-temperature furnace, and heated up to 923 K with a heating rate of $5 \text{ K}\cdot\text{min}^{-1}$. The temperature was kept for 96 h and the samples were subsequently quenched in water in order to prevent a decrease of the pressure during the cooling of the samples. The synthesized light-gray and metallic-shiny samples were dried in a furnace at 383 K for 24 h. In table 3.2 the yields of all synthesis are summarized.

3.2 Sample characterization

3.2.1 Powder diffraction

In-house powder diffraction measurements have been performed with a Huber G670 Guinier Camera using monochromatic $\text{CuK}_{\alpha,1}$ radiation and an image plate detector which covers an angular range of $2\Theta=0-100^\circ$ with an angular resolution of $\Delta 2\Theta=0.005^\circ$. For temperature-dependent powder diffraction measurements, the diffractometer is equipped with a He closed cycle cryostat which allows to reach temperatures down to 15 K. The temperature setpoint is adjusted by the diffractometer software and the temperature in the sample chamber is monitored by a temperature sensor.

Low-temperature powder diffraction (LTXRPD) measurements on the $\text{GeSe}_x\text{Te}_{1-x}$ ($x=0, 0.2, 0.5, 0.75, 1$) mixed crystals were performed between 25-300 K. The samples were cooled down to 25 K and the temperature was stabilized for about 10 minutes. Powder diffraction patterns were collected in 5 K steps using an exposure time of 120 min. The sample temperature was raised by $5 \text{ K}\cdot\text{min}^{-1}$ to the next temperature point. Before the subsequent measurement was started, a dwell time of 5 min was chosen in order to stabilize the temperature in the sample chamber.

3.3 Low-temperature heat capacity measurements

Heat capacity measurements on the $\text{Sb}_2\text{Te}_{3-x}\text{Se}_x$ mixed crystals ($x=0, 0.6, 1.2, 1.8, 3$) were performed between 2-300 K using a PPMS DynaCool from Quantum Design. For the addenda measurement, a small droplet of Apiezon-N-grease was added on the sample platform of the puck and measurements were performed between 2-300 K with 120 points. For the measurements, thin plates of the samples polished on both sides were prepared using sand paper. Table 3.3 summarizes the masses of the samples. Afterwards, the samples were placed in the center of the puck and slightly fixed in the grease. 56 temperature points were measured from each sample in the temperature range 2-30 K and additional 90 points between 30-300 K. Both, the

TABLE 3.3: Masses of the $\text{Sb}_2\text{Te}_{3-x}\text{Se}_x$ ($x=0, 0.6, 1.2, 1.8, 3$) samples used for low-temperature heat capacity measurements.

Sample	Sb_2Te_3	$\text{Sb}_2\text{Se}_{0.6}\text{Te}_{2.4}$	$\text{Sb}_2\text{Se}_{1.2}\text{Te}_{1.8}$	$\text{Sb}_2\text{Se}_{1.8}\text{Te}_{1.2}$	Sb_2Se_3
Mass / mg	9.0(1)	9.7(1)	9.1(1)	10.5(1)	11.0(1)

sample and addenda measurements, were performed with two repetitions per temperature step. A linear temperature increase and a heating rate of 2% based on the actual temperature were chosen. In order to determine the addenda heat capacity at the temperatures of the sample, a polynomial interpolation between two neighboring data points was performed using the automatic procedure implemented in the PPMS software.

3.4 High-pressure diffraction

3.4.1 Diamond anvil cell

Mechanical pressure, $p = F/A$, is defined as the ratio between a force, F , applied to an area, A . Thus, pressure can be exerted by minimization of the area and/or a maximization of the applied force.

Figure 3.2 shows a schematic construction of a diamond anvil cell (denoted as "DAC" in the following) [76]. Diamonds are suitable anvil materials due to their extreme

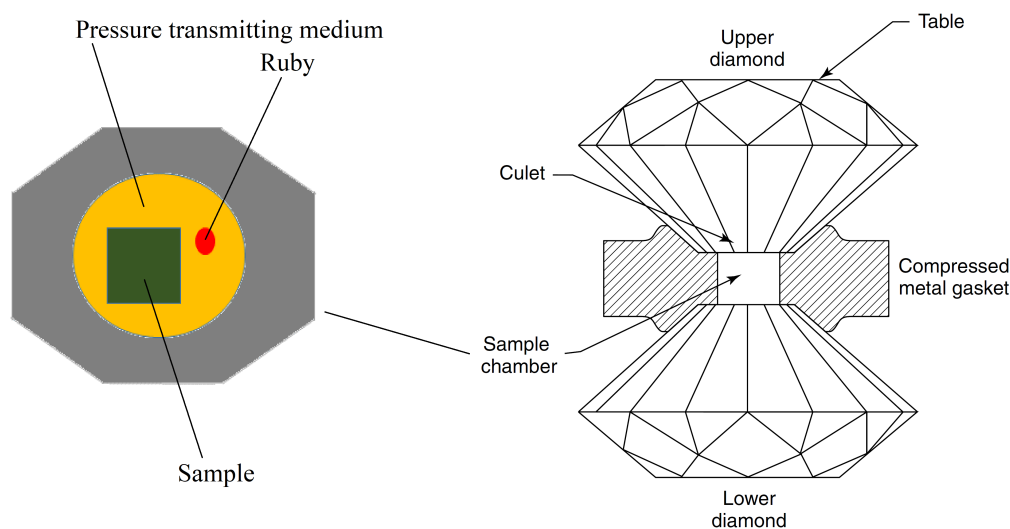


FIGURE 3.2: Right: Scheme of diamond anvil cell [76]. Left: Enlargement of the sample chamber. The sample chamber contains the sample, a pressure transmitting medium and a pressure standard, e. g. ruby.

hardness [77, 78, 79, 80, 81]. Moreover, diamonds are transparent for a part of the electromagnetic spectrum and hence, in-situ studies by diffraction or spectroscopic techniques are feasible [82, 76]. In order to exert pressures up to the megabar regime

the diamond anvils are equipped with a culet. The size of the culet determines the reachable pressure. The pressure is increased or released by applying a moderate force via moving the anvils either by screws [83, 76] or by a membrane [83, 84]. A metal foil called gasket is placed between the opposing diamonds [82, 76]. A hole in the gasket serves as a sample chamber [82, 76]. The resulting sample volumes are typically in the order of 10^4 - $10^6 \mu\text{m}^3$. The sample chamber contains the sample, a pressure transmitting medium and a ruby chip [82, 76]. The pressure transmitting medium is used to transmit the applied uniaxial pressure either quasi-hydrostatically or non-hydrostatically to the sample. For a quasi-hydrostatic pressure transmission usually noble gases e. g. Ne, He, .. or liquids, e. g. a methanol/ethanol mixture are used [82, 76]. For a non-hydrostatic pressure transmission e. g. salts like NaCl are used [82, 76]. In this case, the pressure is not transmitted homogeneously to the sample and hence, a strain is applied [82, 76]. The ruby chip deals as a pressure standard and allows the estimation of the pressure on the sample [82, 76, 85, 86].

3.4.2 Ruby fluorescence method

The estimation of pressure in a DAC is possible either from diffraction [87, 88, 89, 90] or through spectroscopic methods [85, 86]. In the spectroscopic estimation, pressure-induced shifts of either Raman active modes (e. g. cubic BN [91], ^{12}C [91]) or fluorescence lines (e. g. ruby [85, 86], $\text{SrB}_4\text{O}_7:\text{Sm}^{2+}$ [92]) are considered. Based on the pressure-induced shift of the R1 fluorescence line of ruby a method for the pressure estimation in DACs was developed [85] and later improved [86]. Equation (3.1) describes the relation between the pressure and the wavelength of the R1 fluorescence line of ruby,

$$p = \frac{A}{B} \cdot \left(\left(\frac{\lambda}{\lambda_0} \right)^B - 1 \right) \quad (3.1)$$

where λ_0 is the wavelength determined under ambient conditions and λ represents the wavelength at an elevated pressure. The empirical parameters A and B are $A=19.04 \text{ MPa}$ and $B=7.665$ [86].

3.4.3 The Extreme Conditions Beamline P02.2 at PETRA III, DESY

All high-pressure diffraction experiments reported in this study have been performed at the extreme conditions beamline P02.2 at PETRA III, DESY. Figure 3.3 shows a sketch of the beamline. A detailed description of the technical setup and the infrastructure of the beamline is given in [93]. Therefore, in this chapter only a brief overview of the beamline is given.

After the incident beam passes the undulator and a series of slits, it is monochromatized by a silicon double crystal monochromator. The monochromatized beam is focused by Al and Be compound refractive lenses (CRL) to a spot size of $8 \times 3 \mu\text{m}^2$. High-pressure experiments were performed at the general purpose sample stage (figure 3.3).

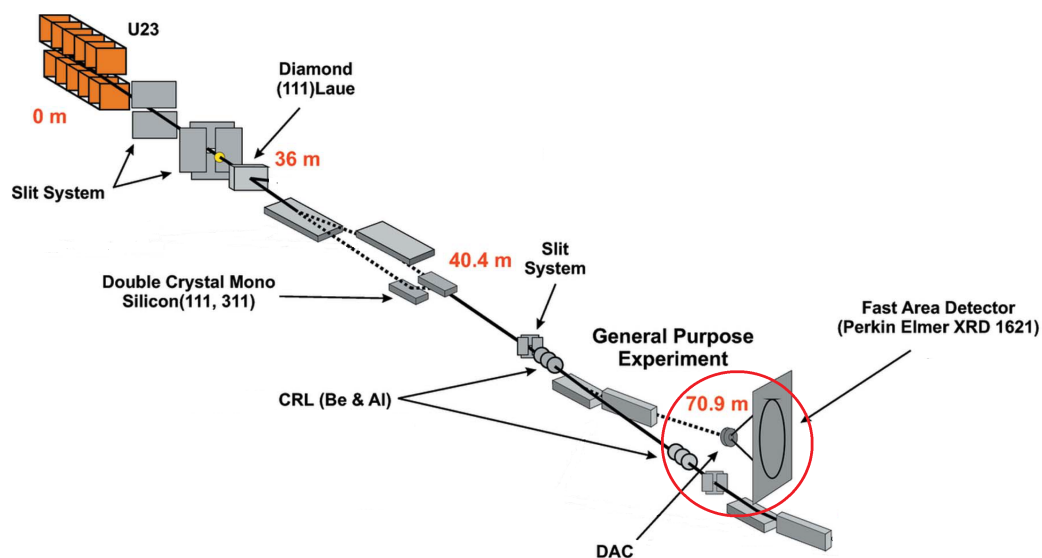


FIGURE 3.3: Setup of the Extreme Conditions Beamline P02.2 at PETRA III (adapted from [93]). Red circle: Sample stage.

An online ruby system allows an in-situ determination of the pressure. Prior to the measurement the DAC was carefully centered [94] and during exposure the DAC was rotated along the ω -axis by a few degrees to gain better statistics.

3.4.4 High-pressure powder diffraction

All measurements were performed at a wavelength of 0.2905 \AA (beam energy of 42.7 keV). The powdered samples were loosely compressed between two glass plates and then loaded together with small ruby chips in BX90 diamond anvil cells equipped with a membrane to drive the pressure. Rhenium gaskets, pre-indented to a thickness of $80 \mu\text{m}$ and with a hole of $150 \mu\text{m}$ drilled by electro-corrosion, were used. For the high-pressure experiments on the $\text{GeSe}_x\text{Te}_{1-x}$ ($x=0, 0.2, 0.5, 0.75, 1$) mixed crystals Neon was used as a pressure-transmitting medium. The measurements on Sb_2Te_3 were performed at non-hydrostatic conditions. The cells were placed at a distance of 500 mm (exception GeTe : 450 mm) to the Perkin Elmer detector (Type XRD1621). The distance was calibrated using a CeO_2 standard. Pressure in the measurements on the $\text{GeSe}_x\text{Te}_{1-x}$ mixed crystals and Sb_2Te_3 was increased in steps of approximately 1 GPa . The pressure in the cell was determined before and after each measurement using the ruby luminescence method. Datasets for GeTe and $\text{GeSe}_{0.2}\text{Te}_{0.8}$ were collected up to maximum pressures of about $20\text{-}21 \text{ GPa}$, while for $\text{GeSe}_{0.5}\text{Te}_{0.5}$ and $\text{GeSe}_{0.75}\text{Te}_{0.25}$ the maximum pressure was approximately 25 GPa . The measurement on Sb_2Te_3 was performed up to a maximum pressure of about

18 GPa. At all pressure points the diffraction patterns were collected using an exposure time of 12 sec and an angular rotation of 3° . In order to confirm the homogeneity of pressure-transmission in the cells, 3×3 grids with setoff of $5 \mu\text{m}$ steps in x and y direction were measured. The data were integrated to yield 1-dimensional powder diffraction diagrams using the program Dioptas [95]. Reflections from the diamonds of the cell were masked prior to integration.

3.5 Inelastic neutron scattering: Experimental details

Powdered samples of $\text{Sb}_2\text{Se}_{0.6}\text{Te}_{2.4}$, $\text{Sb}_2\text{Se}_{1.2}\text{Te}_{1.8}$ and $\text{Sb}_2\text{Se}_{1.8}\text{Te}_{1.2}$ were prepared according to the procedure described in section 3.1.1.3 For the endmembers Sb_2Te_3 (STREM USA, 99.96 %) and Sb_2Se_3 (99.999 %, Sigma Aldrich) commercially available samples were studied. All samples were filled in Al cans which were filled to a height of about 1.5-2 cm in He atmosphere and sealed with an In ring. The following amounts of powder were used: Sb_2Te_3 : 10.1 g, $\text{Sb}_2\text{Se}_{0.6}\text{Te}_{2.4}$: 13.865(1) g, $\text{Sb}_2\text{Se}_{1.2}\text{Te}_{1.8}$: 11.557(1) g, $\text{Sb}_2\text{Se}_{1.8}\text{Te}_{1.2}$: 13.329(1) g, Sb_2Se_3 : 17.234(1) g. The opening of each can was cleaned carefully in order to avoid any leakages and then, closed with a plug of the same material. In addition, one empty Al can, which served as reference sample, was prepared. The cans were placed into the cryostat of the ARCS beamline and the can position was adjusted to the maximal intensity scattered by the sample. A first measurement was performed at the temperature corresponding to the ^{121}Sb NIS data (Sb_2Te_3 : 35 K, $\text{Sb}_2\text{Se}_{0.6}\text{Te}_{2.4}$: 35 K, $\text{Sb}_2\text{Se}_{1.2}\text{Te}_{1.8}$: 37 K, $\text{Sb}_2\text{Se}_{1.8}\text{Te}_{1.2}$: 45 K, Sb_2Se_3 : 39 K, Al: 35 K), further measurements at temperatures of 150 K and 300 K. TOF spectra were taken for about 1 h and with an initial energy of 45 meV and 60 meV, respectively. In order to gain a sufficient statistics, two measurements per temperature point and energy were performed. For the 45 meV measurements the frequency of the T_0 chopper was set to 90 Hz and the one of the Fermi chopper to 300 Hz. For the 60 meV measurements the same frequency for the T_0 chopper was adjusted whereas the one of the Fermi chopper was set to 360 Hz. It is noteworthy that the data quality of the 60 meV data was inferior compared to the corresponding 45 meV data. Thus, for the further data treatment only the 45 meV data were considered.

3.6 Nuclear inelastic scattering

3.6.1 Experimental details

Using two $1 \times 1 \text{ cm}^2$ sized strips of Aluminum tape a $0.5 \times 0.5 \text{ cm}^2$ sample chamber was prepared (figure 3.4). The sample chamber was filled with small amounts of powdered $\text{Sb}_2\text{Te}_{3-x}\text{Se}_x$ which was evenly distributed in order to form a thin layer. The sample was covered by a third strip of Al tape and then fixed on a NIS sample holder which in turn was mounted on the holder of a cold head. The cold head was placed in a cryostat. The temperatures for the samples estimated

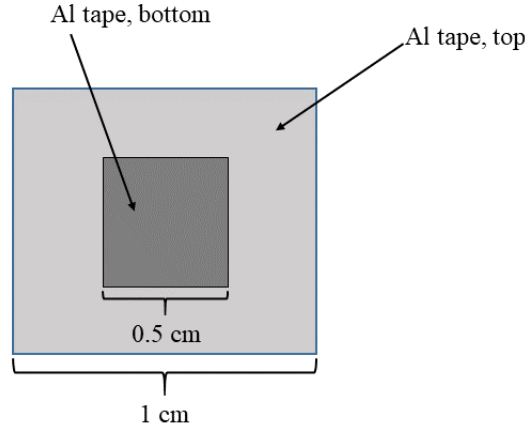


FIGURE 3.4: Sample container for NIS measurements.

by the Bose-Einstein-statistics were: Sb_2Te_3 : 35 K, $\text{Sb}_2\text{Se}_{0.6}\text{Te}_{2.4}$: 35 K, $\text{Sb}_2\text{Se}_{1.2}\text{Te}_{1.8}$: 37 K, $\text{Sb}_2\text{Se}_{1.8}\text{Te}_{1.2}$: 45 K, Sb_2Se_3 : 39 K. For each sample, the ^{121}Sb nuclear absorption spectra as well as the instrumental resolution function of the sapphire backscattering monochromator were measured several times (5-10 repetition per sample) in order to gain sufficient statistics. In addition, ^{125}Te nuclear absorption spectra of $\text{Sb}_2\text{Se}_{0.6}\text{Te}_{2.4}$ (25 K) and $\text{Sb}_2\text{Se}_{1.8}\text{Te}_{1.2}$ (21 K) (6 repetitions per sample) were measured.

3.6.2 Energy resolution

In figure 3.5a) and b), the instrumental resolution functions of the sapphire monochromator obtained from the ^{121}Sb and ^{125}Te nuclear inelastic scattering scattering experiments performed on $\text{Sb}_2\text{Se}_{1.8}\text{Te}_{1.2}$ are shown as a representative example. The ^{121}Sb resolution function was fitted with three pseudo Voigt functions, whereas the ^{125}Te

TABLE 3.4: Results from fits on the instrumental resolution functions obtained from the ^{121}Sb and ^{125}Te nuclear inelastic scattering experiments on the $\text{Sb}_2\text{Te}_{3-x}\text{Se}_x$ ($x=0, 0.6, 1.2, 1.8, 3$) mixed crystals. The values of the FWHM (FHWM1-3) and relative area (Area1-3) of each fit function are shown.

Sample	Sb_2Te_3	$\text{Sb}_2\text{Se}_{0.6}\text{Te}_{2.4}$	$\text{Sb}_2\text{Se}_{1.2}\text{Te}_{1.8}$	$\text{Sb}_2\text{Se}_{1.8}\text{Te}_{1.2}$	Sb_2Se_3
^{121}Sb instrumental resolution					
FHWM1/meV	1.39	1.39	1.39	1.39	1.39
FHWM2/meV	4.94	4.94	4.94	4.94	4.94
FHWM3/meV	4.38	4.38	4.39	4.38	4.38
Area1/%	56.5	56.0	56.0	56.1	56.1
Area2/%	33.5	33.6	33.5	33.5	33.5
Area3/%	10.0	10.4	10.5	10.4	10.4
^{125}Te instrumental resolution					
FHWM1/meV		1.38		1.15	
FHWM2/meV		2.41		3.94	
Area1/%		35.0		35.0	
Area2/%		65.0		65.0	

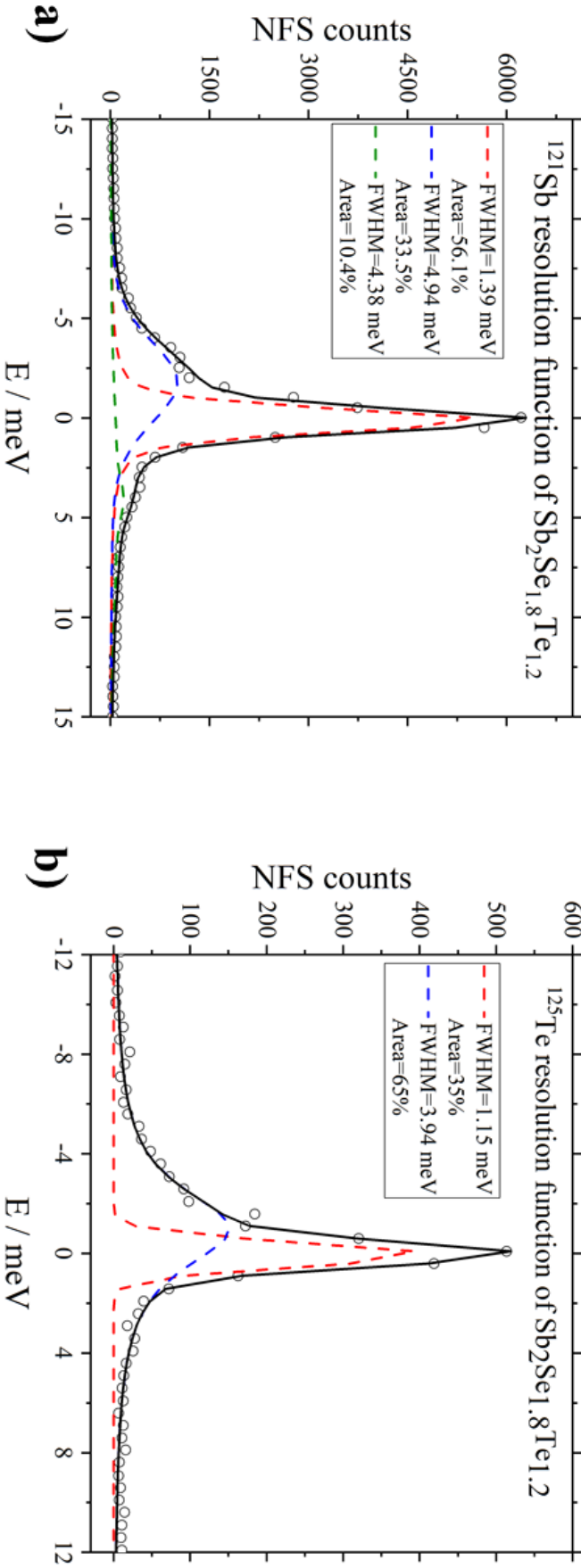


FIGURE 3.5: Instrumental resolution functions of the sapphire backscattering monochromator obtained from the ^{121}Sb and ^{125}Te nuclear inelastic scattering experiments performed on $\text{Sb}_2\text{Se}_{1.8}\text{Te}_{1.2}$.

data were described by two Voigt functions. Analogous fits have been performed also on the other $\text{Sb}_2\text{Te}_{3-x}\text{Se}_x$ ($x=0, 0.6, 1.2, 3$) mixed crystals (appendix B.2). Table 3.4 summarizes the values obtained for the full width at half maximum (FWHM) and the relative area of each fit function. The fits on the instrumental resolution functions from the ^{121}Sb nuclear inelastic measurements yielded nearly the same results independent of the chemical composition. This demonstrates unambiguously that the instrumental resolution function of the sapphire backscattering monochromator remained unchanged over the entire beamtime. The fit parameters obtained from the fits on the ^{125}Te instrumental resolution functions for the individual samples differ slightly, indicating small variations of the setup during the experiments.

Chapter 4

Data processing

4.1 Determination of lattice parameter from powder data

In order to determine the lattice parameter of the polycrystalline $\text{Sb}_2\text{Te}_{3-x}\text{Se}_x$ and $\text{GeSe}_x\text{Te}_{1-x}$ samples, Le Bail refinements on the collected powder patterns have been performed with the program JANA2006 [96]. The temperature-dependent powder patterns were refined using the following refinement strategy. First, the background was described by 100 points and fitted by a 20 parameter Legendre polynomial and the zero shift was refined. Then, the lattice parameter, taking starting values from the literature [97, 67, 98, 63, 15, 79], were refined and the peaks were fitted using a pseudo-Voigt profile function with a Lorentzian (LX) and an angle-dependent Gaussian (GW , GU) contribution. Berar's correction was applied to obtain realistic standard deviations [99].

For the refinement of the high-pressure powder data the parameter LX and GW were sufficient to adjust the profile. The zero shift was kept at zero.

4.2 Processing of high-pressure single crystal diffraction data

In the diffraction data collected at 18.8 GPa on the GeTe sample single crystal reflections appeared together with the powder pattern of the sample. These single crystal peaks were hand-picked with the program CrysAlis Pro [100] and indexed and integrated with an orthorhombic lattice ($a=7.3690(18)$ Å, $b=3.9249(10)$ Å and $c=5.698(9)$ Å). Based on the analysis of systematic extinctions ($Pnma$: $k+l=2n$ for $(0kl)$; $h=2n$ for $(hk0)$) and the internal agreement factor, the space group $Pnma$ was chosen and the new high-pressure structure of the polymorph GeTe-III was solved via direct methods with the program SIR2014 [101]. A structure refinement was performed with the program JANA2006 [96]. As only a limited number of reflections was available, the Ge and Te atoms were refined only isotropically. A careful inspection of the GeTe data collected at higher and lower pressures showed that due to the strong overlay of the powder rings with the single crystal reflections of the GeTe-III phase it was not possible to reliably integrate the single crystal reflections.

4.3 Extraction of (partial) phonon density of states from inelastic neutron and nuclear inelastic scattering data

4.3.1 Binning of INS and NIS raw data

As inelastic neutron scattering (INS) and nuclear inelastic scattering (NIS) raw data contain contributions of elastic, single-phonon and multi-phonon scattering it is necessary to separate these contributions to obtain the (partial) phonon density of states from the raw data (see sections 2.2.2 and 2.3.3.3).

Nuclear absorption spectra and INS raw data, respectively, measured on the same sample and at the same temperature show usually slight origin shifts and thus, the first step of the data treatment involves the combination of different raw data to one single data file with one origin. In case of the INS data the binning of the TOF spectra was done using the program DAVE [102]. For the binning of the NIS data the program "sumscan" available at the beamline P01 was used [103]. This program was also used to bin the data of the elastic line measured at the NFS detector.

4.3.2 Processing of inelastic neutron scattering (INS) data

4.3.2.1 Extraction of total phonon density of states from INS data

Step 1: Binning and exclusion of artefacts

The transformation from time-of-flight spectra to $S(Q, E)$ data was done using the software DAVE [102]. For the data analysis of each sample a phonon dispersion was calculated from the binned 45 meV data using the program DAVE [102]. This is illustrated in figure 4.1 for the example of $\text{Sb}_2\text{Se}_{0.6}\text{Te}_{2.4}$. At around 40 meV and $Q \approx 6 \text{ \AA}^{-1}$ an experimental artefact is clearly visible in the phonon dispersions of the isostructural samples Sb_2Te_3 , $\text{Sb}_2\text{Se}_{0.6}\text{Te}_{2.4}$ (figure 4.1a) and b)), $\text{Sb}_2\text{Se}_{1.2}\text{Te}_{1.8}$ and $\text{Sb}_2\text{Se}_{1.8}\text{Te}_{1.2}$. For Sb_2Se_3 two additional artefacts occur at around 3 and 6 \AA^{-1} . In order to exclude these artefacts, the considered angular range of the detector was reduced to $30\text{-}95^\circ$ using the program DAVE [102] (figure 4.1c) and d)).

Step 2: Subtraction of the Al contribution

In the next step, the phonon modes originated from the Al can were excluded. For this, the binned data were loaded together with the corresponding empty can data. The Al data, I_{Al} , were subtracted from the total spectra, I_{tot} , by adjusting the self-shielding factor SF ($I_{\text{sample}} = I_{\text{tot}} - \text{SF} \cdot I_{\text{Al}}$). The difference spectra, I_{sample} , correspond to the scattering contribution of the sample. To obtain a reliable value for SF, powder patterns of the sample were calculated and the factor SF was decreased until the intensities corresponding to Al became negative.

Step 3: Subtraction of the elastic line

In the next step, the scattering function, $S(E)$, was calculated between -20 meV to 45 meV and for $Q=2\text{-}8 \text{ \AA}^{-1}$ from the corrected phonon dispersion (obtained from

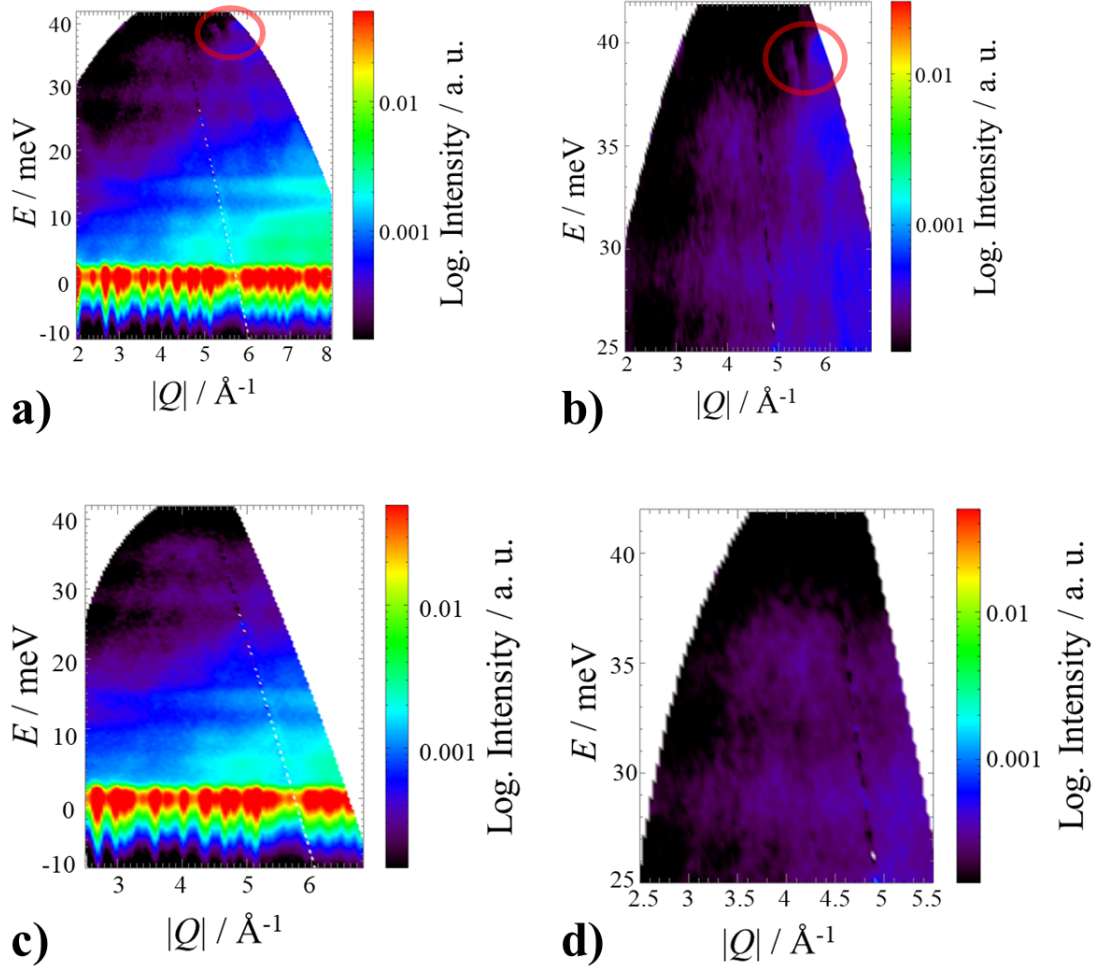


FIGURE 4.1: (Un)corrected phonon dispersion of $\text{Sb}_2\text{Se}_{0.6}\text{Te}_{2.4}$. An experimental artefact (red circle) was observed in the high-energy range.

the pure sample spectra). In order to subtract the elastic line from the total $S(E)$, a Bragg peak at around 2.75 \AA^{-1} was selected for each sample (figure 4.2a) and the scattering function of the reflection was calculated between -20 meV to 45 meV and for $Q \pm 0.005 \text{ \AA}^{-1}$ around its center. All scattering functions were calculated with energy steps of 0.5 meV using the program DAVE [102]. The elastic line was scaled and subtracted from the total $S(E)$ using the program "subs02" [103] available at the beamline P01 (figure 4.2b)). This step includes also a normalization of the difference spectrum (see section 2.3.3.3).

Step 4: Determination of the total density of states

The total phonon density of states was calculated using a modified version of the program DOS [104]. As this program was originally developed for the data treatment of NIS data, a value for the recoil energy had to be adjusted and was set to a value of 2 keV . This value is based on previous experience from similar experiments [105].

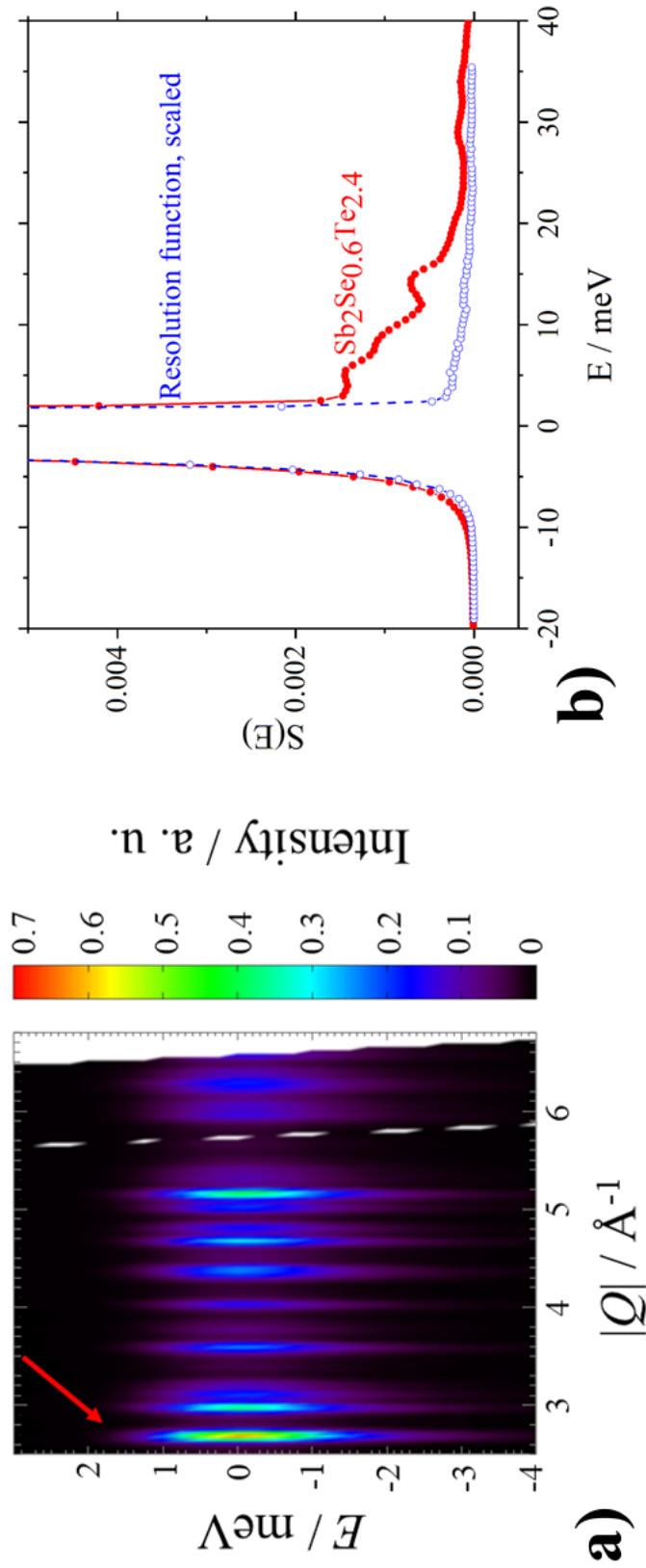


FIGURE 4.2: The selected Bragg peak is shown in a). The $S(E)$ of the sample and the elastic line are depicted in b).

4.3.2.2 Normalization of total phonon density of states

For the further data treatment, the extracted total phonon density of states were normalized. In order to exclude all high-energy contributions to the total phonon density of states, cut-off energies as summarized in table 4.1 were estimated. The

TABLE 4.1: Cut-off energies (in meV) estimated from the total phonon density of states of the $\text{Sb}_2\text{Te}_{3-x}\text{Se}_x$ ($x=0, 0.6, 1.2, 1.8, 3$) mixed crystals measured at around 40 K, 150 K and 300 K.

Sample	ca. 40 K	150 K	300 K
Sb_2Te_3	22.5	23.0	23.0
$\text{Sb}_2\text{Se}_{0.6}\text{Te}_{2.4}$	23.5	22.0	21.5
$\text{Sb}_2\text{Se}_{1.2}\text{Te}_{1.8}$	24.0	23.0	23.0
$\text{Sb}_2\text{Se}_{1.8}\text{Te}_{1.2}$	25.5	25.5	24.5
Sb_2Se_3	32.5	32.5	32.5

total phonon density of states were normalized to the corresponding area between 0 and the cut-off energies and then multiplied with an averaged scattering coefficient, $\langle b_c^2/M \rangle$, which was calculated according to equation (4.1),

$$\langle \frac{b_c^2}{M} \rangle = \sum_i x_i \cdot \frac{b_{c,i}^2}{M_i}. \quad (4.1)$$

Here, $b_{c,i}^2/M_i$ are the isotope/element-specific weighting coefficients (^{121}Sb : $1.62(4) \text{ cm}^2 \cdot \text{kg}^{-1}$, ^{125}Te : $1.21(4) \text{ cm}^2 \cdot \text{kg}^{-1}$, Se : $4.84(6) \text{ cm}^2 \cdot \text{kg}^{-1}$), which were calculated from the isotope/element-specific coherent neutron scattering length $b_{c,i}$ (^{121}Sb : $0.571(6) \cdot 10^{-12} \text{ cm}$, ^{125}Te : $0.502(8) \cdot 10^{-12} \text{ cm}$, Se : $0.797(9) \cdot 10^{-12} \text{ cm}$ [106]), and the masses of the isotopes/element M_i (^{121}Sb : $200.925 \cdot 10^{-27} \text{ kg}$, ^{125}Te : $207.567 \cdot 10^{-27} \text{ kg}$, Se : $131.134 \cdot 10^{-27} \text{ kg}$). The element-specific weighting coefficients were multiplied with the mole fraction, x_i , of the corresponding element in the considered mixed crystal.

4.3.2.3 Calculation of heat capacity from INS data

By using the expression shown in equation (2.28) and the normalized total phonon density of states (see section 4.3.2.2), the isochoric low-temperature heat capacity, $c_{V,\text{INS}}(T)$, of the samples Sb_2Te_3 (150 K data), $\text{Sb}_2\text{Se}_{0.6}\text{Te}_{2.4}$ (35 K), $\text{Sb}_2\text{Se}_{1.2}\text{Te}_{1.8}$ (35 K), $\text{Sb}_2\text{Se}_{1.8}\text{Te}_{1.2}$ (35 K) and Sb_2Se_3 (150 K) were calculated in the temperature range from 1-300 K. For the mixed crystals, the lowest temperature data allowed the best determination of the heat capacity, whereas for both endmembers the 150 K data provided the most reliable results. The integration in equation (2.28) was performed up to the cut-off energy listed in table 4.1.

4.3.3 Processing of nuclear inelastic scattering (NIS) data

4.3.3.1 Extraction of the partial phonon density of states from NIS data

After binning of the raw data, the corresponding elastic line measured with the NFS detector was subtracted from the total nuclear absorption spectrum using the program "subs02" [103] available at the beamline P01. For this, the elastic line was scaled to the nuclear absorption spectrum of the sample. After the elastic line was subtracted, the ^{121}Sb and ^{125}Te partial phonon density of states were extracted using a modified version of the program DOS [104]. The recoil energy was set to the transition energy of the corresponding Mössbauer isotope (see appendix B.1).

4.3.3.2 Normalization of partial phonon density of states

For the further data treatment, the partial phonon density of states were normalized to the area. The ^{121}Sb data were normalized between 0 and a value between the last positive and the first negative data point which allows an easier comparison between the ^{121}Sb partial phonon density of states of different mixed crystals. For the normalization of the ^{125}Te phonon data of $\text{Sb}_2\text{Se}_{0.6}\text{Te}_{2.4}$ and $\text{Sb}_2\text{Se}_{1.8}\text{Te}_{1.2}$ a cut-off energy of 21 meV and 22.5 meV, respectively, was estimated.

4.3.3.3 Application of the homology relation

In order to evaluate whether the observed mode shifts in the ^{121}Sb and ^{125}Te partial phonon density of states of the $\text{Sb}_2\text{Te}_{3-x}\text{Se}_x$ ($x=0, 0.6, 1.2, 1.8$) mixed crystals are exclusively caused by the composition-induced changes of the lattice parameter/the unit cell volume and the Se/Te mass ratio or whether there is an additional contribution to the mode shift caused by a change of the bonding, the homology relation (see section 2.4; equation (2.31)) was applied.

As all mixed crystals are composed of the same mole fraction of antimony, the mass ratio $M_{\text{Sb,A}}/M_{\text{Sb,B}} = 1$ (equation (2.31)). Thus, according to equation (2.31) for the ^{121}Sb data, the homology relation only depends on the lattice parameter ratios/the ratio of the unit cell volumes. In contrast to this, the Tellurium content in all samples is varying and thus, the mass fraction $M_{\text{Te,A}}/M_{\text{Te,B}} \neq 1$. In order to calculate the mass fraction, the Tellurium content of each sample was expressed by the sum, $x \cdot M(^{125}\text{Te}) + (3 - x) \cdot M(\text{Se})$, where $M(^{125}\text{Te})$ represents the mass of the ^{125}Te isotope, $M(\text{Se})$ is the mass of natural Selenium ($M=78.97 \text{ g}\cdot\text{mol}^{-1}$), and x describes the mole fraction of Tellurium according to the chemical formula of the considered sample.

In table 4.2, the lattice parameter, a and c , and the unit cell volumes of the $\text{Sb}_2\text{Te}_{3-x}\text{Se}_x$ ($x=0, 0.6, 1.2, 1.8$) mixed crystals taken from [107] (see also appendix D.4) are given for the temperature extracted via the Bose-Einstein-relation (section 3.6.1) from the NIS measurements (see section 5.2.5.2). All scaling factors were calculated with respect to the ^{121}Sb and ^{125}Te [14] partial density of states of Sb_2Te_3 (table 4.2). From the

TABLE 4.2: Scaling factors for the ^{121}Sb and ^{125}Te partial phonon density of states of the $\text{Sb}_2\text{Te}_{3-x}\text{Se}_x$ ($x=0, 0.6, 1.2, 1.8$) samples. The lattice parameter and unit cell volumes [107] are given for the following temperatures: Sb_2Te_3 : 30 K, $\text{Sb}_2\text{Se}_{0.6}\text{Te}_{2.4}$: 35 K, $\text{Sb}_2\text{Se}_{1.2}\text{Te}_{1.8}$: 35 K, $\text{Sb}_2\text{Se}_{1.8}\text{Te}_{1.2}$: 45 K.

Sample	Sb_2Te_3	$\text{Sb}_2\text{Se}_{0.6}\text{Te}_{2.4}$	$\text{Sb}_2\text{Se}_{1.2}\text{Te}_{1.8}$	$\text{Sb}_2\text{Se}_{1.8}\text{Te}_{1.2}$
$a / \text{\AA}$	4.2354(8)	4.2048(8)	4.1558(9)	4.1123(6)
$c / \text{\AA}$	30.169(9)	30.007(10)	29.699(8)	29.445(8)
$V / \text{\AA}^3$	464.64(20)	459.47(20)	444.20(20)	431.23(49)
^{121}Sb				
$E_{\text{Sb}_2\text{Te}_3}/E_A(\text{a})$	1	0.9928(3)	0.9812(3)	0.9709(3)
$E_{\text{Sb}_2\text{Te}_3}/E_A(\text{c})$	1	0.9946(5)	0.9844(4)	0.9760(4)
$E_{\text{Sb}_2\text{Te}_3}/E_A(\text{V})$	1	0.9934(2)	0.9823(2)	0.9727(4)
^{125}Te				
$M_A/M_{\text{Sb}_2\text{Te}_3}$	1	0.9264		0.7792
$E_{\text{Sb}_2\text{Te}_3}/E_A(\text{a})$	1	0.9555(3)		0.8571(3)
$E_{\text{Sb}_2\text{Te}_3}/E_A(\text{c})$	1	0.9573(5)		0.8615(4)
$E_{\text{Sb}_2\text{Te}_3}/E_A(\text{V})$	1	0.9562(2)		0.8586(4)

lattice parameter a and c the direction-dependent scaling factors $E_{\text{Sb}_2\text{Te}_3}/E_A(\text{a})$ and $E_{\text{Sb}_2\text{Te}_3}/E_A(\text{c})$ were deduced, whereas a comparison of the unit cell volumes yield the average scaling factors $E_{\text{Sb}_2\text{Te}_3}/E_A(\text{V})$.

4.3.4 Calculation of Debye temperatures from INS and NIS data

By fitting the heat capacity derived from the INS data with the Debye model (equation (2.36)), the Debye temperatures were determined (see appendix D.1). All isotope/element-specific Debye temperatures given in this study were determined from the corresponding partial phonon density of states by using equation (2.29). While the ^{121}Sb and ^{125}Te Debye temperatures were extracted from the NIS data, the Se Debye temperatures were determined from the calculated partial phonon density of states (4.3.5). Integrations according to equation (2.29) were performed between the following energy ranges: $\text{Sb}_2\text{Se}_{0.6}\text{Te}_{2.4}$: ^{125}Te : 0-21 meV; Se: 0-16.5 meV; $\text{Sb}_2\text{Se}_{1.8}\text{Te}_{1.2}$: ^{125}Te : 0-22.5 meV; Se: 0-25 meV; Sb_2Se_3 : ^{121}Sb : 0-32.5 meV; Se: 0-32.5 meV. An extraction of isotope-specific Debye temperatures from the ^{121}Sb partial phonon density of states of the mixed crystals $x=0, 0.6, 1.2, 1.8$ using equation (2.29) was impossible due to the additional high energy peaks (probably caused by experimental artefacts) and the not clearly defined cut-off energies.

4.3.5 Extraction of Se partial phonon density of states

For the samples $\text{Sb}_2\text{Se}_{0.6}\text{Te}_{2.4}$ and $\text{Sb}_2\text{Se}_{1.8}\text{Te}_{1.2}$, the ^{121}Sb and ^{125}Te partial phonon density of states, $g(\omega)_{^{121}\text{Sb}}$ and $g(\omega)_{^{125}\text{Te}}$, as well as the total ones, $G(\omega)$, were measured with INS and NIS and normalized according to sections 4.3.2.2 and 4.3.3.2, respectively. By subtracting the partial phonon density of states from the total one according to equation (4.2), the Se partial phonon density of states, $g(\omega)_{\text{Se}}$, can be

determined [14],

$$\frac{x_{\text{Se}} \cdot b_{c,\text{Se}}^2}{M_{\text{Se}}} \cdot g(\omega)_{\text{Se}} = G(\omega) - \frac{x_{^{121}\text{Sb}} \cdot b_{c,^{121}\text{Sb}}^2}{M_{^{121}\text{Sb}}} \cdot g(\omega)_{^{121}\text{Sb}} - \frac{x_{^{125}\text{Te}} \cdot b_{c,^{125}\text{Te}}^2}{M_{^{125}\text{Te}}} \cdot g(\omega)_{^{125}\text{Te}}. \quad (4.2)$$

In equation (4.2), $b_{c,i}^2 / M_i$ is the element-specific weighting factor which was already introduced in section 4.3.3.3, and x_i is the fraction of the isotope/element in the corresponding mixed crystal. As for $\text{Sb}_2\text{Se}_{0.6}\text{Te}_{2.4}$ two additional modes were found in the high-energy range (>25 meV) in the INS data whose origin is not completely clear, the subtraction was only performed between 0-25 meV.

In an analogous way ($x_{^{125}\text{Te}}=0$) the Se partial phonon density of states of Sb_2Se_3 was determined by a subtraction of the normalized ^{121}Sb partial from the normalized total PDOS via equation (4.2).

Chapter 5

Results

5.1 High-pressure and low-temperature behavior of $\text{GeSe}_x\text{Te}_{1-x}$ compounds

5.1.1 Introduction

5.1.1.1 The $\text{GeSe}_x\text{Te}_{1-x}$ solid solution: state of the art

Figure 5.1 depicts the high-temperature and ambient pressure phase diagram of the $\text{GeSe}_x\text{Te}_{1-x}$ solid solution determined from a powder diffraction study performed by Wiedemeier and Siemers [108]. At room temperature, three phases - a rhombohe-

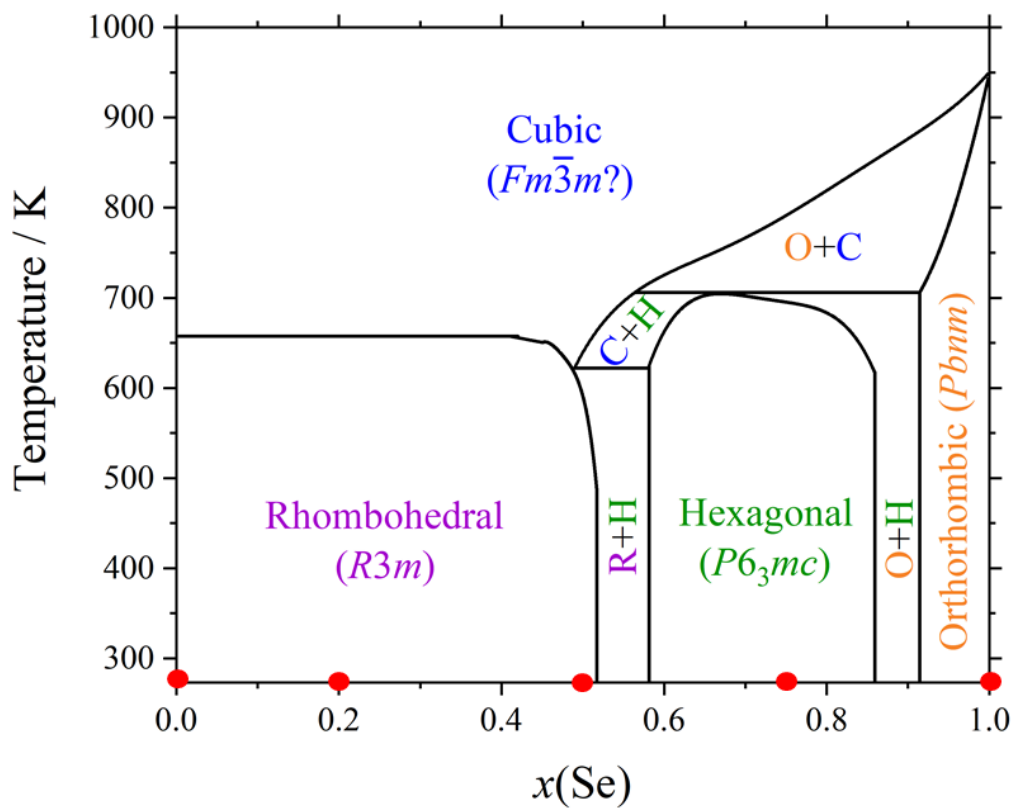


FIGURE 5.1: Phase diagram of the $\text{GeSe}_x\text{Te}_{1-x}$ solid solution adapted from Wiedemeier and Siemers [108]. Red dots indicate the compositions studied in this thesis.

dral ($0 \leq x(\text{Se}) \leq 0.52$) one, a hexagonal ($0.58 \leq x(\text{Se}) \leq 0.86$) one and an orthorhombic ($0.91 \leq x(\text{Se}) \leq 1$) one - have been observed. For Selenium contents of about $0.52 \leq x(\text{Se}) \leq 0.58$ and $0.86 \leq x(\text{Se}) \leq 0.91$ a rhombohedral/hexagonal and hexagonal/orthorhombic two-phase region, respectively, was found. At high temperatures, all phases transform into a face-centered cubic structure [108]. While the rhombohedral compounds transform directly into the FCC phase, for the hexagonal and orthorhombic mixed crystals intermediate high-temperature two-phase regions have been observed.

The crystal structures of the endmembers GeTe and GeSe are reported in the literature [109, 110]. The GeTe-I phase of GeTe crystallizes in a trigonal structure with space group $R\bar{3}m$ and lattice parameter of $a = 4.172(1) \text{ \AA}$ and $c = 10.710(2) \text{ \AA}$ [109]. After the corresponding transformation to the pseudo-cubic setting (appendix A) lattice parameter of $a = 5.996(1) \text{ \AA}$ and $\alpha = 88.18^\circ$ are obtained. The angle α shows only a small deviation from the cubic metric. Therefore, it is straightforward to consider the structure as a distorted variant of a FCC structure [113]. Figure 5.2 shows a projection of the GeTe-I structure on the ac plane. The structure is formed by layers of six-membered Ge-Te rings (figure 5.3) which are arranged in the chair conformation and stacked along the [001] direction. Both, Ge (WP $3a; 0, 0, z$; site symmetry $3m$ [109]) and Te atoms (WP $3a; 0, 0, z$; site symmetry $3m$ [109]), occupy Peierl's distorted octahedra and show a [3+3] coordination formed by three shorter and three longer Ge-Te bonds [109] (figure 5.3). In a previous study [108], it was suggested that mixed crystals with Selenium contents between $0 \leq x(\text{Se}) \leq 0.52$ are isostructural to GeTe-I. It is important to mention that this is only valid for a complete Se/Te disorder. A preferred Se incorporation into one specific layer of the GeTe-I structure would lead to a reduction of the symmetry and in specific cases also to a multiplication of the c lattice parameter and thus, to the occurrence of superstructure reflections which are not in agreement with the GeTe-I structure.

The GeSe-I phase crystallizes in a GeS type structure with space group $Pbnm$ and lattice parameter of $a = 4.388(4) \text{ \AA}$, $b = 10.825(9) \text{ \AA}$ and $c = 3.833(4) \text{ \AA}$ [114]. The crystal structure is formed by layers of six-membered and strongly puckered Ge-Se rings (figure 5.3), which are stacked along the [010] direction (figure 5.2). The Ge-Se rings are arranged in the chair conformation. The coordination around Ge (WP $4c; 0.1115(3), 0.1211(1), \frac{1}{4}$; site symmetry m) is characterized by three covalent Ge-Se bonds ($1 \times 2.563(3) \text{ \AA}$; $2 \times 2.574(3) \text{ \AA}$), three Ge \cdots Se interactions ($1 \times 3.367(3) \text{ \AA}$; $2 \times 3.316(3) \text{ \AA}$) and two Ge \cdots Ge contacts ($3.392(3) \text{ \AA}$). The Se atoms (WP $4c; 0.5020(2), 0.8534(1), \frac{1}{4}$; site symmetry m) are surrounded by three covalent Ge-Se bonds ($1 \times 2.563(3) \text{ \AA}$; $2 \times 2.574(3) \text{ \AA}$), three Ge \cdots Se interactions ($1 \times 3.367(3) \text{ \AA}$; $2 \times 3.316(3) \text{ \AA}$) and four long-ranged Se \cdots Se contacts ($4 \times 3.674(3) \text{ \AA}$) [114]. Mixed crystals with selenium contents between about $0.91 \leq x(\text{Se}) \leq 1$ are isostructural to GeSe-I [108, 114]. Mixed crystals with selenium contents between $0.58 \leq x(\text{Se}) \leq 0.86$ crystallize in a hexagonal structure that was recently determined for $\text{GeSe}_{0.75}\text{Te}_{0.25}$ [63]. They reported space group $P6_3mc$ with lattice parameter of $a = 3.822(2) \text{ \AA}$ and $c = 15.680(6) \text{ \AA}$.

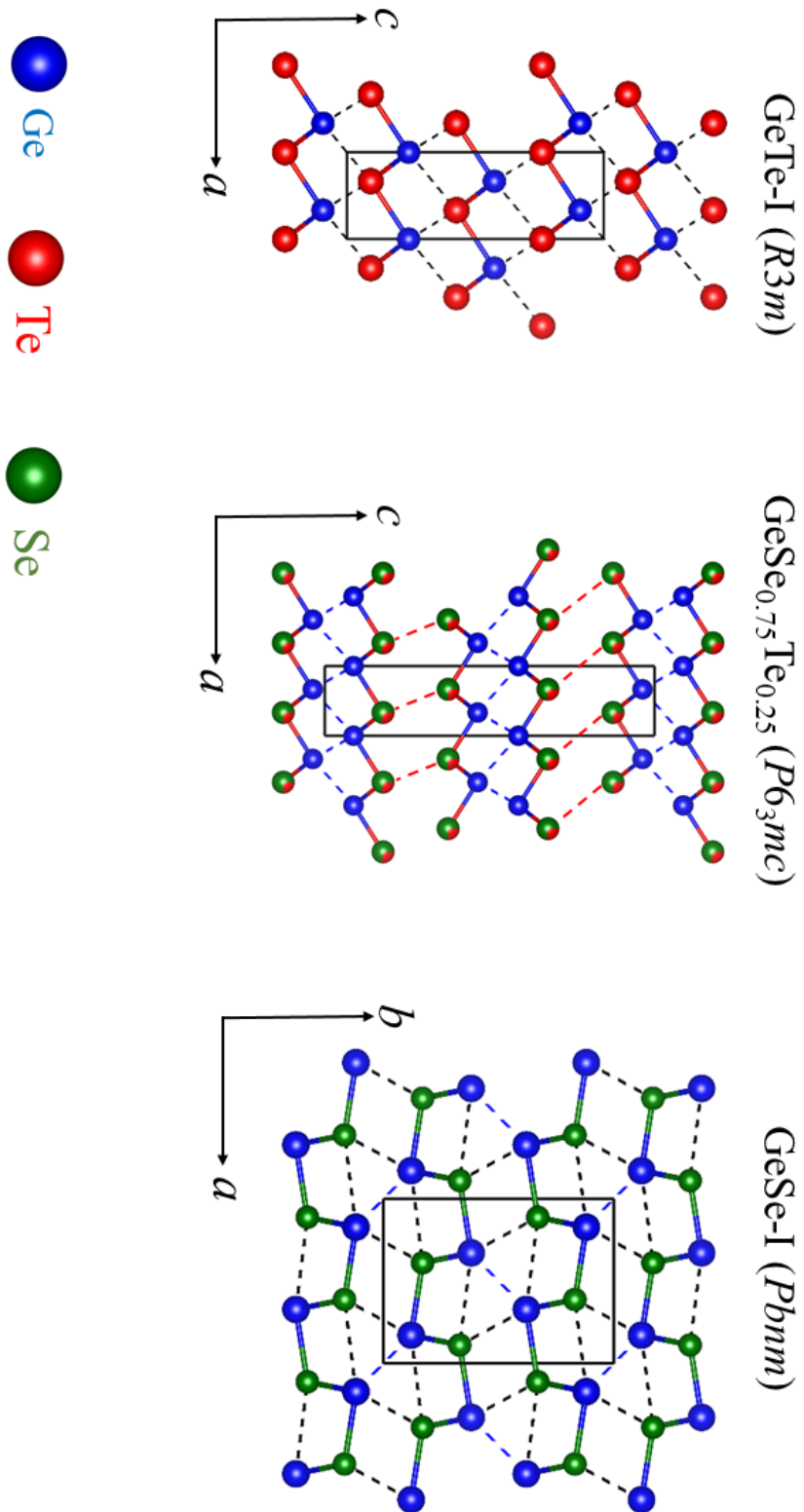


FIGURE 5.2: Projections of the crystal structures of GeTe-I [109], GeSe_{0.75}Te_{0.25} [63] and GeSe-I [110].

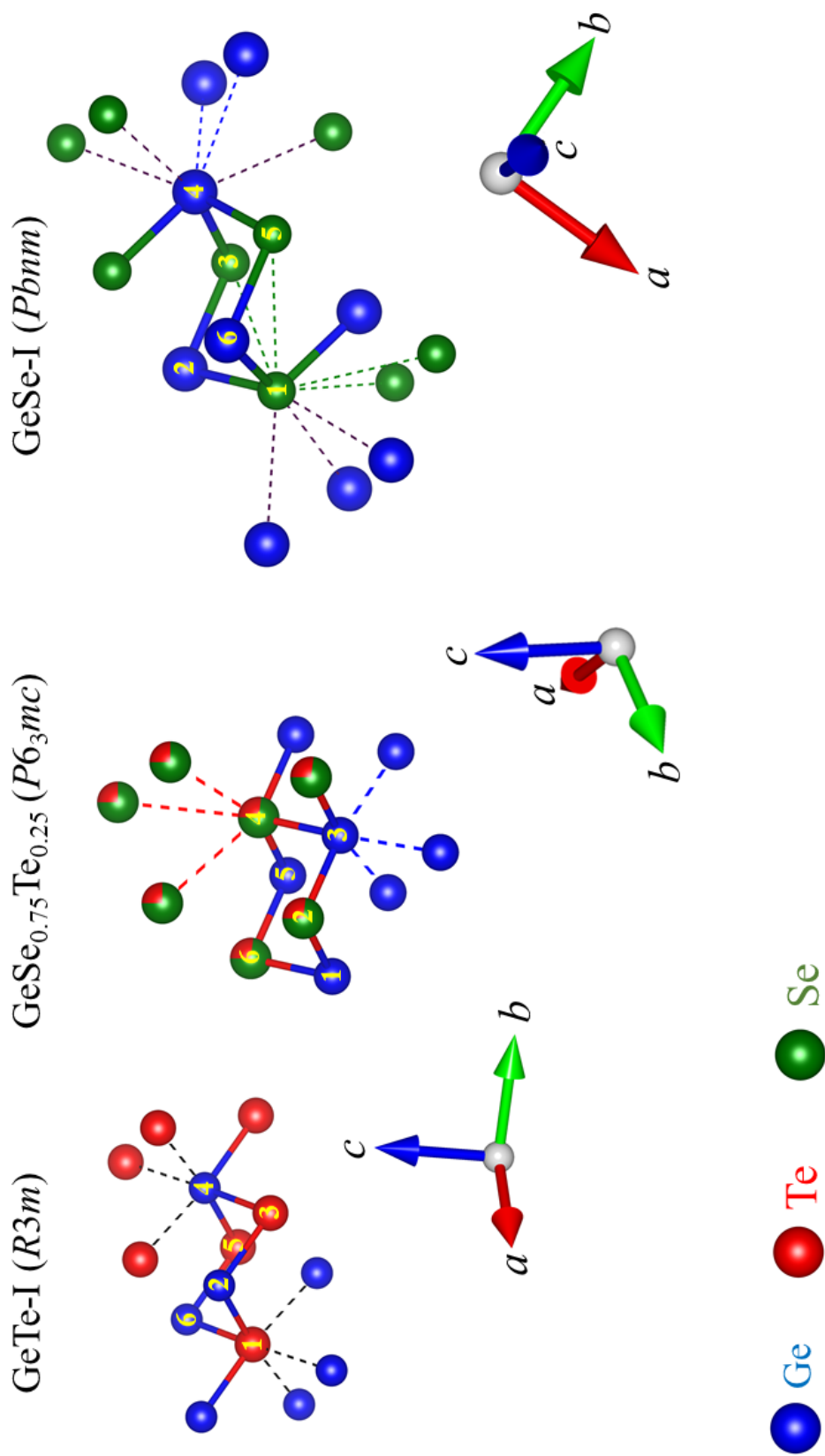


FIGURE 5.3: Six-membered Ge-Se/Te rings in the GeTe-I, $\text{GeSe}_{0.75}\text{Te}_{0.25}$ and GeSe-I structure. The coordination of representative Ge, Se and Te atoms is demonstrated.

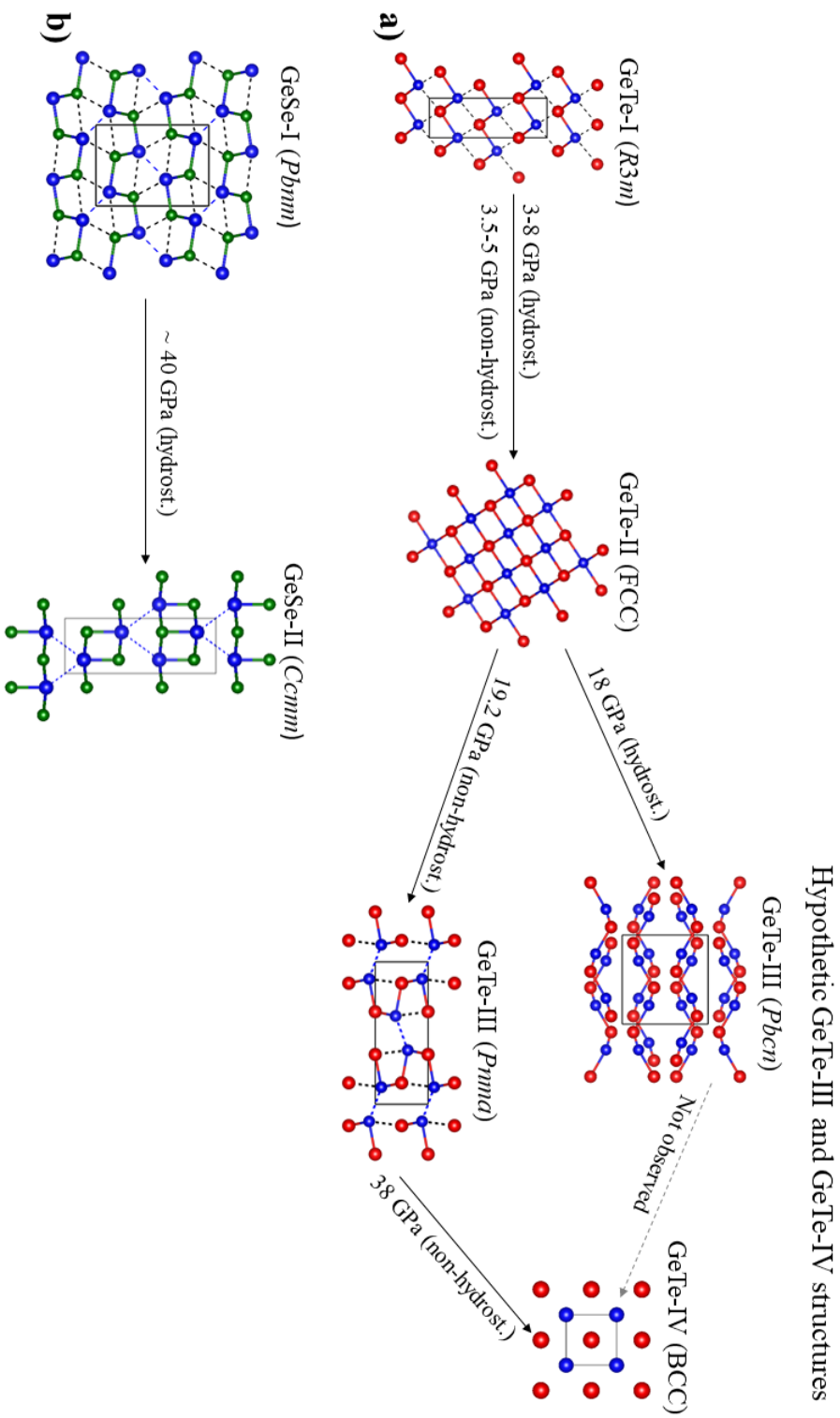


FIGURE 5.4: High-pressure behavior of GeTe and GeSe. GeTe-I: [109], GeTe-II: [108], postulated GeTe-III ($Pbcm$): [79], postulated GeTe-III ($Pnma$): [111], postulated GeTe-IV: [112].

The structure is formed by layers of six-membered Ge-Se/Te rings (figure 5.3), which are arranged in the chair conformation and stacked along the [001] direction (figure 5.2). The $\text{GeSe}_{0.75}\text{Te}_{0.25}$ structure can be derived from the GeTe-I structure if each second layer is rotated by 180° around the [010] direction [63]. Hence, in $\text{GeSe}_{0.75}\text{Te}_{0.25}$ additional Ge \cdots Ge and long-ranged Se/Te \cdots Se/Te van der Waals interactions are present, which cause a pronounced enlargement of the c lattice parameter compared to the GeTe-I structure. In $\text{GeSe}_{0.75}\text{Te}_{0.25}$, the atoms Ge1 (WP1 2b; $\frac{1}{3}$, $\frac{2}{3}$, 0.4637(2); site symmetry $3m$) and Ge2 (WP2 2a; 0, 0, 0.5873(2); site symmetry $3m$) are coordinated by three covalent Ge-Se/Te bonds as well as three Ge \cdots Ge interactions [63]. Se1/Te1 (WP3 2b; $\frac{2}{3}$, $\frac{1}{3}$, 0.6768(2); site symmetry $3m$) and Se2/Te2 atoms (WP4 2a; $\frac{2}{3}$, $\frac{1}{3}$, 0.3743(2); site symmetry $3m$) are surrounded by three covalent Ge-Se/Te bonds and three long-ranged and Se/Te \cdots Se/Te interactions (figure 5.3).

The low-temperature behavior of the endmembers was investigated in previous studies whereas no information is available for the $\text{GeSe}_x\text{Te}_{1-x}$ mixed crystals. The lattice dynamics of GeTe was studied by nuclear inelastic scattering measurements and the ^{125}Te partial phonon density of states of the rhombohedral GeTe-I phase was determined at 30 K [15]. Furthermore, Lewis [115] has measured heat capacity data of the GeTe-I phase between 1.2-22 K and Hein *et al.* [116] reported a superconducting phase below about 0.05 K on the basis of temperature-dependent susceptibility measurements. Low-temperature Raman measurements on GeSe single crystals and thin films were performed [117, 118] and the occurrence of two new Raman modes after cooling GeSe below 150 K was reported [117]. This might indicate a phase transition, but no detailed structural information on the low-temperature phase is available. In contrast to this, Taube *et al.* [118] found that the $Pbnm$ structure of GeSe-I is stable down to at least 70 K.

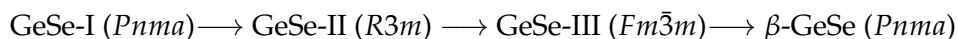
The high-pressure behavior of the $\text{GeSe}_x\text{Te}_{1-x}$ solid solution is less understood and only for the endmembers information is available. At room temperature and pressures between 0-20 GPa, three polymorphs of GeTe are postulated (figure 5.4). The transition of the GeTe-I phase to the face-centered cubic structure of GeTe-II was intensively studied [119, 120, 79, 112, 121], however, up to now, the order of this transition is unclear. In previous studies, the FCC phase is assumed to crystallize in a NaCl type structure, however, no full structure determination was performed. The transition pressure depends strongly on the degree of hydrostaticity. While for non-hydrostatic conditions transition pressures ranging from 3.5-5 GPa have been reported [112, 120], in a hydrostatic pressure-transmitting medium the transition was observed between 3 GPa [79] to 8 GPa [120]. Under non-hydrostatic conditions, the transition is accompanied by a pronounced volume change of 3-3.5 % [120, 112], whereas in case of hydrostatic conditions no volume anomalies have been observed [120, 79]. At about 18-19 GPa, GeTe-II is supposed to transform into an orthorhombic GeTe-III phase, however, based on powder diffraction data contradicting data on the crystal symmetry and the lattice parameter have been published previously for this polymorph [79, 112, 119, 111]. Karbanov *et al.* [111] have reported a structure

isotypical to the GeS structure type (space group symmetry $Pbnm$; lattice parameter of $a=3.98(5)$ Å, $b=10.60(1)$ Å, $c=3.929(5)$ Å), which is also isostructural to GeSe-I. Onodera *et al.* [79] found a structure with space group symmetry $Pbcn$ ($a=7.441(6)$ Å, $b=7.678(22)$ Å, $c=3.929(5)$ Å). In none of these two publications a full structural refinement is provided. Moreover, the structure reported by Onodera *et al.* [79] has unreasonable short Ge-Te bonds with bond lengths of only about 1.6 Å.

Onodera *et al.* [79] have reported values for the bulk modulus B_0 and its first derivative B'_0 of 49.9(32) GPa and 3.7(8) GPa, respectively, for the GeTe-I and GeTe-II polymorph, whereas they suggested $B_0=95.1(51)$ GPa and $B'_0=5.3(3)$ GPa for the GeTe-III phase.

Serebryanaya *et al.* [112] proposed a further phase transition at 38 GPa and suggested a CsCl type structure for the GeTe-IV polymorph, however, this phase transition was not observed in [79] (figure 5.4).

The high-pressure behavior of GeSe is not completely understood. Onodera *et al.* [79] studied the high-pressure behavior of a polycrystalline GeSe sample up to 82 GPa by X-ray powder diffraction and resistivity measurements and did not observe any phase transitions. Other authors also did not observe any phase transitions in this pressure range [122]. In contrast to this, a pronounced jump in the high-pressure resistivity curve of single crystalline GeSe was reported [123] already around 6 GPa and ascribed to the formation of a metallic face-centered cubic phase. The high-pressure behavior of GeSe thin films was recently reported [124] and a phase transition from the GeSe-I phase into a structure with $Ccmm$ symmetry ($a=3.52$ Å, $b=3.61$ Å, $c=9.68$ Å) was observed, yet no intermediate FCC phase (figure 5.4). Similarly, a $Pbnm$ to $Cmcm$ transition has been reported for numerous isostructural compounds, e. g. SnS [125], SnSe [126], GeS [127]. Recently, the crystal structure of a new high-pressure and high-temperature polymorph of GeSe, the so-called β -GeSe, was reported [128]. β -GeSe crystallizes in space group $Pnma$ ($a=8.0892(6)$ Å, $b=3.8261(3)$ Å, $c=5.8089(5)$ Å) and the crystal structure is formed by layers of six-membered Ge-Se rings which are stacked along the [100] direction. The Ge-Se rings are arranged in the so-called boat conformation. The high-pressure behavior of GeSe was studied by first-principles calculations and in a laser-heated DAC [129] and the following pressure transition pathway from GeSe-I to β -GeSe was suggested:



5.1.1.2 Aims of this study

In order to understand the influence of compositional changes and high pressure on the bonds and coordination in compounds from the stability field of the GeTe-I structure type (figure 5.1), the endmember GeTe and two mixed crystals, $\text{GeSe}_{0.2}\text{Te}_{0.8}$ and $\text{GeSe}_{0.5}\text{Te}_{0.5}$, have been selected. This provides important information on the

influence of the Se content on the stability fields of the three high-pressure polymorphs. Furthermore, the study of the high-pressure behavior of $\text{GeSe}_{0.75}\text{Te}_{0.25}$ elucidates the influence of high-pressure on the Ge-Ge interactions in the structure of the hexagonal phase. Low-temperature powder diffraction studies were performed on GeTe , $\text{GeSe}_{0.2}\text{Te}_{0.8}$, $\text{GeSe}_{0.5}\text{Te}_{0.5}$, $\text{GeSe}_{0.75}\text{Te}_{0.25}$ and GeSe in order to extend the temperature-composition phase diagram of the $\text{GeSe}_x\text{Te}_{1-x}$ system. From this, the influence of different Se contents on the low-temperature behavior can be characterized.

5.1.2 Sample characterization

Appendix C.1 depicts the powder patterns of the $\text{GeSe}_x\text{Te}_{1-x}$ ($x=0, 0.2, 0.5, 0.75, 1$) mixed crystals measured at ambient conditions. For all compounds, the detected

TABLE 5.1: The c/a ratios of the $\text{GeSe}_x\text{Te}_{1-x}$ ($x=0, 0.2, 0.5, 0.75$) mixed crystals as determined in this study. Data from literature [108, 63] are included for comparison.

	Sample	GeTe	$\text{GeSe}_{0.2}\text{Te}_{0.8}$	$\text{GeSe}_{0.5}\text{Te}_{0.5}$	$\text{GeSe}_{0.75}\text{Te}_{0.25}$
c/a	this study	2.561(1)	2.578(2)	2.589(2)	4.105(6)
	References	2.556(4) [108]	2.581(4) [108]	2.593(4) [108]	4.103(3) [63]

peaks were indexed with the lattice parameter reported previously [15, 63, 114] and there is no evidence for any impurities. In appendix C.1.1, the composition-induced changes of the peak positions are elucidated by gray dashed lines.

In figure 5.5, the lattice parameter of the $\text{GeSe}_x\text{Te}_{1-x}$ ($x=0, 0.2, 0.5$) samples with GeTe-I structure type are shown in dependence of the Se content. They are compared to data from the literature [108] which are transformed to the $R3m$ cell in hexagonal setting (for the transformation matrices see appendix A). The unit cell volumes determined in this study approximately follow Vegard's law, whereas the individual lattice parameter show a non-ideal mixing behavior as function of the composition (figure 5.5). Wiedemeier and Siemers [108] also reported a non-ideal mixing behavior which is clearly visible in both lattice parameters and the unit cell volumes.

In table 5.1, the c/a ratios of the compounds investigated in this study are compared to the literature values [108, 63]. For all compounds, the c/a ratios are in a very good agreement with the reference data.

For the orthorhombic GeSe sample, the lattice parameter have been determined as $a=4.3895(3)$ Å, $b=10.8247(7)$ Å and $c=3.8346(3)$ Å. Again, the calculated values are in excellent agreement with the literature data [114] (table 5.2).

TABLE 5.2: The a/c , b/c and a/b ratio of the GeSe sample. The values determined in this study are compared to literature data [114].

a/c	b/c	a/b	Reference
1.1447(1)	2.8229(2)	0.4055(1)	This study
1.145(2)	2.824(4)	0.4054(4)	[114]

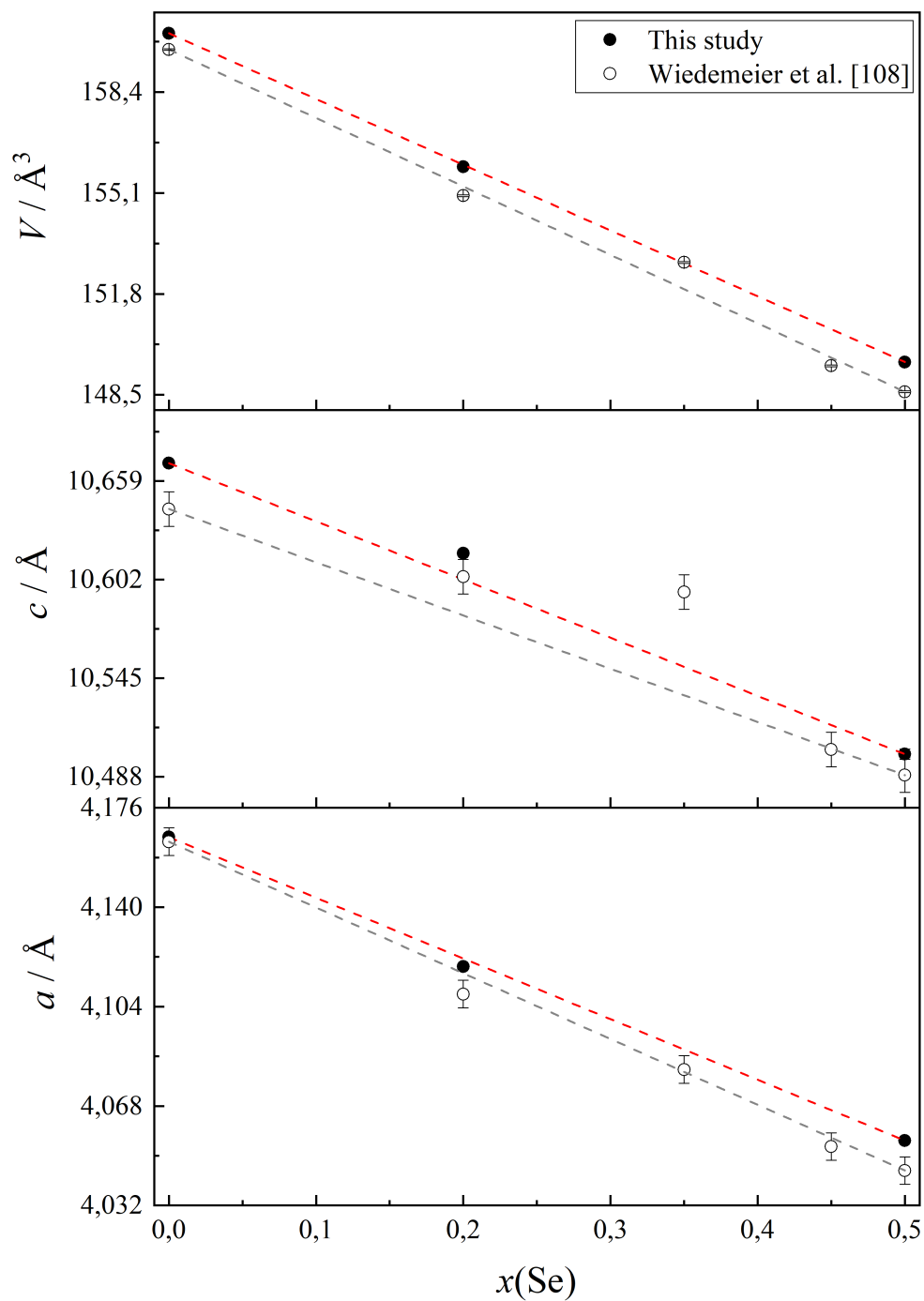


FIGURE 5.5: Lattice parameter of the $\text{GeSe}_x\text{Te}_{1-x}$ ($x=0, 0.2, 0.5$) samples. The values obtained in this study are compared to literature data [108].

5.1.3 Low-temperature behavior

5.1.3.1 GeTe , $\text{GeSe}_{0.2}\text{Te}_{0.8}$, $\text{GeSe}_{0.5}\text{Te}_{0.5}$ and $\text{GeSe}_{0.75}\text{Te}_{0.25}$

In the low-temperature powder patterns of all samples no additional peaks nor significant intensity changes have been observed and thus, there is no indication for any phase transitions.

For the isostructural compounds GeTe , $\text{GeSe}_{0.2}\text{Te}_{0.8}$ and $\text{GeSe}_{0.5}\text{Te}_{0.5}$, the relative lattice parameter a_i/a_0 shows a positive thermal expansion of up to about 0.4 % and a very similar temperature dependence between 25-300 K (figure 5.6). Thus, the thermal behavior of the [100] direction is hardly influenced by the Selenium content of the samples. In contrast to this, the relative lattice parameter c_i/c_0 shows a negative thermal expansion which increases with an increasing Selenium content from about -0.1 % (GeTe) up to about -0.25 % ($\text{GeSe}_{0.5}\text{Te}_{0.5}$). A negative thermal expansion along one of the crystallographic axis over such a wide temperature range is a surprising finding as most of the binary chalcogenides (e. g. PbX ($X=\text{S}, \text{Se}, \text{Te}$), ZnSe [130], $M_2\text{Te}_3$ ($M=\text{Bi}$ [131], Sb [131], Cr [132]) show an exclusively positive thermal expansion along their crystallographic axis. Only the orthorhombic SnSe exhibits a negative thermal expansion along its c axis [133] which is comparable to the one observed for the compounds in the stability field of the GeTe structure type. In order to evaluate the distortion of the crystal structures in the rhombohedral stability field with respect to a face-centered cubic (FCC) unit cell, the c/a ratio can be compared to the ideal value of 2.4495 (figure 5.7) which results from the transformation of the FCC cell to the R -centered unit cell in hexagonal setting (see transformation matrices in appendix A). The larger the deviation from the ideal ratio, the more distorted is the structure with respect to the cubic unit cell. The c/a ratios of the rhombohedral compounds decrease with elevated temperatures. This result is in agreement with the high-temperature phase transition from the GeTe -I phase into a FCC structure reported previously [108]. Moreover, the c/a ratio of the rhombohedral compounds increase with an increasing Se content of the sample and thus, the larger the Se content, the larger the distortion.

In contrast to the compounds from the stability field of the GeTe -I structure type (figure 5.6a), both lattice parameter of $\text{GeSe}_{0.75}\text{Te}_{0.25}$ show an exclusively positive thermal expansion (figure 5.6a). The a lattice parameter of $\text{GeSe}_{0.75}\text{Te}_{0.25}$ shows a temperature-induced change of up to about 0.2 % which is much smaller than what is observed for the compounds with GeTe -I type structure. For the c lattice parameter a positive thermal expansion of up to about 0.4 % is observed. Moreover, for $\text{GeSe}_{0.75}\text{Te}_{0.25}$ an increase of the c/a ratio with increasing temperatures was found (figure 5.7).

For all studied compounds, the unit cell volumes show a positive thermal expansion. Obviously, the unit cell volumes of $\text{GeSe}_{0.75}\text{Te}_{0.25}$ and GeTe show comparable temperature-induced changes of up to about 0.8 %. The unit cell volumes of $\text{GeSe}_{0.2}\text{Te}_{0.8}$ and $\text{GeSe}_{0.5}\text{Te}_{0.5}$ are less influenced by the temperature and exhibit a

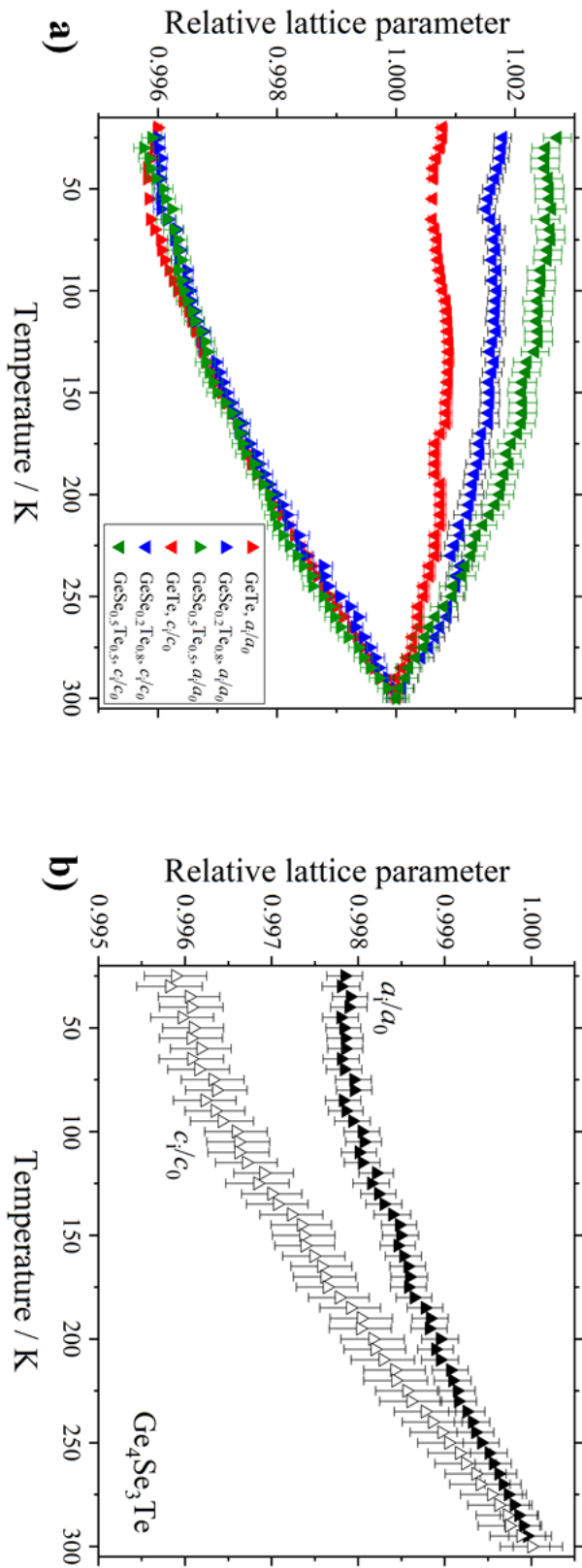


FIGURE 5.6: Relative lattice parameter of the GeSe_xTe_{1-x} ($x=0, 0.2, 0.5, 0.75$) samples.

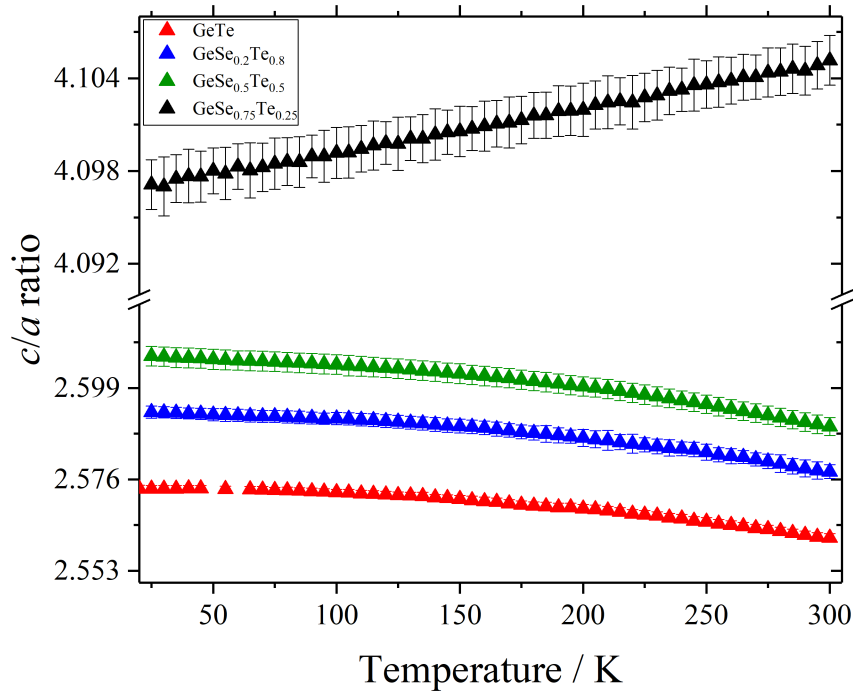


FIGURE 5.7: Temperature dependence of the c/a ratio of the $\text{GeSe}_x\text{Te}_{1-x}$ ($x=0, 0.2, 0.5, 0.75$) samples.

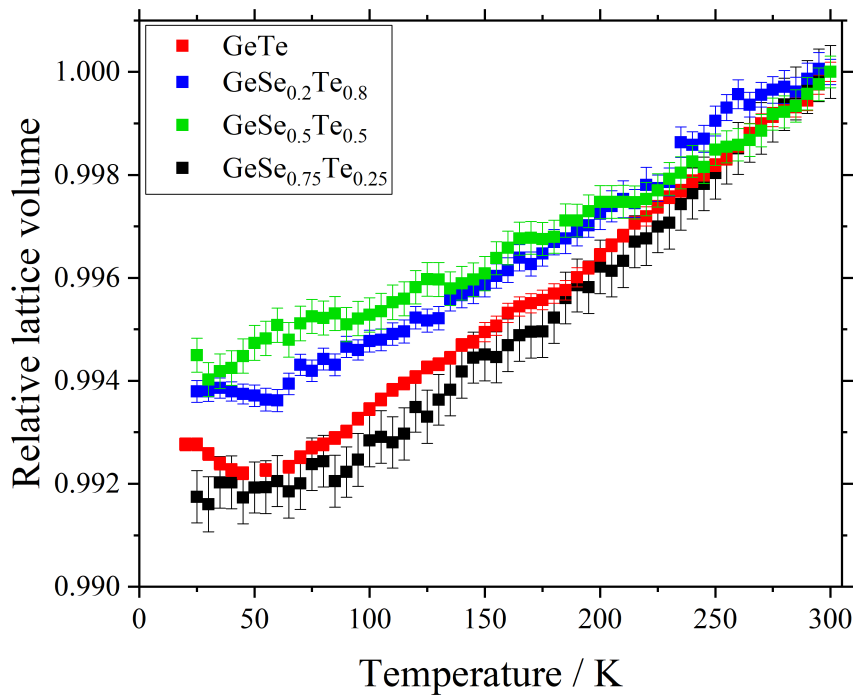


FIGURE 5.8: Temperature-dependence of the unit cell volumes of the $\text{GeSe}_x\text{Te}_{1-x}$ ($x=0, 0.2, 0.5, 0.75$) samples.

thermal expansion of up to about 0.6 %.

The difference in the low-temperature behavior of the compounds in the stability field of the GeTe-I structure type compared to the one of the hexagonal phase might be due to the additional Ge··Ge interactions and the long-ranged Se/Te··Se/Te van der Waals gaps which are exclusively present in the hexagonal phase [63]. However, to elucidate this in more details, single crystal diffraction experiments at low temperatures would have to be carried out which are out of the scope of this work.

5.1.3.2 GeSe

All lattice parameter of GeSe show an exclusively positive thermal expansion (figure 5.9). The influence of the temperature on the a lattice parameter is small and temperature-induced changes of only up to about 0.1 % are observed. In contrast

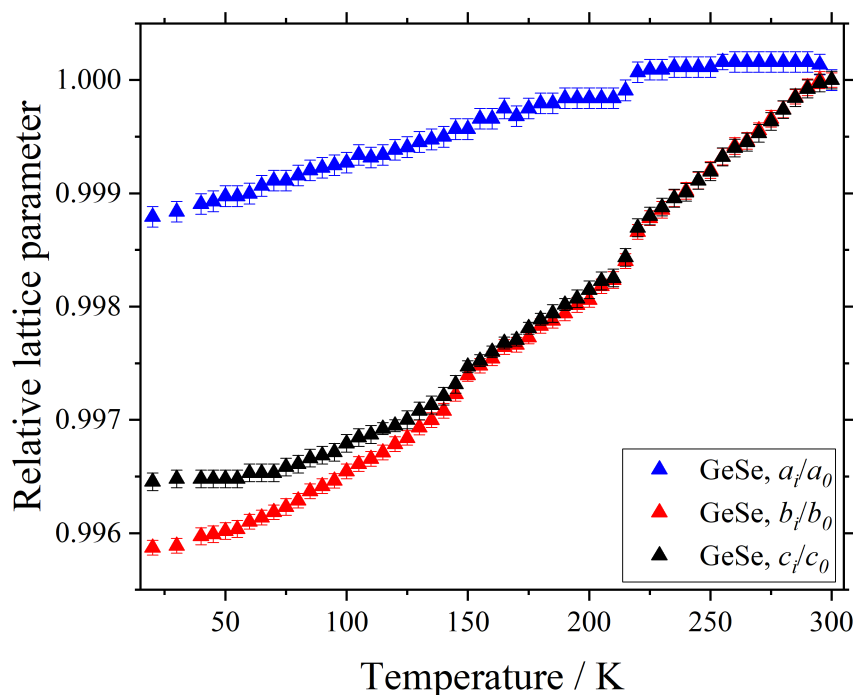


FIGURE 5.9: Temperature-dependence of the lattice parameter of GeSe-I.

to this, the b and c lattice parameter show a stronger thermal expansion of up to about 0.4 % and 0.35 %, respectively. The b and c lattice parameter show nearly identical temperature-induced changes down to about 150 K, whereas below this temperature the [010] direction is more strongly influenced by the temperature than the [001] direction. This corresponds to the temperature at which new Raman modes were observed previously [117]. However, in the powder pattern of the GeSe sample investigated in this study there is no evidence for new peaks and/or changed intensity ratios and thus, there is no evidence for a structural phase transition. The

results obtained here are in good agreement with [118], where it was reported that the GeSe-I phase is stable at least down to about 70 K.

5.1.4 High-pressure behavior

In figure 5.10, the pressure dependence of the formula volumes of the rhombohedral compounds GeTe, $\text{GeSe}_{0.2}\text{Te}_{0.8}$ and $\text{GeSe}_{0.5}\text{Te}_{0.5}$ and the hexagonal $\text{GeSe}_{0.75}\text{Te}_{0.25}$ is depicted. For GeTe, $\text{GeSe}_{0.2}\text{Te}_{0.8}$ and $\text{GeSe}_{0.5}\text{Te}_{0.5}$, two phase transitions have been

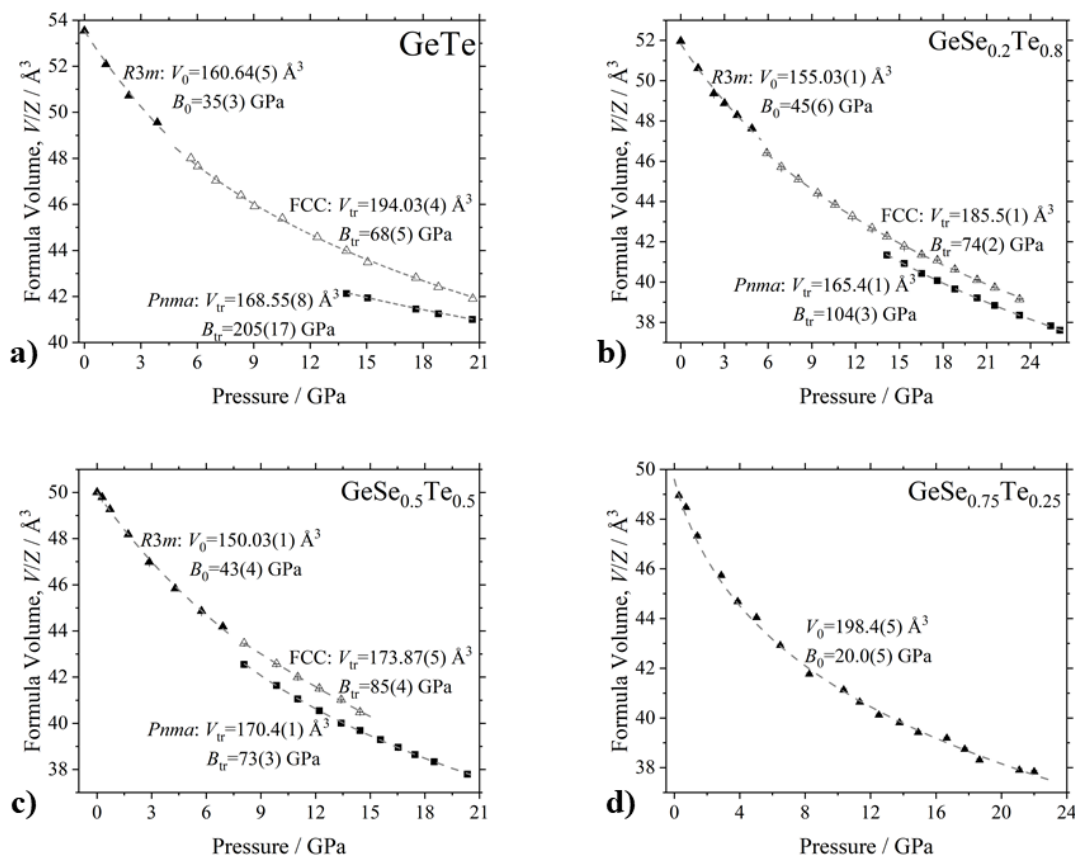


FIGURE 5.10: Pressure dependence of the formula volumes of the $\text{GeSe}_x\text{Te}_{1-x}$ ($x=0, 0.2, 0.5, 0.75$) mixed crystals.

observed in the respective pressure range, whereas the hexagonal phase is stable up to at least 23 GPa.

In Appendix C.2, powder patterns are shown at representative pressure points and at decompression to ambient pressure ("quenched"). For all compounds, the powder pattern of the quenched sample correspond to the ones of the ambient pressure phase indicating unambiguously that all phase transitions are reversible. The powder patterns of GeTe contain additional peaks and an indexing of these peaks assuming the phases Ge, GeO_2 , Te, TeO_2 (oxidation of GeTe), Diamond, Rhenium and Ruby failed. A careful inspection of our diffraction data showed that these peaks originate from a single crystalline impurity. In some measurements the reflections of the impurity are not visible (e. g. 9.0 GPa) which is attributed to the fact that the

contamination was not illuminated by the beam. The powder patterns measured at 1.1 GPa and on the quenched sample contain the same reflections which clearly shows that the impurity did not react with our GeTe sample. After the beamtime, we have measured the powder pattern of the part of our GeTe sample which was not used for the high-pressure study and we did not observe evidence for any impurities (see appendix C.2). Therefore, we presume that we have inadvertently transferred the single crystalline impurity together with our GeTe sample in the sample chamber of the DAC. The powder patterns of the samples $\text{GeSe}_{0.2}\text{Te}_{0.8}$, $\text{GeSe}_{0.5}\text{Te}_{0.5}$ and $\text{GeSe}_{0.75}\text{Te}_{0.25}$ show exclusively reflections which can be indexed with the known cells (appendix C.2).

At the first phase transition, the GeTe-I polymorph transforms into the face-centered cubic GeTe-II phase. For GeTe, $\text{GeSe}_{0.2}\text{Te}_{0.8}$ and $\text{GeSe}_{0.5}\text{Te}_{0.5}$, transition pressures of 4.2 GPa, 5.8 GPa and 7.7 GPa, respectively, were determined experimentally. Obviously, the transition pressure of the GeTe-I to GeTe-II transition increases with increasing Selenium content of the samples.

In order to understand the GeTe-I to GeTe-II transition in more detail, the lattice parameter of both phases have been transformed to the primitive rhombohedral unit cell (figure 5.11; for the transformation matrices see appendix A). This is straightforward as the GeTe-I structure can be considered as a distorted FCC structure composed of Peierl's-distorted octahedra [113]. For the primitive unit cell of the FCC phase, all angles are exactly 60° .

Obviously, for each compound the phase transition is accompanied by a pronounced discontinuous change in the lattice parameter indicating the first-order nature of this transition. In previous studies, it was concluded that for the GeTe-I to GeTe-II transition a non-hydrostatic pressure transmission leads to such anomalies in the lattice parameter [120, 112]. However, a high degree of non-hydrostaticity can be excluded in our high-pressure experiments as the detected signal in fluorescence did not show an unusual broadening. Moreover, the lattice parameter obtained from the powder patterns measured at the same pressure point but at different locations in the sample chamber (3×3 grid) did not indicate strong deviations. Thus, there is no evidence for non-hydrostatic conditions and the results of this thesis disagree with previous studies [120, 112]. This emphasize that the observed discontinuities are not necessarily a result of a non-hydrostatic pressure transmission.

At higher pressures, a further phase transition of the GeTe-II polymorph into the orthorhombic GeTe-III phase (figure 5.10) was observed. For GeTe, $\text{GeSe}_{0.2}\text{Te}_{0.8}$ and $\text{GeSe}_{0.5}\text{Te}_{0.5}$, transition pressure of 13.9 GPa, 13.2 GPa and 8,1 GPa, respectively, have been determined. For all compounds, the GeTe-II and GeTe-III phases coexist over a wide pressure range indicating the possible first-order nature of the phase transition. For $\text{GeSe}_{0.2}\text{Te}_{0.8}$ and $\text{GeSe}_{0.5}\text{Te}_{0.5}$, a one-phase region of the pure GeTe-III polymorph was determined at pressure above about 25 GPa and 15 GPa, respectively. It seems that the stability field of the GeTe-III phase becomes smaller with increasing Se content. For GeTe, the one-phase region was not reached even at the highest pressure

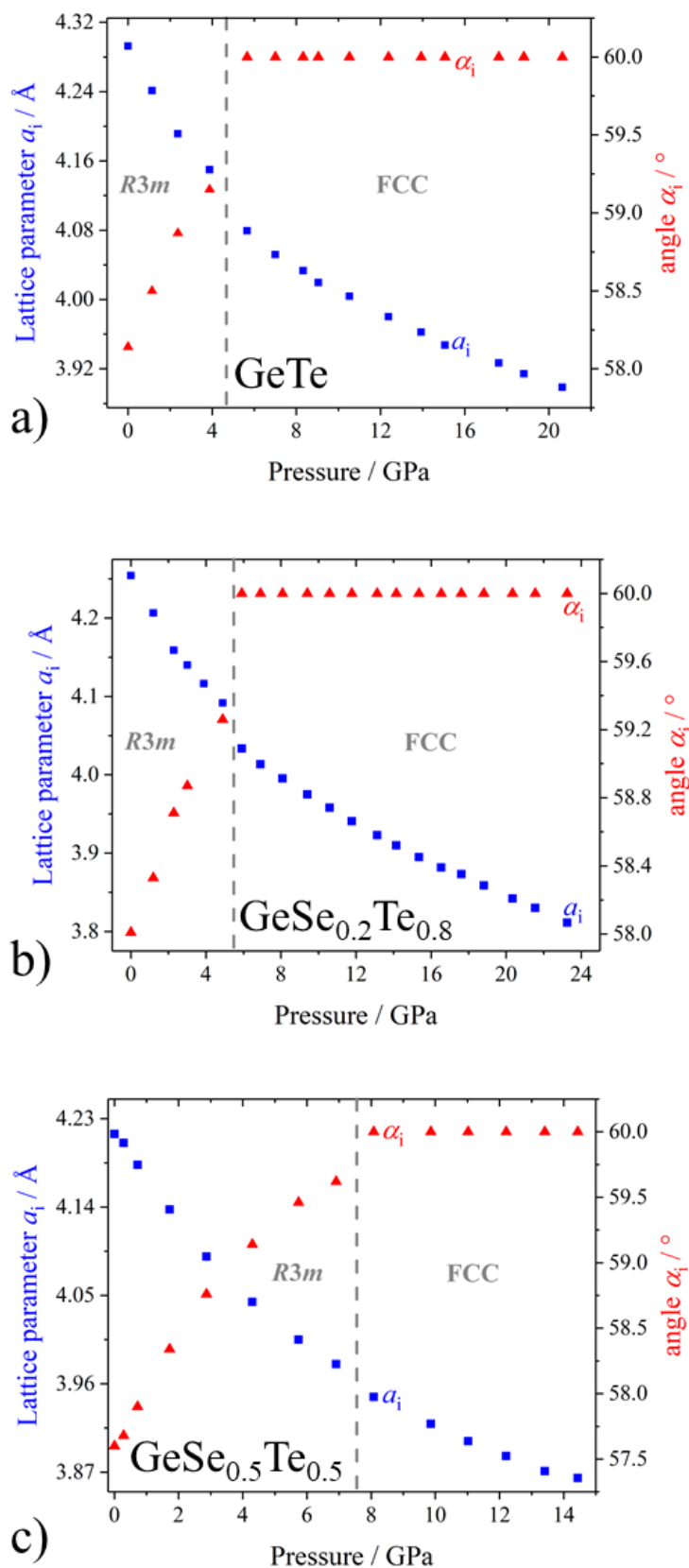


FIGURE 5.11: Pressure dependence of the primitive lattice parameter of the GeTe-I and GeTe-II phase, respectively. GeTe (a), $\text{GeSe}_{0.2}\text{Te}_{0.8}$ (b) and $\text{GeSe}_{0.5}\text{Te}_{0.5}$ (c). The transition pressure is marked by the gray dashed line.

TABLE 5.3: Bulk moduli, formula volumes, and transition pressures of the $\text{GeSe}_x\text{Te}_{1-x}$ ($x=0, 0.2, 0.5, 0.75$) samples. B_0 and V_0/Z refer to ambient pressure, B_{tr} and V_{tr}/Z refer to the transition pressures.

Phase Compound	GeTe-I			GeTe-II			GeTe-III			Hexagonal	
	B_0 / GPa	V_0/Z / \AA^3	p_{tr} / GPa	B_{tr} / GPa	V_{tr}/Z / \AA^3	p_{tr} / GPa	B_{tr} / GPa	V_{tr}/Z / \AA^3	B_0 / GPa	V_0/Z / \AA^3	
GeTe	35(3)	53.55(5)	4.2	68(5)	48.51(4)	13.9	205(17)	42.14(8)			
$\text{GeSe}_{0.2}\text{Te}_{0.8}$	45(6)	51.8(1)	5.8	74(2)	46.4(1)	13.2	104(3)	41.4(1)			
$\text{GeSe}_{0.5}\text{Te}_{0.5}$	43(4)	50.01(1)	7.7	85(4)	43.47(5)	8.1	73(3)	42(6)			
$\text{GeSe}_{0.75}\text{Te}_{0.25}$									20(4)	49.6(5)	

(21 GPa).

In order to determine the Bulk moduli, B_0 , and the ambient pressure formula volumes, V_0/Z , of the GeTe-I type phases and the hexagonal $\text{GeSe}_{0.75}\text{Te}_{0.25}$, the formula volumes have been fitted by third-order Birch-Murnaghan equations of states (equation (2.32); figure 5.10). For the fits of GeTe, $\text{GeSe}_{0.2}\text{Te}_{0.8}$ and $\text{GeSe}_{0.5}\text{Te}_{0.5}$, a constant value of $B'_0=4$ was used, whereas for $\text{GeSe}_{0.75}\text{Te}_{0.25}$ the parameter B'_0 was included as a fit parameter and yielded a value of $B'_0=13(4)$. This is, as the selected equations of states yielded the best fits of the experimental data. The data for the GeTe-II and GeTe-III type polymorphs were fitted using a Murnaghan equation of states (equation (2.33)), as this yielded a better fit compared to the the results obtained from the Birch-Murnaghan equation of states. The bulk moduli, B_{tr} , and formula volumes, V_{tr}/Z , at the corresponding transition pressure, p_{tr} , were determined and are summarized in table 5.3.

The literature value of $B_0=49.9(51)$ GPa for the GeTe-I phase of GeTe [79] is in poor agreement with the one determined here (35(3) GPa). For the GeTe-I type polymorphs, the bulk modulus, B_0 , of $\text{GeSe}_{0.2}\text{Te}_{0.8}$ is significantly larger than the one of GeTe, whereas it is very similar to the one of $\text{GeSe}_{0.5}\text{Te}_{0.5}$. In other words, the initial incorporation of Se has a large effect on the bulk modulus, whereas a further increase of the Se content has comparatively little effect.

Although, the bulk moduli of the GeTe-II and GeTe-III polymorphs correspond to slightly different transition pressures, it is possible to compare them for the three compounds GeTe, $\text{GeSe}_{0.2}\text{Te}_{0.8}$ and $\text{GeSe}_{0.5}\text{Te}_{0.5}$. The bulk modulus of the GeTe-II phase increases with increasing Se content indicating that the material becomes more incompressible. The value of $B_0=49.9(51)$ GPa reported in the literature [79] for the GeTe-II type phase of GeTe is in poor agreement with the value found in this study (68(5) GPa).

The bulk modulus of the GeTe-III phase decreases significantly with increasing Selenium content and the compounds become more compressible. In general, the bulk modulus of the GeTe-III polymorph shows larger composition-induced changes than the one of the GeTe-II polymorph and the compressibility of this phase is more sensitive to the Selenium content.

The bulk modulus of the hexagonal $\text{GeSe}_{0.75}\text{Te}_{0.25}$ compound is much smaller than the ones of the GeTe-I phases indicating a larger compressibility. This is probably due to the Ge·Ge interactions and the large Se/Te·Se/Te van der Waals gaps which are not present in the GeTe-I type structure. The experimentally determined formula volume of $\text{GeSe}_{0.75}\text{Te}_{0.25}$ is in good agreement with the value reported in the literature ($V_0/Z=49.58(3) \text{ \AA}^3$; [63]).

5.1.5 Comparison of the effect of high-pressure and low-temperature

A comparison of the changes in the c/a ratio of the rhombohedral compounds as induced by temperature and pressure is provided in figure 5.12 and given as a function of the formula volume in the plot. Obviously, both heating and compressing of

the samples causes a decrease of the the c/a ratio and thus, the distortion of the unit cell with respect to the cubic FCC cell ($c/a=2.4495$) is lowered till it finally disappears when the transition to the cubic phase takes place.

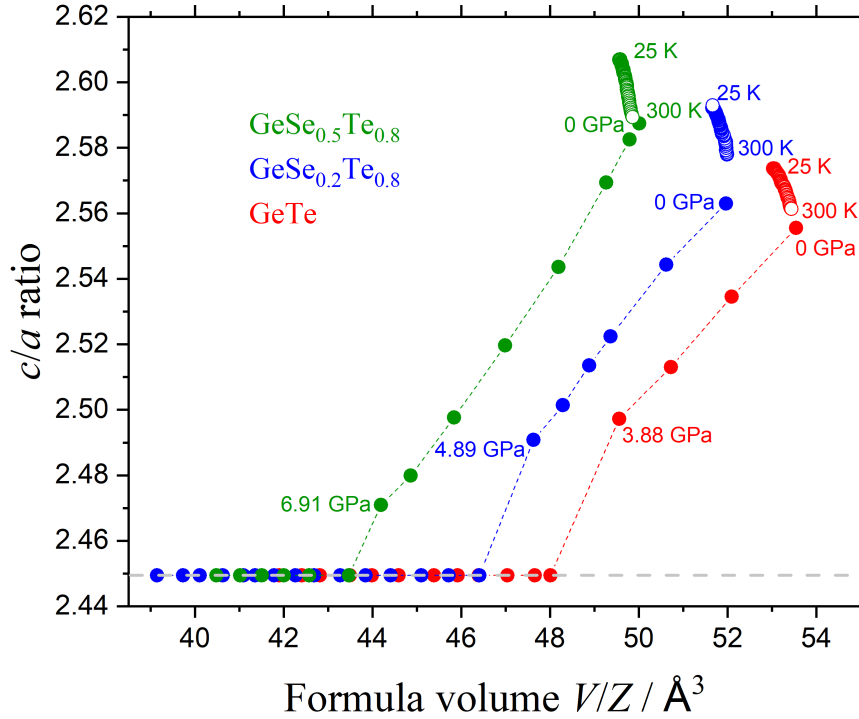


FIGURE 5.12: Comparison between the temperature- and pressure-induced changes of the c/a ratios of the GeTe-I and GeTe-II phases of the compounds GeTe, GeSe_{0.2}Te_{0.8} and GeSe_{0.5}Te_{0.5}.

5.1.6 The GeTe-III polymorph

At 18.8 GPa, GeTe-III crystallizes in the orthorhombic space group $Pnma$ with lattice parameter $a=7.3690(18) \text{\AA}$, $b=3.9249(10) \text{\AA}$ and $c=5.698(9) \text{\AA}$, and an unit cell volume of $V=164.8(3) \text{\AA}^3$ ($Z=4$). Details on the structure refinement and the atomic positions and displacement parameters are summarized in tables 5.4 and 5.5.

Figure 5.13 depicts projections of the GeTe-III structure. The structure is composed of six-membered Ge-Te rings (figure 5.14) which are arranged in the boat conformation and stacked along the $[100]$ direction. Neighboring layers are connected by Ge-Te and Ge-Ge interactions. The coordination of Ge and Te is indicated in figures 5.14 and 5.15 (distances are given in appendix C.4).

Ge is covalently bonded to three Te atoms at distances of $2.684(9) \text{\AA}$ ($1\times$) and $2.756(7) \text{\AA}$ ($2\times$). Two additional Ge-Te ($2.888(7) \text{\AA}$) and two Ge-Ge ($2.971(7) \text{\AA}$) interactions are present at larger distances. The covalent Ge-Te bonds and the two Ge-Te interactions form a pyramidal coordination on one side of Ge, whereas the Ge-Ge contacts are arranged on the opposite side (figure 5.15). In addition, two even longer

Ge··Te interactions at 3.208(10) Å and 3.396(10) Å are present. The results of a detailed bonding analysis on the GeTe-III type structure of GeTe [64] have indicated that the shorter distance at 3.208(10) Å has a significant contribution to the bonding and thus, it is considered to belong to the Ge coordination. In contrast to this, the bonding contribution of the 3.396(10) Å distance is negligibly small and hence, there

TABLE 5.4: Details of the structure refinement on the new GeTe-III structure at 18.8 GPa.

Crystal data	
Chemical formula	GeTe
$M_r / \text{g}\cdot\text{mol}^{-1}$	200.2
Crystal system	orthorhombic
Space group	$Pnma$ (No. 62)
Temperature / K	293
$a, b, c / \text{Å}$	7.3690(18), 3.9249(10), 5.698(9)
$V / \text{Å}^3$	164.8(3)
Z	4
$\rho_{\text{calc}} / \text{g}\cdot\text{cm}^{-3}$	8.0683
Radiation type	Synchrotron
Wavelength / Å	0.2905
Diffractometer	P02.2 at PETRA III, DESY (Hamburg)
μ / mm^{-1}	10.39
$F(000)$	336
No of measured, independent and observed ($I > 3\sigma(I)$) reflections	135, 86, 84
h, k, l min/max	$-1 \leq h \leq 3,$ $-6 \leq k \leq 6,$ $-9 \leq l \leq 8,$
R_{int}	0.040
$(\sin \frac{\Theta}{\lambda})_{\text{max}} / \text{Å}^{-1}$	0.825
$R[F^2 > 2\sigma(F^2)], wR(F^2), S$	0.047, 0.054, 2.39
No. of reflections	86
No. of parameter	13
$\Delta\rho_{\text{max}}, \Delta\rho_{\text{min}} / (\text{e}\ \text{Å}^{-3})$	2.11, -1.60

TABLE 5.5: Ge and Te atomic position and isotropic thermal displacement parameter in the crystal structure of GeTe-III at 18.8 GPa.

Atom	Wyckoff position	x	y	z	$U_{\text{iso}} / \text{Å}^{-2}$
Ge	4c	0.0703(13)	$\frac{1}{4}$	0.8267(4)	0.025(8)
Te	4c	0.1716(5)	$\frac{1}{4}$	0.37428(19)	0.019(3)

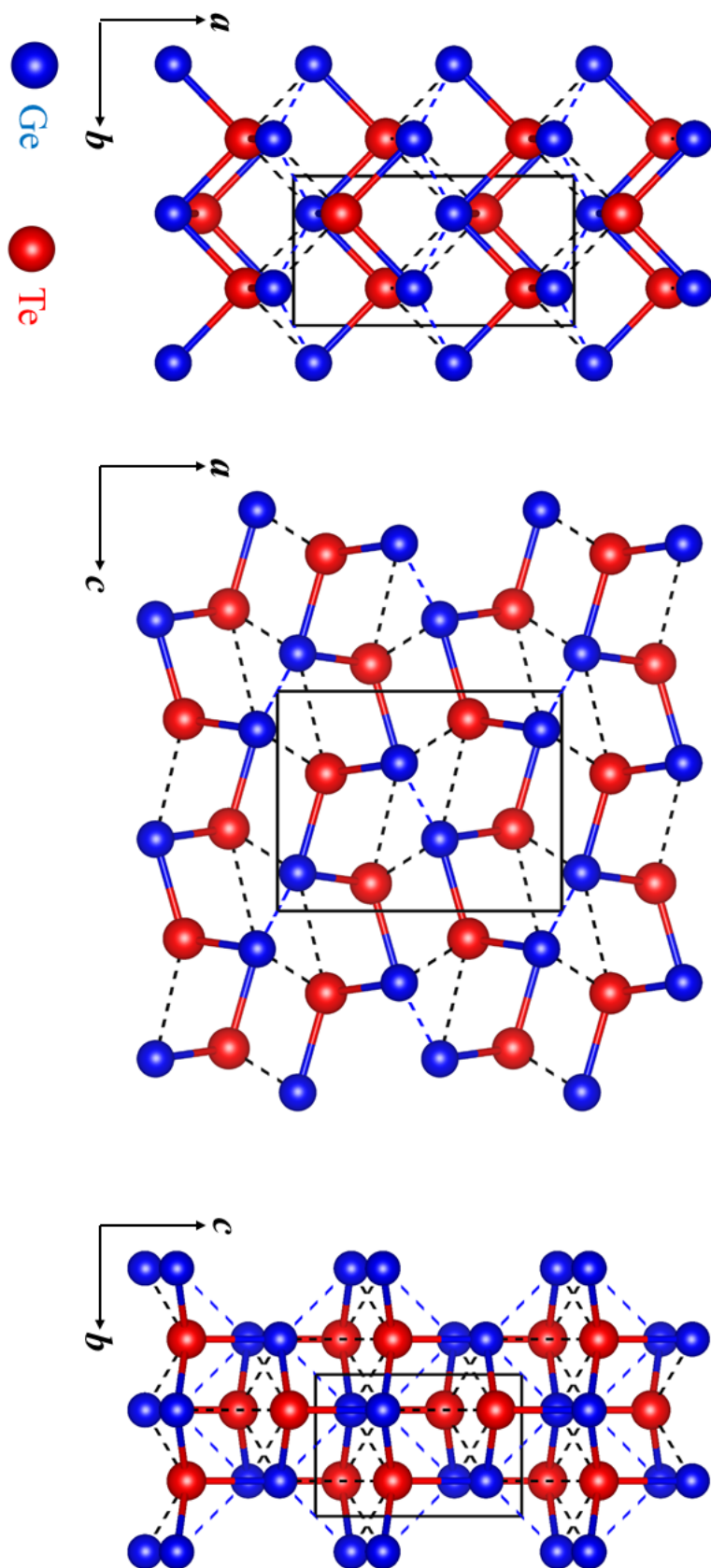
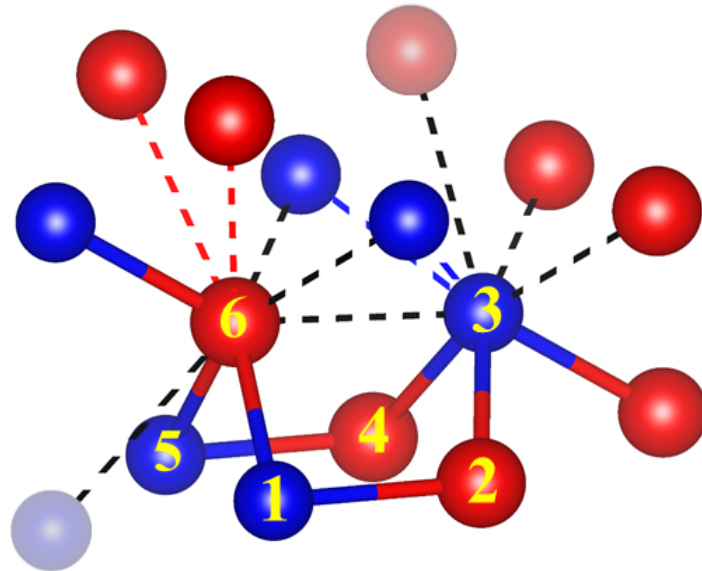


FIGURE 5.13: Projections of the ab , ac and bc plane of the GeTe-III structure.

GeTe-III



β -GeSe

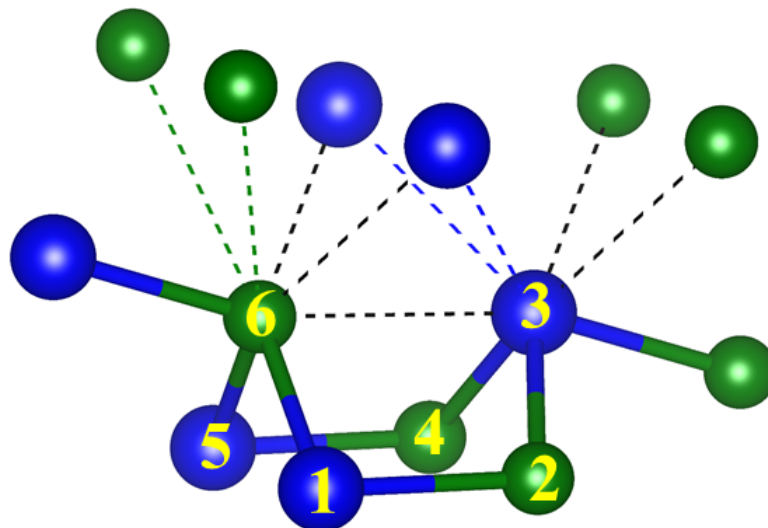


FIGURE 5.14: Six-membered Ge-Te/Se rings in the GeTe-III and β -GeSe structure. The coordination around Ge and Te/Se is included. Light-red/blue atom: 3.396(10) Å distance (contact e/f in appendix C.4).

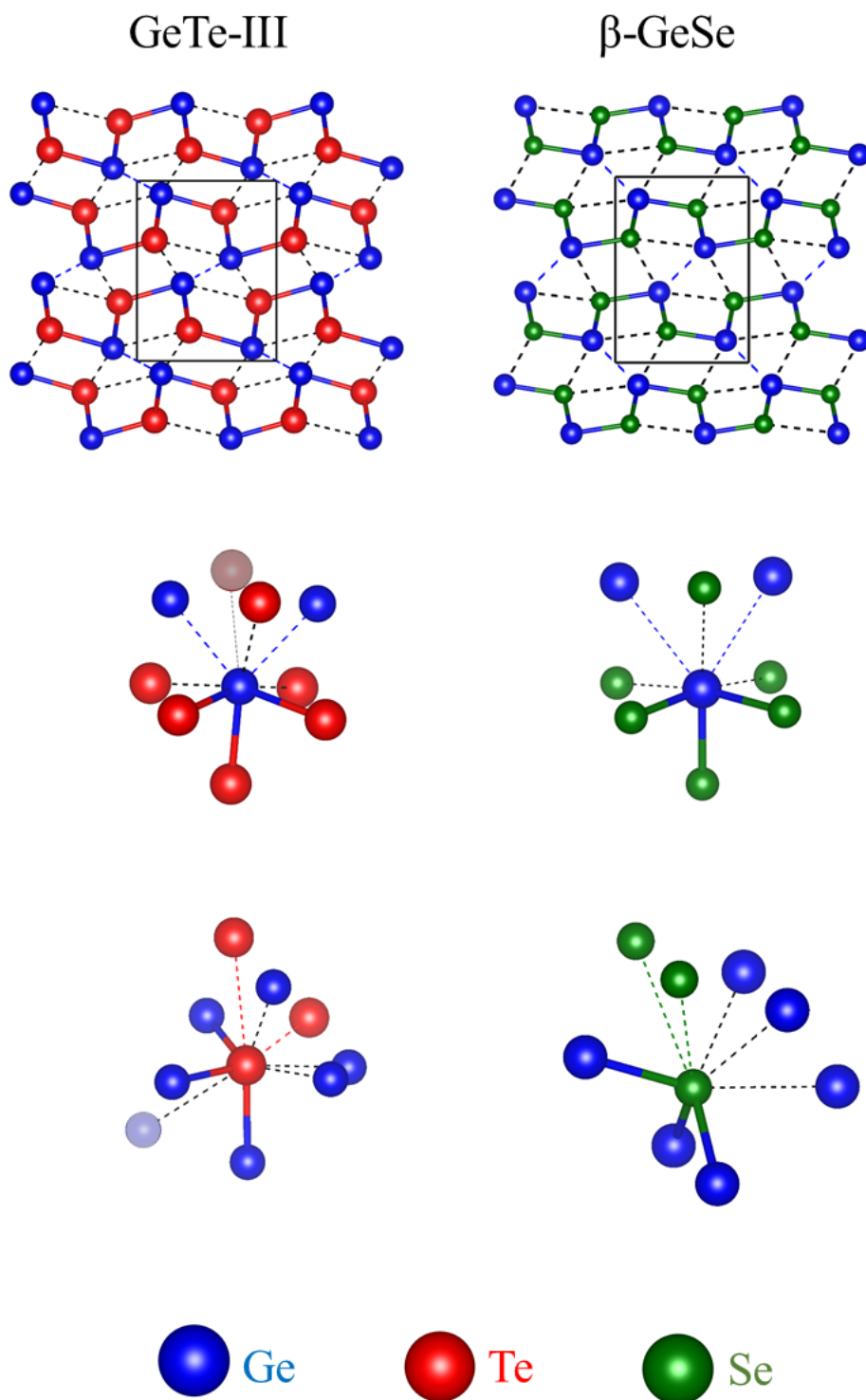


FIGURE 5.15: Top: Comparison between the crystal structures of GeTe-III and β -GeSe [128]. Middle: Ge coordination polyhedra; Bottom: Te/Se coordination polyhedra in both structures. Light-red/blue atom: $3.396(10)$ Å distance (contact e/f in appendix C.4).

is no contribution to the Ge coordination [64]. It is noteworthy that GeTe-III is supposed to undergo a further phase transition into the CsCl structure type at around 38 GPa [112] which is accompanied by a further increase of the coordination number. With elevated pressure all distances will become shorter and thus, the 3.396(10) Å contact probably becomes important at this phase transition.

The Te atoms in GeTe-III also show a [3+3+2] coordination (figures 5.14 and 5.15) which is formed by three covalent Te-Ge bonds, three Te··Ge and two long-ranged Te··Te interactions (bond lengths are summarized in appendix C.4). The above-mentioned 3.396(10) Å Te··Ge interaction (which has no bonding contribution [64]) is shorter than the Te··Te contacts (3.507(4) Å). However, it is noteworthy that the Te··Te contacts in GeTe-III are significantly shorter than the ones in $\text{GeSe}_{0.75}\text{Te}_{0.25}$ (3.802(3) Å) [63] and therefore, we assume that the Te··Te contacts in GeTe-III belong to the Te coordination.

The GeTe-III structure is isostructural to the one of β -GeSe [128] in which the Ge and Se atoms show a very similar [3+3+2] coordination (figure 5.14 and 5.15). A comparison between the Ge- X and Se/Te- X ($X=\text{Ge}, \text{Se}, \text{Te}$) bond lengths is given in appendix C.4. In both compounds Ge··Ge interactions and long-ranged groupVI··groupVI interactions are present.

The powder patterns of the GeTe-III polymorphs can be all indexed (appendix C.3) with the newly determined GeTe-III structure, while the proposed models from the literature [111, 79] do not agree with the observed patterns and even the proposed lattice parameter do not index our powder pattern. This is demonstrated in ap-

TABLE 5.6: Comparison between the peak positions reported previously [79] and the ones calculated based on the new structural model for the GeTe-III polymorph.

Peak position $2\Theta/^\circ$		
[79]	This study	(hkl)
13.909	13.787	(111)
15.219	14.961	(210)
15.280	15.369	(102)
18.691	16.822	(211)
20.923	18.590	(112)

pendix C.3 on the powder pattern of the pure GeTe-III polymorph of $\text{GeSe}_{0.5}\text{Te}_{0.5}$ measured at 18.8 GPa. As the experimental evidence for both structural models [111, 79] is very weak and in addition at least in one of them unrealistically short interatomic distances are present, we assume that both of them have been determined erroneously. From the powder pattern provided in [79] the approximate peak position were extracted between $2\Theta=10-22^\circ$ (table 5.6) and compared to the ones calculated from our newly determined GeTe-III structure. Although the powder pattern from the literature shows fairly broad peaks and the pattern was measured at a different pressure (23 GPa), an indexing with the new structural model is possible (table 5.6). Le Bail refinements on the powder patterns of the GeTe-III phase of the compounds

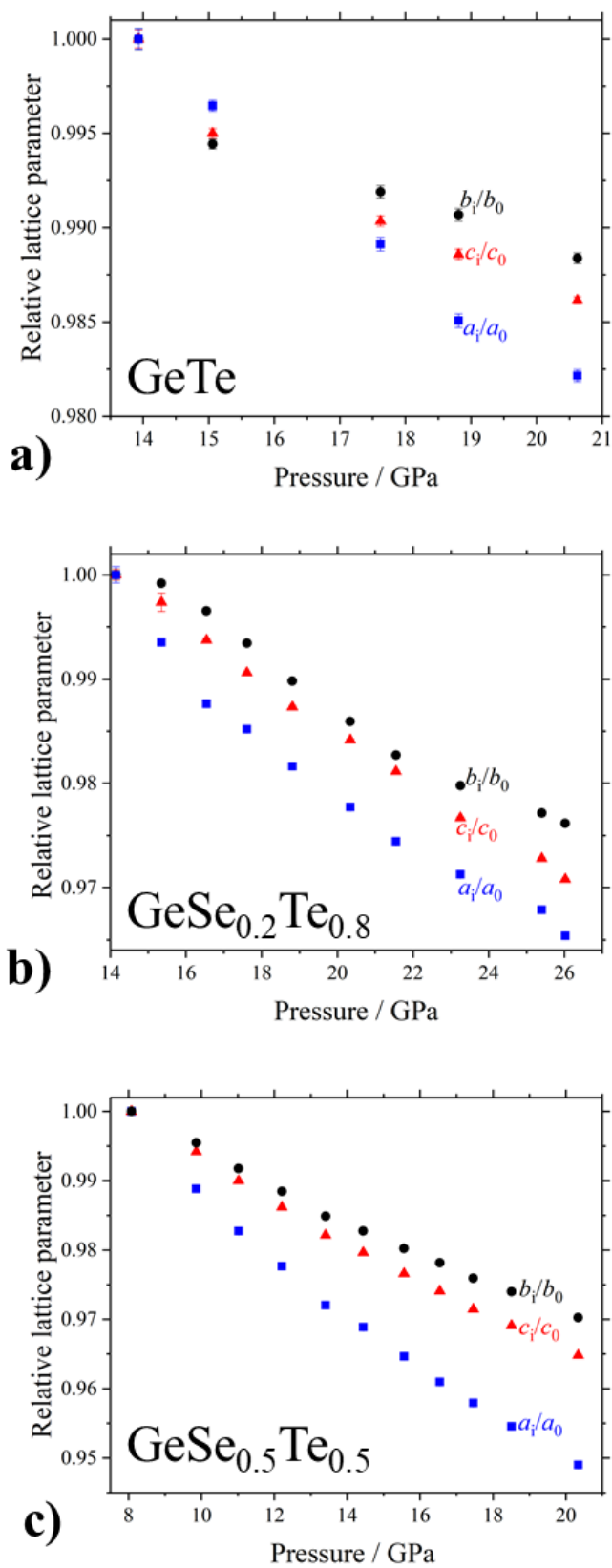


FIGURE 5.16: Pressure dependence of the relative lattice parameter of the GeTe-III phase of a) GeTe, b) GeSe_{0.2}Te_{0.8}, c) GeSe_{0.5}Te_{0.5}.

GeTe , $\text{GeSe}_{0.2}\text{Te}_{0.8}$ and $\text{GeSe}_{0.2}\text{Te}_{0.8}$ have been performed using the new GeTe-III structure type as a starting model and yielded the relative lattice parameter a_i/a_0 , b_i/b_0 and c_i/c_0 as shown in figure 5.16. For all compounds, the compressibility along the [100] direction is the largest, whereas the pressure-induced changes along [010] and [001] are comparable. Along [100] the layers of the six-membered Ge-Te rings are stacked and thus, the large compressibility in this direction is mainly due to compression between neighboring layers. The compressibility along the [100] direction increases with increasing Selenium contents of the samples. This might be explained by the fact that the replacement of the larger Tellurium by the smaller Selenium reduces the repulsion between neighboring layers and thus, they can be compressed closer together. Along the [010] and [001] direction, respectively, the pressure is applied parallel to the layers and thus, the covalent Ge-Te bonds are compressed. Our results suggest that along the [010] and [001] direction the network of covalent bonds is affected by the pressure in a similar way.

5.1.7 High-pressure phase diagram

The derived pressure-composition phase diagram is shown in figure 5.17. While the hexagonal phase of $\text{GeSe}_{0.75}\text{Te}_{0.25}$ is stable up to at least 23 GPa, all compounds from the stability field of the GeTe-I structure type follow the pressure-transition pathway:

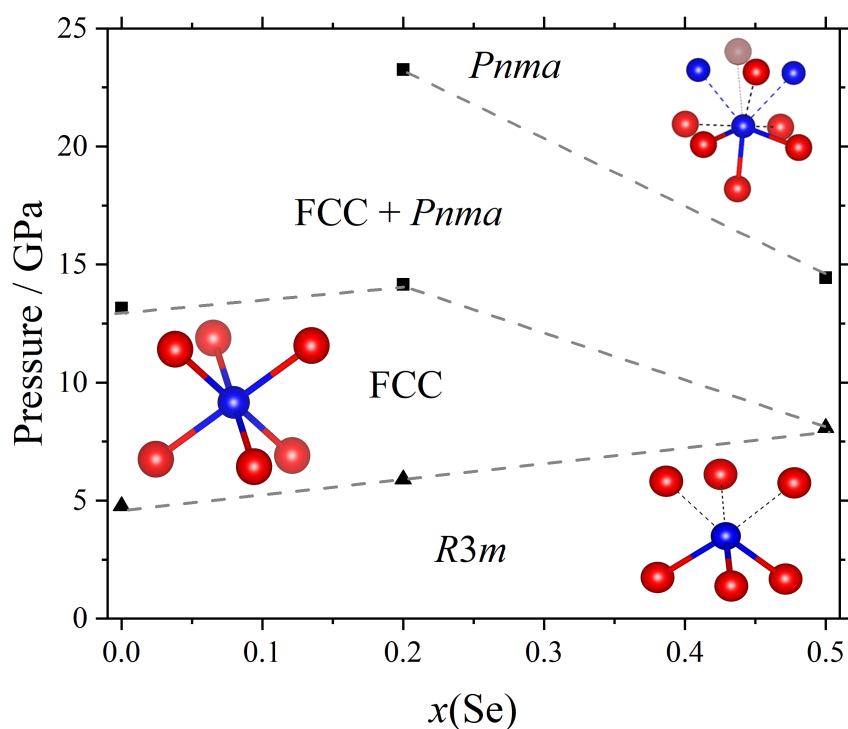


FIGURE 5.17: The pressure-composition phase diagram of the $\text{GeSe}_x\text{Te}_{1-x}$ solid solution. Insets: Ge coordination.

For the $R3m \rightarrow \text{FCC}$ transition, the transition pressure increases with increasing Se content of the samples and the transition is accompanied by a pronounced change of the lattice parameter indicating a first order character. The transition pressure to the one-phase region of the $Pnma$ phase is lowered with increasing Se content and also this transition seems to be of first order.

5.2 Lattice dynamics of the $\text{Sb}_2\text{Te}_{3-x}\text{Se}_x$ solid solution

5.2.1 Introduction

5.2.1.1 The $\text{Sb}_2\text{Te}_{3-x}\text{Se}_x$ solid solution: state of the art

Sb_2Se_3 crystallizes in the orthorhombic space group $Pnma$ with lattice parameter of $a=11.7938(9)$ Å, $b=3.9858(6)$ Å and $c=11.6478(7)$ Å (unit cell volume $V=547.54(10)$ Å³) at room temperature (figure 5.18) [134]. In the crystal structure of Sb_2Se_3 , all atoms

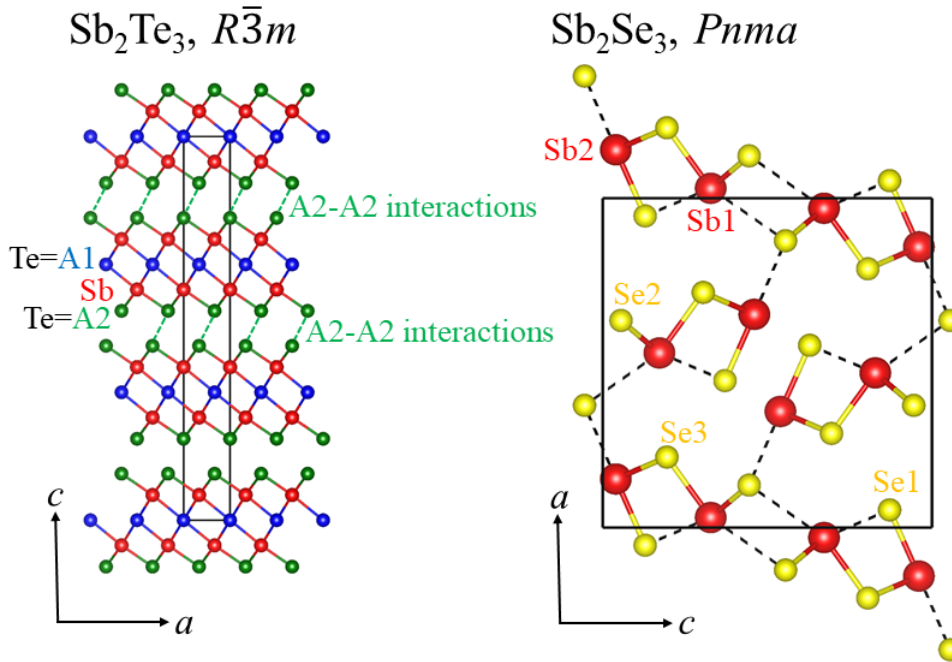


FIGURE 5.18: Projections of the crystal structure of Sb_2Te_3 (left) and Sb_2Se_3 (right). Intra- and inter-chain interactions in the Sb_2Se_3 structure are marked by dashed lines.

occupy Wyckoff position $4c$ ($x, \frac{1}{4}, z$; site symmetry m). Two symmetrically independent Sb and three symmetrically independent Se positions exist. The crystal structure is formed by infinite -Se-Sb-Se- chains which are arranged along the $[010]$ direction. Deringer *et al.* [19] have studied the bonding properties of Sb_2Se_3 by first-principles calculations and found that the chains are covalently bonded. In addition, they found several kinds of weaker intra- and inter-chain interactions.

$\alpha\text{-Sb}_2\text{Te}_3$ crystallizes in the rhombohedral space group $R\bar{3}m$ (tetradymite structure type) with lattice parameter of $a=4.2674(4)$ Å and $c=30.450(3)$ Å and a unit cell volume of $V=480.23(9)$ Å³ at 298 K (figure 5.18) [97, 135]. The crystal structure is formed by repeated $\cdot\cdot\text{A2-Sb-A1-Sb-A2}\cdot\cdot$ quintuple layers, where A1 (WP $3a$; $0, 0, 0$; site symmetry $\bar{3}m$) and A2 (WP $6c$; $0, 0, 0.7878(1)$; site symmetry $3m$) represent two symmetrically independent Wyckoff positions between which the Sb atoms (WP $6c$; $0, 0, 0.3986(1)$; site symmetry $3m$) are located [97]. In $\alpha\text{-Sb}_2\text{Te}_3$, the A1 and A2 site are completely filled by Tellurium. Between neighboring layers A2 $\cdot\cdot$ A2 interactions are present [97]. In the $\alpha\text{-Sb}_2\text{Te}_3$ structure, Sb is coordinated by three A1 and three A2

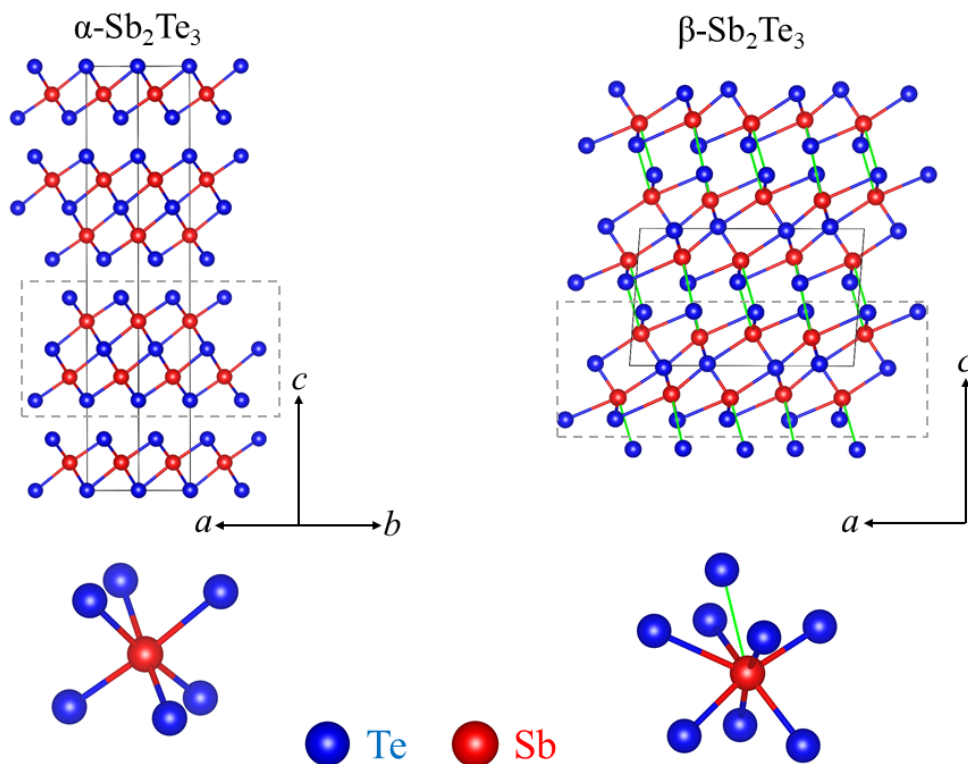


FIGURE 5.19: Projections of the crystal structure of α - Sb_2Te_3 (left) [97] and β - Sb_2Te_3 (right) [77]. The quintuple Sb_2Te_3 layers are marked by gray dashed boxes in both structures. In the structure of β - Sb_2Te_3 there are additional Sb-Te bonds, where the ones between neighboring layers are marked by green lines. The Sb coordination in both structures is shown at the bottom.

atoms resulting in a distorted octahedral coordination. While the Tellurium atoms in the A1 site show an ideal octahedral coordination formed by six Sb-A1 bonds, the A2 atoms are surrounded by three Sb-A2 bonds and three A2··A2 interactions resulting in a distorted octahedral coordination.

A metavalent bonding scheme was suggested for α - Sb_2Te_3 [11, 17], whereas Sb_2Se_3 is predominately covalently bonded [19]. Lee *et al.* [17] postulated that the metavalent bonding in the tetradyomite structure type has to be limited to the layers as it cannot be mediated by the A2··A2 interactions.

Ma *et al.* [77] have studied the high-pressure behavior of a polycrystalline Sb_2Te_3 sample up to about 52.7 GPa and reported the following structural transition pathway:



For β - Sb_2Te_3 , they reported lattice parameter of $a=14.449(1)\text{ \AA}$, $b=4.063(2)\text{ \AA}$, $c=17.519(7)\text{ \AA}$ and $\beta=149.64(5)^\circ$ at 11.4 GPa with an unusual large monoclinic angle. These lattice parameter can be transformed to a more standard monoclinic setting ($a=14.449(1)\text{ \AA}$,

$b=4.063(2)$ Å, $c=8.8798(7)$ Å, $\beta=94.31(5)^\circ$; see appendix A for the transformation matrix). Figure 5.19 compares projections of the crystal structures of α - and the transformed structure of β - Sb_2Te_3 . Also the crystal structure of monoclinic β - Sb_2Te_3 is formed by repeated $\cdot\cdot\text{Te}_2\text{-Sb-Te}_1\text{-Sb-Te}_2\cdot\cdot$ quintuple layers, however, in contrast to α - Sb_2Te_3 , the layers are significantly distorted which causes additional covalent Sb-Te bonds (one per Sb atom) and an increase of the Sb coordination number from 6 to 7. Moreover, in β - Sb_2Te_3 there are additional Sb-Te bonds (one per Sb atom) which connect neighboring layers to each other and cause a further increase of the Sb coordination number from 7 to 8.

The temperature-composition phase diagram of the $\text{Sb}_2\text{Te}_{3-x}\text{Se}_x$ solid solution at ambient pressure was studied previously between about 573 K and 1173 K (figure 5.20) [73] and it was found that mixed crystals with Selenium contents between

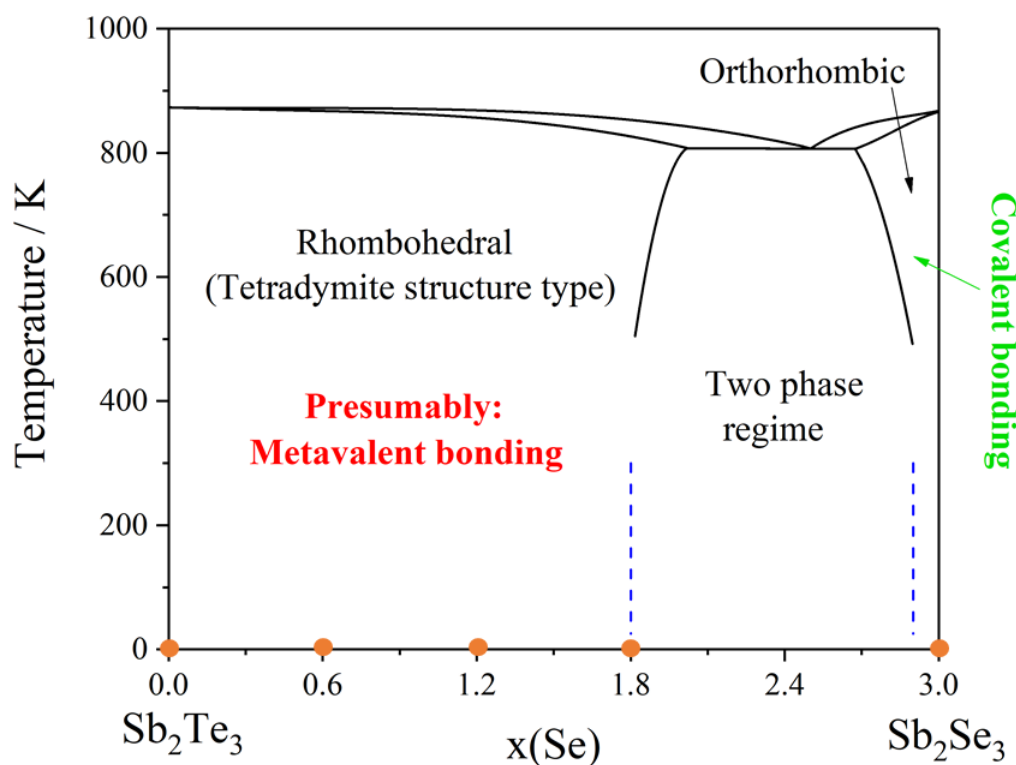


FIGURE 5.20: Temperature-composition phase diagram of the $\text{Sb}_2\text{Te}_{3-x}\text{Se}_x$ solid solution. High-temperature data (black lines) have been adapted from [73]. Low-temperature data (dashed lines) were taken from [107] (see details in appendix D.4). Compositions studied in this thesis are marked by orange dots.

$0 \leq x(\text{Se}) \leq 1.8$ are isostructural to Sb_2Te_3 . For compounds with Selenium contents between about $1.8 \leq x(\text{Se}) \leq 2.95$ a two-phase regime was observed. Selenium-rich mixed crystals with $2.95 \leq x(\text{Se}) \leq 3$ crystallize in the Sb_2Se_3 structure type. The low-temperature behavior of several $\text{Sb}_2\text{Te}_{3-x}\text{Se}_x$ mixed crystals ($x=0, 0.6, 1.2, 1.8, 3$) was studied previously ([63], [107] and appendix D.4) between 25-300 K by powder

diffraction and no evidences for structural phase transitions were observed indicating that all phases are stable in this temperature range. Previously, it was demonstrated that $\text{Sb}_2\text{Te}_{3-x}\text{Se}_x$ mixed crystals from the stability field of the tetradymite structure type are hopeful candidates for applications in non-volatile data storage e. g. [68, 136] and thus, these compounds are presumably metavalently bonded, however, a confirmation of this hypothesis is missing.

The lattice parameter of several $\text{Sb}_2\text{Te}_{3-x}\text{Se}_x$ mixed crystals were determined from powder diffraction measurements [137, 66] and a significant deviation from Vegard's rule was observed [137]. Molodkin *et al.* [137] concluded that this deviation is caused by a preferred incorporation of Selenium into the A1 site of the tetradymite structure type as suggested also by Anderson and Krause [135]. The electrical [138] and thermal [137] conductivity of several $\text{Sb}_2\text{Te}_{3-x}\text{Se}_x$ mixed crystal were measured and a significant increase of both physical properties was observed for compositions around $\text{Sb}_2\text{Te}_2\text{Se}$. Again, the observed anomaly was ascribed to the preferred Se incorporation into the A1 site of the Sb_2Te_3 structure.

Recently, Küpers *et al.* [139] have synthesized a series of $\text{Sb}_2\text{Te}_{3-x}\text{Se}_x$ ($x=0-1.6$) single crystals and performed a detailed single crystal analysis which confirmed the preferred Se incorporation into the A1 site of the Sb_2Te_3 structure. For mixed crystals with $0 \leq x(\text{Se}) \leq 1$, Se (nearly) exclusively occupies the A1 site and surprisingly as a consequence the A2··A2 distance increases with increasing Se content. Once the A1 site is completely filled by Se, further Se starts to occupy the A2 site ($x(\text{Se}) > 1$). This leads to a decrease in the A2··A2 distance. If the experimentally determined A2··A2 bond lengths, $d_{\text{A2-A2}}$, are normalized to the value of an ideal A2··A2 van der Waals interaction (Sb_2Te_3 : $d_{\text{vdW}}=4.12 \text{ \AA}$) a value of $d_{\text{A2-A2}}/d_{\text{vdW}} \approx 0.9$ is found for Sb_2Te_3 and thus, the A2··A2 bond length is shorter than the distance of an ideal Te2··Te2 van der Waals interaction. This was attributed to attractive electrostatic effects of the Sb-A1 bonds inside the layers which lead to an increase of the polarity of this bonding and reduce the bond length of the A2··A2 interactions at cost of the van der Waals character. Similar analysis on several $\text{Sb}_2\text{Te}_{3-x}\text{Se}_x$ ($x=0-1.6$) mixed crystals showed that the $d_{\text{A2-A2}}/d_{\text{vdW}}$ ratio increases linearly from about 0.9 (Sb_2Te_3) to about 0.92 ($\text{Sb}_2\text{Se}_{1.6}\text{Te}_{1.4}$) with increasing Selenium contents, indicating an increase of the van der Waals character of the A2··A2 interactions.

5.2.1.2 Lattice dynamics of $\text{Sb}_2\text{Te}_3\text{-Se}_x$ compounds

The lattice dynamics of Sb_2Te_3 was studied previously by inelastic neutron and nuclear inelastic scattering [14, 12]. While the former analysis gave access to the total phonon density of state [12], from the later experiments, the ^{121}Sb and ^{125}Te partial phonon density of states were determined [14] (figure 5.21). Based on group-theoretical analysis and first-principles calculations, the symmetries and Γ -point mode energies of the Raman- (g -modes) and IR-active (u -modes) phonon modes of Sb_2Te_3 have been determined [140] and the theoretically predicted mode energies are compared to the phonon spectra of the compound (figure 5.21). In total,

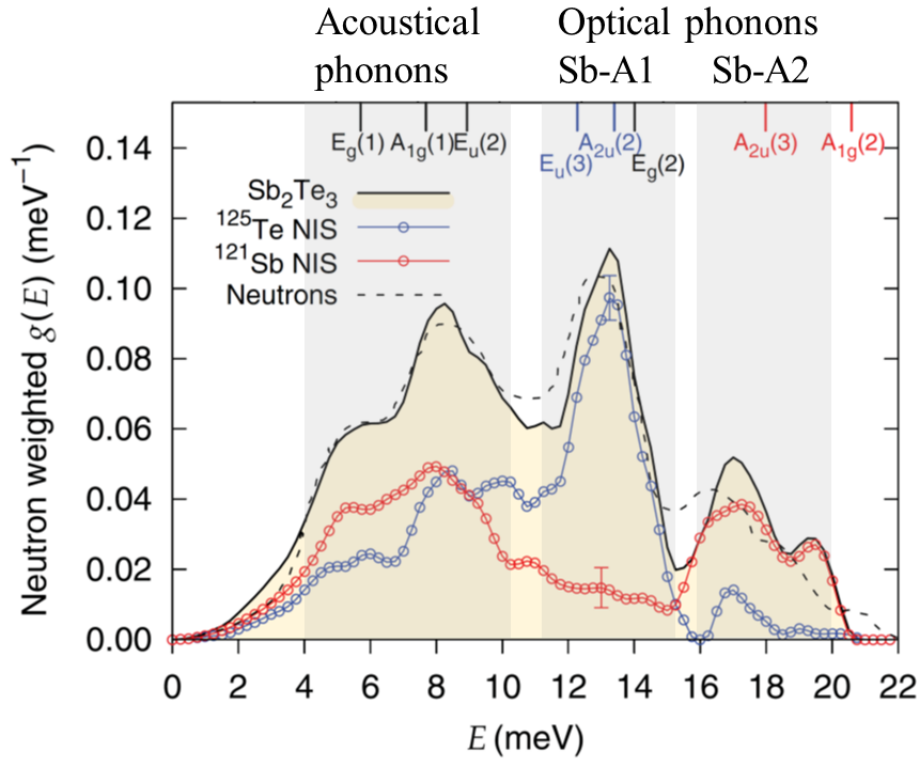


FIGURE 5.21: ^{121}Sb and ^{125}Te partial phonon density of states of Sb_2Te_3 adapted from [14]. For comparison, the total phonon density of state (denoted as "neutrons") reported by Rauh *et al.* [12] is shown. Symmetries and calculated Γ -point mode energies were taken from Sosso *et al.* [140] and are labeled by tics.

Sb_2Te_3 exhibits eight vibrational modes, where the A -modes describe vibrations along the c -axis and the E -modes are correlated with vibrations in the ab -plane of the tetradymite structure [140]. The modes $E_g(1)$, $A_{1g}(1)$ and $E_u(2)$ correspond to acoustical phonon branches, whereas the other modes are optical ones. The modes $A_{2u}(3)$ and $A_{1g}(2)$ both originate from vibrations of the Sb-A2 bonds. According to figure 5.21, these modes are dominated by vibrations of the Sb atoms [14, 12]. Obviously, in the energy range in which the modes $E_u(3)$, $A_{2u}(2)$ and $E_g(2)$ occur, the phonon density of states of Sb_2Te_3 is dominated by the Te. The mode $E_g(2)$ corresponds to an intra-plane vibration of the Sb-A2 bond. $E_u(3)$ and $A_{2u}(2)$ are both pure Tellurium modes which are caused exclusively by simultaneous vibrations of the atoms in the A1 and A2 site of the tetradymite structure [140]. The element-specific Debye temperatures were determined as 157(5) K and 135(5) K for ^{125}Te and ^{121}Sb , respectively [14]. An analysis of the temperature-dependent Raman shifts of the modes $A_{1g}(1)$, $E_g(2)$ and $A_{1g}(2)$ of a metallic and a semiconducting polycrystalline Sb_2Te_3 sample was performed and a softening of all phonon branches with increasing temperature was reported [141].

The vibrational properties of Sb_2Se_3 were analysed by DFT calculations and the total phonon density of states was determined [19]. In addition, the site-specific phonon

density of states for both Sb (Sb1, Sb2) and three Se (Se1, Se2, Se3) positions was reported and a detailed interpretation of the calculated phonon spectra was provided. The effect of high pressure on the Raman-active modes of Sb_2Se_3 was also studied previously [78, 142].

A low-temperature heat capacity measurement on Sb_2Te_3 led to a macroscopic Debye temperature of 179(5) K [14] which differs significantly from the earlier determined value (165 K) [143]. Both, a Schottky anomaly [14] and an additional electronic contribution [143] at low temperatures was suggested for Sb_2Te_3 . Both authors reported a significant improvement of their fits after adding the low-temperature contribution. Moreover, a strong anharmonicity above about 100 K was reported in [14] which was not observed in other studies [143]. This anharmonic behavior was explained by either additional electronic degrees of freedom or self-doping [14].

A low-temperature heat capacity measurement on Sb_2Se_3 between 53-300 K was performed previously [144]. The elastic parameters of Sb_2Se_3 were analysed by first-principles calculations using two different theoretical models and Debye temperatures of 292.50 K (LDA-VASP) and 262.78 K (LDA-SIESTA) were predicted [145]. Temperature-dependent heat capacity data of Sb_2Se_3 ($\Theta_D=162$ K) were derived from the calculated total phonon density of states of this compound. For these calculations the theoretical approach described in [19, 146] was used.

The low-temperature heat capacity of $\text{Sb}_2\text{Se}_{0.2}\text{Te}_{2.8}$, $\text{Sb}_2\text{Se}_{0.6}\text{Te}_{2.4}$ and Sb_2SeTe_2 were investigated between 4-300 K and Debye temperatures of 172 K, 174 K and 177 K, respectively, were reported [147]. For each sample and in agreement with the results of [14], a strong anharmonicity above about 150 K resulting in a significant deviation from the Petit-Dulong law was found. By using the model suggested in [143] for Sb_2Te_3 , the heat capacity data of the mixed crystals were fitted with an electronic and a Debye contribution [147]. However, the reported c_p/T^3 vs. T plots do not support the hypothesis of an additional electronic contribution to the low-temperature heat capacity of these compounds. The temperature dependence of the mode energy of the acoustical $A_{1g}(1)$ mode of $\text{Sb}_2\text{Se}_{0.2}\text{Te}_{2.8}$, $\text{Sb}_2\text{Se}_{0.6}\text{Te}_{2.4}$ and Sb_2SeTe_2 was investigated [147] and a softening of this mode with elevated temperature for each compound was observed. In addition, the temperature dependence of the heat capacity of several $\text{Sb}_2\text{Te}_{3-x}\text{Se}_x$ ($x=0, 0.6, 1.2, 1.8, 3$) mixed crystals was studied from first-principles calculations [146]. Several $\text{Sb}_2\text{Te}_{3-x}\text{Se}_x$ mixed crystals were studied by Mössbauer spectroscopy and an increase of the bonding polarity with increasing Se content was found [148].

5.2.1.3 Aims of this study

The general aim of this study is to understand the influence of the preferred Se incorporation on the lattice dynamics and the bonding properties, especially with respect to the postulated metavalent bonding, of the tetradymite structure type. Moreover, up to now, the vibrational properties of Sb_2Se_3 have been studied mostly by first-principles calculations and an experimental confirmation of the predicted phonon

spectra and heat capacity data is missing and will be provided here. This will allow an evaluation of the theoretical data reported previously [19, 146, 145].

Five $Sb_2Te_{3-x}Se_x$ ($x=0, 0.6, 1.2, 1.8, 3$) mixed crystals have been selected, where the samples $Sb_2Se_{0.6}Te_{2.4}$, $Sb_2Se_{1.2}Te_{1.8}$ and $Sb_2Se_{1.8}Te_{1.2}$ are isostructural to Sb_2Te_3 . As the lattice dynamics of Sb_2Te_3 was studied intensively in the past, the endmember serves as a benchmark. For the sample $Sb_2Se_{0.6}Te_{2.4}$, the A1 site is partially filled with Se, whereas the A2 site is exclusively occupied by Te. In contrast to this, the A1 site of the samples $Sb_2Se_{1.2}Te_{1.8}$ and $Sb_2Se_{1.8}Te_{1.2}$ is completely filled by Se and there is a smaller and larger excess of Se also on the A2 site, respectively.

The phonon density of states in the energy range of the modes $A_{2u}(3)$ and $A_{1g}(2)$ is correlated with vibrations of the Sb-A2 bonding (figure 5.21) and thus, this energy range is expected to reflect composition-induced changes on this bonding. As the elemental contribution of Sb to the total phonon density of states is dominating in this energy range (figure 5.21), an analysis of the ^{121}Sb partial phonon density of states is most promising to obtain information of the Sb-A2 bonding.

For Sb_2Te_3 , the modes $E_u(3)$ and $A_{2u}(2)$ are correlated with vibrations of the atoms in the A1 and A2 site of the tetradymite structure [140] and the elemental contribution of Te to the total phonon density of states is dominating (figure 5.21). Thus, analysis of the ^{125}Te partial phonon density of states of the $Sb_2Te_{3-x}Se_x$ ($x=0, 0.6, 1.2, 1.8$) mixed crystals are expected to provide information on the Sb-A1 bonding. The ^{121}Sb contribution to the total density of states in the energy range of the modes $E_u(3)$, $A_{2u}(2)$ and $E_g(2)$ is considered to reflect the reaction of the Sb atoms to vibrations of the A1 and A2 atoms. Thus, it is expected that composition-induced changes on the A1 (and A2) site also influence the ^{121}Sb partial phonon density of states in this energy range.

In this study, a macroscopic analysis of the vibrational properties is provided from low-temperature heat capacity measurements and temperature-dependent inelastic neutron scattering experiments. Further low-temperature ^{121}Sb and ^{125}Te nuclear inelastic scattering experiments give access to the partial phonon density of states from which atom-specific information on the lattice dynamics are obtained. The Se partial phonon density of states of the $Sb_2Te_{3-x}Se_x$ ($x=0.6, 1.8, 3$) mixed crystals are determined as described in section 4.3.5.

Finally, for a future high-pressure nuclear inelastic scattering experiment, a diffraction experiment up to about 18 GPa on polycrystalline Sb_2Te_3 was performed to determine the transition-pressure and stability fields of the different high-pressure polymorphs of Sb_2Te_3 . As the high-pressure nuclear inelastic scattering experiment using the currently existing setup at the beamline P01 can only be performed under non-hydrostatic conditions [149], also the diffraction experiment was performed under non-hydrostatic conditions.

5.2.2 Sample characterization

For all $\text{Sb}_2\text{Te}_{3-x}\text{Se}_x$ ($x = 0, 0.6, 1.2, 1.8, 3$) samples, powder diffraction data were measured at ambient conditions (figure 5.22). For the isostructural compounds Sb_2Te_3 ,

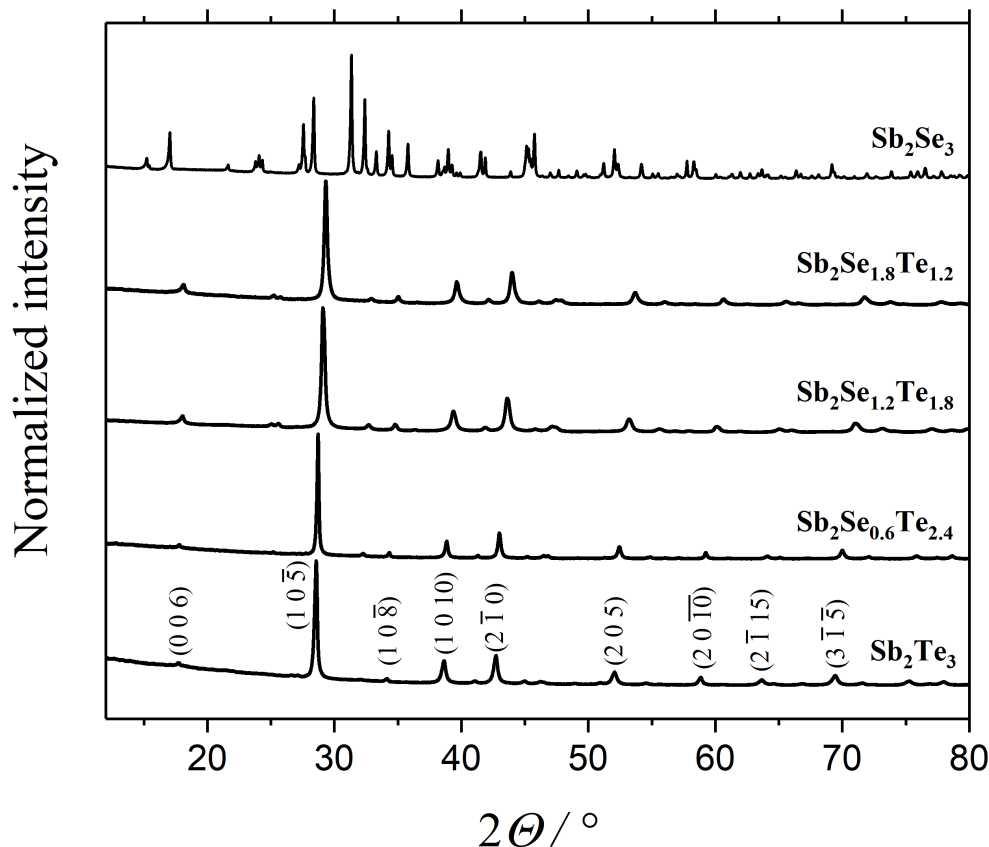


FIGURE 5.22: Powder pattern of the $\text{Sb}_2\text{Te}_{3-x}\text{Se}_x$ ($x = 0, 0.6, 1.2, 1.8, 3$) samples.

$\text{Sb}_2\text{Se}_{0.6}\text{Te}_{2.4}$, $\text{Sb}_2\text{Se}_{1.2}\text{Te}_{1.8}$ and $\text{Sb}_2\text{Se}_{1.8}\text{Te}_{1.2}$, all detected peaks could be indexed with the structural data reported earlier for Sb_2Te_3 [97] and there was no evidence for any impurities (figure 5.22). The powder pattern of Sb_2Se_3 were indexed using the lattice parameter reported in [134] (appendix D.3) and there is also no indication for any impurities.

In figure 5.23, the lattice parameter a and c and the unit cell volumes, V , of the compounds from the stability field of the tetradymite structure type studied in this work are shown in dependence of the Se content, $x(\text{Se})$. While for the compound $\text{Sb}_2\text{Se}_{0.6}\text{Te}_{2.4}$ a deviation from Vegard's law clearly can be seen in all parameters, $\text{Sb}_2\text{Se}_{1.2}\text{Te}_{1.8}$ shows an ideal mixing behavior. Lostak *et al.* [66] found a deviation from Vegard's law in the c lattice parameter of compounds with Se contents up to $x(\text{Se})=0.38$, whereas they reported an ideal mixing behavior for mixed crystals with larger Se contents. Thus, the results from this study and the one from the literature [66] seem to indicate that the non-ideal mixing behavior is limited to compounds with small Se contents. In contrast to this, Molodkin *et al.* [137] reported a non-ideal

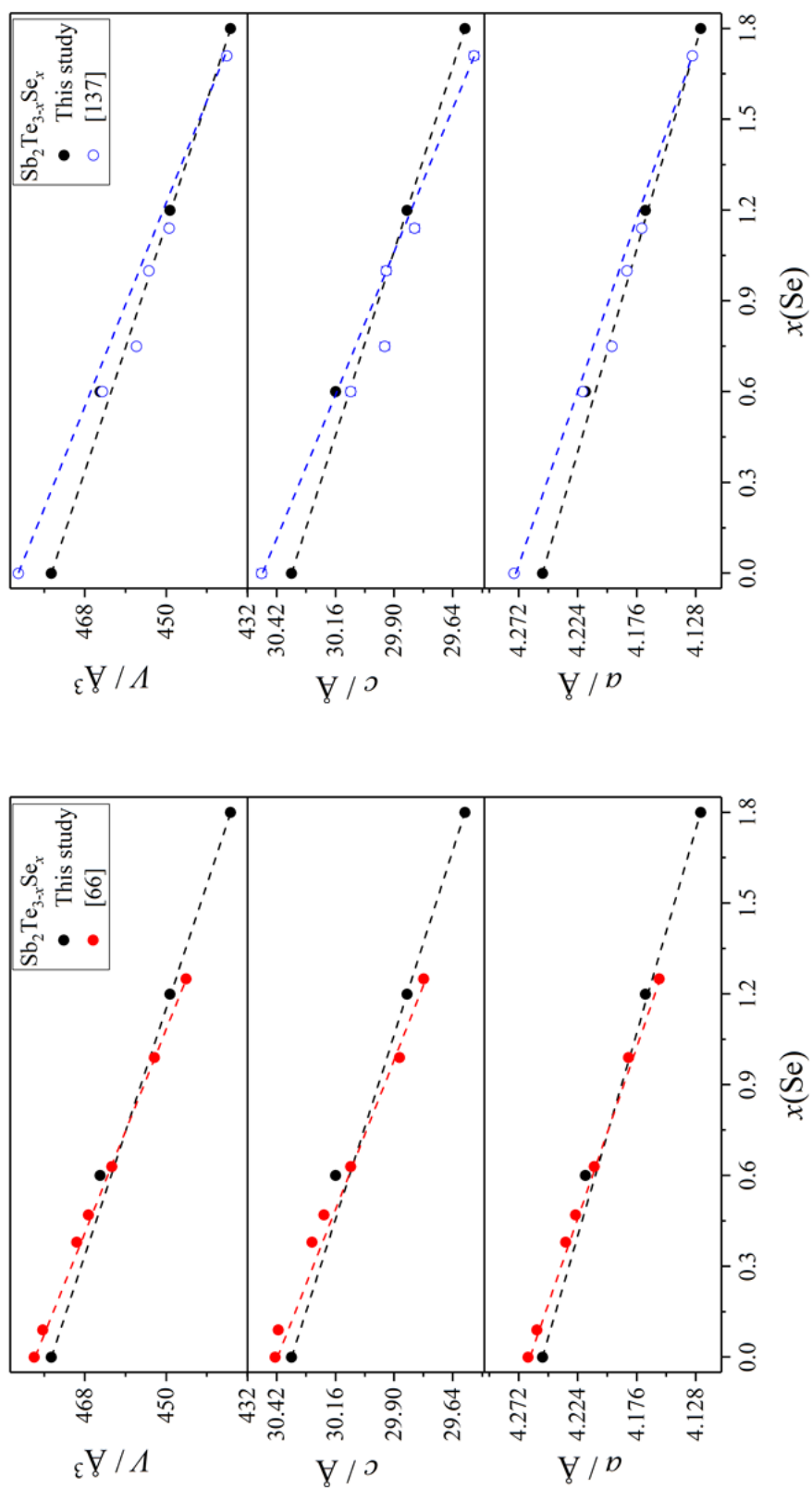


FIGURE 5.23: The lattice parameter a and b and the unit cell volume of the samples with tetradymite structure type in dependence of the Se content. The experimentally determined values are compared to the results of previous studies [66, 137]. Errors are smaller than the symbols.

mixing behavior over the entire compositional range of the tetradymite structure type (exception: a of $x(\text{Se})=0.6$; c of $x(\text{Se})=1$). It is noteworthy that the samples studied here and by Lostak *et al.* [66] were synthesized from stoichiometrically weighted amounts of the elements and at temperatures above the melting points of the starting materials and the products, whereas the samples in [137] were synthesized from stoichiometric mixtures of Sb_2Te_3 and Sb_2Se_3 and at temperatures below the melting points of the reactants. As no chemical analysis of the samples is provided in [137], it is very difficult to evaluate the influence of the route of sample preparation on the properties of the $\text{Sb}_2\text{Te}_{3-x}\text{Se}_x$ mixed crystals.

For the isostructural compounds Sb_2Te_3 , $\text{Sb}_2\text{Se}_{0.6}\text{Te}_{2.4}$ and $\text{Sb}_2\text{Se}_{1.2}\text{Te}_{1.8}$, the experimentally determined c/a ratios are in good agreement with the literature data [97, 66, 134] (table 5.7) and only small deviations are observed which might be due to slight differences in the chemical compositions. The c/a ratios reported in [137] are

TABLE 5.7: The lattice parameter ratios of the $\text{Sb}_2\text{Te}_{3-x}\text{Se}_x$ ($x=0, 0.6, 1.2, 1.8, 3$) samples. For the samples $x=0, 0.6, 1.2, 3$ the ratios determined in this study are compared to the corresponding ones from the literature.

Sample	c/a	a/b	c/b	Reference
Sb_2Te_3	7.138(3)			this study
	7.136(1)			[97]
$\text{Sb}_2\text{Se}_{0.6}\text{Te}_{2.4}$	7.151(3)			this study
	7.147(2)			[66]
$\text{Sb}_2\text{Se}_{1.2}\text{Te}_{1.8}$	7.158(3)			this study
	7.160(3)			[66]
$\text{Sb}_2\text{Se}_{1.8}\text{Te}_{1.2}$	7.174(3)			this study
Sb_2Se_3	0.9872(1)	2.9625(3)	2.9246(3)	this study
	0.9876(1)	2.9590(5)	2.9223(5)	[134]

significantly smaller than the ones found in this study which might be a consequence of the above-mentioned differences in the sample preparation.

For Sb_2Se_3 , lattice parameter of $a=11.7795(8)$ Å, $b=3.9762(3)$ Å and $c=11.6289(7)$ Å and a unit cell volume of $V=544.67(8)$ Å³ were determined (table 5.7). The lattice parameter are in very good agreement with literature data [134].

5.2.3 High-pressure behavior of Sb_2Te_3

In figure 5.24, the result of a high-pressure study on polycrystalline Sb_2Te_3 is shown. α - Sb_2Te_3 is stable up to about 12 GPa, however, above about 10 GPa it coexists with the β -phase. Compared to the literature (8.0 GPa) [77], an increased transition pressure is observed. The pure β - Sb_2Te_3 phase is stable up to at least 18 GPa indicating a higher transition pressure from the β - to the γ -phase when compared to reference (13.2 GPa) [77].

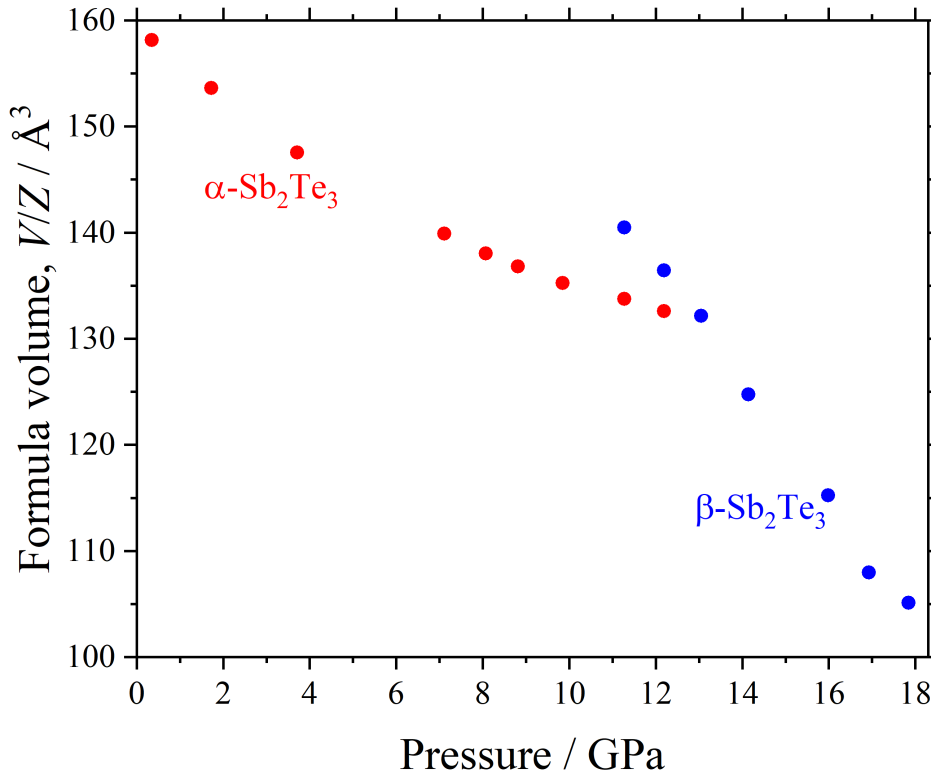


FIGURE 5.24: High-pressure stability fields of α - and β - Sb_2Te_3 between 0-18 GPa.

5.2.4 Low-temperature heat capacity

Low-temperature heat capacity data of the samples Sb_2Te_3 , $Sb_2Se_{0.6}Te_{2.4}$, $Sb_2Se_{1.2}Te_{1.8}$, $Sb_2Se_{1.8}Te_{1.2}$ and Sb_2Se_3 were measured between 2-300 K (figures 5.25; Appendix D.2). The heat capacity data of Sb_2Te_3 reach the Petit-Dulong limit at around 250 K and for temperatures above about 290 K they clearly exceed this value. For the isostructural compounds $Sb_2Se_{0.6}Te_{2.4}$, $Sb_2Se_{1.2}Te_{1.8}$ and $Sb_2Se_{1.8}Te_{1.2}$, the heat capacity data are close to the Petit-Dulong limit for temperatures between 280-300 K. Between 2-300 K the heat capacity data of the Sb_2Se_3 sample are significantly smaller than the Petit-Dulong limit. As mentioned in section 5.2.1.2, the heat capacity of $Sb_2Te_{3-x}Se_x$ ($x=0, 0.6, 1.2, 1.8, 3$) mixed crystals was also calculated from DFT calculations [146]. Our experimental data are in excellent agreement with the results from theory (a comparison is shown in [146]).

In order to determine whether there are significant anharmonic contributions to the low-temperature heat capacity, the experimental data were fitted with the fit functions shown in equations (2.39) and (2.40). While equation (2.39) describes the heat capacity of an assembly of harmonic lattice oscillators, equation (2.40) contains additional anharmonicity coefficients which serve for the correction of anharmonic effects.

For the isostructural compounds Sb_2Te_3 , $Sb_2Se_{0.6}Te_{2.4}$, $Sb_2Se_{1.2}Te_{1.8}$ and $Sb_2Se_{1.8}Te_{1.2}$,

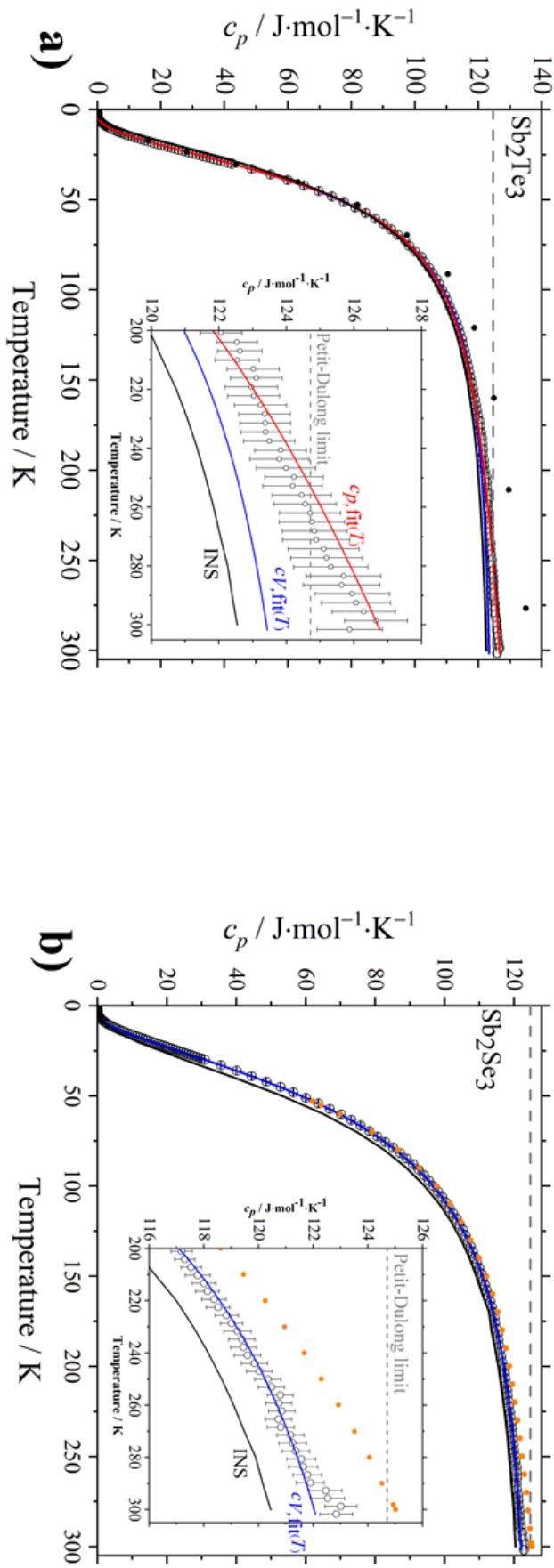


FIGURE 5.25: The low-temperature heat capacity of the samples Sb_2Te_3 and Sb_2Se_3 . The experimental data were fitted with the functions shown in equations (2.39) (blue line) and (2.40) (red line). In addition, the heat capacity derived from the inelastic neutron scattering data (black line) are shown. The data reported in the literature [14, 144] (colored dots) are depicted for comparison.

TABLE 5.8: Fit parameters obtained from the fits using equation (2.40) (for Sb_2Se_3 equation (2.39)) for the heat capacity data of the $Sb_2Te_{3-x}Se_x$ ($x=0, 0.6, 1.2, 1.8, 3$) mixed crystals. In all fits, the parameter c_5 became zero. The goodness of the fits is given by the χ^2 values.

Sample	Sb_2Te_3	$Sb_2Se_{0.6}Te_{2.4}$	$Sb_2Se_{1.2}Te_{1.8}$	$Sb_2Se_{1.8}Te_{1.2}$	Sb_2Se_3
$c_3 / J \cdot mol^{-1} \cdot K^{-1}$	0.00205(14)	0.00183(10)	0.00163(13)	0.00159(10)	0.00175(10)
$c_7 / J \cdot mol^{-1} \cdot K^{-8}$	$1.11(9) \cdot 10^{-6}$	$8.8(6) \cdot 10^{-7}$	$6.8(6) \cdot 10^{-7}$	$8.3(6) \cdot 10^{-7}$	$6.4(6) \cdot 10^{-7}$
b_6	0.13(20)	0.11(15)	0.12(23)	0.39(62)	1.2(19)
b_8	0.004(8)	$3.6(76) \cdot 10^{-4}$	-0.0023(62)	-0.0026(70)	$-5.8(121) \cdot 10^{-4}$
b_{10}	0.0023(60)	0.0017(40)	0.0017(56)	0.012(32)	0.12(33)
b_{12}	$3.9(120) \cdot 10^{-5}$	$2.9(80) \cdot 10^{-5}$	$2.7(100) \cdot 10^{-5}$	$3.0(93) \cdot 10^{-4}$	0.006(21)
b_{14}	$3.9(14) \cdot 10^{-7}$	$2.5(82) \cdot 10^{-7}$	$2.7(53) \cdot 10^{-7}$	$3.1(114) \cdot 10^{-7}$	$5.9(223) \cdot 10^{-5}$
T_0 / K	4.9(12)	4.9(11)	5.0(16)	5.9(16)	7.6(20)
A_1 / K^{-1}	$2.4(4) \cdot 10^{-4}$	$2.0(4) \cdot 10^{-4}$	$2.7(5) \cdot 10^{-4}$	$1.9(4) \cdot 10^{-4}$	
χ^2	3.71	3.11	3.91	4.40	5.11

the fits obtained from equation (2.40) are in excellent agreement with the experimental data and the obtained fit parameter are summarized in table 5.8. For all samples, it was found that a first-order anharmonicity coefficient, A_1 , is sufficient for a reliable fitting of the experimental data and the fits performed with equation (2.40) yielded values between $2\text{-}3\cdot 10^{-1}\text{ K}^{-1}$ for A_1 . The fits using equation (2.39) yielded an underestimation of the experimental data at higher temperatures, indicating that there is an anharmonic contribution to the total heat capacity which becomes significant with elevated temperatures.

For Sb_2Se_3 , fits using equation (2.39) and (2.40) yielded very similar results independent of the number of anharmonicity coefficients included to the fit. This clearly indicates that anharmonic contributions to the total heat capacity of Sb_2Se_3 are negligible small between 2-300 K and thus, the compound is considered to be a harmonic lattice oscillator in the studied temperature range. Therefore, in figure 5.25 and table 5.8 only the results obtained from equation (2.39) are shown.

A comparison of the low-temperature heat capacity of the compounds Sb_2Te_3 and $\text{Sb}_2\text{Se}_{0.6}\text{Te}_{2.4}$ with corresponding data from the literature [14, 147] shows that the heat capacities reported previously are significantly larger than the ones measured in this study, a fact that was attributed in the earlier studies by a strong anharmonicity above about 100 K which results in a pronounced deviation from the Petit-Dulong limit. Although the results obtained from the fits to our experimental data using equation (2.40) indicate a small anharmonic contribution to the total heat capacity of these compounds, the strong deviation from the Petit-Dulong limit as suggested in the literature could not be confirmed. As no detailed description of the investigated samples and the measurement conditions are given in the literature, it is very difficult to find reasons which might explain the discrepancies. The data reported for Sb_2Se_3 [144] are in a good agreement with the ones determined in this study and there is only a small mismatch in the high-temperature range.

A comparison between the heat capacity derived from the inelastic neutron scattering (INS) data (see section 4.3.2.3) with the ones obtained from the PPMS measurements shows that for the isostructural samples Sb_2Te_3 , $\text{Sb}_2\text{Se}_{0.6}\text{Te}_{2.4}$, $\text{Sb}_2\text{Se}_{1.2}\text{Te}_{1.8}$, $\text{Sb}_2\text{Se}_{1.8}\text{Te}_{1.2}$ the calculated heat capacity from INS underestimates the experimental data in the high-temperature range above about 150-200 K (figures 5.25; Appendix D.2). However, it has to be taken into account that from the inelastic neutron scattering data only the isochoric heat capacity were calculated and thus, the thermal expansion of the unit cell and other anharmonic effects are ignored. Therefore, the deviations between the measured and calculated values can be considered as a further hint that for an accurate description of the low-temperature heat capacity data a correction for the thermal expansion and anharmonic effects is mandatory.

For Sb_2Se_3 an underestimation of the experimental data was found even over the entire temperature range. The strong deviation between the calculated and measured heat capacity data of Sb_2Se_3 is surprising as this sample was considered to behave

like a harmonic lattice oscillator in the studied temperature range (see above). However, it is noteworthy that the sample studied in the low-temperature heat capacity measurement was synthesized as described in section 3.1.1.2, whereas the sample investigated by inelastic neutron scattering was a commercially available one which we had to use as it was found to be very challenging to synthesize the required large amounts of Sb_2Se_3 with the route described above. Although, it was confirmed by powder diffraction that both samples were pure phases, property measurements were not performed and thus, it is not evident that both samples have the same amount of charge carriers and defects which would also contribute to the heat capacity.

According to equation (2.38), the Debye temperatures of all samples, $\Theta_{D,PPMS}$, were calculated from the fit parameter c_3 (table 5.8, equations (2.39) and (2.40)). Moreover,

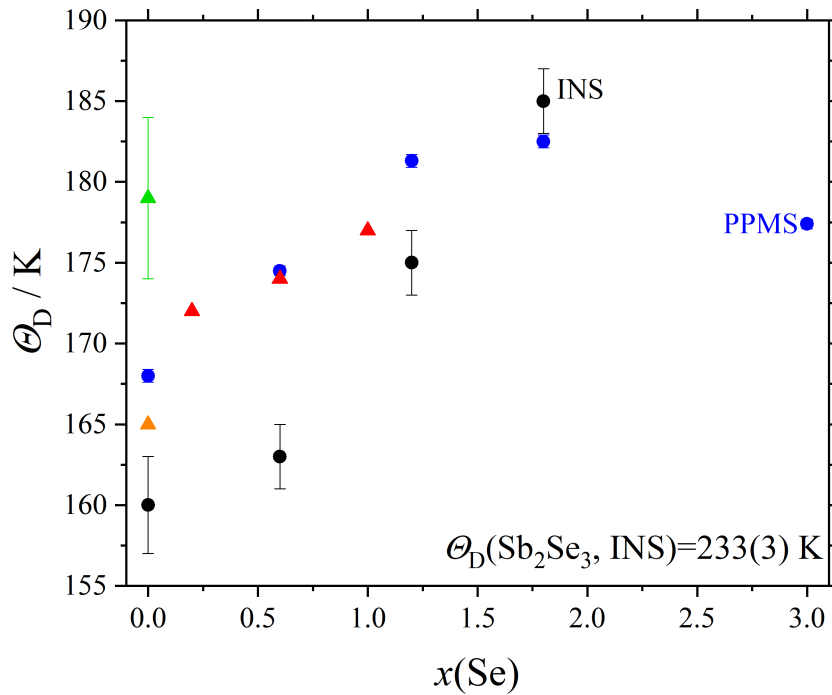


FIGURE 5.26: The Debye temperatures of the $\text{Sb}_2\text{Te}_{3-x}\text{Se}_x$ ($x=0, 0.6, 1.2, 1.8, 3$) mixed crystals as determined from low-temperature heat capacity measurements (blue dots) and as derived from the inelastic neutron scattering data (black dots). The data from the literature are marked by triangles ([14] (green), [143] (orange), [147] (red)).

the heat capacity data calculated from the inelastic neutron data were fitted with the Debye model given in equation (2.36) and the Debye temperatures, $\Theta_{D,INS}$, were also extracted. The values for $\Theta_{D,PPMS}$ and $\Theta_{D,INS}$ can be found in appendix D.1. In figure 5.26, the Debye temperatures, $\Theta_{D,PPMS}$ and $\Theta_{D,INS}$, are shown in dependence of the Selenium content of the samples and compared to the literature data [14, 143, 147]. In general, the Debye temperatures of the isostructural compounds Sb_2Te_3 ,

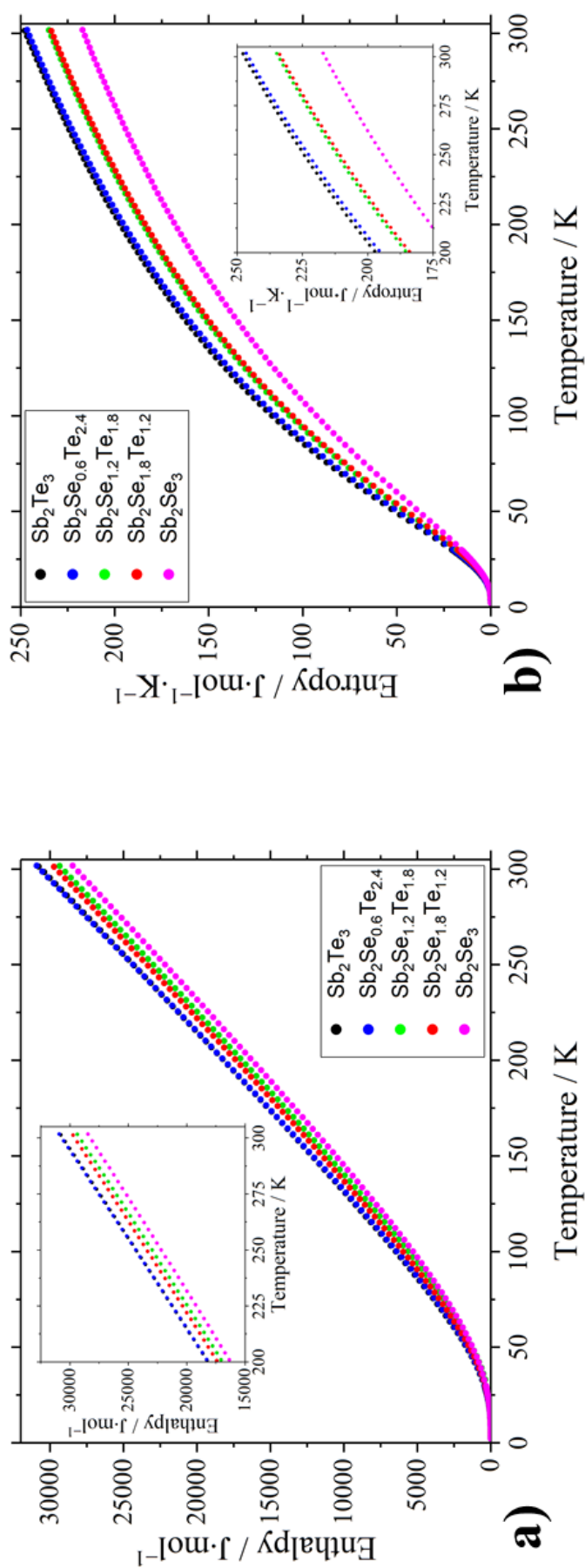
$\text{Sb}_2\text{Se}_{0.6}\text{Te}_{2.4}$, $\text{Sb}_2\text{Se}_{1.2}\text{Te}_{1.8}$ and $\text{Sb}_2\text{Se}_{1.8}\text{Te}_{1.2}$ show an increase with increasing Se content indicating a hardening of the bonding. Results of a Mössbauer spectroscopic study on several $\text{Sb}_2\text{Te}_{3-x}\text{Se}_x$ mixed crystals [148] suggest an increase of the bonding polarity with an elevated Se content and the results obtained in this study seem to support this hypothesis. Also Das *et al.* [147] reported an increase of the Debye temperature with increasing Se contents of the samples (fig. 5.26).

For Sb_2Se_3 , a Debye temperature of 177.1(4) K was found from the low-temperature heat capacity measurement, whereas the inelastic neutron data yielded a Debye temperature of 233(2) K. Again, this deviation might be caused by sample-specific differences (see above). However, both Debye-temperatures are significantly smaller than the ones (292.50 K and 262.78 K) obtained from a theoretical analysis of the elastic parameter [145]. This indicates that the applied theoretical models [145] are not suitable for an accurate prediction of the Debye temperature of this compound. In contrast to this, the Debye temperature (162 K) calculated from DFT calculations in [146] is in much better agreement with the one derived from the PPMS measurement. Thus, the theoretical approach introduced in [19, 146] is more suitable for an accurate prediction of the vibrational properties of Sb_2Se_3 than the ones reported by [145].

In figures 5.27a) and b), the enthalpy and entropy of the $\text{Sb}_2\text{Te}_{3-x}\text{Se}_x$ ($x=0, 0.6, 1.2, 1.8, 3$) mixed crystals calculated from the low-temperature heat capacity data (PPMS) with equations (2.35a) and (2.35b) are shown in the temperature range between 2-300 K. Sb_2Te_3 exhibits the largest enthalpy and entropy values of all compounds. $\text{Sb}_2\text{Se}_{0.6}\text{Te}_{2.4}$ shows only slightly smaller enthalpy and entropy values compared to the ones of Sb_2Te_3 . Enthalpy and entropy of the samples $\text{Sb}_2\text{Se}_{1.2}\text{Te}_{1.8}$ and $\text{Sb}_2\text{Se}_{1.8}\text{Te}_{1.2}$ show a very similar temperature-dependence. Sb_2Se_3 yielded the smallest enthalpy and entropy of all studied compounds.

In order to gain more detailed information on the mixing behavior in the stability field of the tetradymite structure type, the excess heat capacity of the samples $\text{Sb}_2\text{Se}_{0.6}\text{Te}_{2.4}$ and $\text{Sb}_2\text{Se}_{1.2}\text{Te}_{1.8}$ were determined (figures 5.28). For this, the compounds Sb_2Te_3 and $\text{Sb}_2\text{Se}_{1.8}\text{Te}_{1.2}$ have been considered as endmembers. By using the heat capacity data of these compounds, the heat capacity of $\text{Sb}_2\text{Se}_{0.6}\text{Te}_{2.4}$ and $\text{Sb}_2\text{Se}_{1.2}\text{Te}_{1.8}$ were calculated under the assumption of an ideal mixing behavior using the Kopp-Neuman rule (equation (2.41)). The excess heat capacity of $\text{Sb}_2\text{Se}_{0.6}\text{Te}_{2.4}$ and $\text{Sb}_2\text{Se}_{1.2}\text{Te}_{1.8}$ were determined by subtracting the calculated ideal data from the measured ones.

The temperature-dependence of the excess heat capacity of $\text{Sb}_2\text{Se}_{0.6}\text{Te}_{2.4}$ and $\text{Sb}_2\text{Se}_{1.2}\text{Te}_{1.8}$, respectively, is shown in figure 5.28a). Both compounds show a significant non-ideal mixing behavior which is probably due to the preferred Se incorporation into the A1 site of the tetradymite structure type. At temperatures below about 25 K, both compounds show a slightly positive excess heat capacity. Between 25-300 K, $\text{Sb}_2\text{Se}_{0.6}\text{Te}_{2.4}$ and $\text{Sb}_2\text{Se}_{1.2}\text{Te}_{1.8}$, respectively, exhibit a pronounced negative excess heat capacity. At around 50 K, a local minimum is observed for both compounds.

FIGURE 5.27: Enthalpy and Entropy of $\text{Sb}_2\text{Te}_{3-x}\text{Se}_x$ ($x=0, 0.6, 1.2, 1.8, 3$) mixed crystals.

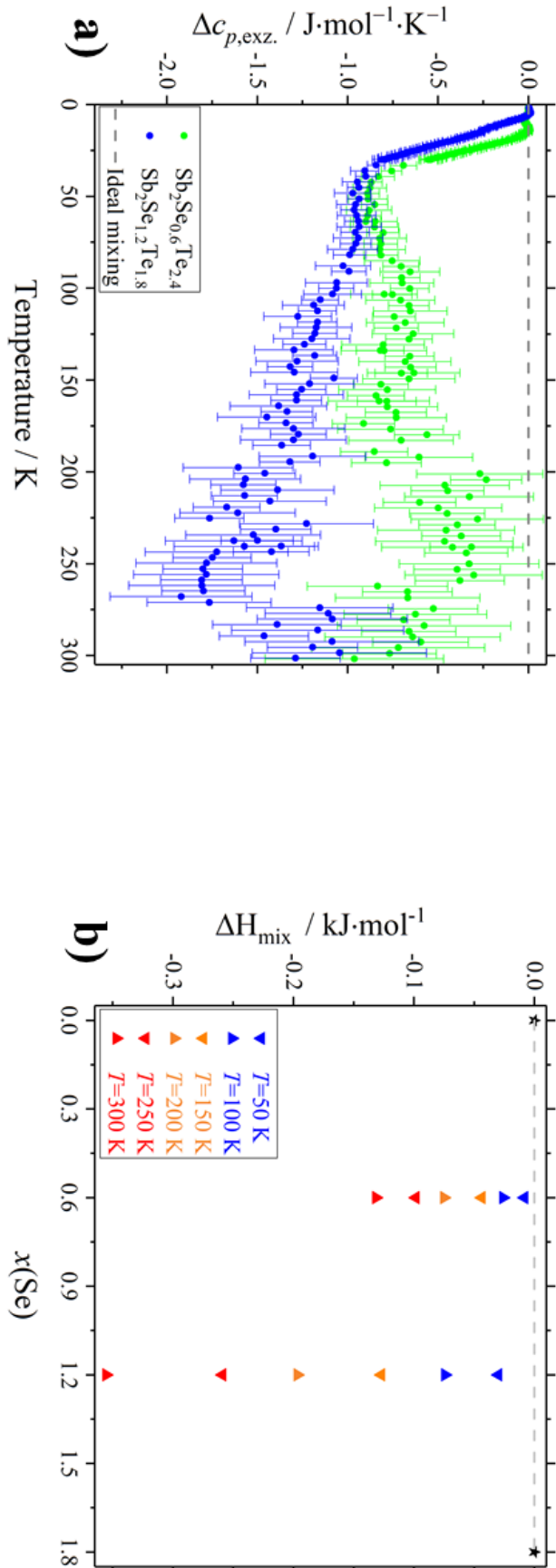


FIGURE 5.28: Temperature dependence of the excess heat capacity of $\text{Sb}_2\text{Se}_{0.6}\text{Te}_{2.4}$ and $\text{Sb}_2\text{Se}_{1.2}\text{Te}_{1.8}$ (a). In b), the excess enthalpy of both samples is compared at several temperatures.

In general, the amplitude of the excess heat capacity is comparable to the one of the Pyrope-Grossular solid solution, one of most non-ideal natural mixing systems [150]. In [146] the excess heat capacity of $Sb_2Se_{0.6}Te_{2.4}$ and $Sb_2Se_{1.2}Te_{1.8}$ was determined from first-principles calculations. Although, the theoretical calculations suggest a smaller magnitude for the excess heat capacity data of both compounds, the predicted temperature-dependence is comparable to the corresponding experimentally determined ones.

The excess enthalpy (denoted as " ΔH_{mix} ") of $Sb_2Se_{0.6}Te_{2.4}$ and $Sb_2Se_{1.2}Te_{1.8}$, respectively, was calculated from the corresponding excess heat capacity data using equation (2.35a). In figure 5.28b), the excess enthalpy of $Sb_2Se_{0.6}Te_{2.4}$ and $Sb_2Se_{1.2}Te_{1.8}$ are compared for several temperatures. Obviously, the excess enthalpy of $Sb_2Se_{1.2}Te_{1.8}$ is larger compared to the one of $Sb_2Se_{0.6}Te_{2.4}$ –also at room temperature– indicating that not only the preferred Se incorporation into the A1 site affects the mixing behavior, but also the incorporation of Se in A2 site seems to have an effect on the mixing behavior. This is surprising, as the results from the powder diffraction analysis performed in this study (figure 5.23) indicate that at room temperature $Sb_2Se_{0.6}Te_{2.4}$ shows a significant non-ideal mixing behavior, whereas $Sb_2Se_{1.2}Te_{1.8}$ exhibits ideal mixing properties. In order to understand this in more details, further measurements e. g. temperature-dependent resistivity measurements are mandatory, however, this is out of the scope of this study.

5.2.5 Lattice dynamics of $Sb_2Te_{3-x}Se_x$ ($x=0, 0.6, 1.2, 1.8$)

5.2.5.1 Inelastic neutron scattering

Figure 5.29 shows a comparison between the total phonon density of states of the $Sb_2Te_{3-x}Se_x$ ($x=0, 0.6, 1.2, 1.8$) mixed crystals determined from inelastic neutron scattering experiments performed at around 40 K between 0-40 meV. Analogous plots for the 150 K and 300 K data can be found in appendix D.5. In agreement with previous studies [14, 12, 140], three domains of vibrations have been identified in the total phonon density of states of each compound (see also section 5.2.1.2). While the acoustical phonons occur between about 0-10 meV, the optical Sb-A1 and Sb-A2 modes are present between about 10-18 meV and 18-25 meV, respectively. In the energy range between 0-25 meV, all phonon modes show a significant hardening with increasing Se content which can be seen clearly at all temperatures. This indicates a hardening of the chemical bonds with increasing Se content of the samples.

At energies above 25 meV two additional peaks were detected in the 40 K data (figure 5.29) of the samples $Sb_2Se_{0.6}Te_{2.4}$ and $Sb_2Se_{1.2}Te_{1.8}$ which are unusually broadened at higher temperature (figure 5.30; Appendix D.5). For Sb_2Te_3 and $Sb_2Se_{1.8}Te_{1.2}$ there are only low-intense contributions present in this energy range.

Four possible sources to explain the additional high energy peaks and the observed unusual broadening have been considered which are a) an inaccurate Al subtraction, b) experimental artefacts, c) structural or element/isotope-specific effects and

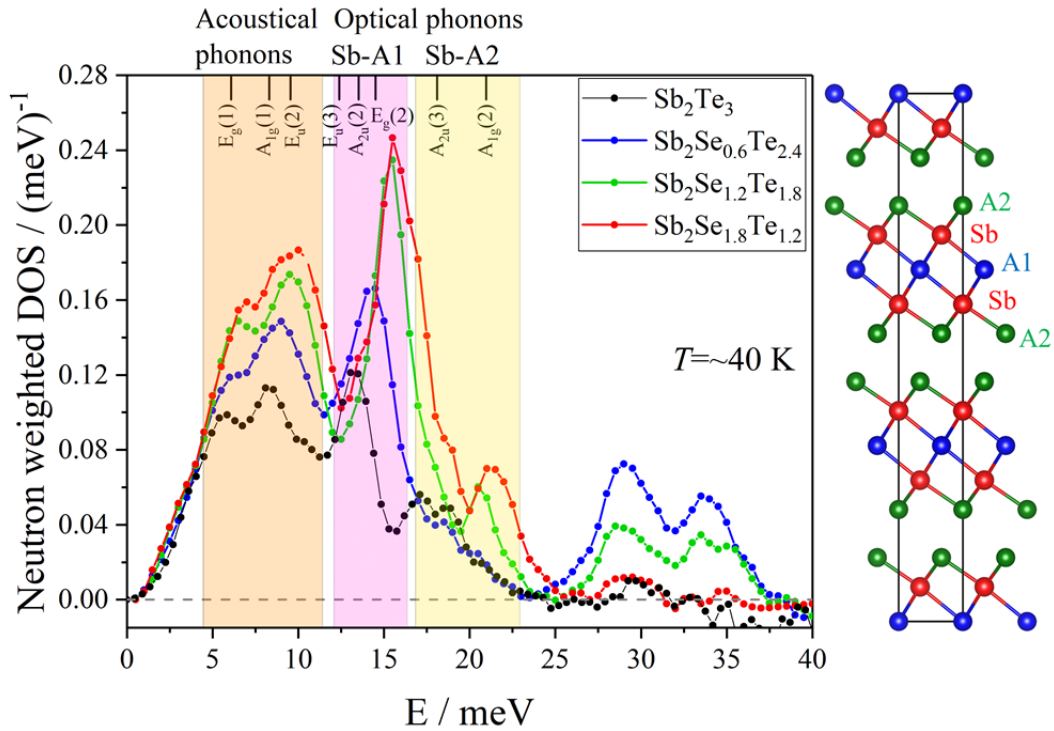


FIGURE 5.29: The total phonon density of states of the $\text{Sb}_2\text{Te}_{3-x}\text{Se}_x$ ($x=0, 0.6, 1.2, 1.8$) mixed crystals measured at around 40 K between 0-40 meV. Energies of theoretically predicted Raman modes from the literature [140] are shown for comparison. Right: Sb_2Te_3 structure type.

d) multi-phonon processes.

In order to evaluate whether these peaks are the result of an inaccurate subtraction of the Al data, the total scattering functions of each $\text{Sb}_2\text{Te}_{3-x}\text{Se}_x$ ($x=0, 0.6, 1.2, 1.8, 3$) sample before the Al subtraction were inspected and the data were compared to the total scattering function of the empty can (figure 5.31). Analogous plots for the 150 and 300 K data can be found in appendix D.6. Obviously, the additional features cannot be explained only by the Al, in particular as for the samples with $x(\text{Se})=0.6$ and 1.2 two additional contributions at slightly different energies are observed.

An experimental artefact as possible source for the additional peaks cannot be completely excluded, however, it should be mentioned that in the measurements performed at the beamline ARCS directly after our study such contributions to the phonon data were not observed [105]. Also, according to the experience of the beamline staff such features are usually not observed [151].

From the results of ^{121}Sb and ^{125}Te nuclear inelastic scattering experiments performed at comparable temperatures we can exclude that the additional peaks are related to Sb and Te as there is no evidence in the partial phonon density of states of these isotopes. Thus, the additional peaks have to be directly and exclusively related to Se. In the energy range where the additional peaks occur vibrations of covalent Se-Se bonding might be expected. However, in the crystal structures of $\text{Sb}_2\text{Se}_{0.6}\text{Te}_{2.4}$

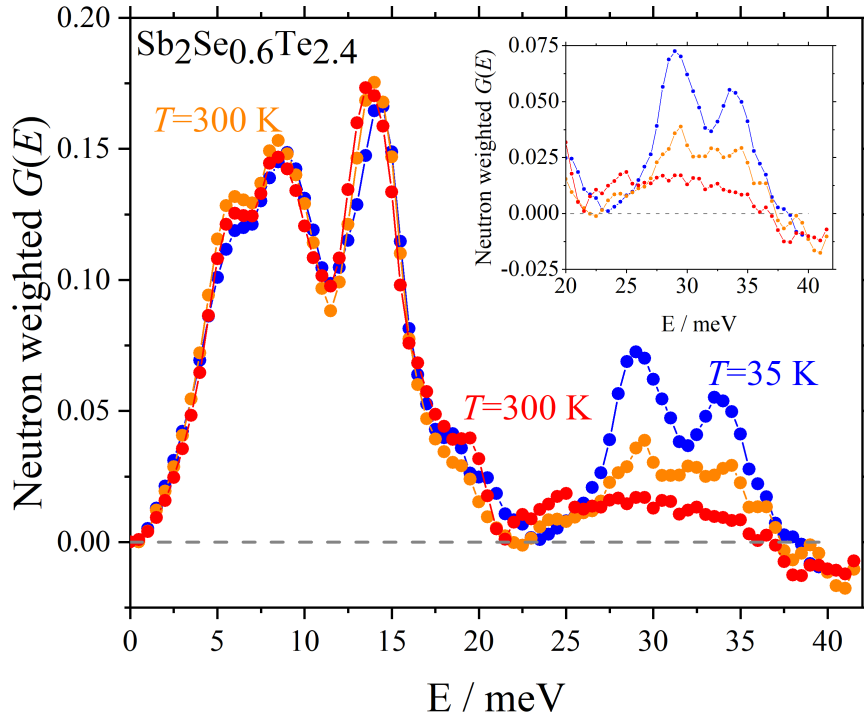


FIGURE 5.30: Total phonon density of states of $Sb_2Se_{0.6}Te_{2.4}$ at 35, 150 and 300 K. A similar plot for $Sb_2Se_{1.2}Te_{1.8}$ is shown in appendix D.5.

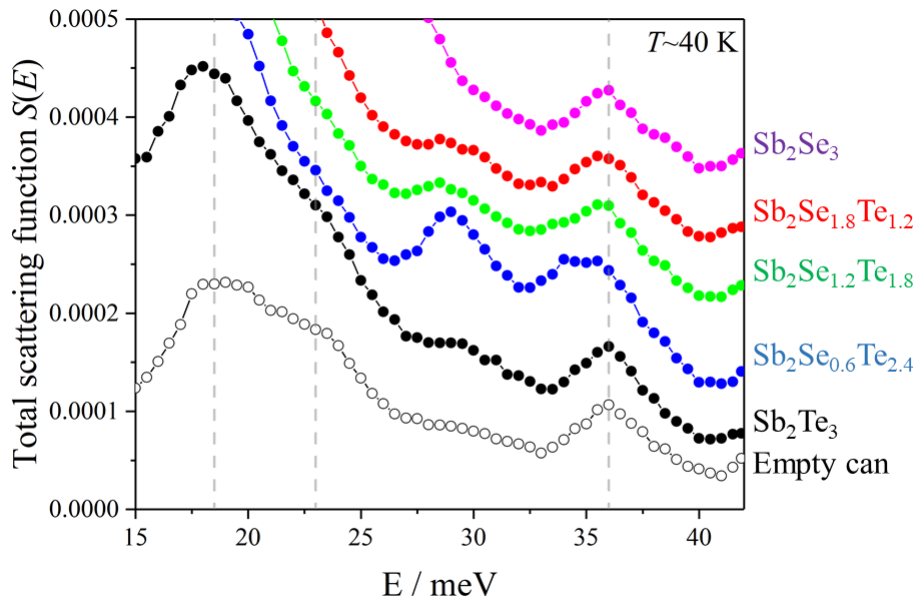


FIGURE 5.31: The total scattering functions of the $Sb_2Te_{3-x}Se_x$ ($x=0, 0.6, 1.2, 1.8, 3$) mixed crystals and the empty can before the Al subtraction measured at around 40 K between 0-42 meV.

and $Sb_2Se_{1.2}Te_{1.8}$ at ambient conditions there was no evidence for any covalent Se-Se bonds [139]. In addition, our low-temperature powder diffraction experiments [107, 139] on these samples do not provide any hint on structural phase transitions which

might lead to the formation of covalent Se-Se bonds. Still, further detailed single crystal investigations at low temperatures would be desirable.

A further explanation for the additional high energy peaks are multi-phonon processes. In the energy range between 15-20 meV both, $\text{Sb}_2\text{Se}_{0.6}\text{Se}_{2.4}$ and $\text{Sb}_2\text{Se}_{1.2}\text{Te}_{1.8}$, have several phonon modes and obviously, the additional high energy peaks occur at roughly twice these energies. At low temperatures, only a limited number of multi-phonon processes are possible which might cause the well developed additional peaks. At higher temperatures more diverse multi-phonon processes are likely which could lead to the unusual broadening of the additional peaks at higher temperatures.

Summarizing, multi-phonon processes are the most likely cause for the additional peaks. It is noteworthy that pronounced multi-phonon processes are limited by the Se content of the samples and further experimental (e. g. low-temperature single crystal diffraction or Raman measurements) and theoretical analysis are mandatory to understand this in more detail. However, this is out of the scope of this thesis.

In figure 5.32, the phonon density of states of $\text{Sb}_2\text{Se}_{1.2}\text{Te}_{1.8}$ measured at 37, 150 and 300 K are compared. (Analogous plots for other samples can be found in appendix

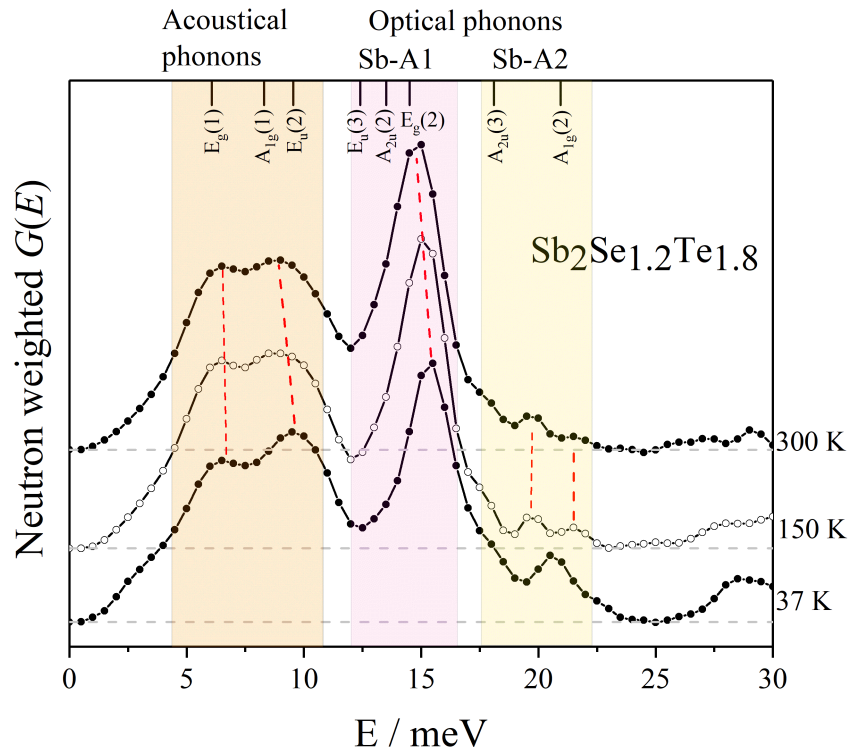


FIGURE 5.32: Temperature-induced mode shifts in the total phonon density of states of $\text{Sb}_2\text{Se}_{1.2}\text{Te}_{1.8}$.

D.7). The results of this study suggest that for all compounds there is a slight softening of the acoustical and Sb-A1 phonon modes with increasing temperatures. For the Sb-A2 phonon modes of the samples Sb_2Te_3 and $\text{Sb}_2\text{Se}_{0.6}\text{Se}_{2.4}$ a hardening with increasing temperatures is observed. While the first observation is in agreement

with previous low-temperature Raman studies, the second observation is in contrast to what was observed earlier [147, 141]. An analysis of the temperature-induced shifts of the Sb-A2 modes of the sample $\text{Sb}_2\text{Se}_{1.2}\text{Te}_{1.8}$ is challenging due to the low and smeared out intensities of the peaks. In the 150 K and 300 K data two small peaks are observed whose energies seem not to be affected by the temperature. At 37 K, only one broad peak is observed and the relation of this peak to the ones detected at higher temperatures remains unclear. For the $\text{Sb}_2\text{Se}_{1.8}\text{Te}_{1.2}$ sample only one broad peak is observed in this energy range and it seems that this peak softens with elevated temperatures. Summarizing, the Sb-A2 vibrations in $\text{Sb}_2\text{Se}_{1.2}\text{Te}_{1.8}$ and $\text{Sb}_2\text{Se}_{1.8}\text{Te}_{1.2}$ seem to be affected differently by the temperature when compared to Sb_2Te_3 and $\text{Sb}_2\text{Se}_{0.6}\text{Se}_{2.4}$.

5.2.5.2 ^{121}Sb and ^{125}Te nuclear inelastic scattering

5.2.5.2.1 Parameters describing the lattice dynamics

Table 5.9 summarizes the values of the Lamb-Mössbauer factor (L.M.F) and the mean force constant (F_i) as obtained from the ^{121}Sb and ^{125}Te NIS data, and the isotope/element-specific Debye temperatures (see section 4.3.4), $\Theta_{\text{D,Te}}$ and $\Theta_{\text{D,Se}}$. For the

TABLE 5.9: Values for the Lamb-Mössbauer factor (L.M.F.), mean force constant (F_i) and ^{125}Te and Se Debye-temperatures ($\Theta_{\text{D},i}$) of the $\text{Sb}_2\text{Te}_{3-x}\text{Se}_x$ ($x=0, 0.6, 1.2, 1.8$) mixed crystals.

Sample	^{121}Sb		^{125}Te			Se
	L.M.F.	$F_i / \text{N}\cdot\text{m}$	L.M.F.	$F_i / \text{N}\cdot\text{m}$	$\Theta_{\text{D,Te}} / \text{K}$	$\Theta_{\text{D,Se}} / \text{K}$
Sb_2Te_3	0.405417	72(5)	—	—	—	—
$\text{Sb}_2\text{Se}_{0.6}\text{Te}_{2.4}$	0.42453	80(5)	0.431517	70(5)	137(6)	162(6)
$\text{Sb}_2\text{Se}_{1.2}\text{Te}_{1.8}$	0.498957	80(5)	—	—	—	—
$\text{Sb}_2\text{Se}_{1.8}\text{Te}_{1.2}$	0.385525	93(5)	0.501263	64(5)	149(6)	192(6)

compounds Sb_2Te_3 , $\text{Sb}_2\text{Se}_{0.6}\text{Te}_{2.4}$ and $\text{Sb}_2\text{Se}_{1.2}\text{Te}_{1.8}$, the mean force constant obtained from the ^{121}Sb data is equal within error, whereas it increases slightly for $\text{Sb}_2\text{Se}_{1.8}\text{Te}_{1.2}$ indicating a lattice hardening. The mean force constants obtained from the ^{125}Te partial phonon density of states are equal within error. As expected, the Se Debye temperatures are larger than the corresponding values for Te, indicating that the Sb-Se bonds are harder than the Sb-Te bonds. The element-specific ^{125}Te Debye temperatures of $\text{Sb}_2\text{Se}_{0.6}\text{Te}_{2.4}$ and $\text{Sb}_2\text{Se}_{1.8}\text{Te}_{1.2}$ are smaller than the value determined by Bessas *et al.* [14] for Sb_2Te_3 (157(5) K).

5.2.5.2.2 Comparison of the ^{121}Sb and ^{125}Te NIS data

Figure 5.33 depicts the area weighted ^{121}Sb phonon density of states of the samples Sb_2Te_3 , $\text{Sb}_2\text{Se}_{0.6}\text{Te}_{2.4}$, $\text{Sb}_2\text{Se}_{1.2}\text{Te}_{1.8}$ and $\text{Sb}_2\text{Se}_{1.8}\text{Te}_{1.2}$ and the area weighted ^{125}Te phonon density of states of $\text{Sb}_2\text{Se}_{0.6}\text{Te}_{2.4}$ and $\text{Sb}_2\text{Se}_{1.8}\text{Te}_{1.2}$ between 0-30 meV. ^{125}Te data of Sb_2Te_3 were taken from the literature [14] and the symmetries and Γ point mode energies predicted in [140] are included for comparison.

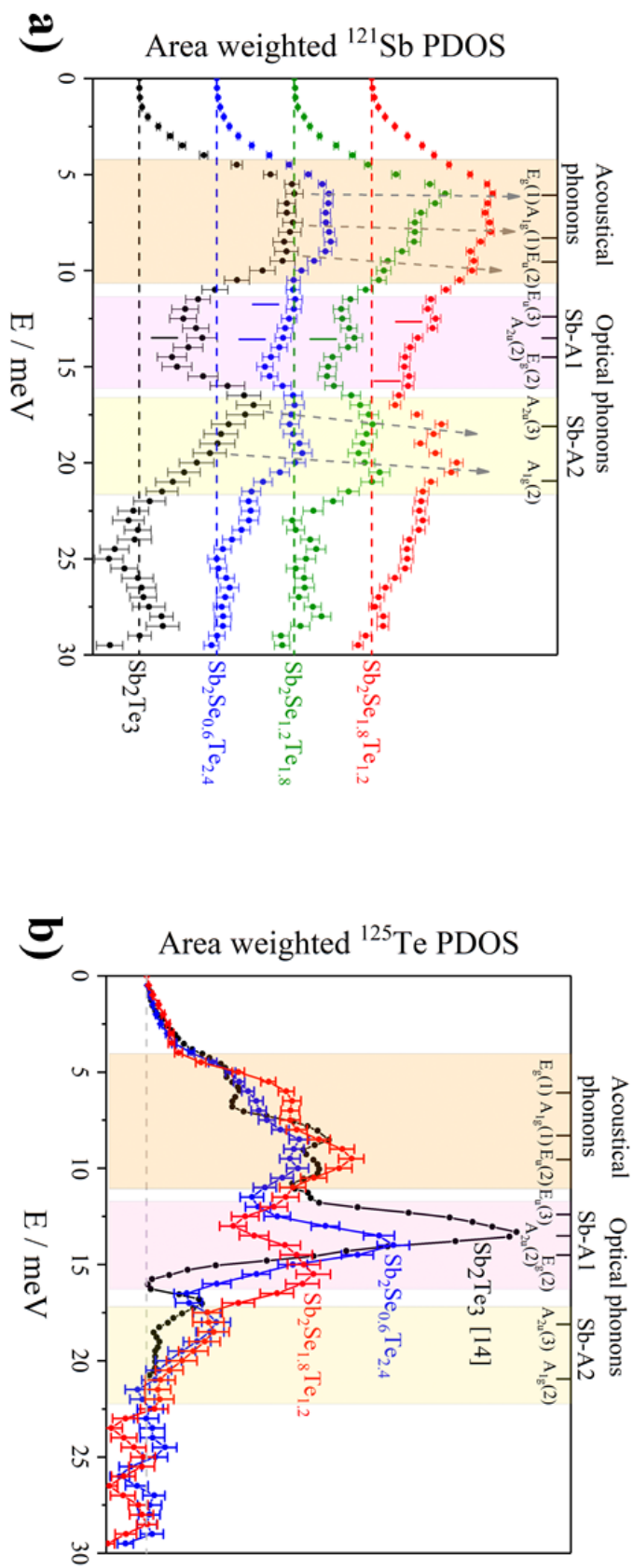


FIGURE 5.33: ^{121}Sb and ^{125}Te partial PDOS of the $\text{Sb}_2\text{Te}_{3-x}\text{Se}_x$ mixed crystals.

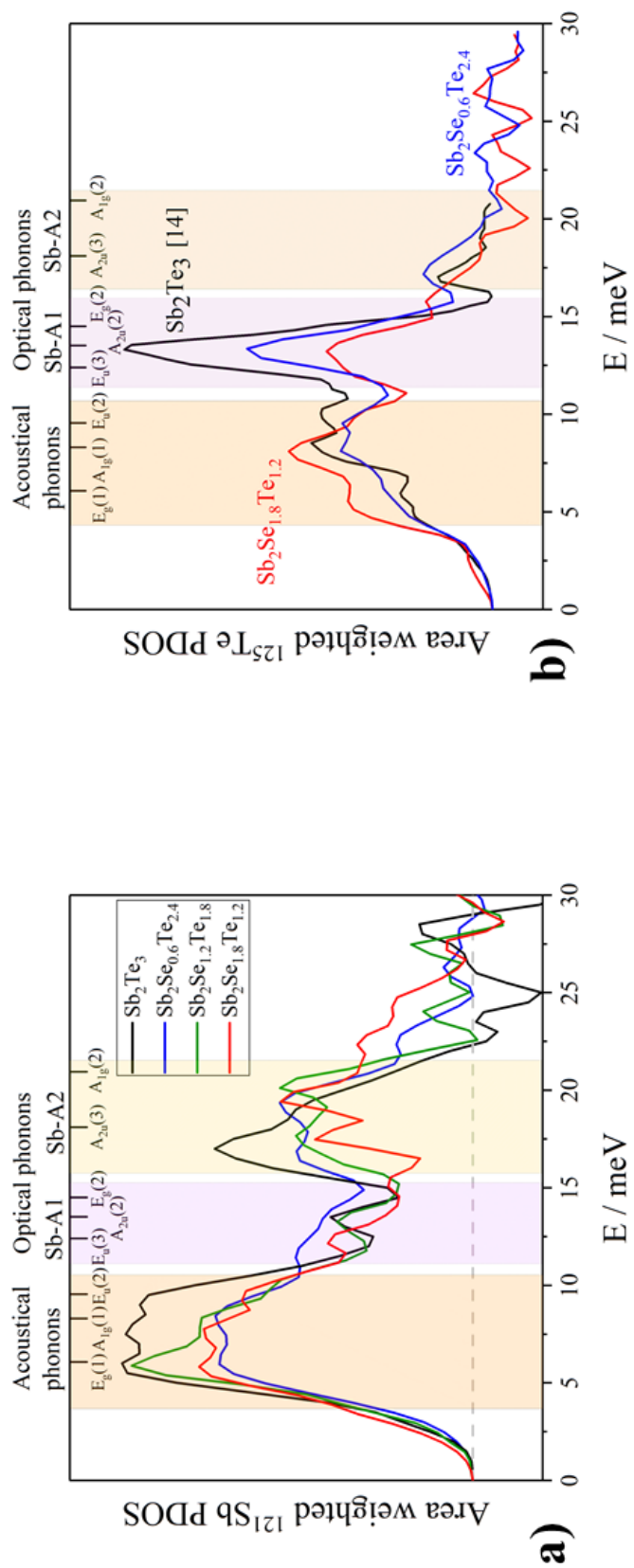


FIGURE 5.34: Partial phonon density of states of the $Sb_2Te_{3-x}Se_x$ mixed crystals after application of the homology relation.

At energies larger than 22 meV several small and not very pronounced peaks occur especially in the partial ^{121}Sb phonon density of states. According to the results of previous studies [14, 12, 140], Sb_2Te_3 does not exhibit such energetically high-lying phonon branches. For the $\text{Sb}_2\text{Te}_{3-x}\text{Se}_x$ mixed crystals, the INS data show no new peaks above 22 meV which coincide with the ones in the element-specific phonon density of states. Thus, the additional peaks are considered to be experimental artefacts.

In the ^{121}Sb and ^{125}Te partial density of states a hardening of the acoustical phonon branches and the optical Sb-A2 modes is observed with increasing Se content of the samples (fig. 5.33). The acoustical modes show a moderate hardening, indicating that these modes are little influenced by the varying Se content. In contrast to this, the composition-induced shifts of the mode energies of both optical Sb-A2 phonon branches is much more pronounced and thus, they are more sensitive to the Se content. In the ^{125}Te partial phonon density there is also a pronounced hardening of the well developed peak in the energy range of the optical Sb-A1 phonons indicating that the modes $E_{ii}(3)$ and $A_{2ii}(2)$ are also sensitive to the Te/Se exchange.

In the ^{121}Sb partial phonon density there is not only a composition-induced hardening of the optical Sb-A1 phonons, but even an increase of the number of modes: one peak was found for Sb_2Te_3 and $\text{Sb}_2\text{Se}_{1.2}\text{Te}_{1.8}$, two peaks are observed for $\text{Sb}_2\text{Se}_{0.6}\text{Te}_{2.4}$ and $\text{Sb}_2\text{Se}_{1.8}\text{Te}_{1.2}$.

In order to understand the observed changes and hardening of modes in the ^{121}Sb and ^{125}Te partial phonon density of states in more detail, the scaling factors (see section 4.3.3.3) calculated with the homology relation (equation (2.31)) have to be considered.

The direction-dependent scaling factors $E_{\text{Sb}_2\text{Te}_3}/E_A(\text{a})$ and $E_{\text{Sb}_2\text{Te}_3}/E_A(\text{c})$ are similar for all compounds indicating that the modes parallel and perpendicular to the [001] direction are influenced by the varying Se content in a comparable way. Obviously, for each composition the average scaling factor, $E_{\text{Sb}_2\text{Te}_3}/E_A(\text{V})$, calculated for the ^{125}Te partial phonon density of states is significantly larger than the corresponding value for the ^{121}Sb data. This is due to the fact that the Tellurium modes are not only affected by the changes of the unit cell volume but also by variations of the Se/Te ratio. In figure 5.34, the average scaling factors are applied to the ^{121}Sb and ^{125}Te partial phonon density of states of the $\text{Sb}_2\text{Te}_{3-x}\text{Se}_x$ ($x=0.6, 1.2, 1.8$) mixed crystals. For a more detailed analysis of the composition-induced changes, in the following sections the scaled ^{121}Sb and ^{125}Te phonon data of the mixed crystals are compared to the corresponding ones of Sb_2Te_3 .

5.2.5.2.3 Lattice dynamics of $\text{Sb}_2\text{Se}_{0.6}\text{Te}_{2.4}$

Figure 5.35 shows a comparison of the scaled ^{121}Sb and ^{125}Te partial phonon density of states of $\text{Sb}_2\text{Se}_{0.6}\text{Te}_{2.4}$ with the corresponding data of Sb_2Te_3 . In the energy range of the Sb-A1 vibrations there are some discrepancies visible in the ^{121}Sb partial phonon density of states of both compounds. This is easy to explain, as in

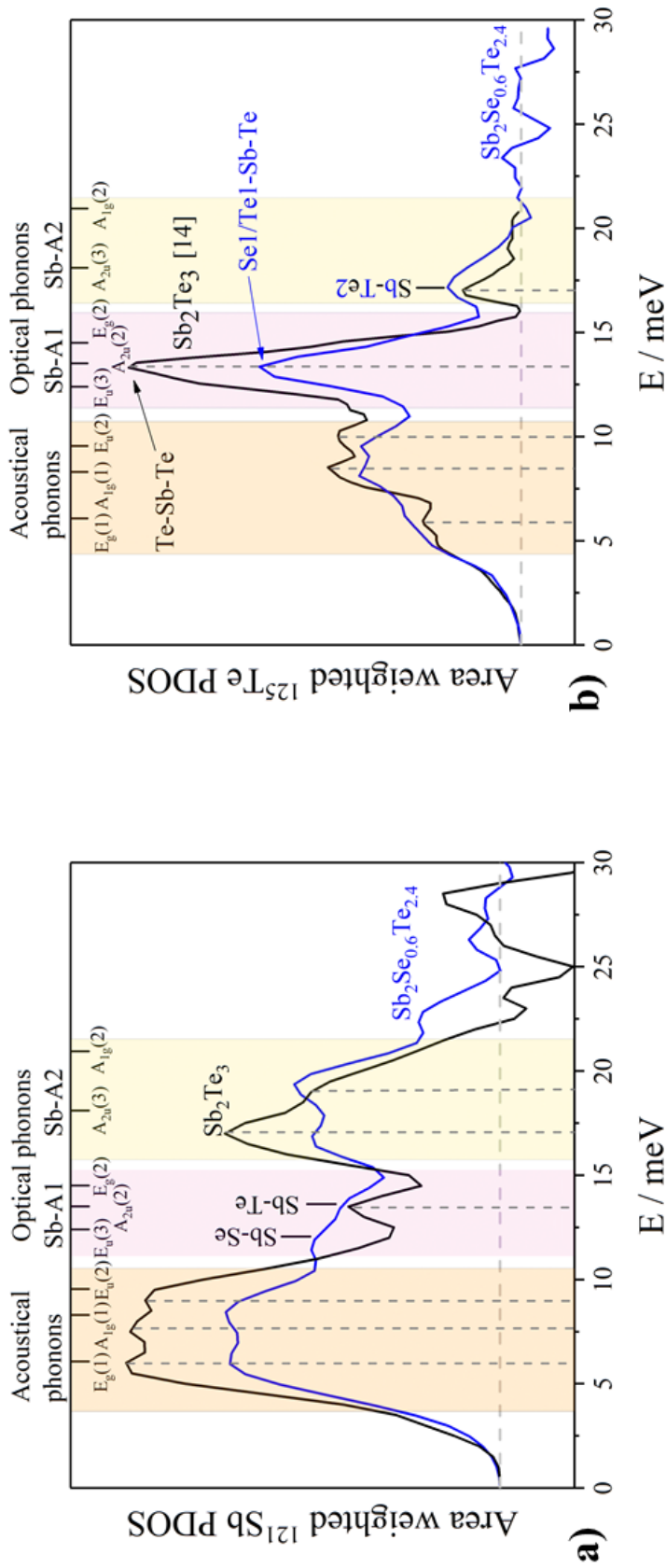


FIGURE 5.35: Comparison between the scaled ^{121}Sb and ^{125}Te partial phonon density of states of $Sb_2Se_{0.6}Te_{2.4}$ with the corresponding data of Sb_2Te_3 . While in $Sb_2Se_{0.6}Te_{2.4}$ the Te1 site is partially filled with Se (resulting in a Se1/Te1-Sb-Te $E_u(3)$ and $A_{2u}(2)$ vibrations), in Sb_2Te_3 both sites are occupied by Te. The mode positions of Sb_2Te_3 are marked by dashed lines.

$\text{Sb}_2\text{Se}_{0.6}\text{Te}_{2.4}$ the A1 site is partially filled with Se due to the preferred Se incorporation, whereas in Sb_2Te_3 there is exclusively Te present in this site. The single peak in the ^{121}Sb data of Sb_2Te_3 is caused by vibrations of the Sb-Te1 bonding whereas the two peaks in the ^{121}Sb partial phonon density of states of $\text{Sb}_2\text{Se}_{0.6}\text{Te}_{2.4}$ are due to the Sb-Te1 and Sb-Se1 vibrations. Previously, a bond length of about 3.15 Å was reported [139] for the Sb-A1 bonds in $\text{Sb}_2\text{Se}_{0.6}\text{Te}_{2.4}$. Based on theoretical calculations on Sb_2Se_3 , Deringer *et al.* [19] introduced an indicator to evaluate the strength of Sb-Se bonds. According to this bonding indicator, the Sb-Se1 bond in $\text{Sb}_2\text{Se}_{0.6}\text{Te}_{2.4}$ is a weak bond and thus, the bonding energy is reduced compared to an ideal covalent Sb-Se bond. In contrast to this, the Sb-Te1 bond length in $\text{Sb}_2\text{Se}_{0.6}\text{Te}_{2.4}$ is only slightly shorter than the one in Sb_2Te_3 [139] and hence, it is expected that the Sb-Te1 modes of both compounds occur at a similar energy which is indeed observed. Thus, the energetically lower lying peak in the ^{121}Sb partial phonon density of states of $\text{Sb}_2\text{Se}_{0.6}\text{Te}_{2.4}$ is considered to be caused by the Sb-Se1 bonds, whereas the energetically higher lying one is ascribed to the Sb-Te1 bonds. As the Sb-Te1 modes in the ^{121}Sb partial phonon density of states of Sb_2Te_3 and the scaled one of $\text{Sb}_2\text{Se}_{0.6}\text{Te}_{2.4}$ occur at similar energies, there are no indications for a change in bonding.

The modes of the scaled ^{125}Te partial phonon density of states of $\text{Sb}_2\text{Se}_{0.6}\text{Te}_{2.4}$ occur at very similar energies as in Sb_2Te_3 . This is also the case for the acoustical and Sb-A2 modes in the ^{121}Sb partial phonon density of states indicating that the observed hardening of these vibrational modes in $\text{Sb}_2\text{Se}_{0.6}\text{Te}_{2.4}$ is mainly due to the change in the unit cell volume and the different Te/Se mass fractions and there is no evidence for a substantial change in bonding.

Summarizing, the observed changes in the ^{121}Sb and ^{125}Te partial phonon density of states of $\text{Sb}_2\text{Se}_{0.6}\text{Te}_{2.4}$ compared to the ones of Sb_2Te_3 could be reduced to composition-induced structural changes and thus, the bonding in both compounds is comparable.

5.2.5.2.4 Lattice dynamics of $\text{Sb}_2\text{Se}_{1.2}\text{Te}_{1.8}$

A comparison between the scaled ^{121}Sb partial phonon density of states of $\text{Sb}_2\text{Se}_{1.2}\text{Te}_{1.8}$ with the corresponding data of the Sb_2Te_3 shows that the energies of the acoustical and the optical Sb-A1 modes of $\text{Sb}_2\text{Se}_{1.2}\text{Te}_{1.8}$ are in very good agreement with the ones of Sb_2Te_3 (figure 5.36). This confirms that the observed mode hardening is exclusively due to the composition-induced changes of the unit cell volume. For both compounds, in the energy range of the Sb-A1 modes a single peak is observed. As for $\text{Sb}_2\text{Se}_{1.2}\text{Te}_{1.8}$ the A1 site is completely filled with Se, this single peak is caused by vibrations of the Sb-Se1 bonds. Obviously, the Sb-Se1 and Sb-Te1 mode occur at nearly the same energy indicating that the Sb-Se1 bonding in $\text{Sb}_2\text{Se}_{1.2}\text{Te}_{1.8}$ is harder than the one in $\text{Sb}_2\text{Se}_{0.6}\text{Te}_{2.4}$. This is not surprising as the distortion of the Sb-A1 octahedra in $\text{Sb}_2\text{Se}_{1.2}\text{Te}_{1.8}$ is significantly smaller compared to the one in $\text{Sb}_2\text{Se}_{0.6}\text{Te}_{2.4}$ and thus, it is expected that the Sb-Se bonds in the former compound are stronger and thus harder than in the later one. In the energy range of the Sb-A2 vibrations the maxima of both peaks differ significantly. While in Sb_2Te_3 the A2 site is completely

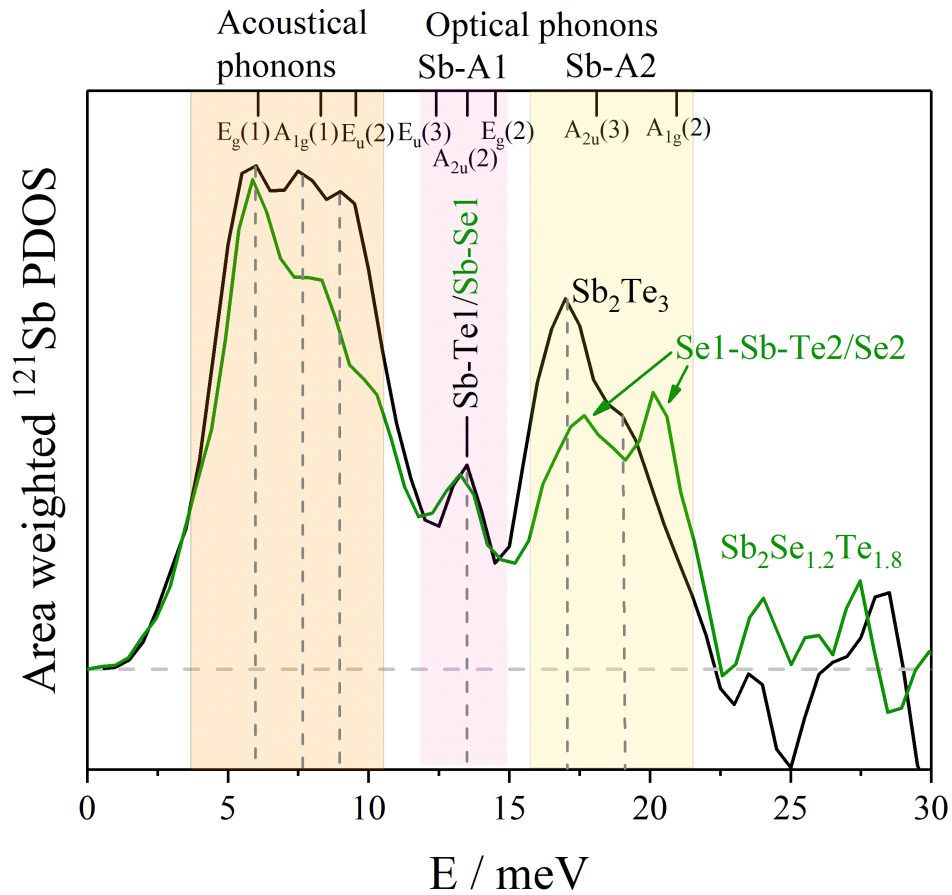


FIGURE 5.36: Comparison between the scaled ^{121}Sb partial phonon density of states of $\text{Sb}_2\text{Se}_{1.2}\text{Te}_{1.8}$ with the corresponding data of Sb_2Te_3 . The mode positions of Sb_2Te_3 are marked by dashed lines.

filled by Te, for $\text{Sb}_2\text{Se}_{1.2}\text{Te}_{1.8}$ there is also a small amount of Se present on this site. The mismatch in the mode energies of the Sb-A2 vibrations indicate that the Sb-A2 bonding is different in both compounds.

5.2.5.2.5 Lattice dynamics of $\text{Sb}_2\text{Se}_{1.8}\text{Te}_{1.2}$

Figure 5.37 shows a comparison between the scaled ^{121}Sb and ^{125}Te partial phonon density of states of $\text{Sb}_2\text{Se}_{1.8}\text{Te}_{1.2}$ with the corresponding data of Sb_2Te_3 . Like for $\text{Sb}_2\text{Se}_{1.2}\text{Te}_{1.8}$, for $\text{Sb}_2\text{Se}_{1.8}\text{Te}_{1.2}$ the mode energies of the acoustical modes in the ^{121}Sb and ^{125}Te phonon data are in good agreement with the ones in Sb_2Te_3 confirming again that the observed hardening is exclusively due to the composition-induced changes of the unit cell volume and the different Se/Te mass fractions. The ^{125}Te phonon data of both compounds show a single peak in the energy range of the Sb-A1 vibrations. Obviously, the Sb-A1 peak in the scaled ^{125}Te partial phonon density of states of $\text{Sb}_2\text{Se}_{1.8}\text{Te}_{1.2}$ occurs at the same energy as the one of Sb_2Te_3 . This indicates that although the Te in both sites of the tetradymite structure type is (partially)

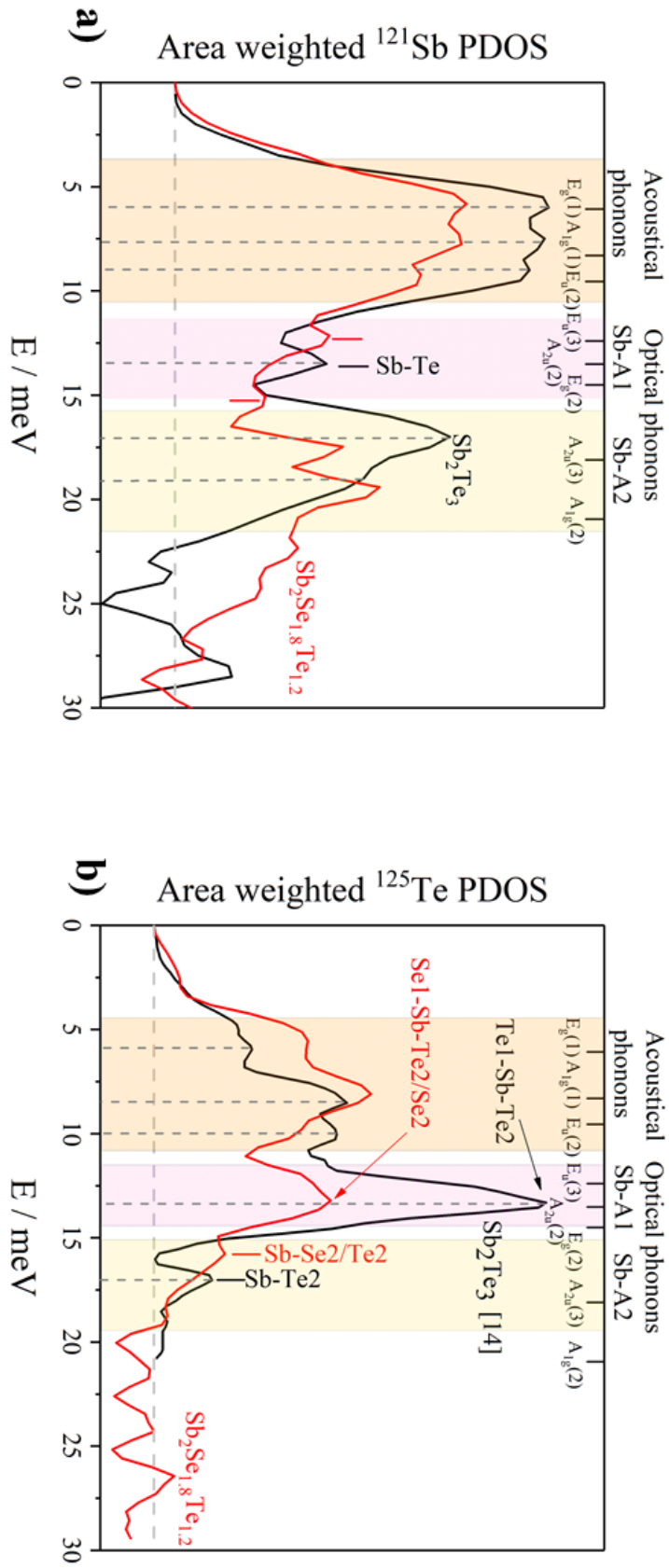


FIGURE 5.37: Comparison between the scaled ^{121}Sb and ^{125}Te partial phonon density of states of $\text{Sb}_2\text{Se}_{1.8}\text{Te}_{1.2}$ with the corresponding data of Sb_2Te_3 . The mode positions of Sb_2Te_3 are marked by dashed lines.

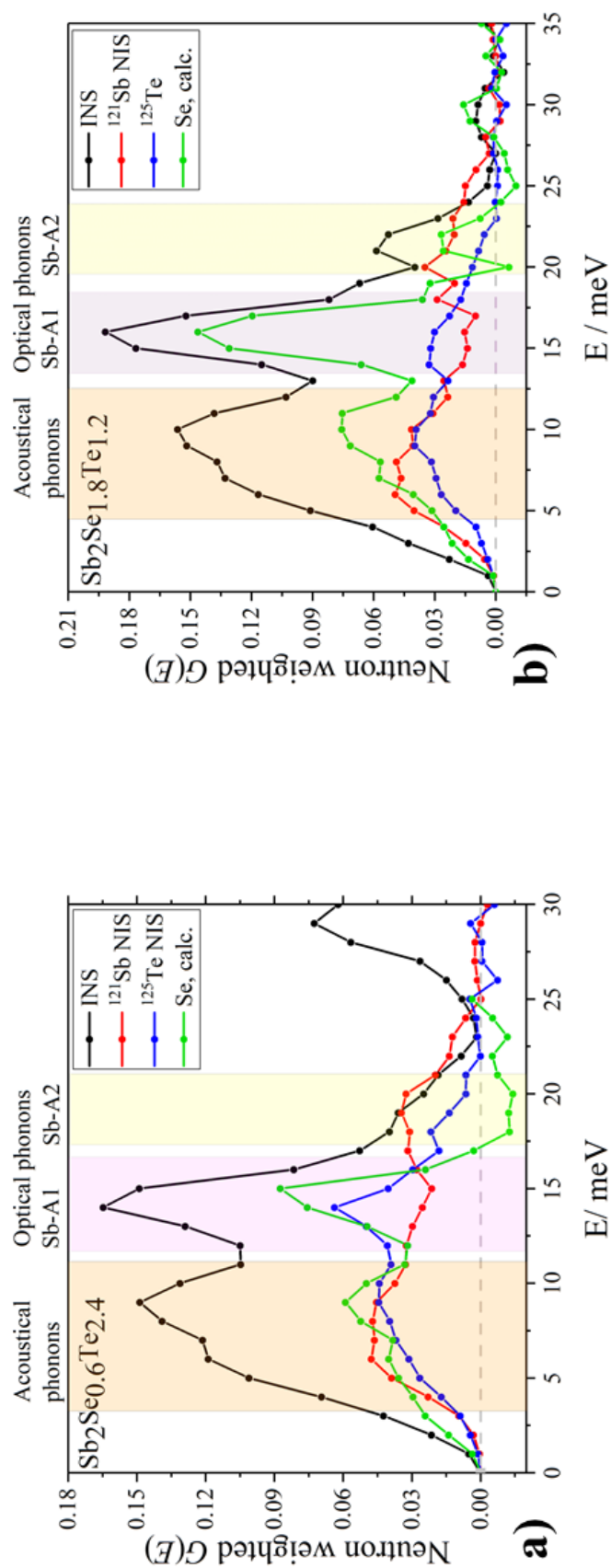


FIGURE 5.38: Se partial density of states of $Sb_2Se_{0.6}Te_{2.4}$ (a) and $Sb_2Se_{1.8}Te_{1.2}$ (b). In addition, the corresponding total (black line dots) and ^{121}Sb (red line dots) and ^{125}Te (blue line dots) partial phonon density of states are shown.

replaced by Se, the observed mode hardening is also a result of the composition-induced changes of the unit cell volume and the different Se/Te mass fractions. In the ^{121}Sb phonon data of $\text{Sb}_2\text{Se}_{1.8}\text{Te}_{1.2}$ two peaks are observed in the energy range of the Sb-A1 vibrations. However, the energetically higher lying peak at 15 meV is very weak and might be an experimental artefact. The energetically lower lying one is slightly softer than the Sb-A1 mode in Sb_2Te_3 . In the energy range of the Sb-A2 modes, deviations between the scaled ^{121}Sb and ^{125}Te partial phonon density of states of $\text{Sb}_2\text{Se}_{1.8}\text{Te}_{1.2}$ and the corresponding data of Sb_2Te_3 can be clearly seen. While in the ^{121}Sb phonon data of $\text{Sb}_2\text{Se}_{1.8}\text{Te}_{1.2}$ the Sb-A2 vibrations occur at higher energies, the Sb-A2 peak in the ^{125}Te partial phonon density of states is observed at a lower energy compared to the one of Sb_2Te_3 . Like for $\text{Sb}_2\text{Se}_{1.2}\text{Te}_{1.8}$, these discrepancies indicate that the bonding character of the Sb-A2 bonds in $\text{Sb}_2\text{Se}_{1.8}\text{Te}_{1.2}$ differs from the one in Sb_2Te_3 .

5.2.5.3 Se partial phonon density of states

Figure 5.38 shows the extracted Se partial phonon density of states of $\text{Sb}_2\text{Se}_{0.6}\text{Te}_{2.4}$ and $\text{Sb}_2\text{Se}_{1.8}\text{Te}_{1.2}$ (see section 4.3.5) together with the total and ^{121}Sb and ^{125}Te PDOS. The intensities of the Se modes in $\text{Sb}_2\text{Se}_{0.6}\text{Te}_{2.4}$ are significantly smaller than the ones in $\text{Sb}_2\text{Se}_{1.8}\text{Te}_{1.2}$ which is due to the different Se contents in both samples, especially on the A1 site. In the energy range of the Sb-A2 modes, no Se contribution to the total phonon density of states of $\text{Sb}_2\text{Se}_{0.6}\text{Te}_{2.4}$ is found. In contrast to this, in the same energy range, for $\text{Sb}_2\text{Se}_{1.8}\text{Te}_{1.2}$ a significant Se contribution to the total phonon density of states of this compound is observed. This can be easily understood as for $\text{Sb}_2\text{Se}_{0.6}\text{Te}_{2.4}$ there is no Se present on the A2 site and thus, no Se phonon density is expected in the energy range of these modes. For $\text{Sb}_2\text{Se}_{1.8}\text{Te}_{1.2}$ the A2 site is partially filled by Se and thus, partial Se phonon density of states in the energy range of these phonon modes is expected.

5.2.6 Lattice dynamics of Sb_2Se_3

Figure 5.39a) shows the experimentally determined total and ^{121}Sb partial phonon density of states and the calculated Se partial PDOS (see section 4.3.5) of Sb_2Se_3 . In table 5.10, the values obtained for the Lamb-Mössbauer factor (L.M.F.), the mean

TABLE 5.10: Element-specific Lamb-Mössbauer factors (L.M.F.), mean force constants (F_i) and Debye temperatures ($\Theta_{D,i}$) of Sb_2Se_3

Element	L.M.F.	$F_i / \text{N}\cdot\text{m}$	$\Theta_{D,i} / \text{K}$
^{121}Sb	0.46590	120(6)	160(6)
Se	—	—	239(6)

force constant (F_i) and element-specific Debye temperatures (see section 4.3.4), $\Theta_{D,\text{Sb}}$ and $\Theta_{D,\text{Se}}$, obtained from the ^{121}Sb and Se data are summarized. In agreement with the literature [19], the larger cut-off frequency and energetically higher lying

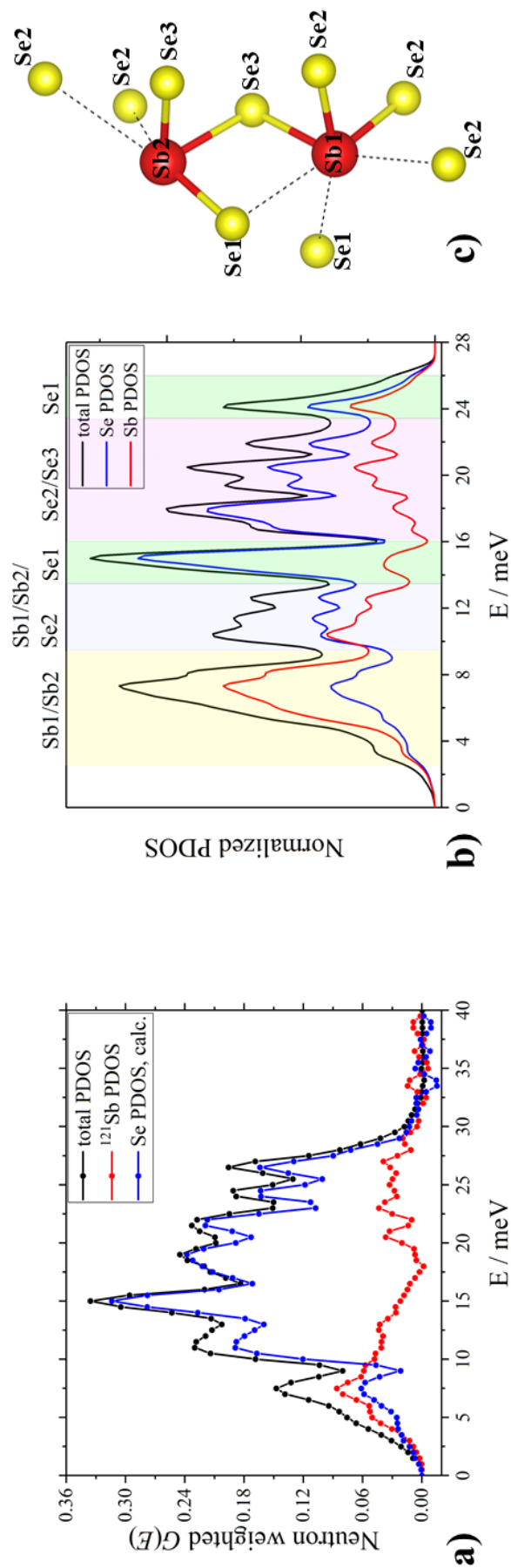


FIGURE 5.39: The total and element-specific phonon density of states of Sb_2Se_3 from experiment (a) and theory (b)). Domains in which certain atoms dominate the PDOS are marked. A fragment of a -Se-Sb-Se- chain is shown in c).

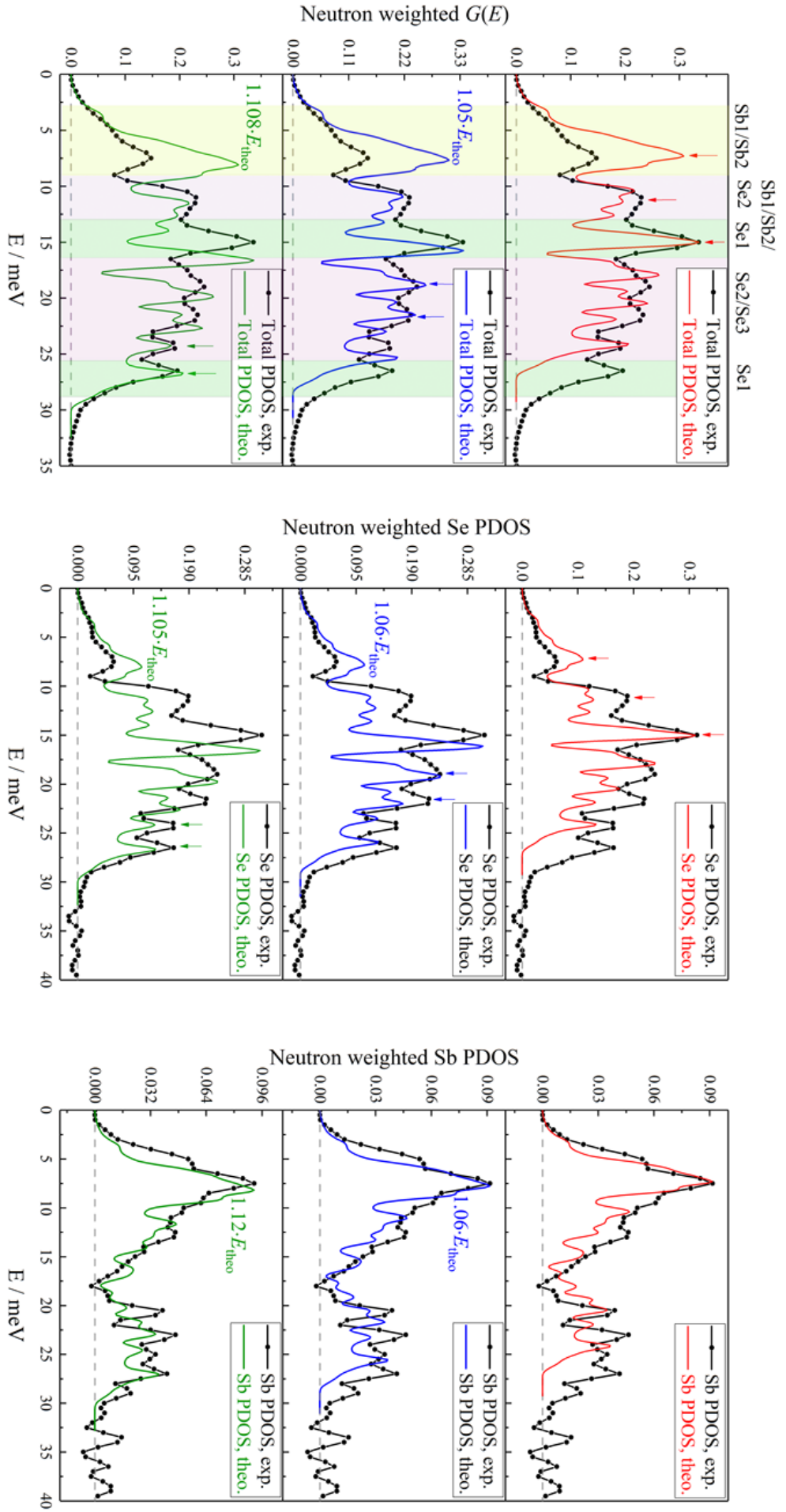


FIGURE 5.40: Comparison between the experimentally determined and theoretically predicated total phonon density of states of Sb_2Se_3 (left). Analogous comparison for the Sb and Se partial phonon density of states are also shown (middle, right). Scaling factors as shown in the figures were applied to the theoretical data.

optical phonons as well as the larger mean force constants indicate that Sb_2Se_3 is harder than the compounds from the stability field of the tetradymite structure type. In figure 5.39b), the Sb and Se partial phonon density of states and the total one as predicted by Deringer *et al.* [19] are shown. Domains in which certain atoms are dominating the total phonon density of states [19] are marked in figure 5.39b). The theoretical data show much more features, however, this could be due to the fact that the experimental data are limited by an experimental resolution larger than 1 meV. Both, the experimental and theoretical data show that antimony contributes especially to the modes in the energy range between about 0-10 meV, whereas at higher energies Se vibrations are dominating the total phonon density of states of Sb_2Se_3 . A comparison between the experimentally determined and theoretically predicted total phonon density of states of Sb_2Se_3 shows that between 0-16 meV the experimental and theoretical data are in excellent agreement (figure 5.40, left). The three theoretically calculated features between 9-13 meV seem to occur as one broad peak in the experimental data which can probably be attributed to the experimental resolution. In order to establish the significant mismatch between the experimental and theoretical data at higher energies, the theoretical phonon density was scaled by a factor of 1.05 and 1.108, respectively. The application of the former scale factor leads to an overlap in the energy range of the Se2/Se3 dominated vibrations, while the application of the latter scale factor leads to an overlap in the high-energy range of Se2/Se3 and Se1 dominated vibrations (indicated by arrows in the figures). The Se partial phonon density of states were treated in the same way and similar scaling factors were applied (figure 5.40, middle). In case of the Sb data (figure 5.40, right), it is more difficult to gain a reliable overlap since in the theoretical data there are many modes present which seem to be either degenerated or not resolved in the experimental partial phonon density of states. Also, the intensities of the predicted and detected peaks seem to be significantly different. However, scaling factors of 1.06 and 1.12 seem to yield a reliable overlap between the experimentally determined and the theoretically predicted partial PDOS. Summarizing, it is important to emphasize that a complete overlap between the experimental and theoretical data is not given by applying a constant scaling factor for the entire energy range. In order to understand the origin of the deviations between the experimental and theoretical phonon data above 15 meV, the homology relation (equation (2.31)) is used. As the masses of both elements can be considered to be identical in both data,

TABLE 5.11: Lattice parameter and unit cell volume of Sb_2Se_3 as determined in this study and reported previously [19].

	This study	[19]	ratio
$a / \text{\AA}$	11.7405(5)	11.534	1.018
$b / \text{\AA}$	3.9624(1)	3.960	1.001
$c / \text{\AA}$	11.5846(4)	11.221	1.032
$V / \text{\AA}^3$	538.92(5)	512.52	1.052

the homology relation only depends on the ratios of the lattice parameter and unit cell volumes, respectively. According to equation (2.31), these ratios represent the direction-dependent and average scaling factors. Experimentally determined and theoretically predicted lattice parameter of Sb_2Se_3 and their ratios are summarized in table 5.11. The lattice parameter ratios yield values between 1.001 and 1.032 and hence, cannot cause the observed deviations. However, the ratio of the unit cell volumes yields a value of 1.052 which is very comparable to one of the scaling factors chosen above. Thus, part of the deviations might be due to volume effects, however, the strong deviations in the high energy range cannot be explained by them. Another explanation would be that the theoretical data underestimate the bond strength of several Sb-Se bonds. This is likely, as almost for all covalent Sb-Se bonds the predicted bonds length are larger than expected from previous experiments [19].

A comparison of the total phonon density of states of Sb_2Se_3 at different temperatures (figure 5.41) shows a softening of all modes with increasing temperature. This

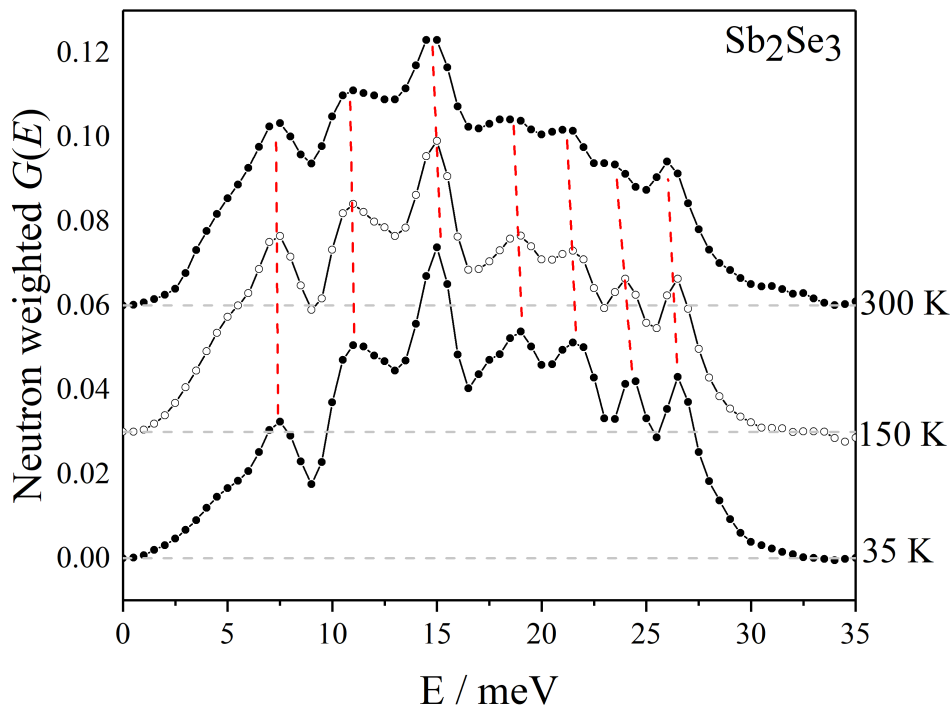


FIGURE 5.41: Temperature-induced mode shifts in the total phonon density of states of Sb_2Se_3

clearly indicates that both, the covalent Sb-Se bonds and the Sb··Se interactions, become weaker. This is expected as the increase of the thermal movement of the atoms is correlated with a weakening of the chemical bonds.

Chapter 6

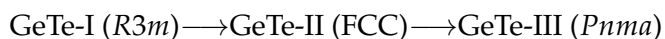
Conclusions

The general aim of this study was to understand the influence of high pressures, low temperatures and composition-induced changes on the crystal structures and the lattice dynamics of phase-change materials. Of particular interest is the effect of these variations on the metavalent bonding. For this, two model systems have been selected which are the $\text{GeSe}_x\text{Te}_{1-x}$ and $\text{Sb}_2\text{Te}_{3-x}\text{Se}_x$ solid solutions. In case of the former system the effect of high pressure, low temperatures and variations of the Se content on the structural features was studied by a combination of single-crystal and powder diffraction experiments. The influence of low temperatures and composition-induced changes on the lattice dynamics was studied on the example of the $\text{Sb}_2\text{Te}_{3-x}\text{Se}_x$ solid solution using a combination of low-temperature heat capacity measurements and X-ray- and neutron-spectroscopic techniques.

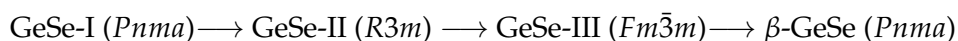
The influence of low temperatures on the lattice parameter of $\text{GeSe}_x\text{Te}_{1-x}$ compounds was studied for the first time and for compounds from the stability field of the rhombohedral GeTe-I phase ($x=0, 0.2, 0.5$) a negative thermal expansion along the [001] direction was observed over the entire temperature range (25-300 K) which is a very rare finding and a similar thermal behavior in binary chalcogenides was observed only for the orthorhombic SnSe [133]. The magnitude of the negative thermal expansion depends strongly on the Se content and the larger the Se content, the more distorted is the unit cell with respect to the cubic phase. In contrast to this, the [100] direction shows a positive thermal expansion and is hardly influenced by variations of the Se content. Compounds from the stability field of the hexagonal phase ($x=0.75$) show an exclusively positive thermal expansion along the [100] and [001] direction which significantly differs from the rhombohedral compounds. This is probably caused by the additional Ge·Ge and long-ranged Se/Te·Se/Te interactions which are exclusively present in the crystal structure of the hexagonal phase. For GeSe, all lattice parameter show a positive thermal expansion between 25-300 K, where down to about 150 K the [010] and [001] direction are affected by the temperature in nearly the same way. Below 150 K, the b lattice parameter shows larger temperature-induced changes than the [001] direction. In a previous study [117] the occurrence of new Raman modes below 150 K was reported, however, in this study no evidence for a structural phase transition was observed and thus, our results do not confirm the ones reported earlier. However, the results of this study support the

observations of [118] who reported that the GeSe-I phase is stable down to at least 70 K.

The high-pressure behavior of $\text{GeSe}_x\text{Te}_{1-x}$ ($x=0, 0.2, 0.5, 0.75$) mixed crystals was studied and for the compounds from the stability of the GeTe-I phase ($x=0, 0.2, 0.5$) the following high-pressure transition pathway was found:



In agreement with previous studies [119, 120, 79, 112, 121], for GeTe a phase transition from GeTe-I to a cubic GeTe-II phase was found. The observed hydrostatic transition pressure of 4.2 GPa agrees with the value (3 GPa) reported in [79], whereas it is significantly smaller than suggested (8 GPa) in [120]. In general, the transition pressure increases with increasing Se content. For all mixed crystals, the phase transition is accompanied by a pronounced anomaly in the lattice parameter indicating a first-order nature for this transition. In previous studies on GeTe [112, 120] this was attributed to non-hydrostatic conditions in the DAC, however, all of our experiments were performed under hydrostatic conditions and thus, we cannot confirm the earlier conclusions. At higher pressure a further phase transition from the GeTe-II phase to the GeTe-III polymorph was observed. For all mixed crystals, the GeTe-II and GeTe-III polymorph coexist over a wide pressure range which was not reported earlier. The coexistence of both phase indicates a first-order nature for this transition. The transition pressure to the one-phase region of the GeTe-III phase decreases with increasing Se content. Thus, the stability field of the GeTe-II polymorph becomes smaller with increasing Se content. In this study, a new crystal structure was determined for the GeTe-III phase and it was demonstrated that the structure models reported earlier [79, 111] are erroneous. The newly determined GeTe-III structure is isostructural to the one of β -GeSe and a [3+3+2] coordination around the Ge atoms formed by three covalent Ge-Te bonds, three Ge \cdots Te interactions and two Ge \cdots Ge contacts was found in both structures. Also the Te/Se atoms in both structures show a similar [3+3+2] coordination which is formed by three covalent Te/Se-Ge bonds, three Te/Se \cdots Ge interactions and two groupVI \cdots groupVI interactions. While the GeTe-III structure is composed by six-membered Ge-Te rings which are arranged in the boat conformation, in GeTe-I the rings are arranged in the chair conformation. Thus, the high-pressure transition pathway from GeTe-I to GeTe-III is accompanied by an inversion of the ring conformation and the cubic polymorph can be considered as an intermediate phase. It is noteworthy that a similar high-pressure transition pathway was reported [129] for the GeSe-I to β -GeSe transition:



While the occurrence of a cubic high-pressure polymorph of GeSe phase was already discussed in the literature [123], the relationship between the above-mentioned high-pressure polymorphs and the $Cmmm$ high-pressure phase reported in [124] is unclear and thus, further high-pressure studies are necessary.

The high-pressure behavior of the hexagonal $\text{GeSe}_{0.75}\text{Te}_{0.25}$ was studied for the first time and it was found that the compound is stable up to at least 23 GPa.

In general, a metavalent bonding scheme was only reported for chalcogenides with a regular or a slightly distorted octahedral coordination of the group IV (Ge, Sn, Pb) and group VI (Te) elements [5]. Based on this model, the GeTe-I and GeTe-II polymorphs are expected to exhibit a metavalent bonding scheme, whereas orthorhombic GeTe-III and the hexagonal phase are proposed to be predominately covalently bonded [11, 9, 152, 5]. Both, the substitution of Te by the smaller Se as well as the application of hydrostatic pressure leads to a reduction of the unit cell volume and favours the formation of additional Ge·Ge interactions and long-ranged groupVI·groupVI contacts in the system $\text{GeSe}_x\text{Te}_{1-x}$. These additional interactions are limited to the GeTe-III polymorph and the hexagonal phase and thus, if there is a metavalent bonding present in GeTe-I and GeTe-II then its collapse seems to be correlated with the formation of these interactions. Following this idea, the GeSe-I phase and β -GeSe would also not be metavalently bonded [152, 9, 5, 10].

The influence of low temperatures and composition-induced changes on the lattice dynamics of the $\text{Sb}_2\text{Te}_{3-x}\text{Se}_x$ system was studied for the first time. In agreement with the literature [148, 146], low-temperature the heat capacity data suggest a lattice hardening with increasing Se content and according to [148] this is correlated with an increase of the bonding polarity. For the compounds from stability field of the tetradymite structure type ($x=0, 0.6, 1.2, 1.8$) it was found that an anharmonicity correction is mandatory for an accurate fitting of the heat capacity data, however, the magnitude of this anharmonic contribution is much smaller than reported in the literature [14, 147]. The low-temperature heat capacity calculated from inelastic neutron scattering data underestimates the heat capacity determined from PPMS measurements in the high-temperature range. As from the INS data only isochoric heat capacity were derived, this is a further hint for the importance of the correction of anharmonic contributions. The heat capacity data of Sb_2Se_3 are significantly smaller than the Petit-Dulong limit and thus, the compound is considered to be a harmonic lattice oscillator. Surprisingly, the isochoric heat capacity data derived from the INS data underestimates the one from the PPMS measurements which is believed to be due to differences between the studied samples. While in previous studies [14, 147, 143] several low-temperature contributions (e. g. electronic contributions, Schottky anomaly) to the low-temperature heat capacity were included for an accurate fitting, in this study a reliable description of the heat capacity data was achieved with the non-Debye model [56, 57] without including such contributions to the fit.

In agreement with the literature [14, 12, 140], three domains of vibrations have been identified in the total and partial phonon density of states of the $\text{Sb}_2\text{Te}_{3-x}\text{Se}_x$ ($x=0, 0.6, 1.2, 1.8$) mixed crystals. The inelastic neutron scattering data show that there is a pronounced hardening of all phonon modes with increasing Se content. This was found at all investigated temperatures. In the high-energy range >25 meV two additional peaks were observed which show an unusual broadening with increasing

temperature. These peaks are probably due to multi-phonon scattering processes, however, further analysis is mandatory to understand their origin in more detail.

According to the literature [17], the metavalent bonding in the tetradymite structure type is presumed to be limited to the center of the -A2-Sb-A1-Sb-A2- quintuple layers. This is, as the A2··A2 interactions are believed not to be able to mediate the metavalent bonding. In addition, while Te is believed to allow the formation of metavalent bonding, Se tends to form covalent bonds [5, 3, 11] and thus, the Te/Se exchange together with the preferred Se incorporation in the A1 site is believed to be accompanied by a weakening of the metavalent bonding. According to this earlier hypothesis, a change of the metavalent bonding character should be visible especially in the Sb-A1 modes.

However, a detailed analysis of the observed mode hardening by ^{121}Sb and ^{125}Te nuclear inelastic scattering experiments shows that in particular the bonding character of the Sb-A2 bond at the periphery of the quintuple layers is changed significantly when Se starts to occupy this site, whereas all composition-induced changes in the energy range of the Sb-A1 modes are correlated with structural changes and there is no evidence for a bonding change. Thus, the results of this study disagree with the hypothesis from the literature.

The changes in the bonding character of the Sb-A2 bonds indicate that, if there is a fingerprint for the weakening of the metavalent bonding visible in the lattice dynamics, then it is correlated with this bonding. Also, the results of a detailed structure analysis [139] have shown that especially the A2··A2 interactions are affected by the Se content and obviously, these interactions are correlated with the Sb-A2 bonds. However, as shown in [139] the changes in the A2··A2 interactions can be alternatively explained by changes of bonding polarity inside the layers introduced by the replacement of Te inside the layers by the more electronegative Se. Up to now, it thus remains unclear whether the changes in the bonding character of the Sb-A2 bonds are a consequence of the changed bonding polarity or related to changes in the metavalent bonding character.

Summarizing, the results of this study have clearly indicated that high-pressure and composition-induced changes induce pronounced changes in the crystal structures and the lattice dynamics of the investigated compounds which might be correlated with a collapse ($\text{GeSe}_x\text{Te}_{1-x}$) or a weakening ($\text{Sb}_2\text{Te}_{3-x}\text{Se}_x$) of the metavalent bonding scheme.

Chapter 7

Outlook

The results of the low-temperature powder diffraction study on the compounds of the system $\text{GeSe}_x\text{Te}_{1-x}$ ($x=0, 0.2, 0.5, 0.75, 1$) have shown that low-temperature single crystal diffraction experiments are mandatory to elucidate the thermal behavior of the compounds and in particular the the role of the effect of the additional Ge·Ge and groupVI·groupVI interactions.

Also for the compounds from the system $\text{Sb}_2\text{Te}_{3-x}\text{Se}_x$ low-temperature single crystal diffraction data would allow a more detailed interpretation of the high-energy peaks in the inelastic neutron scattering data. Although, it seems to be clear that multi-phonon processes cause the additional peaks, it remains an open question why the magnitude of these processes is limited by the Se content of the samples. Low-temperature single crystal data together with theoretical analysis would allow a first interpretation. In order to study the dependence of the multi-phonon scattering from the phonon wave vector, single crystal inelastic neutron scattering experiments would be considered. Moreover, low-temperature single crystal data of these compounds would allow a more detailed interpretation of the role of the Sb-A2 bonds and the A2·A2 interactions on the lattice dynamics. Up to now, an interpretation of the low-temperature NIS data was only performed on the basis of ambient temperature single crystal data.

In this study, the Sb and Te partial phonon density of states of $\alpha\text{-Sb}_2\text{Te}_3$ (see section 5.2.5.2) were determined and in a previous study similar data were provided for the high-pressure δ -phase [153]. Similar information for the β - and γ -high-pressure phase are missing. In order to close this gap, high-pressure nuclear inelastic scattering experiments at the beamline P01 should be performed. Recently, a diamond anvil cell for high-pressure nuclear inelastic scattering experiments was developed and established at the beamline P01 [149] which allows high-pressure experiments under non-hydrostatic conditions, so that these experiments are now feasible. For the ^{125}Te measurements a ^{125}Te enriched Sb_2Te_3 sample is mandatory and would be available [103, 105]. The results of our high-pressure study on Sb_2Te_3 (see section 5.2.3) allows to adjust a pressure which corresponds to the pure β -phase. One expects that the α - to $\beta\text{-Sb}_2\text{Te}_3$ transition is accompanied with a collapse of the metavalent bonding. The metavalent bonding is believed to cause high Grüneisen parameter which are significantly smaller for exclusively covalently bonded compounds

[11]. Thus, the α - to β - Sb_2Te_3 transition is expected to be accompanied by a pronounced reduction of the Grüneisen parameter. The phonon data of the γ -phase would help to understand the already known data of the δ -polymorph in more detail. As the crystal structures of β -, γ - and δ - Sb_2Te_3 were, up to now, derived from powder diffraction experiments [77], a high-pressure single crystal study is mandatory to obtain a reliable and detailed characterization of the crystal structures, which would be an important basis for the interpretation of the inelastic scattering data.

Acknowledgements

I would like to use the opportunity to express my gratitude to my supervisors, advisers, colleagues and collaborators. Without their support many of the milestones of this PhD project would not have been reached. I would like to thank the following people in particular:

PD Dr. Karen Friese for her agreement to take the supervision of my PhD project, for many fruitful discussions, for reviewing my thesis, for the support during several beamtimes, and for always being open for new ideas.

Prof. Dr. Georg Roth for his agreement to be the second reviewer of this thesis.

Prof. Dr. Thomas Brückel for giving me the opportunity to perform my PhD thesis at his institute.

Dr. Raphaël P. Hermann for giving me the opportunity to perform several NIS measurements within his beamtimes, for giving me the chance to come to the USA and to work for five weeks at the ORNL, for the participation on my beamtime at the beamline ARCS (ORNL), for his support during the analysis of the NIS and INS data, and for many fruitful discussions.

Prof. Dr. Richard Dronskowski, Dr. Ralph P. Stoffel and **Michael Küpers** for the very pleasant and successful cooperation we had within the SFB 917 "Nanoswitches". In particular, I thank **Dr. Ralph P. Stoffel** for many DFT calculations by which he supported my PhD project. **Michael Küpers** I thank for the synthesis of several compounds from the $\text{GeSe}_x\text{Te}_{1-x}$ solid solution.

Zikang Li for the very pleasant cooperation we had in the scope of his B.Sc. project which he performed at the institute JCNS-2/PGI-4. He performed temperature-dependent powder diffraction measurements on several $\text{Sb}_2\text{Te}_{3-x}\text{Se}_x$ mixed crystals. This data allowed us the application of the homology relation.

Dr. Ilya Sergueev, Dr. Hans-Christian Wille and **Dr. O Leupold** for the fruitful discussions we had during long beamtime nights and for supporting me with important information around the beamline P01, PETRA III (DESY).

Dr. Doug L. Abernathy, Dr. Gabriele Sala and **Dr. J. Voigt** for supporting me during my experiments at the beamline ARCS (ORNL) and many discussions, which helped me to analyse the INS data.

Dr. Andrzej Grzechnik and my colleagues **Mohammed Ait Haddouch, Andreas Eich, Sabreen Hammouda** and **Johanna Wilden** for the participation on my beamtimes at the beamlines P02.2 (PETRA III, DESY) and ARCS (ORNL) and the pleasant atmosphere we had.

Dr. Konstantin Glazyrin for the assistance during my beamtimes at the beamline P02.2 (PETRA III, DESY) and his support by all kinds of problems with the experimental setup.

Micha Hölzle for the development and manufacturing of a high-pressure diamond anvil cell and a suitable cool-head for the cryostat for high-pressure nuclear inelastic scattering experiments at the beamline P01 (PETRA III, DESY).

Dr. Emmanuel Kentziger for his support during all of my powder diffraction experiments and for being always interested on the progress of my thesis.

Dipl. Phys. Jörg Perßon for his support during the synthesis of my compounds.

PD Dr. Oleg Petravic, Dr. Yinguo Xiao and Berthold Schmitz for their support during my measurements at the DynaCool.

Deutsche Forschungsgemeinschaft within the **SFB 917 "Nanoswitches"** for the financial support.

Deutsches Elektronensynchrotron (DESY) and **Oak Ridge National Laboratory (ORNL)** for the provision of beamtimes and financial support.

My family and friends for their support and patience during the last three years.

I thank all of my colleagues at the institute JCNS-2/PFI-4 for a very pleasant and constructive working atmosphere and for the support during the last three years.

Appendix A

Unit cell transformations

For all transformations performed in this thesis the relation shown in equation (A.1) was used:

$$G_i = M^T \cdot G_j \cdot M \quad (\text{A.1})$$

Here, G_i and G_j are the metrical tensors (equation (A.2)) of the starting (j) and the required (i) unit cell, the transformation matrix M describes the relation between the lattice parameter of both unit cells, and M^T is the corresponding transposed matrix:

$$G = \begin{pmatrix} a^2 & a \cdot b \cdot \cos \gamma & a \cdot c \cdot \cos \beta \\ a \cdot b \cdot \cos \gamma & b^2 & b \cdot c \cdot \cos \alpha \\ a \cdot c \cdot \cos \beta & b \cdot c \cdot \cos \alpha & c^2 \end{pmatrix} \quad (\text{A.2})$$

For the transformations performed in this study the following transformation matrices have been used:

$R3mH \rightarrow R3mR$ and $R3mR \rightarrow R3mH$:

$$M_{R3mH}^{R3mR} = \begin{pmatrix} \frac{2}{3} & \frac{1}{3} & \frac{1}{3} \\ \frac{1}{3} & \frac{1}{3} & \frac{2}{3} \\ \frac{1}{3} & \frac{1}{3} & \frac{1}{3} \end{pmatrix} \quad \text{and} \quad M_{R3mR}^{R3mH} = \begin{pmatrix} 1 & 0 & 1 \\ \bar{1} & 1 & 1 \\ 0 & \bar{1} & 1 \end{pmatrix} \quad (\text{A.3})$$

$R3mH \rightarrow$ pseudo-cubic and pseudo-cubic $\rightarrow R3mH$:

$$M_{R3mH}^{P.C.} = \begin{pmatrix} \frac{4}{3} & \frac{2}{3} & \frac{2}{3} \\ \frac{2}{3} & \frac{2}{3} & \frac{4}{3} \\ \frac{1}{3} & \frac{1}{3} & \frac{1}{3} \end{pmatrix} \quad \text{and} \quad M_{P.C.}^{R3mH} = \begin{pmatrix} \frac{1}{2} & 0 & 1 \\ \frac{1}{2} & \frac{1}{2} & 1 \\ 0 & \frac{1}{2} & 1 \end{pmatrix} \quad (\text{A.4})$$

$R3mR \rightarrow$ pseudo-cubic and pseudo-cubic $\rightarrow R3mR$:

$$M_{R3mR}^{\text{P.C.}} = \begin{pmatrix} \bar{1} & 1 & 1 \\ 1 & \bar{1} & 1 \\ 1 & 1 & \bar{1} \end{pmatrix} \quad \text{and} \quad M_{\text{P.C.}}^{R3mR} = \begin{pmatrix} 0 & \frac{1}{2} & \frac{1}{2} \\ \frac{1}{2} & 0 & \frac{1}{2} \\ \frac{1}{2} & \frac{1}{2} & 0 \end{pmatrix} \quad (\text{A.5})$$

$C2/m$, non-standard $\rightarrow C2/m$, standard:

$$M = \begin{pmatrix} 1 & 0 & 1 \\ 0 & 1 & 0 \\ 0 & 0 & 1 \end{pmatrix} \quad (\text{A.6})$$

Appendix B

Nuclear inelastic scattering

B.1 ^{121}Sb and ^{125}Te Mössbauer spectroscopy

In figure B.1 the decay scheme of a ^{121m}Sn containing source is shown. The ^{121m}Sn nucleus has two different decay channels, which are a β^- decay and an internal conversion (denoted as IC). The β^- decay has a probability of 22.4 % and results in the formation of a $^{121}\text{Sb}(7/2+)$ nucleus, which corresponds to an excited state of ^{121}Sb . This nucleus decays under an emission of a γ -quantum with a characteristic energy of 37.13 keV into its $^{121}\text{Sb}(5/2+)$ ground state. By decaying through an internal conversion $^{121m}\text{Sn}(3/2+)$ decays to $^{121}\text{Sn}(3/2-)$ under an emission of X-ray fluorescence followed by a decay into the $^{121}\text{Sb}(5/2+)$ ground state. At this point it has to be mentioned that the ^{121m}Sn decay is not the only way to reach the $^{121}\text{Sb}(5/2+)$ ground state and the decays of ^{121m}Te and ^{121}Te end finally also in the formation of $^{121}\text{Sb}(5/2+)$ [154, 155]. However, in practice, compounds containing ^{121m}Sn , e. g. ^{121m}Sn embedded in a $A^{121}\text{SnO}_3$ ($A=\text{Ba}$ [148], Ca [156]) matrix, are the most often used source materials and hence, only the ^{121m}Sn decay is discussed here. For ^{125}Te Mössbauer

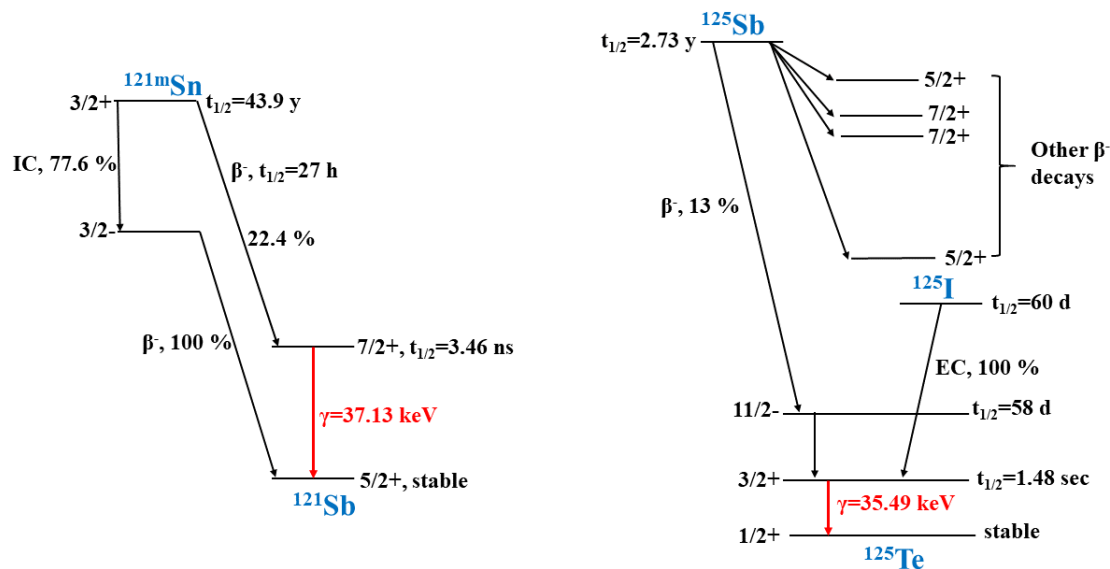


FIGURE B.1: Decay scheme of a ^{121m}Sn [154, 155] (left), ^{125}Sb [157, 158] and ^{125}I [158, 159] (both right) source.

spectroscopy, compounds containing ^{125}Sb , e. g. ^{125}Sb enriched Pd_2MnSb [157], or

^{125}I , e. g. $^{125}\text{I}/\text{Cu}$ [160], have been used as source and the corresponding ^{125}Sb [157, 158] and ^{125}I [158, 159], respectively, decay scheme is shown in figure B.1. ^{125}Sb decays with a probability of about 13 % via a β^- decay to the $S = 11/2^-$ state of ^{125}Te . This state decays over the unstable $S = 3/2+$ state to the $^{125}\text{Te}(1/2+)$ ground state. Other excited ^{125}Te states result from further β^- decays of ^{125}Sb [157, 158]. ^{125}I decays directly via an electron capture process to the unstable $^{125}\text{Te}(3/2+)$ state and, as mentioned above, this state decays to the stable $^{125}\text{Te}(1/2+)$ ground state [158, 159]. The 37.13 keV and 35.49 keV transition of ^{121}Sb and ^{125}Te can be used to measure ^{121}Sb and ^{125}Te nuclear absorption spectra, from which finally the ^{121}Sb and ^{125}Te (partial) phonon density of states, respectively, can be determined.

B.2 Resolution functions

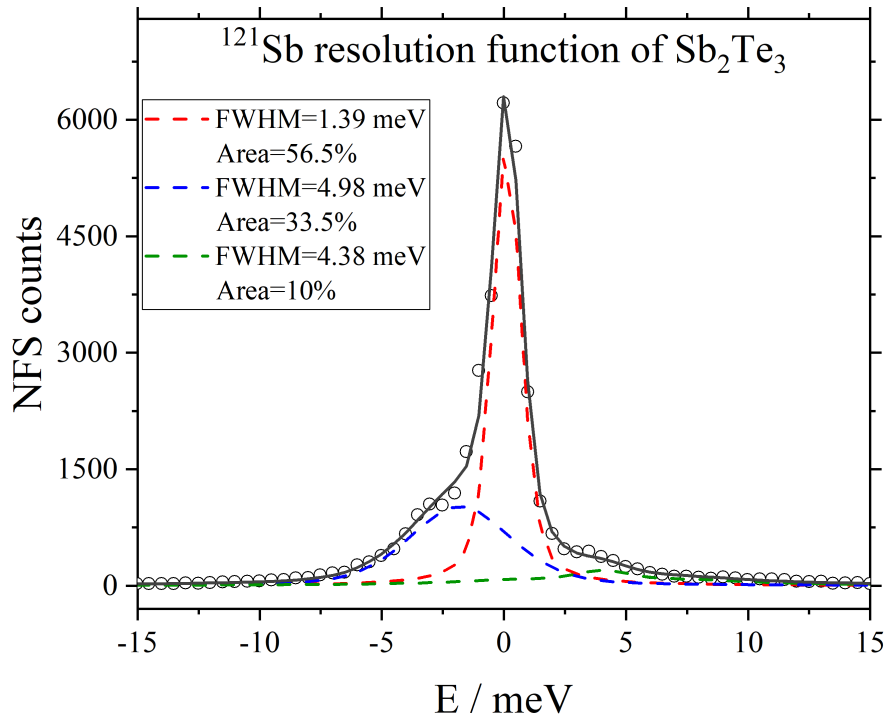


FIGURE B.2: Resolution function of the ^{121}Sb NIS data of Sb_2Te_3 .

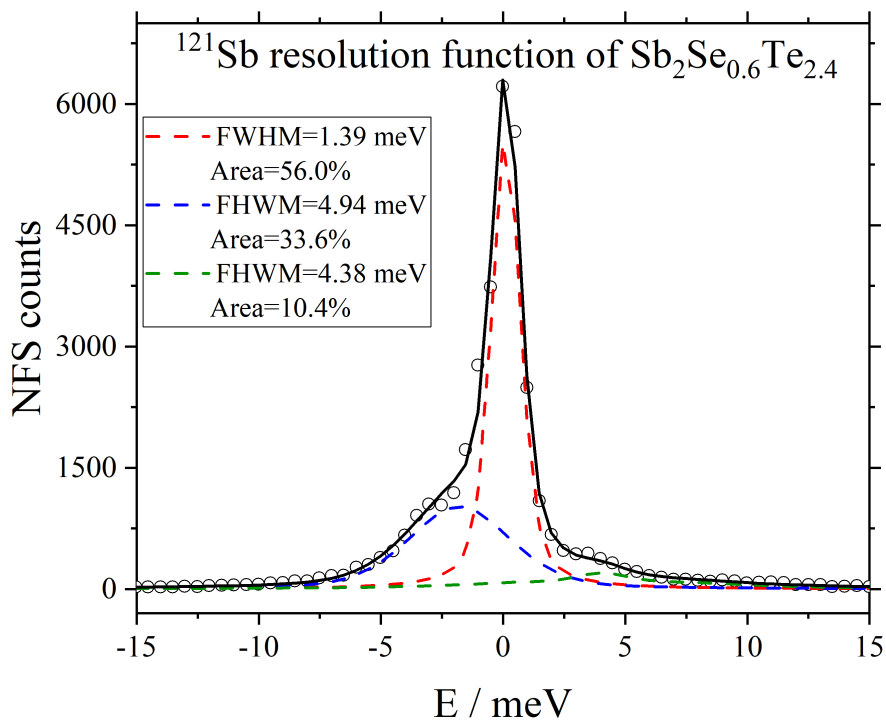


FIGURE B.3: Resolution function of the ^{121}Sb NIS data of $\text{Sb}_2\text{Se}_{0.6}\text{Te}_{2.4}$.

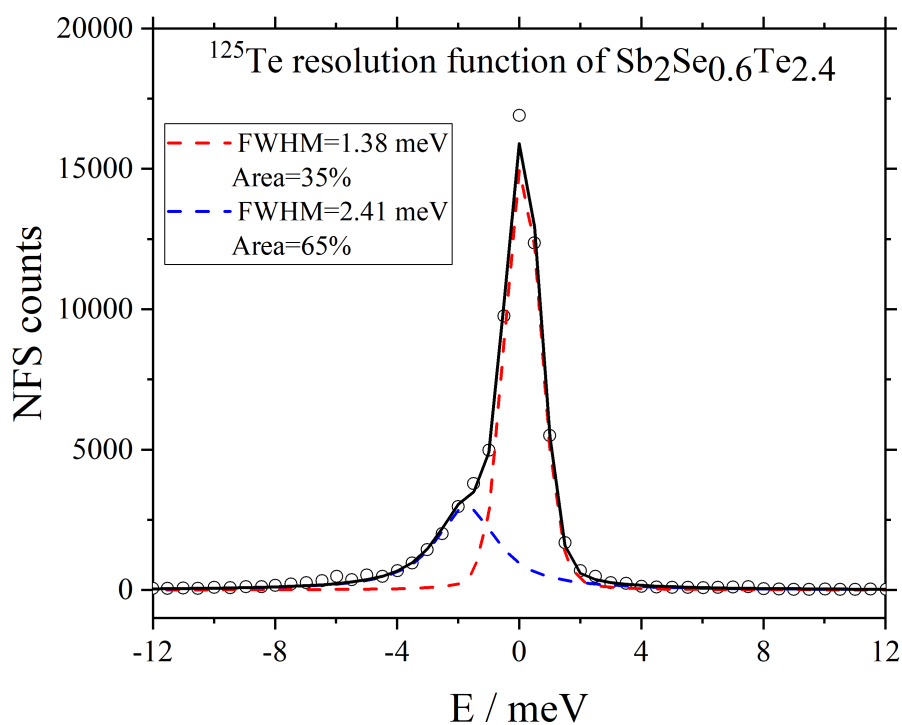


FIGURE B.4: Resolution function of the ^{125}Te NIS data of $\text{Sb}_2\text{Se}_{0.6}\text{Te}_{2.4}$.

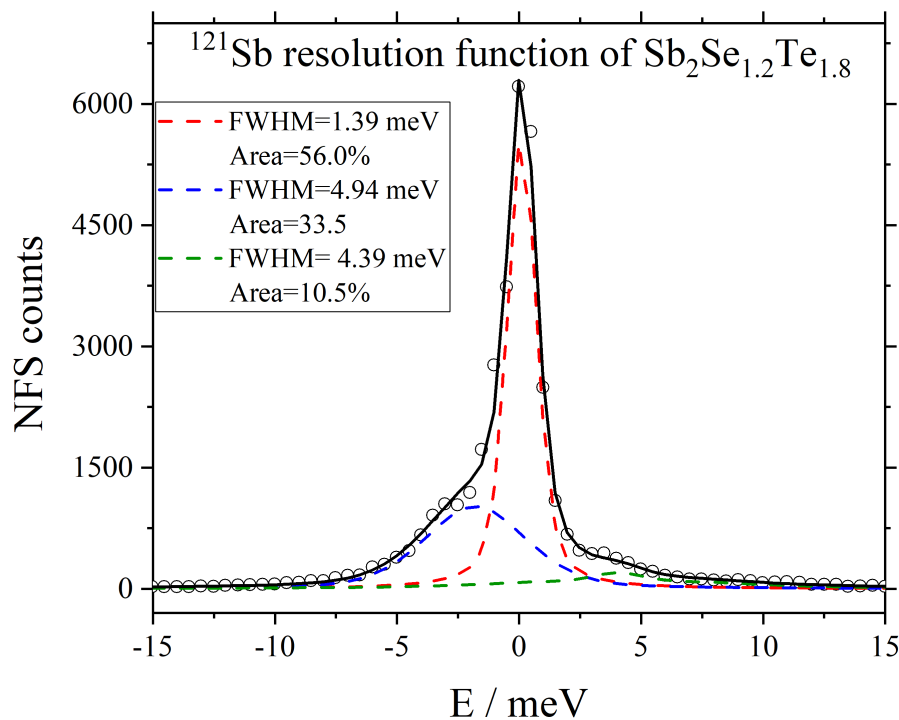


FIGURE B.5: Resolution function of the ^{121}Sb NIS data of $\text{Sb}_2\text{Se}_{1.2}\text{Te}_{1.8}$.

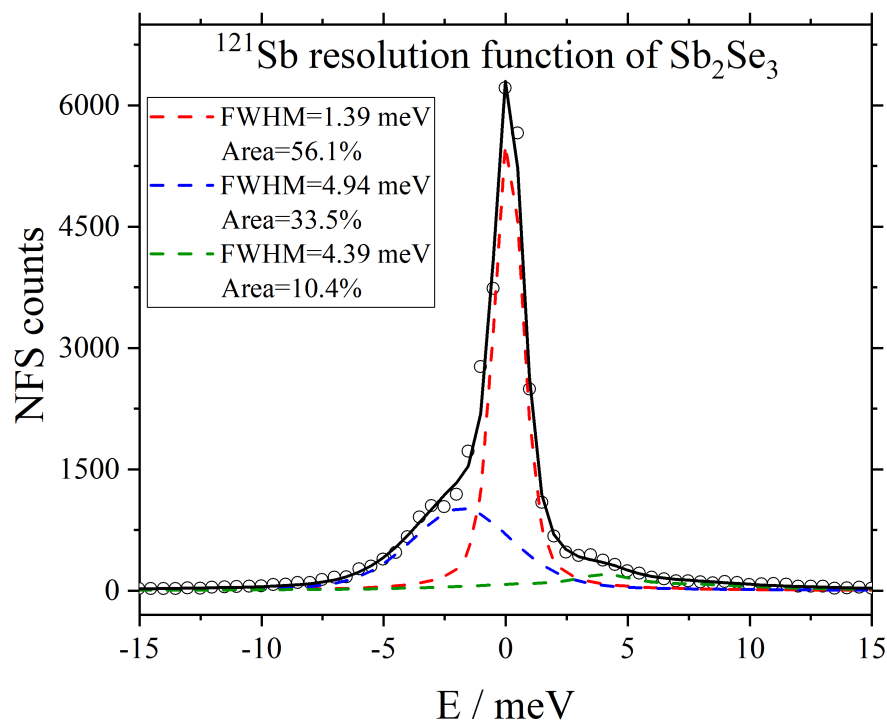


FIGURE B.6: Resolution function of the ^{121}Sb NIS data of Sb_2Se_3 .

Appendix C

GeSe_xTe_{1-x} solid solution

C.1 Indexed powder patterns

C.1.1 GeSe_xTe_{1-x} ($x=0, 0.2, 0.5, 0.75, 1$) mixed crystals

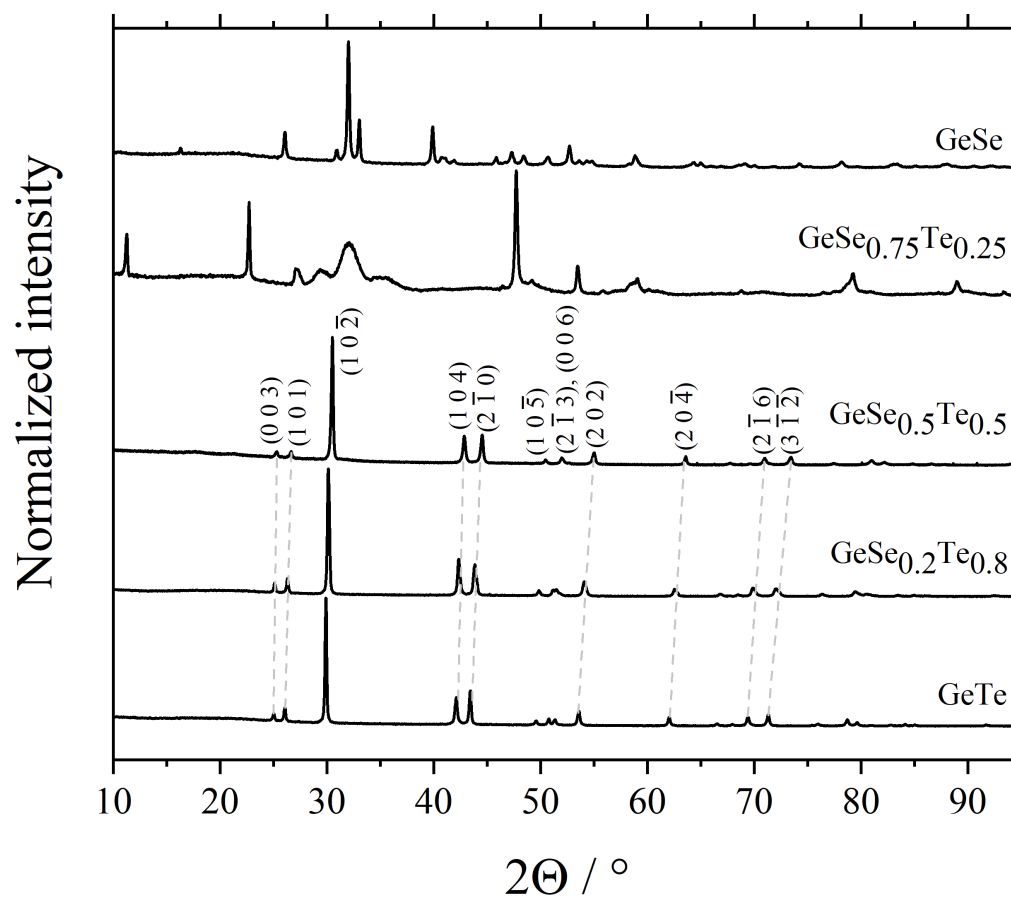


FIGURE C.1: Powder patterns of the GeSe_xTe_{1-x} ($x=0, 0.2, 0.5, 0.75, 1$) samples.

C.1.2 GeSe

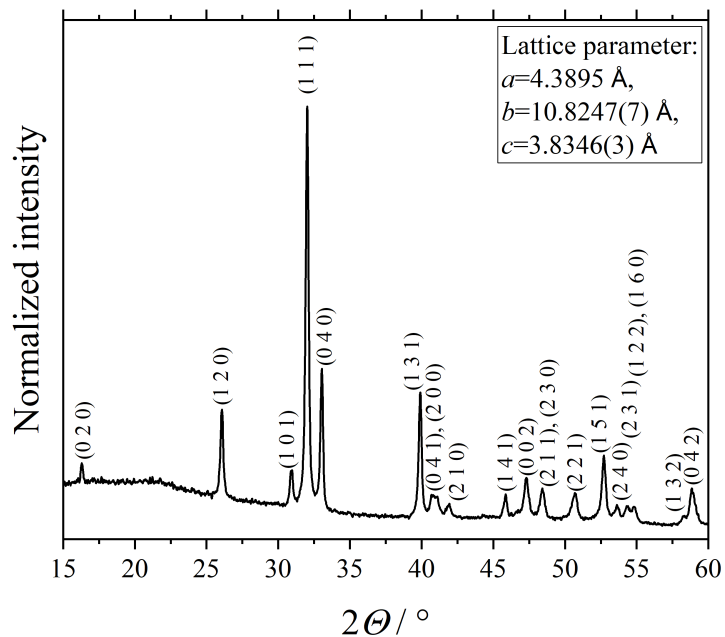


FIGURE C.2: Indexed powder pattern of GeSe between $15\text{-}60^\circ 2\theta$. Lattice parameter as obtained from a Le Bail refinement are given.

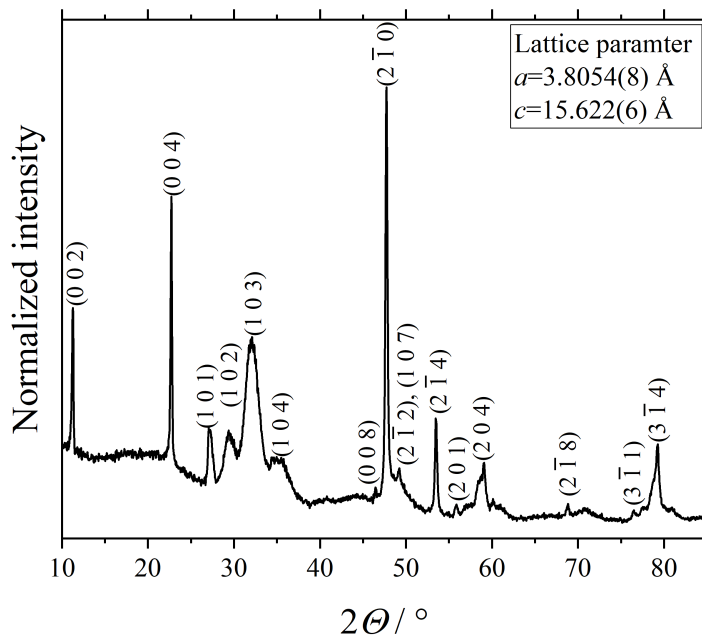
C.1.3 $\text{GeSe}_{0.75}\text{Te}_{0.25}$ 

FIGURE C.3: Indexed powder pattern of $\text{GeSe}_{0.75}\text{Te}_{0.25}$ between $10\text{-}85^\circ 2\theta$. Lattice parameter as obtained from a Le Bail refinement are given.

C.2 High-pressure powder patterns

C.2.1 GeTe

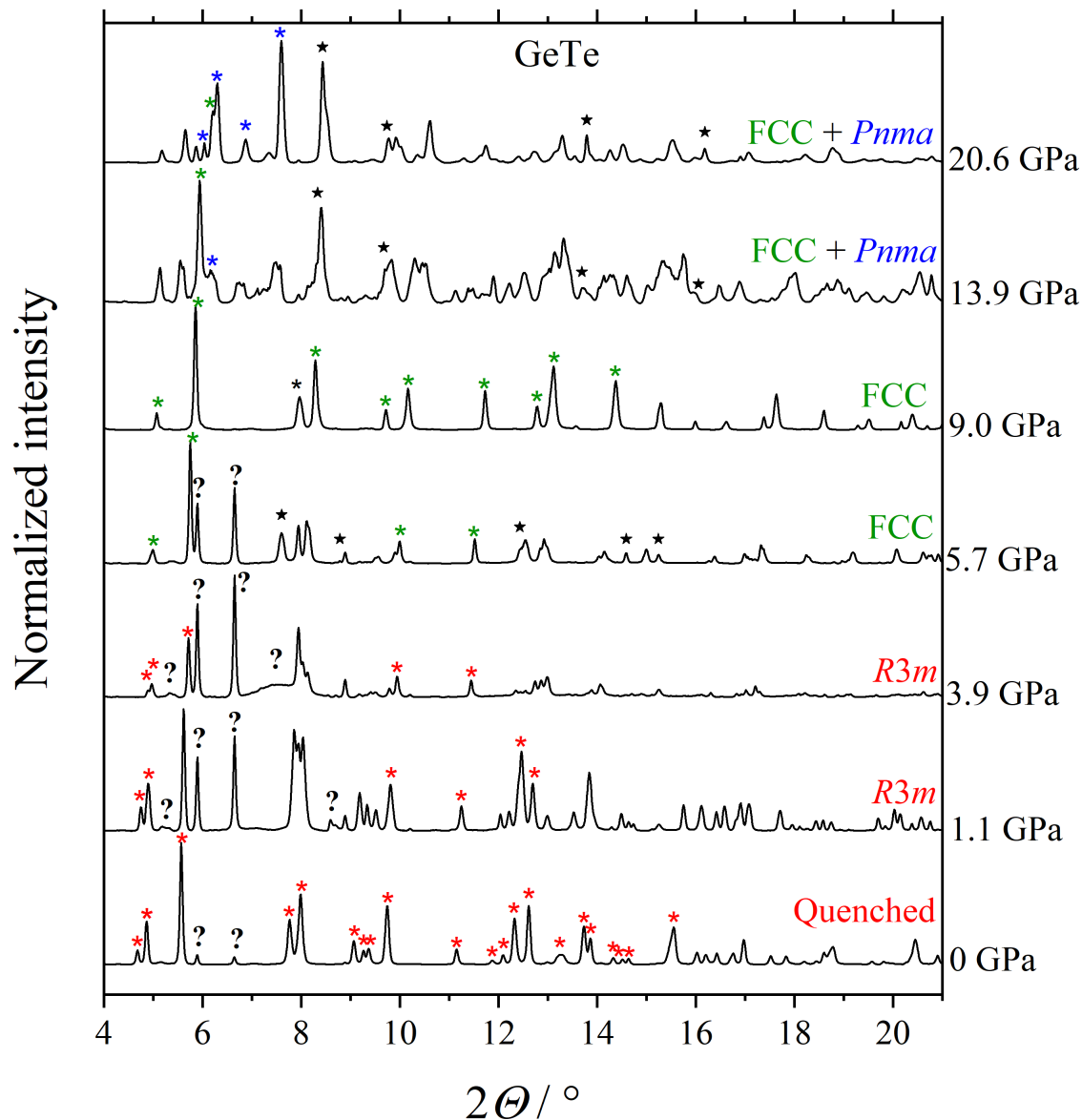


FIGURE C.4: Powder patterns obtained from a high-pressure study on GeTe at representative pressures. Red, green, blue, black asterisks: GeTe-I, GeTe-II, GeTe-III, Neon. Data obtained from the quenched sample are denoted as "Quenched". Peaks of an unknown impurity are marked by ?.

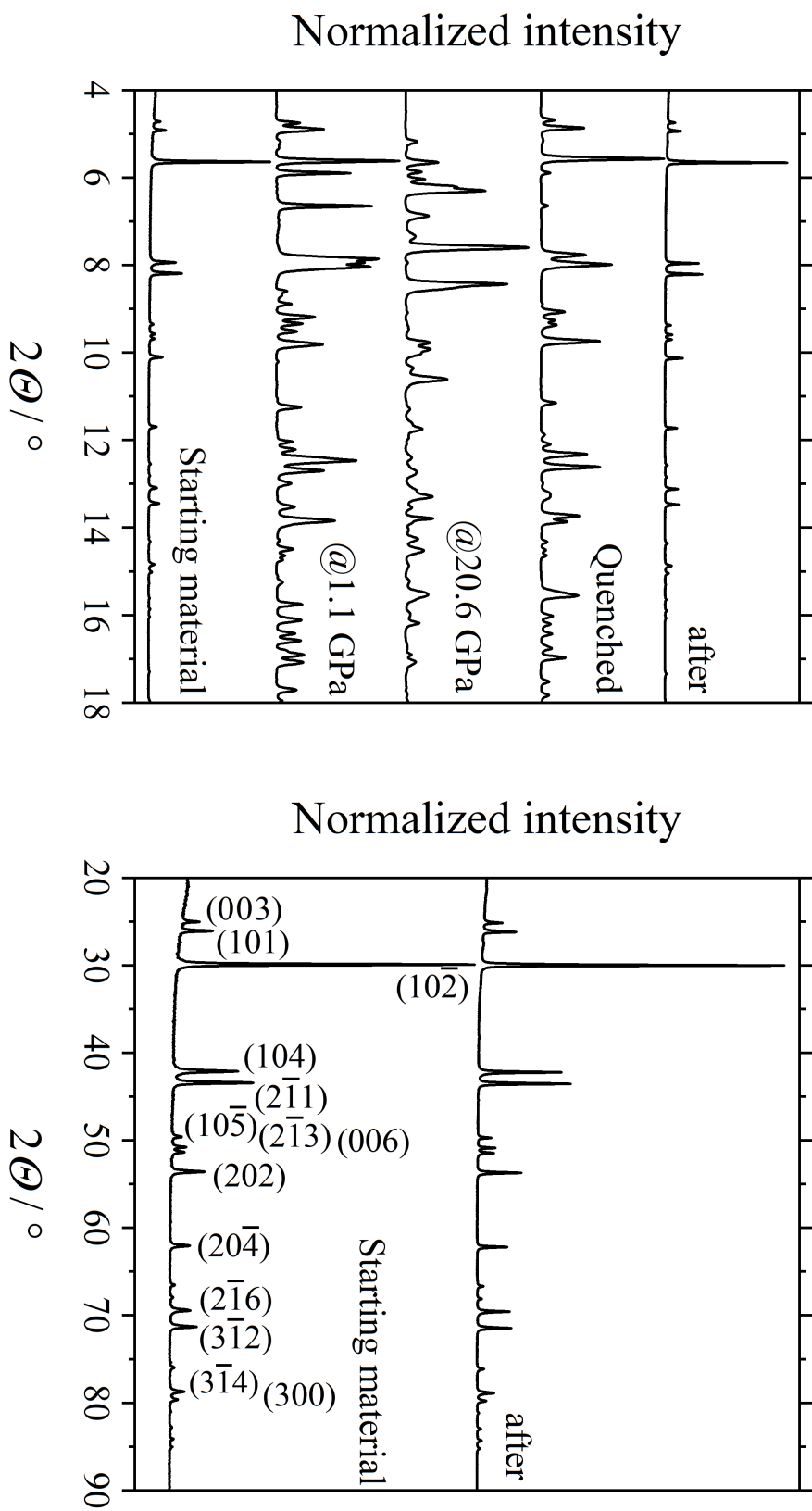


FIGURE C.5: Powder patterns of GeTe at ambient pressure, 1.1 GPa, 20.6 GPa and of the quenched sample. Powder pattern of the starting material which was not used for the high-pressure study ("after") showing the absence of the impurity phase.

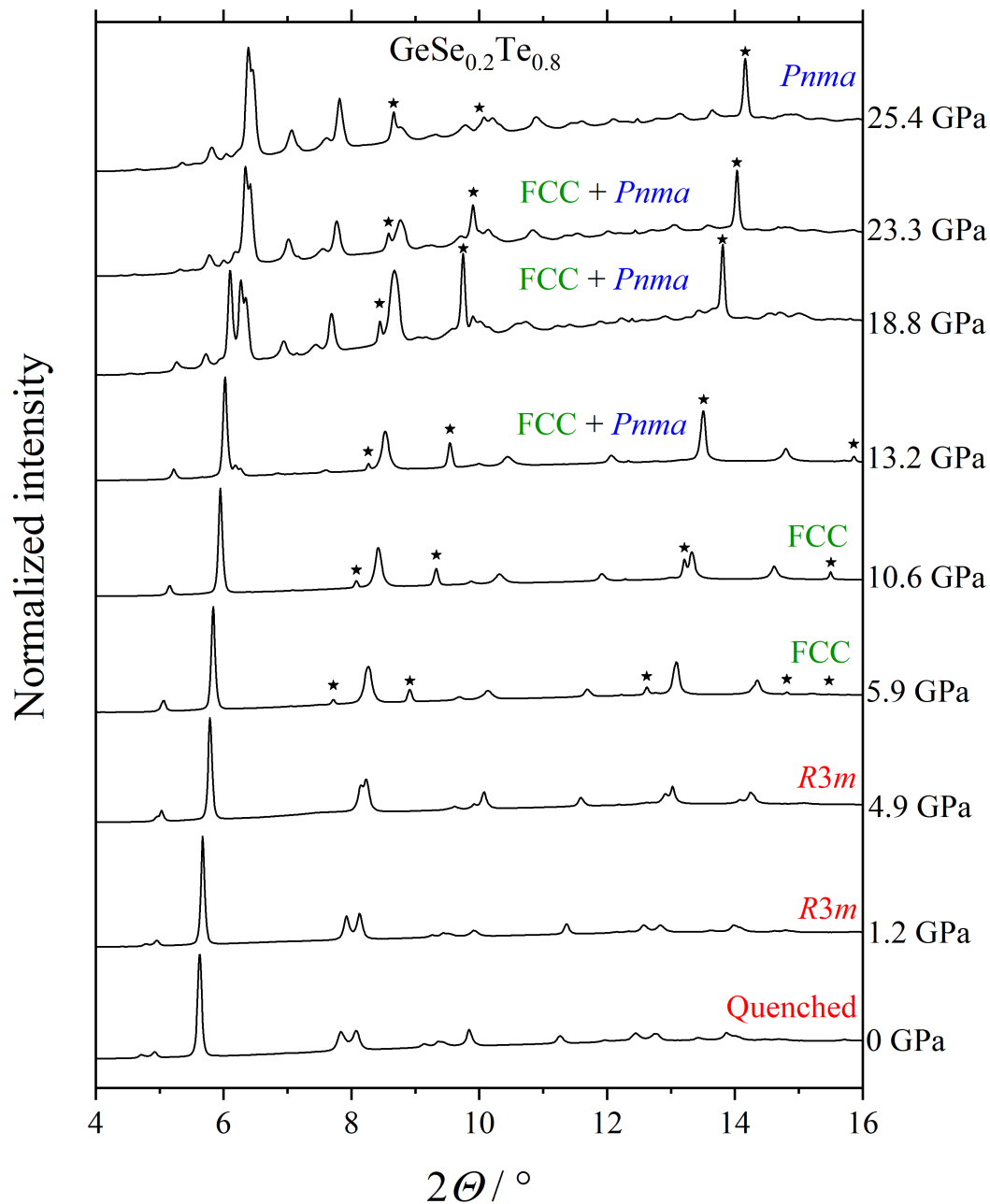
C.2.2 $\text{GeSe}_{0.2}\text{Te}_{0.8}$ 

FIGURE C.6: Powder patterns obtained from the high-pressure study on $\text{GeSe}_{0.2}\text{Te}_{0.8}$ at representative pressures. Red: GeTe-I, green: GeTe-II, blue: GeTe-III, asterisk: Neon.

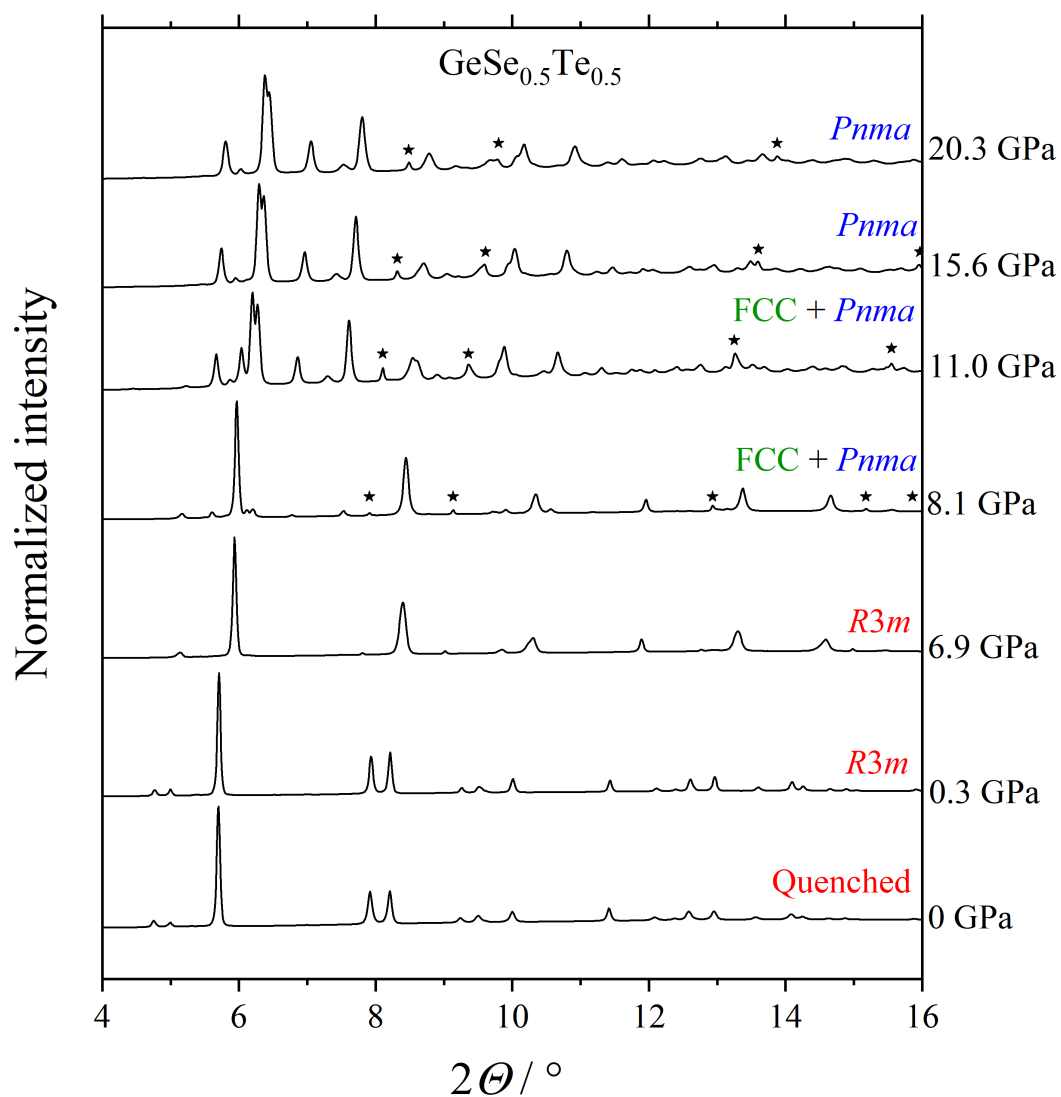
C.2.3 $\text{GeSe}_{0.5}\text{Te}_{0.5}$ 

FIGURE C.7: Powder patterns obtained from the high-pressure study on $\text{GeSe}_{0.5}\text{Te}_{0.5}$ at representative pressures. Red: GeTe-I, green: GeTe-II, blue: GeTe-III, asterisk: Neon.

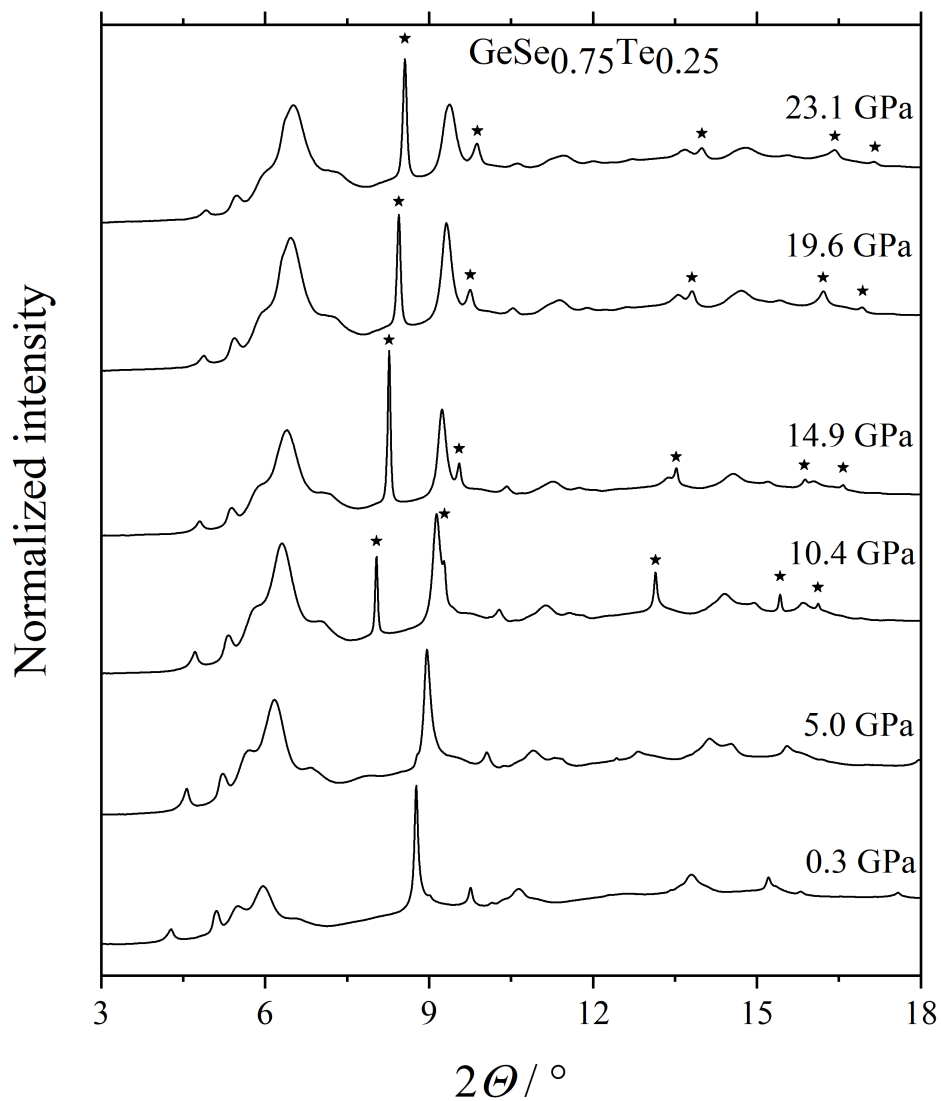
C.2.4 $\text{GeSe}_{0.75}\text{Te}_{0.25}$ 

FIGURE C.8: Powder patterns obtained from the high-pressure study on $\text{GeSe}_{0.75}\text{Te}_{0.25}$ at representative pressures. Neon peaks are marked by asterisks.

C.3 Indexing of the GeTe-III phase of $\text{GeSe}_{0.5}\text{Te}_{0.5}$

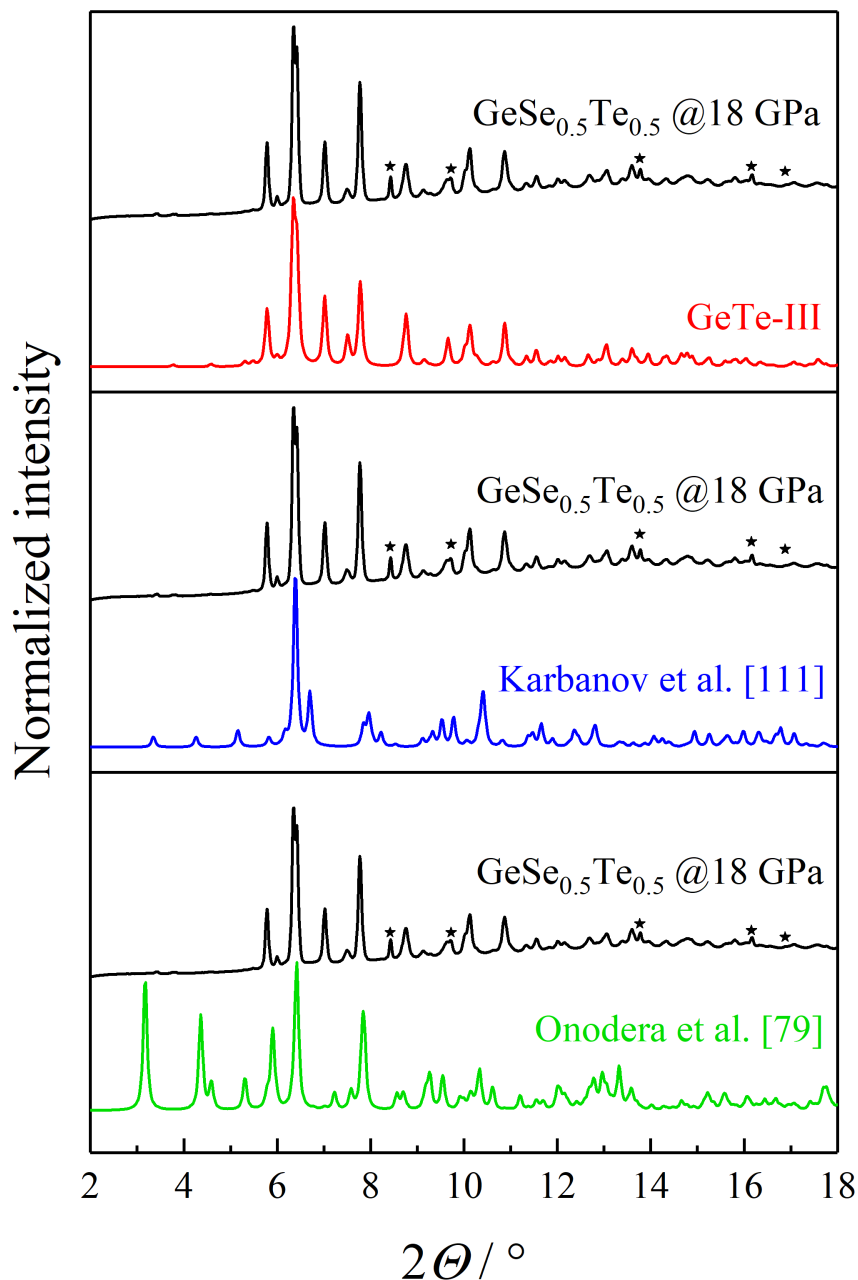


FIGURE C.9: Powder patterns of the GeTe-III phase of $\text{GeSe}_{0.5}\text{Te}_{0.5}$ at 18.8 GPa. Le Bail refinements on the experimental data were performed using the GeTe-III structure determined in this study and the previous structural models from the literature [111, 79]. Neon peaks are marked by asterisks.

C.4 Ge and Te/Se coordination in GeTe-III and β -GeSe

TABLE C.1: Ge coordination in GeTe-III and β -GeSe [128]. The distances between Ge and the neighboring atoms are given for both compounds. GeTe-III: bond f) represents the closest distance which does not significantly contribute to the Ge coordination (see text).

GeTe-III				β -GeSe			
Bond	Type	$d(18.8 \text{ GPa}) / \text{\AA}$	Number	Bond	Type	$d / \text{\AA}$	Number
a	Ge-Te	2.684(9)	1	a	Ge-Se	2.5867(5)	2
b	Ge-Te	2.746(7)	2	b	Ge-Se	2.5876(5)	1
c	Ge \cdots Te	2.888(7)	2	c	Ge \cdots Se	3.2732(6)	2
d	Ge \cdots Ge	2.971(7)	2	d	Ge \cdots Se	3.2777(8)	1
e	Ge \cdots Te	3.208(10)	1	e	Ge \cdots Ge	3.3743(7)	2
f	Ge \cdots Te	3.396(10)	1				

TABLE C.2: Te/Se coordination in GeTe-III and β -GeSe [128]. The distances between Te/Se and the neighboring atoms are given for both compounds. GeTe-III: bond e) represents the closest distance which does not significantly contribute to the Te coordination in GeTe-III (see text).

GeTe-III				β -GeSe			
Bond	Type	$d(18.8 \text{ GPa}) / \text{\AA}$	Number	Bond	Type	$d / \text{\AA}$	Number
a	Te-Ge	2.684(9)	1	a	Se-Ge	2.5867(5)	2
b	Te-Ge	2.746(7)	2	b	Se-Ge	2.5876(5)	1
c	Te \cdots Ge	2.888(7)	2	c	Se \cdots Ge	3.2732(6)	2
d	Te \cdots Ge	3.208(10)	1	d	Se \cdots Ge	3.2777(8)	1
e	Te \cdots Ge	3.396(10)	1	e	Se \cdots Se	3.5861(6)	2
f	Te \cdots Te	3.507(4)	2				

Appendix D

$\text{Sb}_2\text{Te}_{3-x}\text{Se}_x$ solid solution

D.1 Debye temperatures

TABLE D.1: Debye temperatures of the $\text{Sb}_2\text{Te}_{3-x}\text{Se}_x$ ($x=0, 0.6, 1.2, 1.8, 3$) mixed crystals determined from the low-temperature heat capacity data ($\Theta_{\text{D,PPMS}}$) and derived from the inelastic neutron data ($\Theta_{\text{D,INS}}$).

Sample	Sb_2Te_3	$\text{Sb}_2\text{Se}_{0.6}\text{Te}_{2.4}$	$\text{Sb}_2\text{Se}_{1.2}\text{Te}_{1.8}$	$\text{Sb}_2\text{Se}_{1.8}\text{Te}_{1.2}$	Sb_2Se_3
$\Theta_{\text{D,PPMS}} / \text{K}$	168.0(4)	174.5(3)	181.3(4)	182.5(4)	177.1(4)
$\Theta_{\text{D,INS}} / \text{K}$	160(3)	163(2)	175(2)	185(2)	233(3)

D.2 Low-temperature heat capacity

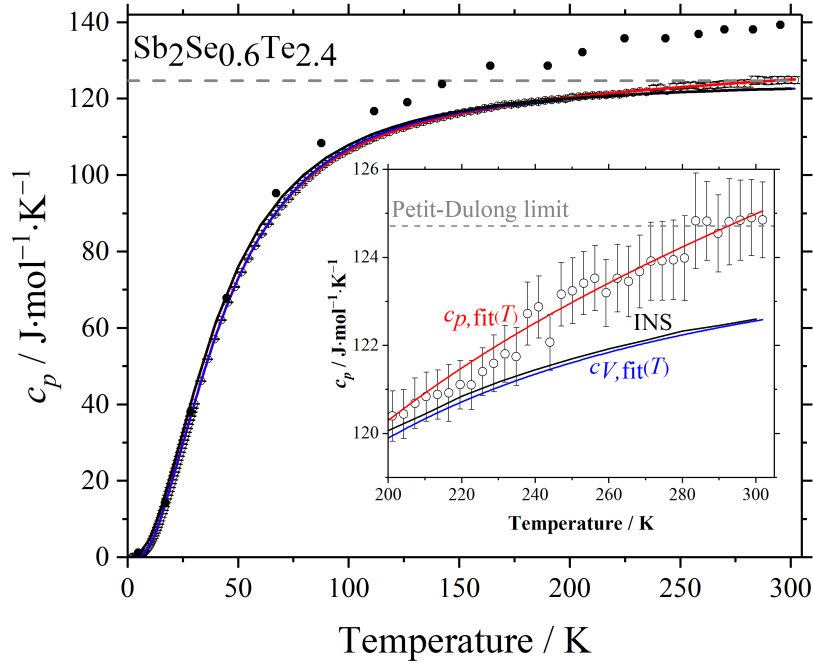


FIGURE D.1: The low-temperature heat capacity of the sample $\text{Sb}_2\text{Se}_{0.6}\text{Te}_{2.4}$. The data reported in the literature [147] (black dots) are depicted for comparison.

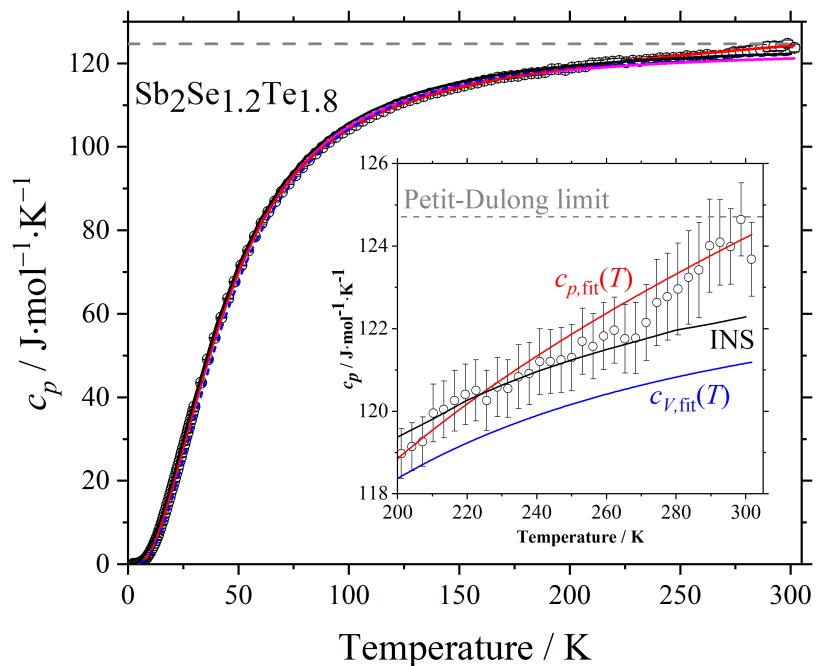


FIGURE D.2: The low-temperature heat capacity of the sample $\text{Sb}_2\text{Se}_{1.2}\text{Te}_{1.8}$.

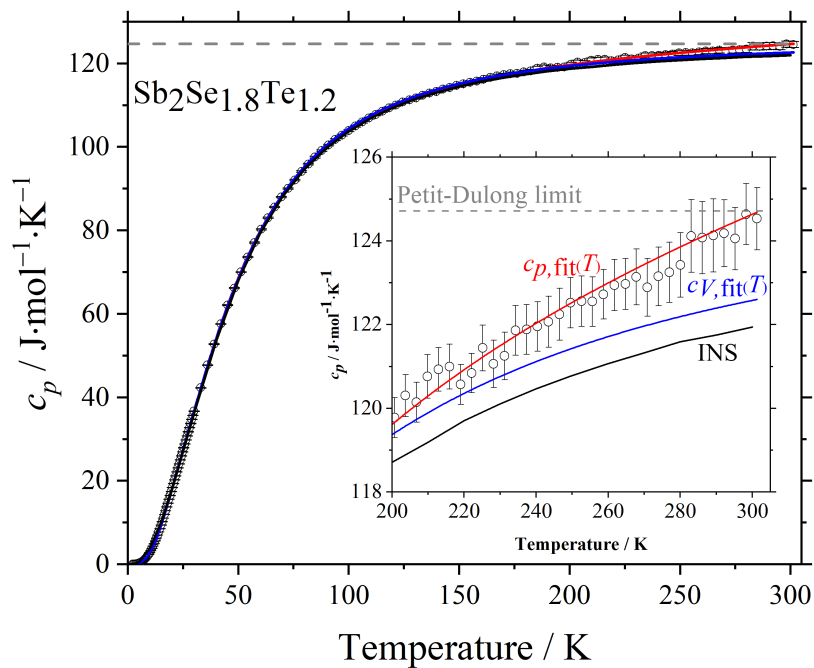


FIGURE D.3: The low-temperature heat capacity of the sample $\text{Sb}_2\text{Se}_{1.8}\text{Te}_{1.2}$.

D.3 Indexed powder patterns

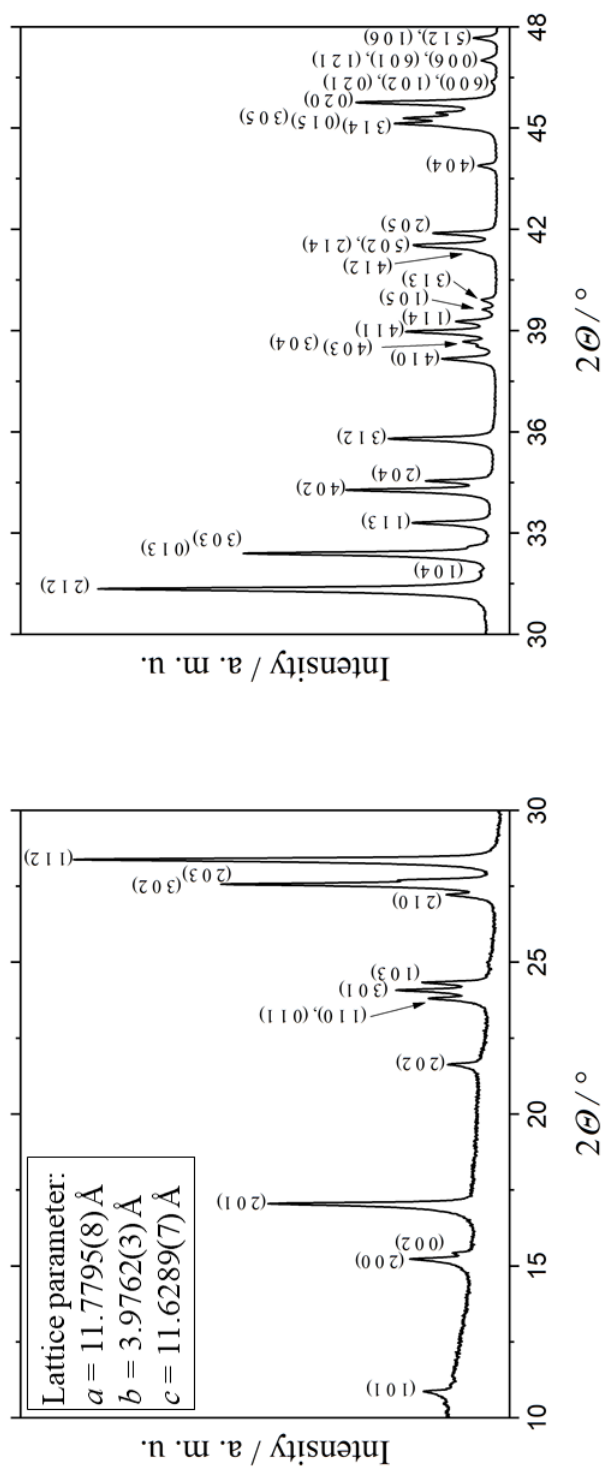
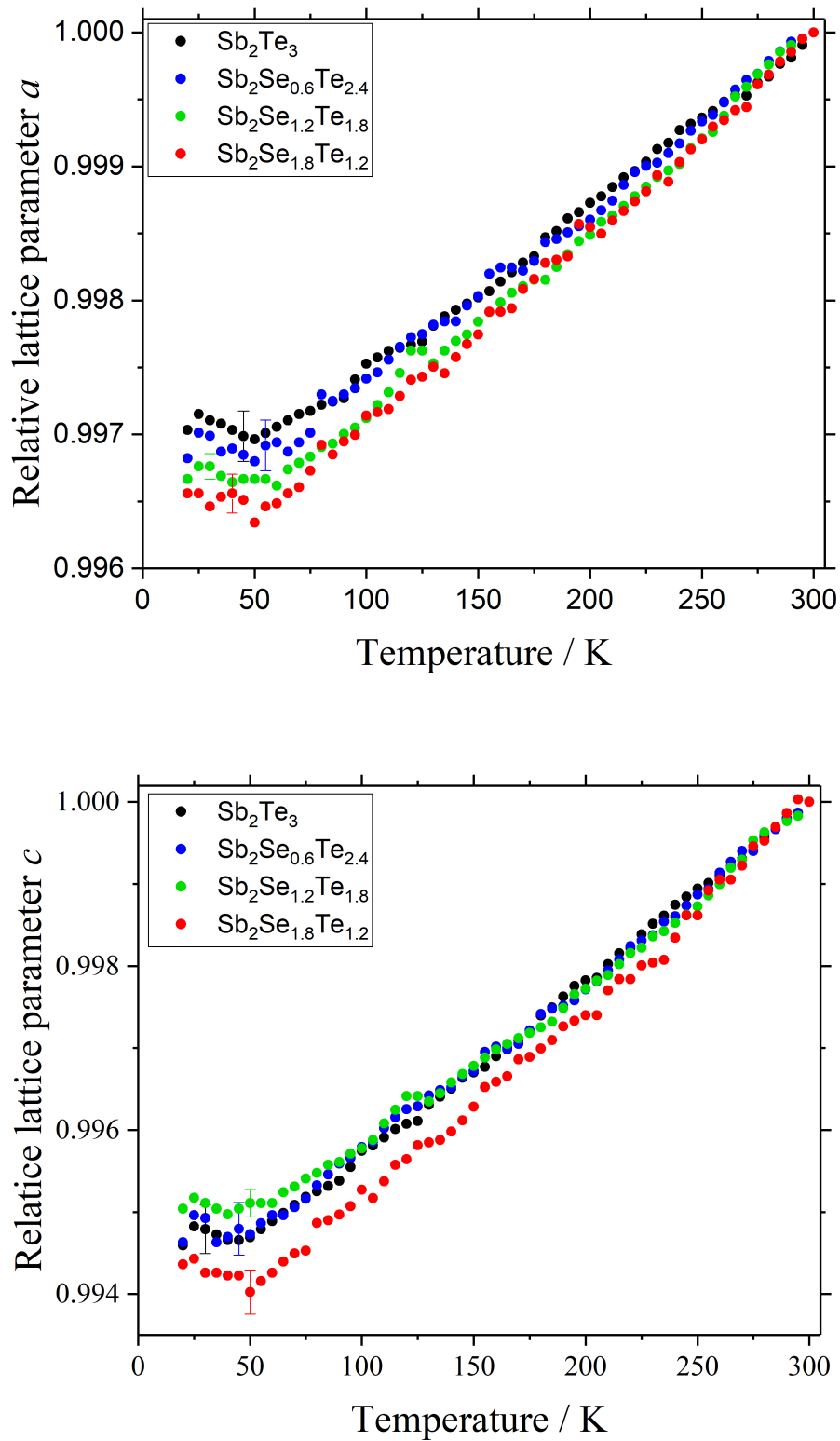


FIGURE D.4: Indexed powder patterns of Sb_2Se_3 between 10-30 (left) and 30-48° 2θ (right). Lattice parameter as obtained from a Le Bail refinement are given.

D.4 Temperature dependence of the lattice parameter

FIGURE D.5: The temperature-dependent normalized lattice parameter of several $\text{Sb}_2\text{Te}_{3-x}\text{Se}_x$ mixed crystals [107].

D.5 Total phonon density of states

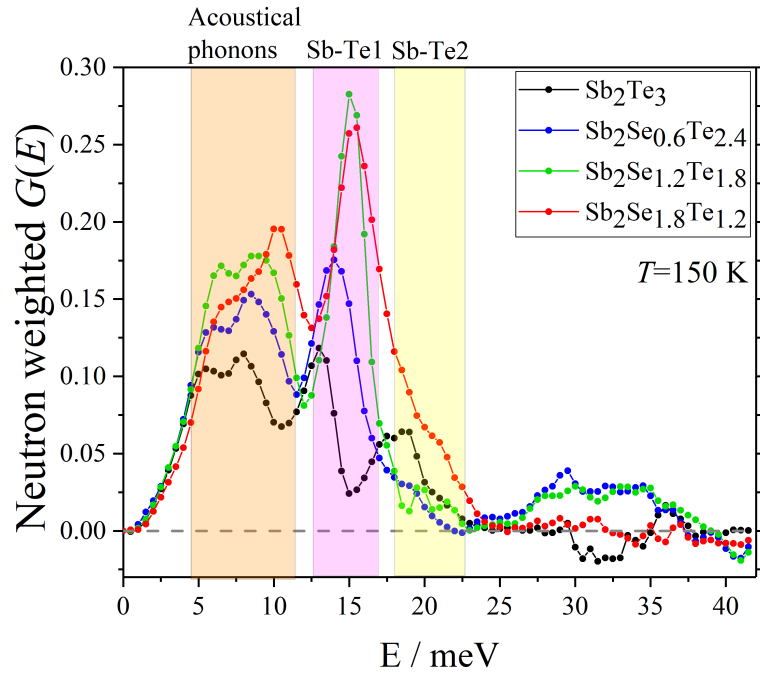


FIGURE D.6: Total phonon density of states of the $Sb_2Te_{3-x}Se_x$ ($x=0, 0.6, 1.2, 1.8$) mixed crystals at 150 K.

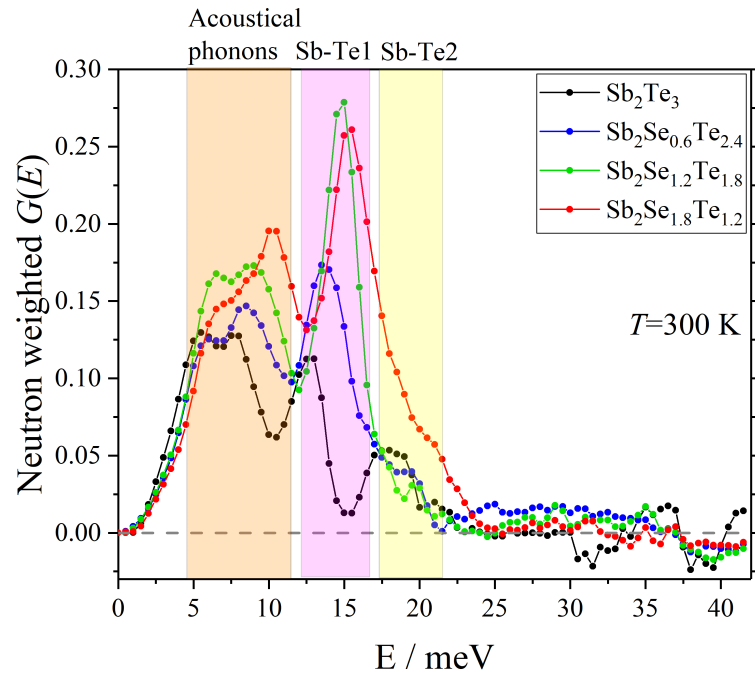


FIGURE D.7: Total phonon density of states of the $Sb_2Te_{3-x}Se_x$ ($x=0, 0.6, 1.2, 1.8$) mixed crystals at 300 K.

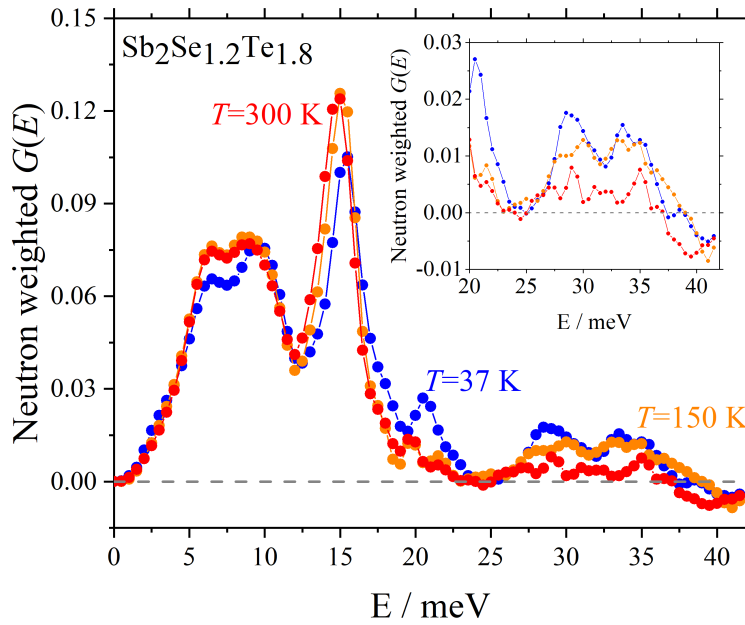


FIGURE D.8: Comparison between the total phonon density of states of $\text{Sb}_2\text{Se}_{1.2}\text{Te}_{1.8}$ measured at 37, 150 and 300 K.

D.6 Total scattering functions

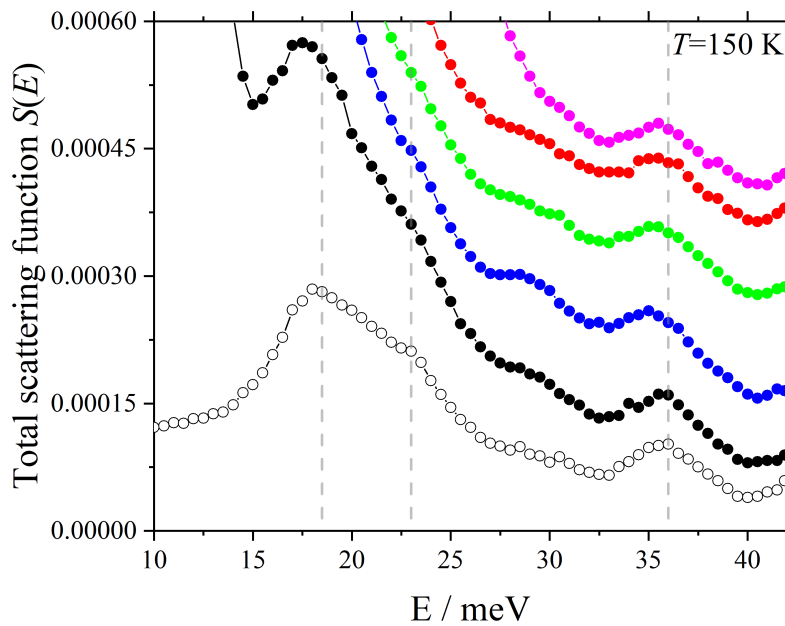


FIGURE D.9: Total scattering functions of the $\text{Sb}_2\text{Te}_{3-x}\text{Se}_x$ ($x=0, 0.6, 1.2, 1.8, 3$) mixed crystals measured at 150 K. For comparison the corresponding data of the empty can are shown.

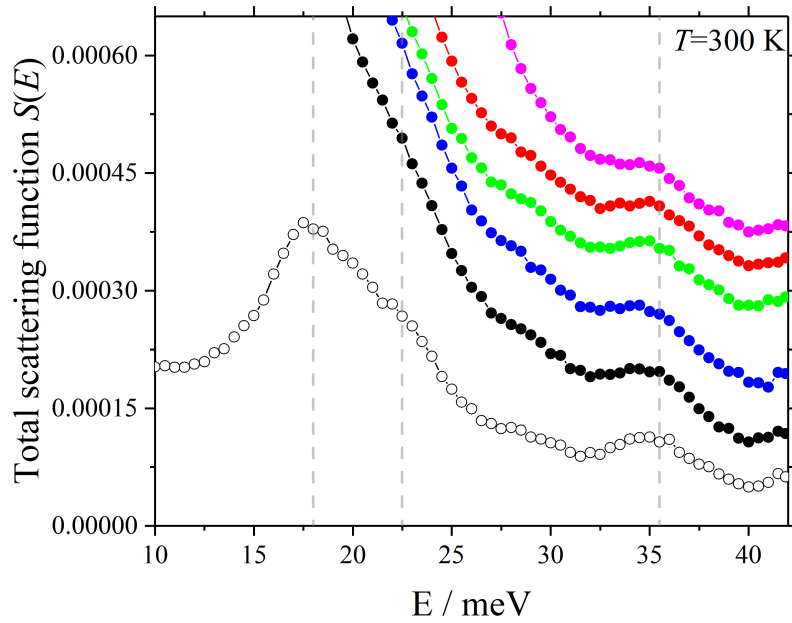


FIGURE D.10: Total scattering functions of the $Sb_2Te_{3-x}Se_x$ ($x=0, 0.6, 1.2, 1.8, 3$) mixed crystals measured at 300 K. For comparison the corresponding data of the empty can are shown.

D.7 Temperature-dependent mode shifts

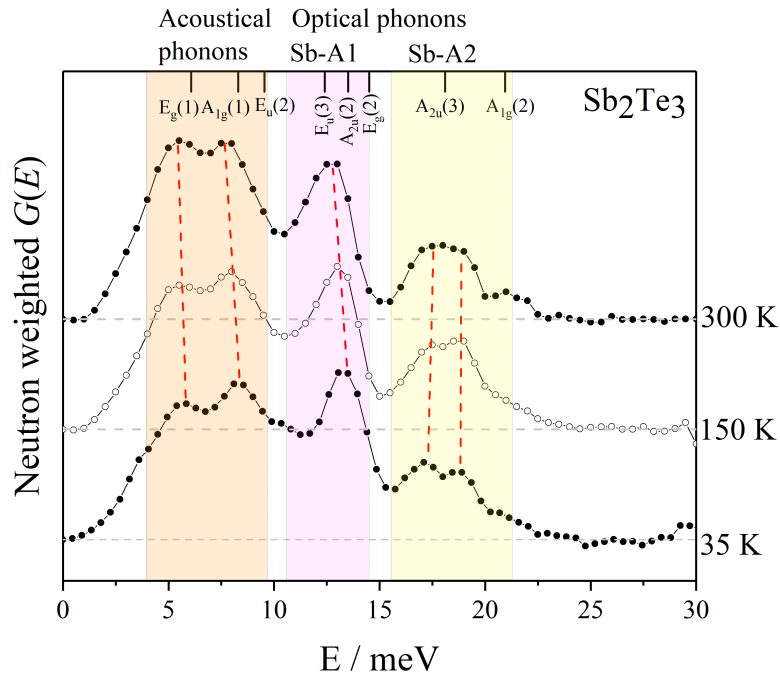


FIGURE D.11: Temperature-dependent mode shifts in the total phonon density of states of Sb_2Te_3 .

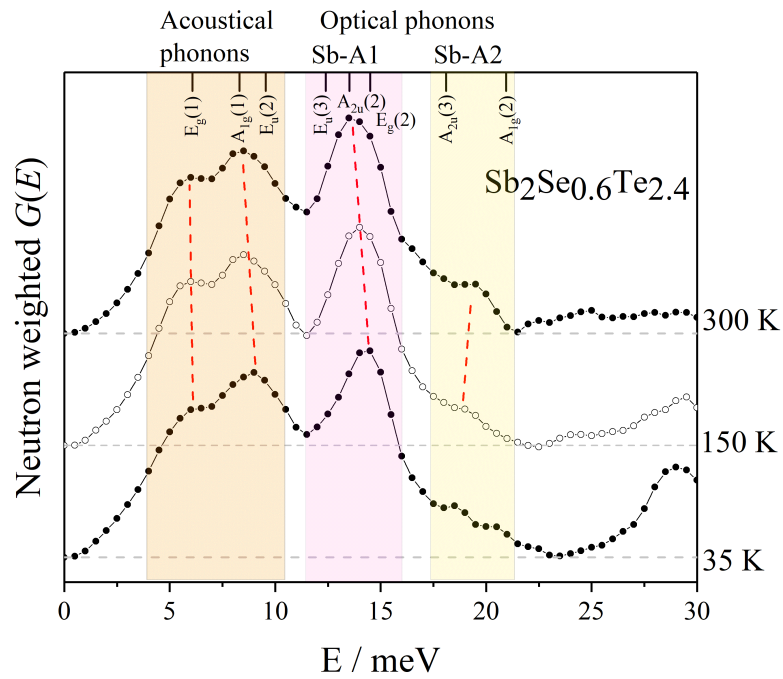


FIGURE D.12: Temperature-dependent mode shifts in the total phonon density of states of $\text{Sb}_2\text{Se}_{0.6}\text{Te}_{2.4}$.

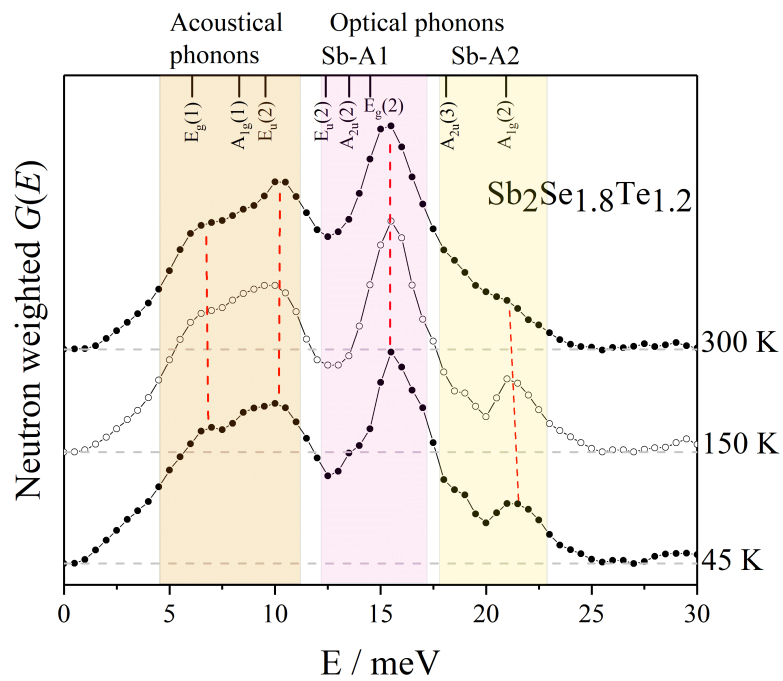


FIGURE D.13: Temperature-dependent mode shifts in the total phonon density of states of $\text{Sb}_2\text{Se}_{1.8}\text{Te}_{1.2}$.

Bibliography

- [1] D. Lencer, M. Salinga, B. Grabowski, T. Hickel, J. Neugebauer, and M. Wuttig, "A map for phase-change materials", *Nature*, vol. 7, pp. 972–977, 2008.
- [2] M. Wuttig and N. Yamada, "Phase-change materials for rewritable data storage", *Nature*, vol. 6, pp. 824–832, 2007.
- [3] K. Shportko, S. Kremers, M. Woda, D. Lencer, J. Robertson, and M. Wuttig, "Resonant bonding in crystalline phase-change materials", *Nature*, vol. 7, pp. 653–658, 2008.
- [4] S. Raoux, "Phase-change materials", *Annu. Rev. Mater. Res.*, vol. 39, pp. 25–48, 2009.
- [5] P. B. Littlewood, "The crystal structure of IV-VI compounds: I. Classification and description", *J. Phys. C: Solid St. Phys.*, vol. 13, pp. 4855–73, 1980.
- [6] L. Yang, J. Q. Li, R. Chen, Y. Li, F. S. Liu, and W. Q. Ao, "Influence of Se substitution in GeTe on phase and thermoelectric properties", *J. Electron. Mater.*, vol. 45, pp. 5533–5539, 2016.
- [7] D. Das, K. Malik, A. K. Deb, V. A. Kublachinskii, V. G. Kytin, S. Chatterjee, D. Das, S. Dhara, S. Bandyopadhyay, and A. Banerjee, "Tuning of thermoelectric properties with changing Se content in Sb_2Te_3 ", *EPL*, vol. 113, no. 47004, 2016.
- [8] A. P. J. M. Jongenelis, J. H. Coombs, W. van Es-Spiekman, and B. A. J. Jacobs, "Laser-induced crystallization phenomena in GeTe-based alloys. III. GeTeSe alloys for a CD compatible erasable disk", *J. Appl. Phys.*, vol. 79, pp. 8349–8356, 1996.
- [9] M. Cagnoni, D. Führen, and M. Wuttig, "Thermoelectric performance of IV–VI compounds with octahedral-like coordination: A chemical-bonding perspective", *Adv. Mater.*, vol. 30, no. 1801787, 2018.
- [10] J.-Y. Raty, M. Schumacher, P. Golub, V. L. Deringer, C. Gatti, and M. Wuttig, "A quantum-mechanical map for bonding and properties in solids", *Adv. Mater.*, vol. 31, no. 1806280, 2019.
- [11] M. Wuttig, V. L. Deringer, X. Gonze, C. Bichara, and J.-Y. Raty, "Incipient metals: Functional materials with a unique bonding mechanism", *Adv. Mater.*, vol. 30, no. 1803777, 2018.
- [12] H. Rauh, R. Geick, H. Köhler, N. Nücker, and N. Lehner, "Generalized phonon density of states of the layer compounds Bi_2Se_3 , Bi_2Te_3 , Sb_2Te_3 and $\text{Bi}_2(\text{Te}_{0.5}\text{Se}_{0.5})_3$, $(\text{Bi}_{0.5}\text{Sb}_{0.5})_2\text{Te}_3$ ", *J. Phys. C: Solid State Phys.*, vol. 14, pp. 2705–2712, 1981.

- [13] U. Wdowik, K. Parlinski, S. Rols, and T. Chatterji, "Soft-phonon mediated structural phase transition in GeTe", *Phys. Rev. B*, no. 224306, 2014.
- [14] D. Bessas, I. Sergueev, H.-C. Wille, J. Perßon, D. Ebling, and R. P. Hermann, "Lattice dynamics in Bi₂Te₃ and Sb₂Te₃: Te and Sb density of phonon states", *Phys. Rev B*, vol. 86, no. 224301, 2012.
- [15] P. Bauer Pereira, I. Sergueev, S. Gorsse, J. Dadda, E. Müller, and R. P. Hermann, "Lattice dynamics and structure of GeTe, SnTe and PbTe", *Phys. Status Solidi B*, vol. 250, pp. 1300–1307, 2013.
- [16] R. Shatlaf and X. Gonze, "Lattice dynamics and specific heat of α -GeTe: Theoretical and experimental study", *Phys. Rev. B*, vol. 79, no. 075204, 2009.
- [17] S. Lee, K. Esfarjani, T. Luo, J. Zhou, Z. Tian, and G. Chen, "Resonant bonding leads to low lattice thermal conductivity", *Nature*, vol. 5, no. 3525, 2014.
- [18] R. P. Stoffel, V. L. Deringer, R. E. Simon, R. P. Hermann, and R. Dronskowski, "A density-functional study on the electronic and vibrational properties of layered antimony telluride", *J. Phys.: Condens. Matter*, vol. 27, no. 085402, 2015.
- [19] V. Deringer, R. P. Stoffel, M. Wuttig, and R. Dronskowski, "Vibrational properties and bonding nature of Sb₂Se₃ and their implications for chalcogenide materials", *Chem. Sci.*, vol. 6, pp. 5255–5262, 2015.
- [20] V. L. Deringer, R. P. Stoffel, and R. Dronskowski, "Vibrational and thermodynamic properties of GeSe in the quasiharmonic approximation", *Phys. Rev. B*, vol. 89, no. 094303, 2014.
- [21] T. Matsunaga, N. Yamada, R. Kojima, S. Shamoto, M. Sato, H. Tanida, T. Uruga, S. Kohara, M. Takata, P. Zalden, G. Bruns, I. Sergueev, H.-C. Wille, R. P. Hermann, and M. Wuttig, "Phase-change materials: Vibrational softening upon crystallization and its impact on thermal properties", *Adv. Funct. Mater.*, vol. 21, pp. 2232–2239, 2011.
- [22] W. Massa, *Kristallstrukturbestimmung*, 7th ed. Vieweg+Teuner Verlag, Wiesbaden, 2011, ISBN: 978-3-8348-1726-6.
- [23] R. Allmann, *Röntgenpulverdiffraktometrie*, 1st ed. Springer-Verlag, Berlin Heidelberg New York, 2003, ISBN: 3-540-43967-6.
- [24] V. K. Pecharsky and P. Y. Zavalij, *Fundamentals of powder diffraction and structural characterization of materials*, 1st ed. Springer, 2005, ISBN: 0-387-24147-7.
- [25] N. M. Woolfson, "Direct methods in crystallography", *Rep. Prog. Phys.*, vol. 34, pp. 369–434, 1971.
- [26] *SHELX-97 manual, chapter 2: Structure Refinement*, <http://www.csb.yale.edu/userguides/datamanip/shelx/97/index.html>, 2019.
- [27] *IUCR-Online Dictionary of Crystallography: R factor*, http://reference.iucr.org/dictionary/R_factor, 2019.

- [28] N. W. Ashcroft and D. N. Mermin, *Festkörperphysik*. Oldenbourg Wissenschaftsverlag GmbH, München, 2012, ISBN: 978-3-486-71301-5.
- [29] C. Kittel, *Einführung in die Festkörperphysik*, 15th ed. Oldenbourg Wissenschaftsverlag GmbH, München, 2013, ISBN: 978-3-486-59755-4.
- [30] H. Schober, "An introduction to the theory of nuclear neutron scattering in condensed matter", *J. Neutron Res.*, vol. 17, pp. 109–357, 2014.
- [31] S. L. Chaplot, R. Mukhopadhyay, P. R. Vijayaghavan, A. S. Deshpande, and K. R. Rao, "Phonon density of states of tetracyanoethylene from coherent neutron scattering at Dhruva reactor", *J. Phys.*, vol. 33, pp. 595–602, 1989.
- [32] J. M. Carpenter and D. L. Price, "Correlated motions in glasses studied by coherent inelastic neutron scattering", *Phys. Rev. Lett.*, vol. 54, pp. 441–443, 1985.
- [33] S. L. Chaplot, N. Choudhury, S. Ghose, M. N. Rao, R. Mittal, and P. Goel, "Inelastic neutron scattering and lattice dynamics of minerals", *Eur. J. Mineral.*, vol. 14, pp. 291–329, 2002.
- [34] K. R. Rao, S. L. Chaplot, N. Choudhury, S. Ghose, J. M. Hastings, L. M. Corliss, and D. L. Price, "Lattice dynamics and inelastic neutron scattering from forsterite, Mg_2SiO_4 : Phonon dispersion relation, density of states and specific heat", *Phys. Chem. Minerals*, vol. 16, pp. 83–97, 1988.
- [35] D. L. Abernathy, M. B. Stone, M. J. Loguillo, M. S. Lucas, O. Delaire, X. Tang, J. Y. Y. Lin, and B. Fultz, "Design and operation of the wide angular-range chopper spectrometer ARCS at the spallation neutron source", *Rev. Sci. Instrum.*, vol. 83, no. 015114, 2012.
- [36] S. O. Diallo, J. Y. Y. Lin, D. L. Abernathy, and R. T. Azuah, "Momentum and energy dependent resolution function of the ARCS neutron chopper spectrometer at high momentum transfer: Comparing simulation and experiment", *Nucl. Instrum. Methods Phys. Res. A*, vol. 835, pp. 34–41, 2016.
- [37] T. Brückel, G. Heger, D. Richter, and R. Zorn, *Neutron Scattering - 5th Laboratory course*. Forschungszentrum Jülich, 2001, ISBN: 3-89336-288-6.
- [38] T. C. Gibb, *Principles of Mössbauer spectroscopy*, 1st ed. Springer US, 1976, ISBN: 978-1-4899-3023-1.
- [39] P. Gütlich, E. Bill, and A. X. Trautwein, *Mössbauer spectroscopy and transition metal chemistry*. Springer Berlin Heidelberg, 2011, ISBN: 978-3-540-88428-6.
- [40] R. Dronskowski, S. Kikkawa, and A. Stein, *Handbook of solid state chemistry*. 2017, vol. 1-6, ISBN: 978-3-527-32587-0.
- [41] A. Chumakov and R. Rüffer, "Nuclear inelastic scattering", *Hyperfine Interact.*, vol. 113, pp. 59–79, 1998.
- [42] R. Rüffer and A. Chumakov, "Nuclear inelastic scattering", *Hyperfine Interact.*, vol. 128, pp. 255–272, 2000.

- [43] P. Alexeev, "Nuclear resonance scattering study of iridates, iridium and antimony based pyrochlores", PhD thesis, University of Hamburg, 2017.
- [44] P. Alexeev, V. Asadchikov, D. Bessas, A. Butashin, A. Deryabin, F.-U. Dill, A. Ehnes, M. Herlitschke, R. P. Hermann, A. Jafari, I. Prokhorov, B. Roshchin, R. Röhlberger, K. Schlage, I. Sergueev, A. Siemens, and H.-C. Wille, "The sapphire backscattering monochromator at the dynamics beamline P01 of PETRA III", *Hyperfine Interact.*, vol. 237, no. 59, 2016.
- [45] A. Jafari, I. Sergueev, D. Bessas, B. Klobes, B. S. Roschin, V. E. Asadchikov, P. Alexeev, J. Härtwig, A. I. Chumakov, H.-C. Wille, and R. P. Hermann, "Rocking curve imaging of high quality sapphire crystals in backscattering geometry", *J. Appl. Phys.*, vol. 121, no. 044901, 2017.
- [46] V. G. Kohn, A. I. Chumakov, and R. Ruffer, "Nuclear resonant inelastic absorption of synchrotron radiation in an anisotropic single crystal", *Phys. Rev. B*, vol. 15, pp. 8437–8444, 1998.
- [47] W. Sturhahn, T. S. Toellner, E. E. Alp, X. Zhang, M. Ando, Y. Yoda, S. Kikuta, M. Seto, C. W. Kimball, and B. Dabrowski, "Phonon Density of States by Inelastic Nuclear Resonant Scattering", *Phys. Rev. Lett.*, vol. 74, pp. 3832–3835, 1995.
- [48] M. Seto, Y. Yoda, S. Kikuta, X. W. Zhang, and M. Ando, "Observation of Nuclear Resonant Scattering accompanied by Phonon excitation using synchrotron radiation", *Phys. Rev. Lett.*, vol. 74, pp. 3838–3821, 1995.
- [49] A. I. Chumakov and W. Sturhahn, "Experimental aspects of inelastic nuclear resonance scattering", *Hyperfine Interact.*, vol. 123/124, pp. 781–808, 1999.
- [50] W. Sturhahn and V. G. Kohn, "Theoretical aspects of incoherent nuclear resonant scattering", *Hyperfine interact.*, vol. 123/124, pp. 367–399, 1999.
- [51] D. W. Johnson and J. C. H. Spence, "Determination of the single-scattering probability distribution from plural-scattering data", *J. Phys. D: Appl. Phys.*, vol. 7, pp. 771–780, 1974.
- [52] D. Bessas, R. E. Simon, K. Friese, M. Koza, and R. P. Hermann, "Lattice dynamics in intermetallic Mg_2Ge and Mg_2Si ", *J. Phys.: Condens. Matter*, vol. 26, no. 485401, 2014.
- [53] H. Cynn and C.-S. Yoo, "Equation of state of tantalum to 174 GPa", *Phys. Rev. B*, vol. 59, pp. 8526–8529, 1999.
- [54] C. S. Menoni, J. Z. Hu, and I. L. Spain, "Germanium at high pressures", *Phys. Rev. B*, vol. 34, pp. 362–368, 1986.
- [55] P. W. Atkins and J. de Paula, *Physikalische Chemie*, 4th ed. Wiley-VCH Verlag, Weinheim, 2006, ISBN: 978-3-527-31546-8.

- [56] R. Pässler, "Limiting Debye temperature behavior following from cryogenic heat capacity data for group-IV, III-V, and II-VI materials", *Phys. Status Solidi*, vol. 247, pp. 77–92, 2010.
- [57] R. Pässler, "Characteristic non-Debye heat capacity formula applied to GaN and ZnO", *J. Appl. Phys.*, vol. 110, no. 043530, 2011.
- [58] W. N. Lawless and A. J. Morrow, "Specific heat and electrocaloric properties of a SrTiO₃ ceramic at low temperatures", *Ferroelectrics*, vol. 15, pp. 159–165, 1977.
- [59] W. N. Lawless and T. K. Gupta, "Thermal properties of tetragonal ZrO₂ at low temperatures", *Phys. Rev. B*, vol. 28, pp. 5507–5510, 1983.
- [60] J. C. Lashley, M. F. Hundley, A. Migliori, J. L. Sarrao, P. G. Pagliuso, T. W. Darling, M. Jaime, J. C. Cooley, W. L. Hults, L. Morales, D. J. Thoma, J. L. Smith, J. Boerio-Goates, B. F. Woodfield, G. R. Stewart, R. A. Fisher, and N. E. Phillips, "Critical examination of heat capacity measurements made on a Quantum Design Physical Property Measurement System", *Cryogenics*, vol. 43, pp. 369–378, 2003.
- [61] H. Suzuki, A. Inaba, and C. Meingast, "Accurate heat capacity data at phase transitions from relaxation calorimetry", *Cryogenics*, vol. 50, pp. 694–699, 2010.
- [62] *Physical Property Measurement System - Heat Capacity Option Users Manual*, 11th ed. Quantum Design, San Diego (USA), 2004.
- [63] M. Küpers, P. M. Konze, S. Maintz, S. Steinberg, A. M. Mio, O. Cojocar-Mirédin, M. Zhu, M. Müller, M. Luysberg, J. Mayer, M. Wuttig, and R. Dronskowski, "Unexpected Ge-Ge contacts in the two-dimensional Ge₄Se₃Te phase and analysis of their chemical cause with the density of energy (DOE) function", *Angew. Chem. Int. Ed.*, vol. 56, pp. 1–6, 2017.
- [64] M. G. Herrmann, R. P. Stoffel, M. Küpers, M. Ait Haddouch, A. Eich, K. Glazyrin, A. Grzechnik, R. Dronskowski, and K. Friese, "New insights on the GeSe_xTe_{1-x} phase diagram from theory and experiment", *Acta Cryst. B*, vol. 75, pp. 246–256, 2019.
- [65] M. Schönreich, M. P. Schmidt, and P. Schmidt, "Chemical vapour transport of bismuth and antimony chalcogenides M₂Q₃ (M=Sb, Bi, Q=Se, Te)", *Z. anorg. allg. Chem.*, vol. 636, pp. 1810–1816, 2010.
- [66] P. Lostak, R. Nowotny, L. Benes, and S. Civis, "Preparation and some physical properties of Sb₂Se_{3-x}Te_x single crystals", *J. Cryst. Growth*, vol. 94, pp. 656–662, 1989.
- [67] S. M. Souza, C. M. Poffo, D. M. Trichês, J. C. de Lima, T. A. Grandi, A. Polian, and M. Gauthier, "High pressure monoclinic phases of Sb₂Te₃", *Physica B*, vol. 407, pp. 3781–3789, 2012.

- [68] D. P. Gosain, T. Shimizu, M. Ohmura, and M. Suzuki, "Some properties of $\text{Sb}_2\text{Se}_{3-x}\text{Te}_x$ for nonvolatile memory based on phase transition", *J. Mater. Sci.*, vol. 26, pp. 3271–3274, 1991.
- [69] Y. Zhang, J. R. G. Evans, and S. Yang, "Corrected values for boiling points and enthalpies of vaporization of elements in handbooks", *J. Chem. Eng. Data*, vol. 56, pp. 328–337, 2011.
- [70] W. Klement jr., A. Yayaraman, and G. C. Kennedy, "Phase diagrams of arsenic, antimony and bismuth at pressure up to 70 kbars", *Phys. Rev.*, vol. 131, pp. 632–637, 1963.
- [71] B. Wunderlich and H.-C. Shu, "The crystallization and melting of selenium", *J. Cryst. Growth*, vol. 48, pp. 227–239, 1980.
- [72] F. C. Kracek, "The melting point of tellurium", *J. Am. Chem. Soc.*, vol. 63, pp. 1989–1900, 1941.
- [73] H. Liu, C. R. Knowles, and L. L. Y. Chang, "Extent of solid solution in Pb-Sn and Sb-Bi chalcogenides", *Canad. Mineral.*, vol. 33, pp. 115–128, 1995.
- [74] E. H. Baker, "The vapor pressure and resistivity of selenium at high temperature", *J. Chem. Soc.*, vol. A, pp. 1089–1092, 1968.
- [75] E. H. Baker, "The boiling point relation for tellurium at elevated pressures", *J. Chem. Soc.*, vol. A, pp. 1558–1560, 1967.
- [76] C. H. Polsky and E. van Valkenburg, *The diamond anvil cell*. 2006, vol. 1, ISBN: 9780470027325.
- [77] Y. Ma, G. Liu, P. Zhu, H. Wang, Q. Cui, J. Liu, and Y. Ma, "Determinations of the high-pressure crystal structures of Sb_2Te_3 ", *J. Phys.: Condens. Matter*, vol. 24, no. 475403, 2012.
- [78] I. Efthimiopoulos, J. Zhang, M. Kucway, C. Park, R. C. Ewing, and Y. Wang, " Sb_2Se_3 under pressure", *Sci. Rep.*, vol. 3, no. 2665, 2013.
- [79] A. Onodera, I. Sakamoto, Y. Fujii, N. Mōri, and S. Sugai, "Structural and electrical properties of GeSe and GeTe at high pressure", *Phys. Rev. B*, vol. 56, pp. 7935–7941, 1997.
- [80] H. K. Mao, Y. Wu, L. C. Chen, and J. F. Shu, "Static compression of iron to 300 GPa and $\text{Fe}_{0.8}\text{Ni}_{0.2}$ alloy to 260 GPa: Implications for composition of the core", *J. Geophys. Res.*, vol. 95, pp. 21 737–21 742, 1990.
- [81] A. L. Ruoff, H. Xia, H. Luo, and Y. K. Vohra, "Miniaturization techniques for obtaining static pressures comparable to the pressure at the center of the earth: X-ray diffraction at 416 GPa", *Rev. Sci. Instrum.*, vol. 61, pp. 3830–3833, 1990.
- [82] A. Yayaraman, "Diamond anvil cell and high-pressure physical investigations", *Rev. Mod. Phys.*, vol. 55, pp. 65–108, 1983.

- [83] I. Kantor, V. Prakapenka, A. Kantor, P. Dera, A. Kurnosov, S. Sinogeikin, N. Dubrovinskaia, and L. Dubrovinsky, "BX90: A new diamond anvil cell design for X-ray diffraction and optical measurements", *Rev. Sci. Instrum.*, vol. 83, no. 125102, 2012.
- [84] R. Letoullec, J. P. Pinceaux, and P. Loubeyre, "The membrane diamond anvil cell: A new device for generating continuous pressure and temperature variations", *High Pressures Res.*, vol. 1, pp. 70–90, 1988.
- [85] R. A. Forman, G. J. Piermarini, J. D. Barnett, and S. Block, "Pressure measurement made by the utilization of ruby sharp-line luminescence", *Science*, vol. 176, pp. 284–285, 1972.
- [86] H. K. Mao, J. Xu, and P. M. Bell, "Calibration of the ruby pressure gauge up to 800 kbar under quasi-hydrostatic conditions", *J. Geophys. Res.*, vol. 91, pp. 4673–4676, 1986.
- [87] Y. Akahama, H. Kawamura, and A. K. Singh, "Equation of state of bismuth to 222 GPa and comparison of gold and platinum pressure scales to 145 GPa", *J. Appl. Phys.*, vol. 92, pp. 5892–5897, 2002.
- [88] A. Dewaele, P. Loubeyre, and M. Mezouar, "Equations of state of six metals above 94 GPa", *Phys. Rev. B*, no. 094112, 2004.
- [89] D. L. Decker, "High-pressure equation of state for NaCl, KCl, and CsCl", *J. Appl. Phys.*, vol. 42, pp. 3239–3244, 1971.
- [90] K. Hirose, N. Sata, T. Komabayashi, and Y. Ohishi, "Simultaneous volume measurements of Au and MgO to 140 GPa and thermal equation of state of Au based on the MgO pressure scale", *Phys. Earth Planet. Inter.*, vol. 167, pp. 149–154, 2008.
- [91] A. F. Goncharov, J. M. Zaug, and J. C. Crowhurst, "Optical calibration of pressure sensors for high pressures and temperatures", *J. Appl. Phys.*, vol. 97, no. 094917, 2005.
- [92] F. Datchi, R. Letoullec, and P. Loubeyre, "Improved calibration of the $\text{SrB}_4\text{O}_7:\text{Sm}^{2+}$ optical pressure gauge: Advantages at very high pressures and high temperatures", *J. Appl. Phys.*, vol. 81, pp. 3333–3339, 1997.
- [93] H.-P. Liermann, Z. Konôpková, W. Morgenroth, K. Glazyrin, J. Bednarčík, E. E. McBride, S. Petigirard, J. T. Delitz, M. Wendt, Y. Bican, A. Ehnes, I. Schwark, A. Rothkirch, M. Tischer, J. Heuer, H. Schulte-Schrepping, T. Kracht, and H. Franz, "The Extreme Conditions Beamline P02.2 and the Extreme Conditions Science Infrastructure at PETRA III", *J. Synchrotron Rad.*, vol. 22, pp. 908–924, 2015.
- [94] W. A. Caldwell, M. Kunz, R. S. Celestre, E. E. Domning, M. J. Walter, D. Walker, J. Glossinger, A. A. MacDowell, H. A. Padmore, R. Jeanloz, and S. M. Clark, "Laser-heated diamond anvil cell at the advanced light source beamline 12.2.2", *Nucl. Instrum. Methods Phys. Res. A*, vol. 582, pp. 221–225, 2007.

- [95] C. Prescher and V. B. Prakapenka, "DIOPTAS: A program for reduction of two-dimensional X-ray diffraction data and data exploration", *High Press. Res.*, vol. 35, pp. 223–230, 2014.
- [96] V. Petricek, M. Dusek, and L. Palatinus, "Crystallographic computing system JANA2006: General features", *Z. Krist.*, vol. 229, pp. 345–352, 2014.
- [97] A. N. Mansour, W. Wong-Ng, Q. Huang, W. Tang, A. Thompson, and J. Sharp, "Structural characterization of Bi_2Te_3 and Sb_2Te_3 as a function of temperature using neutron powder diffraction and extended X-ray absorption fine structure techniques", *J. Appl. Phys.*, vol. 116, no. 083513, 2014.
- [98] M. Krbal, A. V. Kolobov, P. Fons, J. Haines, A. Pradel, M. Ribes, A. A. Piarristeguy, V. Agafonov, M. Hanfland, and J. Tominaga, "Pressure-induced structural transitions in phase-change materials based on Ge-free Sb-Te alloys", *Phys. Rev. B*, vol. 83, no. 024105, 2011.
- [99] J.-F. Bérar and P. Lelann, "E.S.D.'s and estimated probable error obtained in Rietveld refinements with local corrections", *J. Appl. Cryst.*, vol. 24, pp. 1–5, 1991.
- [100] CrysAlis Pro, Rigaku Oxford Diffraction, Yarnton, United Kingdom, 2015.
- [101] M. C. Burla, R. Caliendo, B. Carrozzini, G. L. Cascarano, C. Cuocci, M. Giacovazzo, C. Mallamo, A. Mazzone, and G. Polidori, "Crystal structure determination and refinement via SIR2014", *J. Appl. Cryst.*, vol. 48, pp. 306–309, 2015.
- [102] R. T. Azuah, L. R. Kneller, Y. Qiu, P. L. W. Tregenna-Piggott, C. M. Brown, J. R. D. Copley, and R. M. Dimeo, "DAVE: A comprehensive software suite for the reduction, visualization, and analysis of low energy neutron spectroscopic data", *J. Res. Natl. Inst. Stan. Technol.*, vol. 114, pp. 341–358, 2009.
- [103] I. Sergueev, Deutsches Elektronen-Synchrotron (DESY, Hamburg), PETRA-III, Private Communication, 2019.
- [104] V. G. Kohn and A. I. Chumakov, "DOS: Evaluation of phonon density of states from nuclear resonant inelastic absorption", *Hyperfine Interact.*, vol. 125, pp. 205–221, 2000.
- [105] R. P. Hermann, Oak Ridge National Laboratory (ORNL), Private Communication, 2019.
- [106] V. F. Spears, "Neutron scattering lengths and cross sections", *Neutron News*, vol. 3, pp. 26–37, 1992.
- [107] Z. Li, *Low temperature powder diffraction studies on ternary chalcogenides*, Bachelor Thesis, Fachhochschule Aachen Campus Jülich, 2017.
- [108] H. Wiedemeier and P. A. Siemers, "The temperature-composition phase diagram of the GeSe-GeTe system", *High Temp. Sci.*, vol. 17, pp. 395–408, 1984.

- [109] J. Goldak, C. S. Barrett, D. Innes, and W. Youdelis, "Structure of α -GeTe", *J. Chem Phys.*, vol. 44, pp. 3323–3325, 1966.
- [110] S. N. Dutta and G. A. Jeffrey, "On the structure of germanium selenide and related binary IV/VI compounds", *Inorg. Chem.*, vol. 4, pp. 1363–1366, 1965.
- [111] S. G. Karbanov, V. P. Zlomanov, and A. Novoselova, "Polymorphism of germanium telluride", *Doklady Chemistry*, vol. 182, pp. 862–863, 1968.
- [112] N. R. Serebryanaya, V. D. Blank, and V. A. Ivdenko, "GeTe-phases under shear deformation and high pressure up to 56 GPa", *Phys. Lett.*, vol. 197, pp. 63–66, 1995.
- [113] T. Chatterji, C. M. N. Kumar, and U. D. Wdowik, "Anomalous temperature-induced volume contraction in GeTe", *Phys. Rev. B*, vol. 91, no. 054110, 2015.
- [114] H. Wiedemeier and H. G. von Schnering, "Refinement of the structures of GeS, GeSe, SnS and SnSe", *Z. Krist.*, vol. 148, pp. 295–303, 1978.
- [115] J. E. Lewis, "A low temperature enhancement in the specific heat of germanium telluride", *Phys. Lett. A*, vol. 74, pp. 404–406, 1974.
- [116] R. A. Hein, J. W. Wilson, R. Mazelsky, R. C. Miller, and J. K. Hulm, "Superconductivity in Germanium Telluride", *Phys. Rev. Lett.*, vol. 12, pp. 320–322, 1964.
- [117] T. Fukunaga, S. Sugai, T. Kinosada, and M. Murase, "Observation of new Raman lines in GeSe and SnSe at low temperatures", *Solid State Commun.*, vol. 38, pp. 1059–1062, 1981.
- [118] A. Taube, A. Lapińska, J. Judek, N. Wochtman, and M. Zdrojek, "Temperature induced phonon behaviour in germanium selenide thin films probed by Raman spectroscopy", *J. Phys. D: Appl. Phys.*, vol. 49, no. 315301, 2016.
- [119] S. S. Kabalkina, N. R. Serebryanaya, and L. F. Vereshchagin, "Phase transitions in group IV-VI compounds at high pressure", *Fizika Tverdogo Tela*, vol. 10, pp. 733–739, 1968.
- [120] J. M. Leger and A. M. Redon, "Phase transformations and volume of the IV-VI GeTe semiconductor under high pressure", *J. Phys.: Condens. Matter*, vol. 2, pp. 5655–5662, 1990.
- [121] G.-S. Do, J. Kim, S.-H. Jhi, C.-H. Park, S. G. Louie, and M. L. Cohen, "Ab initio calculations of pressure-induced structural phase transitions of GeTe", *Phys. Rev. B*, vol. 82, no. 054121, 2010.
- [122] H. C. Hsueh, H. Vass, S. J. Clark, G. J. Ackland, and J. Crain, "High pressure effects in the layered semiconductor germanium selenide", *Phys. Rev. B*, vol. 51, pp. 16750–16760, 1995.
- [123] K. L. Bathia, G. Parthasarathy, D. P. Gosain, and E. S. R. Gopal, "Pressure-induced first-order transition in layered crystalline semiconductor GeSe to a metallic phase", *Phys. Rev. B*, vol. 1492–1494, 1986.

- [124] M. Xu, S. Jakobs, R. Mazzarello, J.-Y. Cho, Z. Yang, H. Hollermann, D. Shang, X. Miao, Z. Yu, L. Wang, and M. Wuttig, "Impact of pressure on the resonant bonding in chalcogenides", *J. Phys. Chem. C*, vol. 121, pp. 25 447–25 454, 2017.
- [125] S. Alptekin and M. Durandurdu, "Formation of a *Cmcm* phase in SnS at high pressure; an ab initio constant pressure study", *Solid State Commun.*, vol. 150, pp. 870–874, 2010.
- [126] H. Zhang, Y. Cheng, M. Tang, X. Chen, and G. Ji, "First-principles study of structural, elastic, electronic and thermodynamic properties of topological insulator Sb_2Te_3 under pressure", *Comput. Mater. Sci.*, vol. 96, pp. 342–347, 2015.
- [127] M. Durandurdu, "*Cmcm* phase of GeSe at high pressure", *Phys. Rev. B*, vol. 72, no. 144106, 2005.
- [128] F. O. von Rohr, H. Ji, A. Cevallos, T. Gao, N. P. Ong, and R. J. Cava, "High-pressure synthesis and characterization of β -GeSe – A six-membered-ring semiconductor in an uncommon boat conformation", *J. Am. Chem. Soc.*, vol. 139, pp. 2771–2777, 2017.
- [129] H. Yu, D. Gao, X. Wang, X. Du, X. Lin, W. Guo, R. Zou, C. Jin, K. Li, and Y. Chen, "Unraveling a novel ferroelectric GeSe phase and its transformation into a topological crystalline insulator under high pressure", *NPG Asia Materials*, vol. 82, pp. 882–887, 2018.
- [130] C.-H. Su, S. Feth, and S. L. Lehoczky, "Thermal expansion coefficient of ZnSe single crystal between 17 and 1080°C by interferometry", *Materials Letters*, vol. 63, pp. 1475–1477, 2009.
- [131] X. Chen, H. D. Zhou, A. Kiswandhi, I. Miotkowski, Y. P. Chen, P. A. Sharma, A. L. L. Sharma, M. A. Hekmaty, D. Smirnov, and Z. Jiang, "Thermal expansion coefficients of Bi_2Te_3 and Sb_2Te_3 from 10 K to 270 K", *Appl. Phys. Lett.*, vol. 99, no. 261912, 2011.
- [132] S. Ohta, Y. Adachi, T. Kaneko, M. Yuzuri, and H. Yoshida, "Thermal expansion in chromium chalcogenides Cr_2X_3 ($X = \text{Se}, \text{Te}$)", *J. Phys. Soc. Jpn.*, vol. 63, pp. 2225–2230, 1994.
- [133] D. Bansal, J. Hong, C. W. Li, A. F. May, W. Porter, M. Y. Hu, D. L. Abernathy, and O. Delaire, "Phonon anharmonicity and negative thermal expansion in SnSe", *Phys. Rev. B*, vol. 94, no. 054307, 2016.
- [134] G. P. Voutsas, A. G. Papazoglo, P. J. Rentzeperis, and D. Siapkas, "The crystal structure of antimony selenide, Sb_2Se_3 ", *Z. Krist.*, vol. 171, pp. 261–268, 1985.
- [135] T. L. Anderson and H. B. Krause, "Refinement of the Sb_2Te_3 and $\text{Sb}_2\text{Te}_2\text{Se}$ structures and their relationship to nonstoichiometric $\text{Sb}_2\text{Te}_{3-y}\text{Se}_y$ compounds", *Acta Cryst. B*, vol. 30, pp. 1307–1310, 1974.

- [136] L. Wu, M. Zhu, Z. Song, S. Lv, X. Zhou, C. Peng, F. Rao, S. Song, B. Liu, and S. Feng, "Investigation on Sb-rich Sb–Se–Te phase-change material for phase change memory application", *J. Non Cryst. Solids*, vol. 358, pp. 2409–2411, 2012.
- [137] A. K. Molodkin, V. I. Ivlieva, and E. V. Meshcheryakova, "Ordering in Sb_2Te_3 - Sb_2Se_3 solid solution", *Russ. J. Inorg. Chem.*, vol. 24, pp. 97–101, 1979.
- [138] H.-A. Ullner, "Strukturuntersuchungen am System $\text{Sb}_2\text{Te}_{3-x}\text{Se}_x$ ", *Ann. Phys.*, vol. 476, pp. 45–56, 1968.
- [139] M. Küpers, R. Stoffel, B. Bong, M. Herrmann, Z. Li, A. Meledin, J. Meyer, K. Friese, and R. Dronskowski, "Preferred selenium incorporation and unexpected interlayer bonding in the layered structure of $\text{Sb}_2\text{Te}_{3-x}\text{Se}_x$ ", 2019, To be submitted.
- [140] G. C. Sosso, S. Caravati, and M. Bernasconi, "Vibrational properties of crystalline Sb_2Te_3 from first principles", *J. Phys.: Condens. Matter*, vol. 21, no. 095410, 2009.
- [141] D. Das, K. Malik, S. Das, P. Singha, V. A. Kulbachinskii, A. K. Deb, R. Basu, S. Dhara, A. Dasgupta, S. Bandyopadhyay, and A. Banerjee, "Modulation of thermal conductivity and thermoelectric figure of merit by anharmonic lattice vibration in Sb_2Te_3 thermoelectrics", *AIP Adv.*, vol. 8, no. 125119, 2018.
- [142] A. Bera, K. Pal, D. V. S. Muthu, S. Sen, P. Guptasarma, U. V. Waghmare, and A. K. Sood, "Sharp Raman anomalies and broken adiabaticity at a pressure induced transition from band to topological insulator in Sb_2Se_3 ", *Phys. Rev. Lett.*, vol. 110, no. 107401, 2013.
- [143] P. Dutta, D. Bhoi, A. Midkya, N. Khan, P. Mandal, and S. S. Samathan, "Anomalous thermal expansion of Sb_2Te_3 topological insulator", *Appl. Phys. Lett.*, vol. 100, no. 251912, 2012.
- [144] V. M. Zhdanov, "Low-temperature heat capacity, enthalpy and entropy of antimony selenide", *Russ. J. Phys. Chem.*, vol. 45, p. 1356, 1971.
- [145] H. Koc, A. M. Mamedov, E. Deligoz, and H. Ozisik, "First principles prediction of the elastic, electronic, and optical properties of Sb_2S_3 and Sb_2Se_3 compounds", *Solid State Sci.*, vol. 14, pp. 1211–1220, 2012.
- [146] M. G. Herrmann, R. P. Stoffel, R. Dronskowski, and K. Friese, "The low-temperature heat capacity of the $\text{Sb}_2\text{Te}_{3-x}\text{Se}_x$ solid solution from experiment and theory", *J. Phys.: Condens. Matter*, vol. 30, no. 405702, 2018.
- [147] D. Das, S. Das, P. Singha, K. Malik, A. K. Deb, A. Bhattacharyya, V. A. Kulbachinskii, R. Basu, S. Dhara, S. Bandyopadhyay, and A. Banerjee, "Evolution of phonon anharmonicity in Se-doped Sb_2Te_3 thermoelectrics", *Phys. Rev. B*, vol. 96, no. 064116, 2017.

- [148] J.-C. Jumas, J. Olivier-Fourcade, A. Ibanez, and E. Philippot, "¹²¹Sb Mössbauer studies on antimony III chalcogenides and chalcogenohalides. Application to the structural approach of sulfide glasses", *Hyperfine Interact.*, vol. 28, pp. 777–780, 1986.
- [149] I. Sergueev, K. Glazyrin, M. G. Herrmann, P. Alexeev, H.-C. Wille, O. Leupold, A. F. May, T. Pandey, L. Lindsay, K. Friese, and R. P. Hermann, "High pressure nuclear inelastic scattering with backscattering monochromatization", *J. Synchr. Radiation*, 2019, Accepted.
- [150] E. Dachs and C. A. Geiger, "Heat capacity and entropies of mixing of pyrope-grossular ($\text{Mg}_3\text{Al}_2\text{Si}_3\text{O}_{12}$ - $\text{Ca}_3\text{Al}_2\text{Si}_3\text{O}_{12}$) garnet solid solutions: A low-temperature calorimetric and thermodynamics investigation", *Am. Mineral.*, vol. 91, pp. 894–906, 2006.
- [151] D. L. Abernathy, Oak Ridge National Laboratory (ORNL), Private Communication, 2019.
- [152] M. Zhu, O. Cojocaru-Mirédin, A. M. Mio, J. Keutgen, M. Küpers, Y. Yu, J.-Y. Cho, R. Dronskowski, and M. Wuttig, "Unique bond breaking in crystalline phase change materials and the quest for metavalent bonding", *Adv. Mater.*, vol. 30, no. 1706735, 2018.
- [153] R. E. Simon, I. Sergueev, I. Kantor, J. Perßon, and R. P. Hermann, "¹²¹Sb and ¹²⁵Te nuclear inelastic scattering in Sb_2Te_3 under high pressure", *Semicond. Sci. Tech.*, vol. 29, no. 124001, 2014.
- [154] R. E. Snyder and G. B. Beard, "Decay of ^{121m}Sn and ¹²¹Sn", *Nuclear Physics*, vol. A113, pp. 581–592, 1968.
- [155] S. Ohya, "Nuclear data sheets for A=121", *Nuclear Data Sheets*, vol. 111, pp. 1619–1806, 2010.
- [156] R. P. Hermann, F. Grandjean, T.-S. Chen, D. E. Brown, C. E. Johnson, G. S. Snyder, and G. J. Long, "Antimony-121 Mössbauer spectral study of α - Zn_4Sb_3 ", *Inorg. Chem.*, vol. 46, pp. 767–770, 2007.
- [157] G. Langouche, B. Triplett, N. Dixon, S. Hanna, and P. Boolchand, "Nuclear orientation effects in the Mössbauer spectrum of ¹²⁵Te in Pd_2MnSb ", *J. Phys.*, vol. 37, pp. 653–655, 1976.
- [158] J. Katakura, "Nuclear data sheets for A=125", *Nuclear Data Sheets*, vol. 112, pp. 495–705, 2011.
- [159] A. Y. A. Yasiri and H. F. Abed, "Estimation of energy spectrum and energy deposition of photons emitted from brachytherapy ¹²⁵I seed", *Indian J. Sci. Technol.*, vol. 11, pp. 1–5, 2018.

- [160] B. M. Cheyne, C. H. W. Jones, and P. Vasudev, "The ^{125}Te Mossbauer absorption spectra of the thiourea, ethylenethiourea, and tetramethylthiourea derivatives of Tellurium(II) and Tellurium(IV)", *Canad. J. Chem.*, vol. 50, pp. 3677–3685, 1972.